Linear and Nonlinear Spectroscopy of Doped Carbon Nanotubes

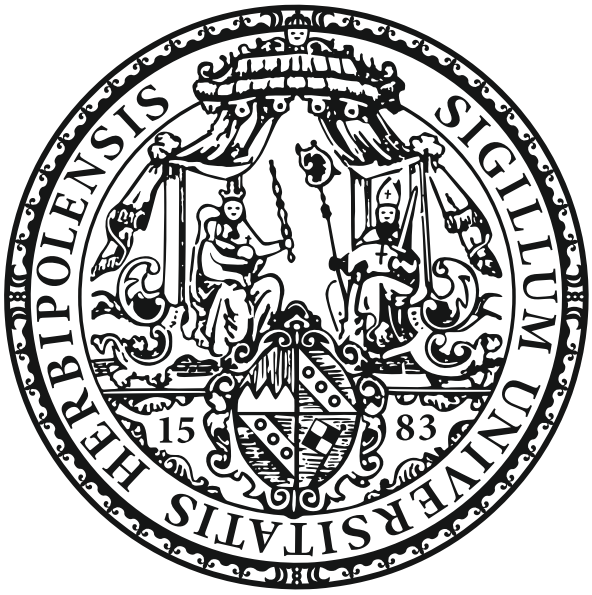

Dissertation zur Erlangung des naturwissenschaftlichen Doktorgrades der Julius-Maximilians-Universität Würzburg

vorgelegt von

Klaus Eckstein

aus Heidenheim an der Brenz

Würzburg, 2019

Eingereicht bei der Fakultät für Chemie und Pharmazie
am _____

Gutachter der schriftlichen Arbeit
1. Gutachter: _____
2. Gutachter: _____

Prüfer des öffentlichen Promotionskolloquiums
1. Prüfer: _____
2. Prüfer: _____
3. Prüfer: _____

Datum des öffentlichen Promotionskolloquiums: _____
Doktorurkunde ausgehändigt am: _____

Contents

List of Abbreviations v

1 Introduction 1

2 Theoretical Background 5

2.1 Fundamentals of Semiconductor Doping . . . 5
2.1.1 Electronic Structure of Solid-State Materials . . . 5
2.1.2 Intrinsic and Doped Semiconductors . . . 6
2.1.3 Gerischer Model and Redox Chemical Doping . . . 9
2.2 Single-Wall Carbon Nanotubes . . . 11
2.2.1 Nomenclature and Geometrical Structure . . . 11
2.2.2 Electronic Structure . . . 11
2.2.3 Photophysical Properties . . . 13
2.3 Spatial Localization . . . 18
2.3.1 General Remarks . . . 19
2.3.2 Carbon Nanotubes . . . 20
2.4 Intraband Absorption of Free and Localized Carriers . . . 22
2.4.1 Drude and Drude-Sommerfeld Model . . . 23
2.4.2 Modifications due to Localization . . . 25
2.4.3 Monte-Carlo Simulations . . . 27

3 Experimental Methods 31

3.1 Sample Preparation . . . 31
3.1.1 Selective Dispersion of (6,5)-SWNTs . . . 31
3.1.2 Preparation of SWNT Films . . . 32
3.1.3 Redox Chemical Doping of SWNT Samples . . . 33
3.2 Steady-State Spectroscopy . . . 34
3.2.1 UV-VIS-NIR Absorption Spectroscopy . . . 34
3.2.2 Fourier-Transform Infrared Spectroscopy . . . 34
3.2.3 Photoluminescence Excitation Spectroscopy . . . 34
3.3 Time-Resolved Spectroscopy . . . 35
3.3.1 The Femtosecond Laser System . . . 35
3.3.2 The Transient Absorption Setup . . . 36
3.3.3 Data Acquisition and Measurement Principle . . . 37
3.3.4 Laser Pulse Characterization . . . 40
3.3.5 Post Measurement Corrections . . . 42

3.4 Spectroelectrochemistry . . . 43
3.4.1 Thin-Film Spectroelectrochemistry . . . 43
3.4.2 Spectroelectrochemistry in Solution . . . 44

4 Comparison of Electro- and Redox Chemical Doping Schemes 45
4.1 Thermodynamical Considerations . . . 46
4.2 Quantification of Doping Levels . . . 48

5 Spectroscopy in the Moderate Doping Regime – Evidence for Charge Localization 49
5.1 State of the Art . . . 49
5.2 Doping-Induced Changes in Interband Absorption . . . 51
5.2.1 First Subband Exciton . . . 53
5.2.2 Second Subband Exciton . . . 59
5.2.3 Discussion of Doping-Induced Absorbance Changes . . . 63
5.3 Dynamical Properties of Excitons and Trions . . . 66
5.3.1 PL Spectroscopy . . . 66
5.3.2 Time-Resolved Spectroscopy . . . 72
5.4 Intraband Absorption of Charge Carriers . . . 77
5.4.1 Broadband Transmission Spectroscopy . . . 77
5.4.2 Transition from Localized to Delocalized Carriers . . . 84
5.5 Metal-Insulator Transition Model . . . 88
5.6 Summary . . . 90

6 Heavy or Degenerate doping 93
6.1 State of the Art . . . 93
6.2 H-band in Linear Absorption Spectroscopy . . . 94
6.3 Nonlinear Optical Response . . . 96
6.3.1 Intrinsic SWNTs . . . 98
6.3.2 Heavily Doped SWNTs . . . 102
6.4 Discussion of the Microscopic Origin of the H-band . . . 104
6.5 Interaction of Degenerately Doped SWNTs with IR Radiation . . . 107
6.5.1 Extended Drude Analysis . . . 107
6.5.2 Infrared Reflectivity . . . 109
6.6 Summary and Outlook . . . 111

7 Quantifying Doping in CNTs Using Absorption Spectroscopy 113
7.1 Exciton Confinement Model . . . 113
7.2 Phase Space Filling Model . . . 115
7.2.1 Low-Temperature Limit . . . 117
7.2.2 Arbitrary Temperatures . . . 118
7.3 First Subband Analysis . . . 119

7.4 Comparison of the Models . . . 121
7.5 Summary and Outlook . . . 122

8 Time-Resolved Spectroelectrochemistry in Solution 125
8.1 Description of the Flow-Electrolysis Cell . . . 126
8.2 Electrochemical Characterization . . . 127
8.3 Proof of Principle TA Measurements . . . 131
8.4 Conclusion and Outlook . . . 133

9 Summary 135

10 Zusammenfassung 137

11 Appendix 139
11.1 Exciton PL Quantum Yield . . . 139
11.2 Drude Analysis of Heavily Doped SWNTs . . . 141

Bibliography 145

List of Figures 169

Acknowledgement 173

List of Abbreviations

1D	one-dimension(al)
2D	two-dimension(al)
3D	three-dimension(al)
BGR	band gap renormalization
CB	conduction band
CCD	charge-coupled device
CMOS	complementary metal-oxide-semiconductor
CoMoCAT®	cobalt molybdenum catalyst
DC	direct current
DLCQ	diffusion limited contact quenching
DOS	density of states
ESR	electron spin resonance
F_4TCNQ	2,3,5,6-Tetrafluoro-7,7,8,8-tetracyanoquinodimethane
FEC	flow-electrolysis cell
FET	field-effect transistor
FWHM	full width at half maximum
IR	infrared
LMB	leucomethylene blue
MB	methylene blue
MC	Monte-Carlo
MO	molecular orbital
NIR	near infrared
OA	triethyloxonium hexachloroantimonate
OPA	optical parametric amplifier
OSR	oscillator strength reduction
PA	photoabsorption
PB	photobleach
PAIEI	phonon-assisted indirect exciton ionization
PFO-BPy	poly[(9,9-dioctylfluorenyl-2,7-diyl)-alt-co-(2,6-bi-pyridine)
PL	photoluminescence
PLE	photoluminescence excitation
PLQY	photoluminescence quantum yield
PSF	phase space filling
SHE	standard hydrogen electrode
SHG	second harmonic generation

SWNT	single-wall carbon nanotube
TA	transient absorption
TCNQ	7,7,8,8-Tetracyanoquinodimethane
TMD	transition metal dichalcogenide
UV	ultraviolet
VAC	vacuum level
VB	valence band
VIS	visible
WE	working electrode

1 Introduction

Most of our present economic and social life is unthinkable without technology based on semiconductors. Maybe the most critical step for the use of semiconductors in electronic devices is the ability to controllably introduce mobile excess charge carriers. This process is called doping and is at the heart of semiconductor processing.

A prominent example of doping-based semiconductor technology is the transistor, invented by Shockley, Brattain and Bardeen about 70 years ago [1, 2]. Their discovery is considered the starting point of the so-called information age, driven by progress in computer, data storage and telecommunication technologies [1, 3]. Closely related is the miniaturization of electronic devices. The number of transistors in modern cell phones is continuously rising and has reached more than one billion [4]. However, the scaling of silicon-based technology has reached its physical limits [5]. For further miniaturization, the use of semiconducting nanomaterials seems intriguing. Semiconducting carbon nanotube transistors, for example, promise to outperform silicon transistors in terms of size and energy efficiency [6–8].

Moreover, carbon nanotubes possess very high carrier mobilities [9] and may exhibit ballistic transport [10]. They also strong light absorption in the near infrared [11] and high sensitivity to the environment [12]. These properties make them an attractive material class not only for purely electronic but also for optoelectronic and sensing applications. However, despite almost 30 years of research, the implementation of semiconducting nanotubes into new technologies does not meet expectations. In the past, this has often been attributed to difficulties with the separation of semiconducting and metallic carbon nanotubes. However, recent progress in nanotube purification and separation now allows the production of semiconducting nanotubes in high purity [8, 13–16] and large quantity [17]. Still, nanotubes are hardly used in technology.

As for bulk silicon crystals, the doping of semiconducting carbon nanotubes is a critical step to provide device functionality. However, in contrast to bulk semiconductors, doping of carbon nanotubes is only poorly understood. This may partly explain the lack of a viable carbon nanotube-based technology.

In order to understand and optimize the doping process, precise knowledge about the density and distribution of excess charges is inevitable. Therefore, the following questions regarding the doping of carbon nanotubes have to be addressed:

- How can charge carrier densities be determined?
- Can charge carriers be described as free or localized?
- How abundant and deep are charge traps?
- Over which length scales are carriers delocalized?

Doping not only changes the electronic properties of low-dimensional, nanoscale semiconductors but it also impacts their optical properties [18–22]. Light absorption by intrinsic carbon nanotubes leads to the formation of strongly bound neutral electron-hole pairs, so-called excitons [23–26]. In doped carbon nanotubes, new absorption bands associated with charged excitons (trions) arise [27–30]. As a consequence, exciton and trion absorption or luminescence can be tuned by doping [18, 31]. Conversely, this property allows probing doping levels and doping behavior using the optical response.

The main goal of this thesis is to gain a better understanding of how excess charges provided by doping change the optical properties of semiconducting carbon nanotubes. In turn, this knowledge is used to understand the doping process better in terms of the carrier concentration and distribution.

Outline of the thesis

Chapter 2 describes the theoretical basics, which are necessary for the understanding of the design of experiments and the interpretation of the experimental results. Besides the physical properties of carbon nanotubes, the fundamentals of semiconductor doping are provided. This is followed by a discussion of the prerequisites for spatial localization and the theoretical models of infrared absorption caused by free and localized carriers. The chapter closes with the description of Monte-Carlo simulations of charge transport.

Chapter 3 outlines the preparation of nanotube samples highly enriched in semiconducting species and the spectroscopic techniques used for their investigation.

The influence of different doping schemes, *i.e.*, electro- or redox chemical doping, on the linear absorption spectra of carbon nanotubes is investigated in **chapter 4**. Both doping schemes are compared using thermodynamical considerations.

Chapter 5 discusses the possible localization of charge carriers in the moderate doping regime using a variety of spectroscopic techniques. The techniques range from broadband absorption spectroscopy from the ultraviolet to the far infrared over photoluminescence to time-resolved spectroscopy. The broad spectroscopic range allows a deep insight not only into the static and dynamical interaction of charge carriers with optically generated species like excitons or trions but also into low energy intraband absorption processes.

Chapter 6 is concerned with linear and nonlinear spectroscopy of heavily doped carbon nanotubes. In this doping regime, the nanotubes are characterized by the absence of exciton and trion absorption and show a broad, featureless and nearly constant absorption over a very broad energy range. The main focus of this chapter is the investigation of the microscopic origin of this absorption band. In addition, the infrared reflection properties caused by free carriers in heavily doped nanotubes are elucidated.

Chapter 7 discusses how nanotube charge carrier concentrations may be determined by optical spectroscopy. The doping-induced absorbance changes are related to the charge density using band structure calculations and different models.

Based on the experience with time-resolved spectroelectrochemistry on carbon nanotube thin-films, **chapter 8** introduces a method that allows the investigation of a wider variety of molecular systems. More specifically, the method aims at ultrafast laser spectroscopy of *in-situ* electrochemically generated and photo-unstable molecular species in solution. For this purpose, a flow-electrolysis cell was integrated into a transient absorption setup. The chapter focuses on the characterization of the flow-electrolysis cell in terms of electrolysis conversion efficiency and errors in the working electrode potential. First results of time-resolved spectroscopic experiments using this newly developed method are also presented.

Lastly, **chapters 9** and **10** summarize the main results in English and German language.

2 Theoretical Background

In this thesis, the spectroscopic properties of intrinsic and doped semiconducting single-wall carbon nanotubes (SWNTs) are investigated. The following chapter intends to provide the background information needed to understand the design of experiments and the interpretation of data.

First, a brief introduction to the electronic structure of solid-state materials is given. This is followed by a more detailed explanation concerning the role of doping for semiconductors. Later, single-wall carbon nanotubes are introduced, and the physical process of spatial localization is explained. Different models of doping-induced intraband absorption are presented. The chapter closes by the description of a Monte-Carlo algorithm for simulating intraband absorption spectra.

2.1 Fundamentals of Semiconductor Doping

2.1.1 Electronic Structure of Solid-State Materials

In the following, a simple molecular orbital picture is used to introduce the notions of energy bands and band gaps. These concepts are explained by regarding a hypothetical linear chain of hydrogen atoms. The hydrogen atom consists of one positive and one negative charge, bound together by the Coulomb interaction. This is therefore also a useful model to describe shallow donors/acceptors and excitons, ideas which are introduced in section 2.1.2 and 2.2.3.

Fig. 2.1a shows the hydrogen atom in the Bohr model as an electron orbiting the positive nucleus and the quantum mechanical treatment using wavefunctions. The exponential 1s ground state wavefunction Ψ decays to 1/e of its maximum amplitude at the Bohr radius $a_0 = 0.53\,\text{Å}$. The electron in the 1s state has a binding energy E_b of one Rydberg $R_\text{H} = 13.6\,\text{eV}$. Fig. 2.1b illustrates what happens if two hydrogen atoms are brought at a distance on the order of the Bohr radius a_0 [33, 34]: The two 1s wavefunctions start to overlap, which results in a doubly occupied bonding σ and an empty antibonding σ^* molecular orbital (MO). These σ and σ^* states are energetically well separated and therefore represent discrete energy levels. The individual electrons are not localized at one atom anymore but delocalized over the whole molecule. The combination of N hydrogen atoms – according to MO theory – leads to the formation of N MOs on which N electrons are distributed according to the Pauli principle and Hund's rule. For a very large number of hydrogen atoms, the energetic spacing of adjacent MOs becomes very small. In this case, the energy levels are no longer discrete but rather continuous, giving rise to the formation of an energy band. The lower half of the energy levels

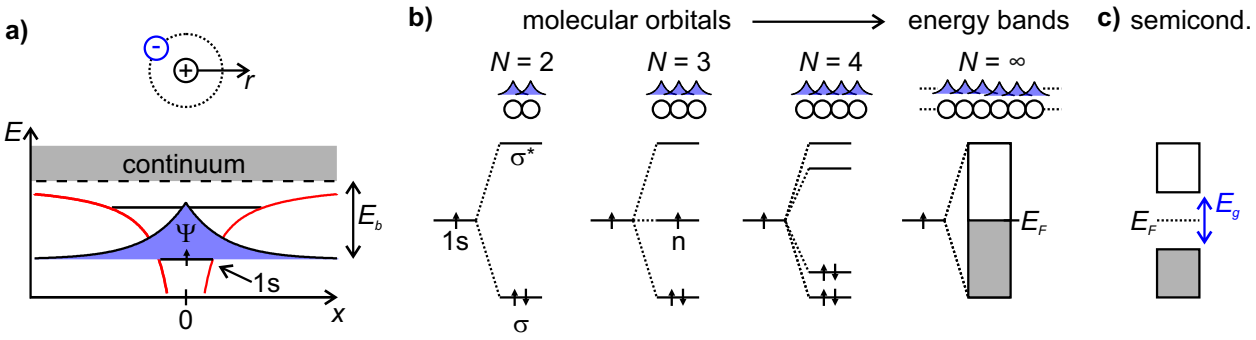

Figure 2.1: a) Illustration of Bohr's model of hydrogen as an electron orbiting around the positively charged nucleus (top) and quantum mechanical treatment (bottom). The Coulomb potential is shown in red, whereas the blue area displays the ground state 1s wavefunction Ψ. b) The interaction of two, three and four close-by 1s atomic orbitals leads to discrete bonding, non-bonding and antibonding molecular orbitals (MOs). The interaction of an infinite number of equally spaced hydrogen atoms causes the formation of an energy band with very close-lying states. The lower half of the states are occupied, and the upper half of the states are empty. The Fermi energy E_F lies within the energy band, which is characteristic of a metal. c) Situation for a semiconductor, in which the Fermi energy is located within the band gap. Drawn after Rühl [32].

are occupied, whereas the upper half of the energy levels are empty. The Fermi level E_F is in the middle of the energy band, which means that this linear chain of hydrogen atoms is metallic.

Fig. 2.1c shows the situation for materials, in which the Fermi level is located between a fully occupied band and an empty band. The energetic separation of the two bands is referred to as the band gap energy E_g and determines if the material behaves like a semiconductor or insulator. Materials with a band gap of $E_g \gtrsim 4\,\text{eV}$, like diamond ($E_g = 5.5\,\text{eV}$), are typically considered insulators. If the band gap is $E_g \lesssim 4\,\text{eV}$, like in the case of silicon ($E_g = 1.1\,\text{eV}$), the material is semiconducting [35, 36].

2.1.2 Intrinsic and Doped Semiconductors

According to Zunger, "the failure to successfully dope certain classes of materials is an important bottleneck for the technical utilization" [37].

Semiconductor doping refers to any intentional process leading to the introduction of free surplus charge carriers into an otherwise intrinsic semiconductor [33, 34, 38, 39]. The primary purpose of doping is to alter the electrical conductivity and Fermi level position necessary for device functionality [40], although the modulation of optical or other physical properties might also be of interest.

Most of the following content, if not cited otherwise, is based on the books *The Physics of Semiconductors* by Grundmann [33], *Dopants and Defects in Semiconductors* by McCluskey and Haller [34] and *Physical Foundations of Solid-State Devices* by Schubert [41].

In a pristine semiconductor, the free carrier concentration is an intrinsic material constant,

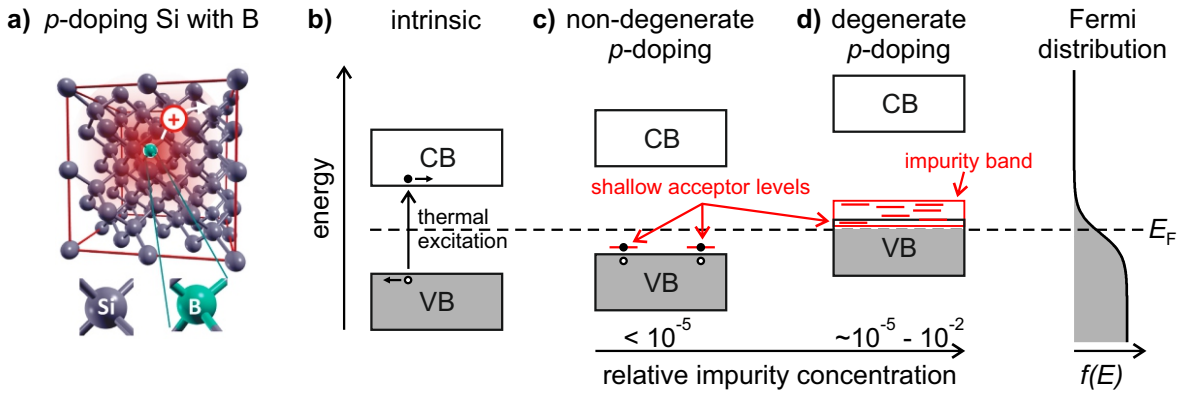

Figure 2.2: a) Illustration of substitutional silicon p-doping with boron atoms. b) Band diagram of intrinsic, c) non-degenerately doped and d) degenerately doped silicon. Adapted from *Journal of Electron Spectroscopy and Related Phenomena*, 204, I. Salzmann and G. Heimel, *Toward a comprehensive understanding of molecular doping organic semiconductors (review)*, 208-222, **2015**, with permission from Elsevier [39].

and the Fermi level is close to the middle of the band gap. Fig. 2.2b shows a simplified band diagram of such an intrinsic semiconductor. At zero temperature and in the absence of light, the valence band (VB) is fully occupied, the conduction band (CB) is empty, and free carriers are absent. At finite temperatures ($T > 0\,\mathrm{K}$), thermal excitation of electrons across the band gap leads to mobile electrons in the CB and mobile holes in the VB. The temperature dependence of intrinsic carrier concentrations $n_\mathrm{i}(T) \propto T^{3/2}\,\exp(-E_g/2kT)$ exponentially depends on the magnitude of the band gap E_g. This exponential band gap dependence is the reason why wide band gap materials ($E_g \gtrsim 4\,\mathrm{eV}$) are considered electrically insulating. As an example, the room temperature free carrier concentration in intrinsic silicon with a 1.1 eV band gap is $n_\mathrm{i} \approx 10^{10}\,\mathrm{cm}^{-3}$ [33]. This carrier density corresponds roughly to only one mobile charge per 10^{12} silicon atoms.

Substitutional doping dramatically enhances the free carrier concentrations in bulk crystalline semiconductors. In silicon, for example, the incorporation of phosphorus or boron impurities (see Fig. 2.2a) into the silicon lattice leads to n- and p-doping, respectively. This produces localized impurity states energetically located near the band edges (see Fig. 2.2c), and these states are classified as shallow donor or acceptor (D/A) levels. The energetic separation between the shallow D/A level and the adjacent band edge determines the ionization/binding energy E_b. The binding energy between the free carrier and the oppositely charged impurity ion as well as the Bohr radius a_0 can be estimated with a modified hydrogen model as long as the appropriate effective carrier masses and dielectric constant of the host semiconductor material are used.

At room temperature ($kT \approx 25\,\mathrm{meV}$), the impurities are easily ionized due to low binding energies on the order of $E_\mathrm{b} \approx 40 - 50\,\mathrm{meV}$ [42, 43]. This ionization process introduces free carriers into the VB or CB, which are considered delocalized and freely movable due to band transport. As a consequence of complete ionization, the free carrier concentration n equals

the donor or acceptor concentration $n = N_{\mathrm{D/A}}$. Therefore, in the weak doping regime of only a few impurities, for example, 1 per 10^8 Si atoms, the free-carrier concentration is increased by already four orders of magnitude compared to intrinsic silicon.

At low temperatures $T \ll E_{\mathrm{b}}/k$, the free carrier concentration n sharply decreases due to preferential localization (trapping) of the excess charges at the oppositely charged dopant ions. The reason for this so-called freeze-out is that ionization energies cannot be overcome thermally anymore. Close to zero temperature, the semiconductor becomes electrically insulating. In the weak doping regime with a D/A concentration $N_{\mathrm{D/A}} \ll a_0^{-3}$, impurity wavefunctions do not overlap, and interactions between impurities can be neglected. As a consequence, there is no preference for the impurity atoms to substitute certain host atoms. Impurity positions can then be assumed to be randomly distributed, and the nearest neighbor distance distribution is Poissonian [38, 41].

In the following, the heavy doping regime, in which the impurity concentration $N_{\mathrm{D/A}}$ approaches a_0^{-3}, is considered. In this case, impurities are not isolated anymore, and interaction occurs like in the case of two hydrogen atoms brought close enough together (see section 2.1.1). The overlap of individual donor/acceptor potentials leads to the possibility of hopping conduction from neutral to ionized donors without the promotion of carriers to the VB/CB. Another consequence arises from the wavefunction overlap at close distances: The impurity energy levels split (see Fig. 2.2d) and a higher degree of delocalization results. At a very high donor/acceptor density $N_{\mathrm{D/A}} \approx a_0^{-3}$, the formation of so-called impurity bands is possible.

If the Fermi level E_{F} is close to (within a few kT) or is even pushed into this newly formed energy band or into the original VB/CB, the highly doped semiconductor behaves more like a metal than a semiconductor. Such a heavily doped semiconductor is referred to being degenerate (see reference [44] for additional details). A consequence of metallic behavior is the temperature independence of the free carrier concentration n and the absence of a low-temperature freeze-out [41, 45, 46].

The transition from an insulating weakly doped semiconductor at low-temperatures to a metallic-like heavily doped semiconductor is a gradual one. Temperature-dependent conductivity and mobility experiments revealed that activation or binding energies continuously decrease for increasing dopant concentrations [41, 45, 46].

In contrast to bulk crystalline semiconductors, low dimensional semiconductors like organic semiconducting polymers are typically doped electro- or redox chemically. Excess charges are then often found to be spatially localized due to self-trapping caused by a lattice deformation around the charge [47]. This self-trapping leads to polaron formation [36, 48]. Carrier localization due to Coulomb interaction with poorly screened counterions, dipoles, or polarizable molecules represents another frequently discussed localization mechanism [49].

SWNTs possess characteristics of both types of materials, crystalline inorganic semiconductors and organic polymers. They share the crystallinity and rigidity with bulk semiconductors, but low dielectric constants ($\epsilon \lesssim 4$) with organic semiconducting polymers [49–51]. As a

consequence of the latter and the so-called antiscreening [52], Coulomb binding energies are largely enhanced if compared to bulk semiconductors ($\epsilon = 11.7$ for silicon [33]).

2.1.3 Gerischer Model and Redox Chemical Doping

Electrochemical experiments in solution are mostly carried out using inert metal electrodes. Nevertheless, semiconductor electrodes can also be used. Gerischer introduced a model to describe electrochemical processes at semiconductor surfaces [53, 54]. He transferred concepts from solid-state physics like the density of states or the Fermi energy to solution electrochemistry in order to describe redox couples with the same terminology. Here, the Gerischer model is briefly introduced but the interested reader finds a more detailed description in the book *Semiconductor electrochemistry* by Memming [54] and in the original work of Gerischer [53, 55].

An electron transfer reaction of the form $\mathrm{Red} \rightleftharpoons \mathrm{Ox} + \mathrm{ze^-}$ defines the redox couple Red/Ox. Molecules in the oxidized form (Ox) can accept electrons, which are transferred to normally unoccupied states according to Gerischer. Molecules in the reduced form (Red) provide electrons residing in occupied states. Fig. 2.3a shows the energy distributions $W_{\mathrm{Red/Ox}}$ of the occupied and unoccupied states, which are given by normalized Gaussian functions [54]:

$$W_{\mathrm{Red}}(E) = (4\pi\lambda kT)^{-1/2} \exp\left(-\frac{(E - E^{\ominus}_{\mathrm{F,redox}} + \lambda)^2}{4\lambda kT}\right) \tag{2.1}$$

$$W_{\mathrm{Ox}}(E) = (4\pi\lambda kT)^{-1/2} \exp\left(-\frac{(E - E^{\ominus}_{\mathrm{F,redox}} - \lambda)^2}{4\lambda kT}\right), \tag{2.2}$$

where λ represents reorganization energies, which for the sake of simplicity are taken to be equal for the oxidized and reduced species. The broadening of the energy distribution is assumed to be dominated by fluctuations in the solvent arrangement around Ox and Red. The standard Fermi level $E^{\ominus}_{\mathrm{F,redox}}$ of the redox couple highlights the analogy to solid-state physics. The density of states $\mathrm{DOS}(E)$ of the occupied and unoccupied energy levels is obtained by multiplying the energy distribution function $W(E)$ with the concentration $c_{\mathrm{Red/Ox}}$ of Ox and Red:

$$\mathrm{DOS}_{\mathrm{Red}}(E) = c_{\mathrm{Red}} W_{\mathrm{Red}} \tag{2.3}$$

$$\mathrm{DOS}_{\mathrm{Ox}}(E) = c_{\mathrm{Ox}} W_{\mathrm{Ox}}. \tag{2.4}$$

Next, electron transfer reactions between a semiconductor electrode and the molecules in solution are considered. Fig. 2.3b shows the situation of a semiconductor electrode in contact with a solution of Red and Ox in equal concentrations. The semiconductor Fermi level E_{F} and that of the redox couple $E_{\mathrm{F,redox}}$ are distinct, which means that both systems are not in thermodynamical equilibrium. Electrons flow from the phase of higher Fermi energy (semiconductor) to the phase of lower Fermi energy (solution phase), which is possible because

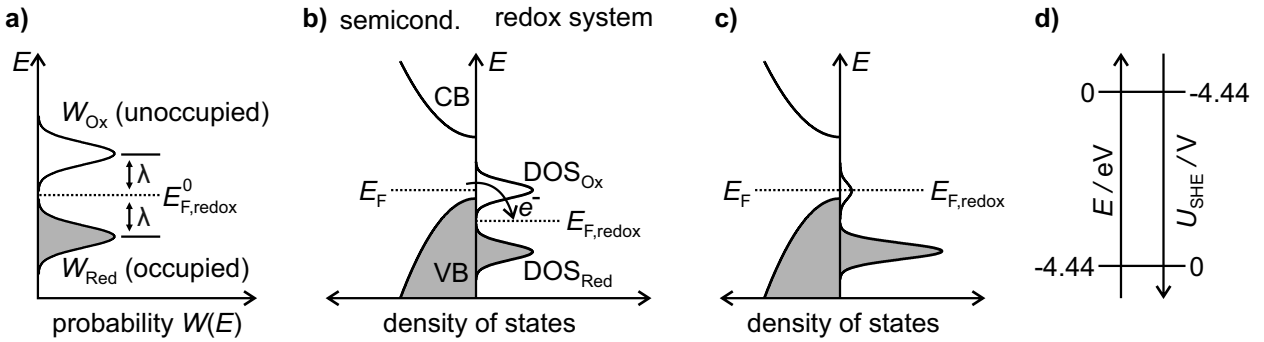

Figure 2.3: Illustration of the Gerischer model. a) Energy distribution function of unoccupied and occupied states associated with molecules Ox and Red. b) Semiconductor electrode in contact with molecules of a redox couple in a non-equilibrium situation (concentration ratio $c_{\mathrm{Ox}}/c_{\mathrm{Red}} = 1$). Electrons flow from the semiconductor electrode to the redox system in solution converting Ox to Red. c) Situation after reaching thermodynamic equilibrium as indicated by a uniform Fermi energy of the semiconductor and the redox couple. d) Comparison of the absolute electron energy E with the redox potential U_{SHE} referenced to the SHE electrode.

of the energetic overlap of occupied states in the semiconductor with unoccupied states in solution. As a consequence Ox is converted to Red. Thermodynamic equilibrium is reached when no net electron flow is occurring anymore, which is the case when both Fermi levels are identical (see Fig. 2.3c). The concentration dependence of $E_{\mathrm{F,redox}}$ is given by:

$$E_{\mathrm{F,redox}} = E^{\ominus}_{\mathrm{F,redox}} + \frac{kT}{z} \ln\left(\frac{c_{\mathrm{red}}}{c_{\mathrm{ox}}}\right). \tag{2.5}$$

By using the relationship $U = -E_{\mathrm{F,redox}}/e$, the Nernst equation describing the concentration dependence of the redox potential U is obtained:

$$U = U^{\ominus} - \frac{kT}{z\,e} \ln\left(\frac{c_{\mathrm{red}}}{c_{\mathrm{ox}}}\right), \tag{2.6}$$

where $U^{\ominus}$ is the standard redox potential. The redox potential U is given in volt and is measured versus a reference electrode like the standard hydrogen electrode (SHE). In contrast, the absolute electron energy E is given in eV and is referenced to the vacuum level. Both quantities are connected by $E = -4.44\,\mathrm{eV} - eU_{\mathrm{SHE}}$ (see Fig. 2.3d) [56].

It was shown that a semiconductor electrode can be used to control the concentration ratio of redox-active molecules in their reduced and oxidized form. However, the opposite process is also possible. Oxidizing (reducing) molecules can be added to an immersed semiconductor in order to withdraw (insert) electrons from (into) the semiconductor. This process shifts the semiconductor Fermi level by introducing holes (electrons) and results in essentially the same physics as the substitutional doping discussed in section 2.1.2. The electrochemical reaction of semiconductors with redox-active molecules is therefore termed *redox chemical doping* in this thesis. Again, electron transfer between the redox active species and the semiconductor occurs until both Fermi levels have aligned.

2.2 Single-Wall Carbon Nanotubes

Carbon nanotubes are another allotrope of carbon besides diamond, graphite, fullerenes, amorphous carbon and graphene. This thesis investigates the spectroscopic properties of doped carbon nanotubes. All experiments were performed using single-wall carbon nanotubes (SWNTs) of only one type, the so-called (6,5)-chirality. The following section explains the nomenclature and geometric structure, as well as the electronic and photophysical properties of (6,5)-SWNTs.

2.2.1 Nomenclature and Geometrical Structure

In a thought experiment, SWNTs can be constructed from a quasi-two-dimensional (2D) graphene sheet (see Fig. 2.4) [57–60]. Graphene is a single layer of graphite and consists of sp^2 hybridized carbon atoms arranged in a planar honeycomb structure of fused six-membered rings. The nomenclature of SWNTs is derived from the formal roll-up of a graphene layer along the so-called roll-up vector $\vec{C}$. This vector is described by the linear combination of the graphene basis vectors $\vec{a}_{1,2}$:

$$\vec{C} = n\,\vec{a}_1 + m\,\vec{a}_2 \quad n \geq m. \tag{2.7}$$

The two indices (n,m) uniquely define the SWNT structure [57–60]. For example, the SWNT diameter d is given by:

$$d = |\vec{C}|\pi^{-1} = \sqrt{3}a_0\pi^{-1}\sqrt{n^2 + nm + m^2}, \tag{2.8}$$

where $a_0 = 142\,\text{pm}$ is the nearest-neighbor C-C distance in graphite [60]. According to equation (2.8), a (6,5)-SWNT has a diameter $d = 0.75\,\text{nm}$. The aspect ratio for typical nanotube samples readily becomes several hundred or more [17, 61, 62], and therefore, SWNTs are termed (quasi-)one-dimensional (1D).

2.2.2 Electronic Structure

Not only the nomenclature but also the electronic structure of carbon nanotubes can be derived from graphene. This is better explained in reciprocal space (k-space) than in real space. The Brillouin zone is the k-space equivalent of the unit cell in real space. Fig. 2.5a shows the first Brillouin zone of graphene as a red hexagon. Analog to real space, two basis vectors $\vec{b}_1$ and $\vec{b}_2$ in reciprocal space are defined, which behave to the basis vectors in real space according to:

$$\vec{a}_i \cdot \vec{b}_k = 2\pi\delta_{ik}, \tag{2.9}$$

where δ_{ik} is the Kronecker delta. The electronic structure of graphene can be calculated via a tight-binding approach taking into account only the overlapping $2p_z$ orbitals [58]. Fig. 2.5b

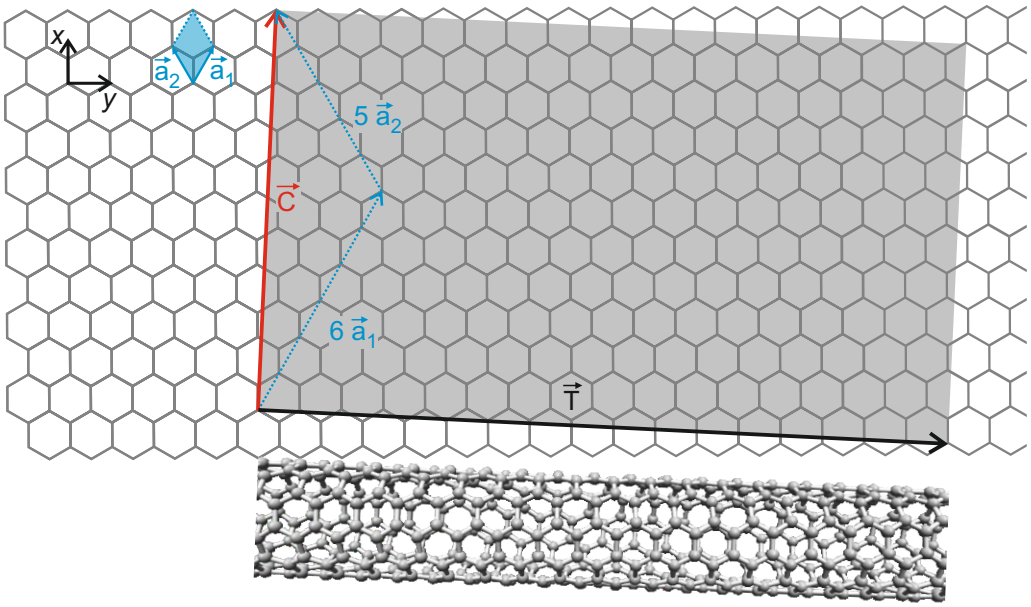

Figure 2.4: Concept of a (6,5)-SWNT as a rolled-up graphene sheet. The honeycomb structure depicts the graphene monolayer, whose unit cell (blue shaded area) is spanned by the two unit vectors $\vec{a}_1$ and $\vec{a}_2$. A (6,5)-SWNT is obtained by rolling up the unit cell of a (6,5)-SWNT (gray shaded area) along the roll-up vector $\vec{C}$, which is given by $\vec{C} = 6\vec{a}_1 + 5\vec{a}_2$. The unit cell of the SWNT is spanned by the roll-up vector $\vec{C}$ and the translational vector $\vec{T}$.

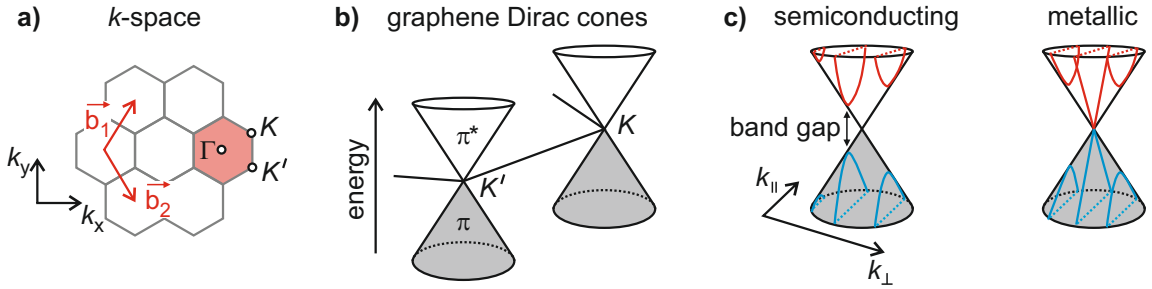

Figure 2.5: a) First Brillouin zone of graphene shown as a red hexagon. b) Near the K and K' points the energy dispersion of graphene can be approximated as a double cone. c) The electronic structure of SWNTs is obtained by one-dimensional cuts through the graphene energy dispersion along quantized $k_\perp$ values. If a cutting line crosses the K and K' points the SWNT is metallic, otherwise semiconducting. Drawn after Hertel [44].

illustrates the energy dispersion $E_{\mathrm{G}}(k)$ with continuous k_{x} and k_{y} values. Near the K and K' points, $E_{\mathrm{G}}(k)$ has the shape of a double cone and is calculated via:

$$E_G(k) = \frac{\epsilon_{2p} \pm \gamma_0\, w(k)}{1 \pm s\, w(k)}, \tag{2.10}$$

where $\epsilon_{2p} = 0$ is the $2p_{\mathrm{z}}$ orbital energy, and $s = 0.129$ is a parameter describing the asymmetry of the bonding π-band (obtained for negative signs) and the antibonding π^* band (positive signs). The parameter γ_0 is the nearest neighbor transfer integral and is typically chosen as $\gamma_0 = 3.033\,\mathrm{eV}$ [58].

The formal rolling up of the graphene sheet into carbon nanotubes leads to periodic boundary conditions for the wave vector component $\vec{k}_\perp$ perpendicular to the nanotube axis. These boundary conditions cause quantized values of $\vec{k}_\perp$ (see Fig. 2.5c). The wave vector component $\vec{k}_\parallel$ along the nanotube axis stays continuous in the limit of an infinitely long SWNT. The band structure of SWNTs is obtained by cutting lines of well-defined $k_\perp$ values onto the graphene band structure [44, 63]. When the cutting lines cross the K or K' point, the SWNTs have no band gap and are metallic. This is the case for one third of all SWNTs, which fulfill the condition $(n - m) \bmod 3 = 0$. Otherwise, like for the (6,5)-type, semiconducting SWNTs are obtained.

Fig. 2.6a shows the calculated band structure of a (6,5)-SWNT. Electron energies E are referenced to the graphene or graphite work function of $\approx 4.52\,\mathrm{eV}$ [64, 65], which is taken as the energy of the band center or Fermi level E_{F}. For comparison with redox potentials commonly used in electrochemistry, the right axis displays the redox potential versus standard hydrogen electrode (SHE) (for the conversion see chapter 2.1.3). The density of states (DOS) shows sharp maxima, the so-called Van Hove singularities, which are characteristic of a 1D solid state-system [66].

2.2.3 Photophysical Properties

Within the single-particle, strong absorption occurs at the band gap energy E_{11}. Fig. 2.6b shows an experimental absorption spectrum of (6,5)-SWNTs dispersed in toluene. At the band gap energy $E_{11} \approx 1.55\,\mathrm{eV}$ [18] hardly any light absorption is observed. The discrepancy between the predictions by tight-binding theory and the experiment can be explained by the strong electronic correlations in 1D SWNTs [18].

Excitons and their dynamics

Fig. 2.7a schematically shows the effect of electronic correlation, *i.e.*, many-body effects and Coulomb interaction, by a comparison of three-dimensional (3D) and quasi-1D semiconductors. The reduction in dimensionality leads to an increase of the band gap and to a nearly complete transfer of oscillator strength from the continuum absorption of free electron-hole (*e*-*h*) pairs to excitonic transitions [67]. Excitons are hydrogen-like quasiparticles consisting

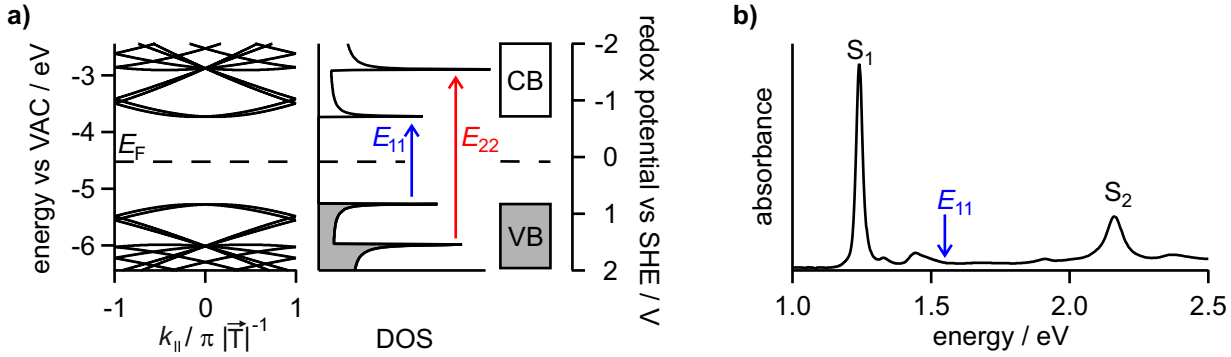

Figure 2.6: a) Bandstructure of a (6,5)-SWNT calculated via the tight-binding approach. The experimentally determined fundamental band gap $E_{11} \approx 1.55\,\text{eV}$ [18] is reproduced for $\gamma_0 = 4.1\,\text{eV}$. b) Experimental absorption spectrum of (6,5)-SWNT dispersed in toluene. At the fundamental band gap E_{11} hardly any absorption is observed. Instead, the absorption spectrum is dominated by two strong exciton bands (S_1, S_2) highlighting the strong electronic correlations in 1D SWNTs.

of mutually attracting electron and hole [67, 68]. The increasing transfer of oscillator strength to the excitonic transition can be understood by the increase of exciton binding energy E_b in quasi-1D systems due to both enhanced Coulomb interaction and wave function constraints in reduced dimensionality [68–71]. For example, exciton binding energies in bulk 3D gallium arsenide (GaAs) are on the order of 5 meV [72, 73]. In contrast, exciton binding energies of the first dipole-allowed singlet exciton (S_1) range between $\approx 300 - 400\,\text{meV}$ for 1D (6,5)-SWNTs in an organic or aqueous environment [18, 23–25]. Because of the small nanotube diameter, the electric field lines strongly leak into the medium outside the SWNT. Therefore, the exciton binding energy and the band gap strongly depend on the dielectric environment (see Fig. 2.7b) [74]. For stronger Coulomb interaction (reduced dielectric constant ϵ_r) both the single-particle band gap energy E_{11} and the exciton binding energy increase. The S_1 energy, however, stays almost constant due to a nearly perfect cancellation of both effects. Apart from the bright dipole-allowed singlet S_1 exciton, there are (due to spin and valley degeneracy) 15 additional dark exciton states [75]. Fig. 2.7c shows a simplified energy level diagram. Two degenerate momentum-forbidden singlet exciton states are located $\approx 30\,\text{meV}$ above the bright exciton (blue line) and are associated with phonon sidebands in absorption and photoluminescence [76–79]. An additional two-photon allowed singlet state is less than ten meV stabilized relative to the bright exciton. This dark state can be brightened in magnetic fields and is claimed to be responsible for the temperature-dependent photoluminescence (PL) of SWNTs [80–86]. The remaining 12 dark excitons are triplets and their direct optical generation is forbidden due to spin selection rules [87–89].

The spatial electron-hole distance between in the S_1 exciton has been experimentally determined in a transient absorption experiment using the phase space filling (PSF) model [90–93]. In such an experiment a strong pump pulse excites the S_1 exciton resonantly, and a weak probe pulse detects the change in excitonic oscillator strength f. The transient reduction of available electron and hole states, the so-called phase space filling, causes the renormaliza-

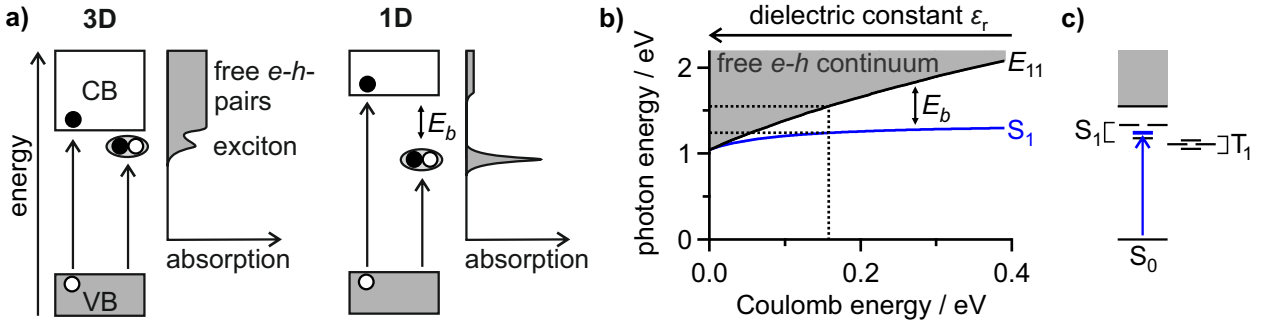

Figure 2.7: a) Comparison of excitonic effects in 3D and 1D. b) Dependence of the band gap energy E_{11} and the S_1 exciton energy of (6,5)-SWNTs on Coulomb interaction strength. The curves were taken from reference [74] and the energies were rescaled by using the experimentally determined band gap $E_{11} = 1.55\,\text{eV}$ [18] and $1.24\,\text{eV}$ S_1 energy for SWNTs in organic environment as marked by the dashed black lines. Higher Coulomb energy corresponds to weaker dielectric screening. c) Simplified energy level diagram depicting bright (blue) and dark (black) singlet S_1 and triplet T_1 exciton states. Drawn after Hertel and Ando [67, 74].

tion of excitonic oscillator strength. Lüer *et al.* found an exciton size $\xi = \sqrt{\pi} d_{e\text{-}h} = 2\,\text{nm}$, where $d_{e\text{-}h}$ is the average distance between electron and hole [91]. A more recent publication on higher-quality samples by Mann and Hertel, however, suggests that the exciton size $\xi = 13\,\text{nm}$ is much larger [90].

The optical generation of S_1 excitons not only occurs by direct absorption into the S_1 state but also by absorption to energetically higher dipole allowed states and subsequent relaxation. For example, internal conversion from the second subband S_2 exciton occurs within only 40 fs [94]. This short time constant makes the relaxation process extremely efficient with an almost quantitative yield [94–97].

Deactivation of the S_1 exciton happens either radiatively as PL or nonradiatively by heat dissipation. The photoluminescence quantum yield (PLQY), defined as the ratio of emitted (N_{PL}) to absorbed photons (N_{abs}), can be expressed by the decay rates of the radiative decay k_{r} and the sum of all nonradiative decay rates k_{nr}:

$$\text{PLQY} = \frac{N_{\text{PL}}}{N_{\text{abs}}} = \frac{k_{\text{r}}}{k_{\text{r}} + k_{\text{nr}}} \approx \frac{k_{\text{r}}}{k_{\text{nr}}}. \tag{2.11}$$

The approximation in equation (2.11) is valid for typical nanotube samples, because the PLQY is on the order of only 1 % [17, 98–100]. Time-resolved photoluminescence measurements show – like the PLQY – strong heterogeneity. Reported PL lifetimes τ_{PL} are between tens and hundreds of ps [98, 101–107]. The heterogeneity suggests that the low PLQY and the efficient nonradiative S_1 exciton deactivation are rather driven by extrinsic factors than based on the intrinsic SWNT properties.

In order to explain the efficient nonradiative decay, Perebeinos and Avouris proposed two microscopic mechanisms [108]. Fig. 2.8a illustrates the multiphonon decay (MPD) mechanism.

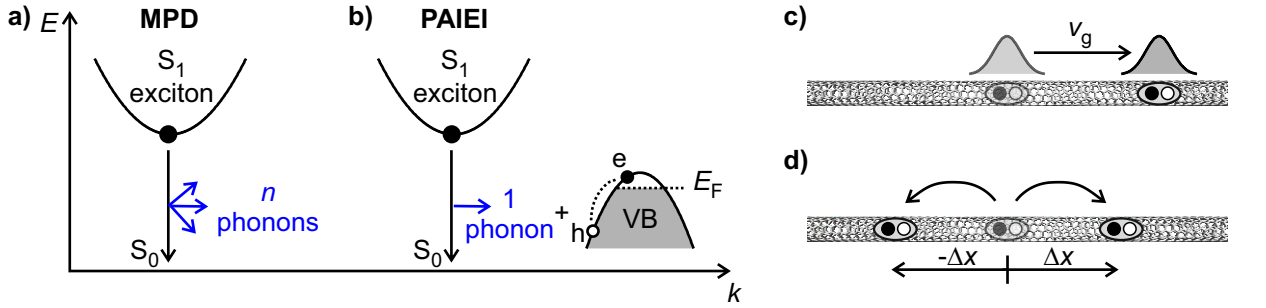

Figure 2.8: Schematic illustration of a) the multiphonon decay (MPD) and b) the phonon-assisted indirect exciton ionization (PAIEI) mechanisms. Drawn after Perebeinos and Avouris [108] c) Coherent 1D exciton transport. The exciton wave packet travels wavelike through the nanotube crystal with group velocity v_g. d) Incoherent, diffusive 1D exciton motion. The exciton jumps with equal probability a distance Δx to the right or to the left within a time interval Δt.

The free and delocalized exciton decays via emission of multiple phonons, which conserve energy and add up to zero momentum. Because many phonons have to be emitted simultaneously to conserve the (6,5)-SWNT exciton energy of 1.24 eV, the nonradiative multiphonon decay process is slow. The calculated nonradiative lifetimes are even longer than the reported radiative lifetimes of $\approx 1-10$ ns [98, 109]. However, the decay rates are significantly enhanced if excitons are localized at defects or due to doping [108]. The second decay mechanism assumes finite doping, for example, *p*-doping due to the presence of water and oxygen [110, 111]. In the phonon-assisted indirect exciton ionization (PAIEI) mechanism, the exciton decays via the emission of one phonon and the simultaneous generation of an intraband electron-hole pair. For nanotubes with comparable diameters to the (6,5)-SWNT, Perebeinos and Avouris predict decay times in the range of 25-100 ps [108].

Additional exciton decay channels arise from defects acting as conduits for nonradiative decay [98, 112]. Regarding the fast population relaxation from higher-energy states to the S_1 exciton state in tens of femtoseconds and the dephasing time $T_2 \approx 200-300$ fs for coherent S_1 excitation [96, 113], exciton transport along the SWNT axis is rather diffusive than coherent (see Fig. 2.8c and d) [107, 114]. SWNT length-dependent PLQY and PL lifetime measurements, as well as PL imaging experiments on single nanotubes, are well explained by diffusion-limited contact quenching (DLCQ) of excitons at defects like the SWNT ends [98, 107, 115–119]. Reported exciton diffusion constants $D = 0.1-44\,\mathrm{cm^2\,s^{-1}}$ and diffusion lengths $L_D = \sqrt{2D\tau_{PL}} = 90-610$ nm strongly vary between different samples and methods used for their determination [91, 98, 114–117, 120–122].

Defects do not only influence exciton dynamics but can also be indirectly observed using resonance Raman spectroscopy [60, 123, 124]. Quantification of the defect density is possible by measuring the intensity ratio I_G/I_D of the G-band (G from graphite) and the defect-induced D-band [61, 125–127].

Under certain circumstances, the D- and G-band also show up in the infrared (IR) spectrum as antiresonances. Lapointe *et al.* reported on such antiresonances in the case of doped SWNTs

and graphene [128, 129]. Both the D- and G-band antiresonances were found to be enhanced for higher defect densities. A discussed prerequisite for such an IR activation of Raman modes is the presence of localized impurities or defects which break the local symmetry [129, 130].

Biexcitons and trions

Strong binding energies allow not only for stable two quasiparticle complexes as the hydrogen atom-like excitons but make also three and four quasiparticle complexes (see Fig. 2.9a) possible.

In intrinsic (6,5)-SWNTs, stable biexcitons with binding energies on the order of 100 meV have been predicted and experimentally observed [131–136]. Biexcitons are bound four quasiparticle complexes consisting of two excitons and can be created at high excitation densities. Following the hydrogen atom analogy for excitons, biexcitons can be considered analogous to the hydrogen molecule H_2 [137].

Lampert predicted charged three-particle complexes, consisting of an exciton plus an extra negative or positive charge, as the semiconductor analog of a positively charged hydrogen molecule H_2^+ or the negatively charged H^- ion (Fig. 2.9a) [137]. Such complexes are called trions or charged excitons $X^{\pm}$ and their bands in absorption and photoluminescence spectroscopy are characteristic optical signatures of doped semiconductors [20–22, 28, 30, 138]. Like in the case of excitons and biexcitons, the spectroscopic observation of trions in doped bulk 3D semiconductors is hampered by the low binding energy, *i.e.*, the energy needed to detach the excess charge from the exciton, on the order of 1 meV [139–141]. Considerable increase in trion binding energy has been predicted for semiconductor nanostructures [142].

Rønnow *et al.* predicted trions in SWNTs in 2009, and they were experimentally confirmed by Santos *et al.* and Matsunaga *et al.* in 2011 [27, 28]. SWNT trion photophysics in linear and nonlinear spectroscopy has been studied using optical [27, 135], redox chemical [28, 29, 143–146], electrochemical [18, 30, 112, 147] or gate-induced generation [31, 148] of excess charges. Trions in SWNTs are best described as the combination of a dark triplet exciton with an additional surplus charge in the valence or conduction band [44, 149]. This combination leads to an optically allowed doublet ($S = 1/2$) state and a dark quartet ($S = 3/2$) state [149]. The fact that trions – in contrast to neutral singlet excitons – possess a charge and a nonzero spin offers the possibility of interaction and manipulation with electric and magnetic fields [150].

The role of triplet excitons in the description of trions is emphasized in the SWNT diameter dependence of the energetic difference $\Delta = E_{\mathrm{ex}} - E_{\mathrm{tr}}$ between the singlet S_1 exciton and the trion (see Fig. 2.9b). Matsunaga *et al.*, Santos *et al.* and Park *et al.* found the following empirical relationship for SWNTs in an aqueous or organic environment:

$$\Delta = \frac{A}{d^2} + \frac{B}{d}, \tag{2.12}$$

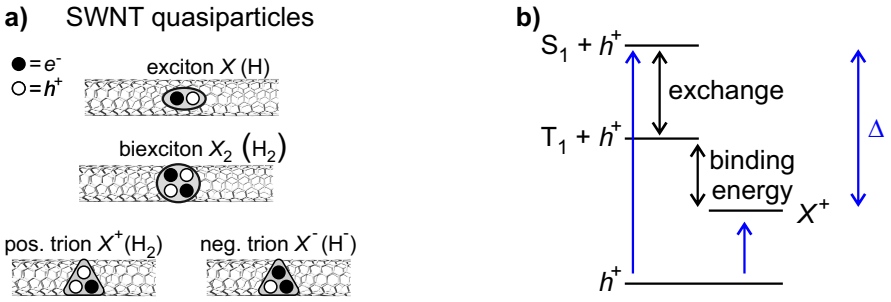

Figure 2.9: a) Experimentally confirmed quasiparticles in neutral and doped SWNTs and their hydrogen analogues in parentheses. b) Energy level diagram in doped SWNTs. The energy separation Δ of bright singlet exciton S_1 and bright doublet trion X^+ as determined in an absorption experiment (blue arrows) is given by the sum of two contributions: The singlet-triplet exciton exchange energy splitting and the trion binding energy. Drawn after Matsunaga *et al.* [28].

where $A = 65 - 85\,\mathrm{meV\,nm^2}$ and $B = 48 - 60\,\mathrm{meV\,nm}$ are constants and d is the SWNT diameter [27, 28, 30]. Fig. 2.9b illustrates the two contributions in equation (2.12). The first term with d^{-2} dependence is associated with the exchange splitting between singlet and triplet excitons [151]. The second term describes the trion binding energy relative to the triplet exciton. According to equation (2.12), (6,5)-SWNTs have a Δ-value of 180-210 meV.

Yoshida *et al.* and Uda *et al.* studied the effect of the dielectric environment on trion stabilization energies by using suspended SWNTs in combination with gate-doping [31, 148]. In contrast to dispersed SWNTs in solvent, suspended SWNTs show a significantly increased Δ-value. An additional trion stabilization on the order of 20 meV was observed upon desorption of adsorbed molecules from the SWNT surface [148]. Park *et al.* investigated the influence of *p*- and *n*-doping on trion energies [30]. Small but detectable differences in positive and negative trion energies $E_{X^\pm}$ were attributed to the small electron-hole asymmetry in SWNTs leading to different effective electron and hole masses [30, 152].

Although the concept of the trion as a three quasiparticle complex seems quite elaborate, recent theoretical investigations seriously question that trions cause the doping-induced spectral features in semiconductor nanostructures [153–157]. Alternative theories are beginning to emerge and attribute these spectral features to so-called exciton-polarons describing the attractive interaction of the exciton with the whole Fermi sea of excess carriers [154–158]. Nevertheless, within this thesis, the established notion of a trion is used in order to describe the doping-induced near infrared (NIR) absorption or emission features energetically below the S_1 exciton.

2.3 Spatial Localization

In the following, the physical basics regarding the spatial localization of charge carriers and examples of quasiparticle localization in SWNTs are presented. If not cited otherwise, the content of this chapter is based on the textbooks *Semiconductor Optics* by Klingshirn [36]

and *Optical properties of solids* by Fox [159].

2.3.1 General Remarks

In a perfect crystal without perturbations, the lattice potential $V(r)$ is periodic:

$$V(r+R) = V(r), \tag{2.13}$$

where R is a translation vector of the lattice. The electron eigenstates are described by fully delocalized Bloch waves $\phi_k(r)$:

$$\phi_k(r) = \mathrm{e}^{ikr}\, u_k(r), \tag{2.14}$$

where $u_k(r) = u_k(r+R)$ is a periodic function accounting for the perfect lattice (see Fig. 2.10a).

In reality, no perfect crystal exists, and always some imperfections are present, which perturb the periodicity of the lattice potential $V(r)$. Such perturbations might be structural imperfections like point defects or grain boundaries, but also temperature-dependent lattice vibrations (phonons) temporally distort the periodicity. Section 2.1.2 introduced the concept of shallow acceptors (donors) producing localized states in the band gap close to the valence (conduction) band edge. The real space wavefunction $\Psi(r)$ of a shallow acceptor (or any localized state in general) can be described by a linear superposition of Bloch states:

$$\Psi(r) = \sum_k c_k \phi_k^{\mathrm{VB}}(r). \tag{2.15}$$

The spread Δk of relevant Bloch states (given by the amplitudes c_k) determines on which length scale the real space wavefunction $\Psi(r)$ is localized (see Fig. 2.10b). A larger Δk leads to a smaller Bohr radius a_0 of the hydrogenic acceptor 1s wavefunction and *vice versa*.

In general, any disorder causes some degree of localization and a departure from the Bloch wave description. This will be explained in more detail by means of Fig. 2.10c - f. Fig. 2.10c shows a spatially fluctuating potential caused by disorder and described by an energy modulation ΔV. If ΔV is zero, the Bloch wave description is valid and all states are fully delocalized. Fig. 2.10d illustrates these extended states as a gray shaded area in the density of states diagram. The width of the energy band is denoted by B. If the magnitude of energetic disorder ΔV is compared to the band width B, two limiting cases can be distinguished.

Fig. 2.10e shows the situation when the disorder is weak compared to the energy band width. In this case, the states at the band center can still be described as extended states, although slightly modified compared to the Bloch description. Especially the long-range phase correlation is lost compared to a Bloch wave. At the band edges, however, localized states form. Mathematically, a localized state could, for example, be described as exponentially damped

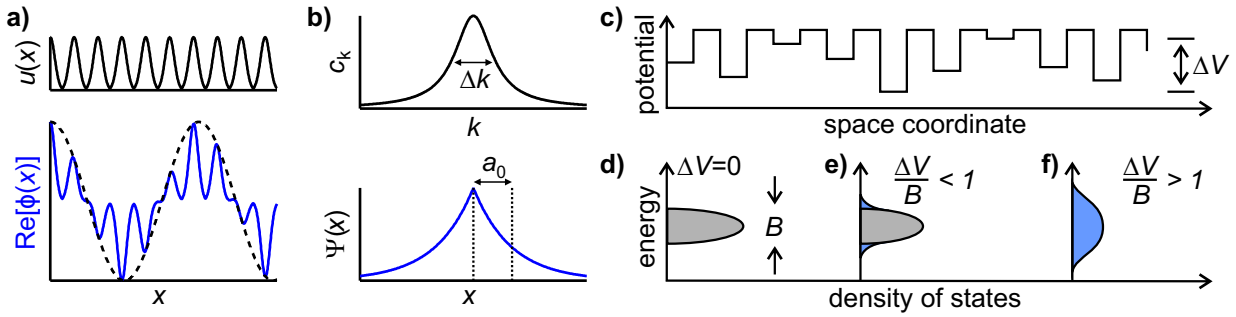

Figure 2.10: a) Illustration of fully delocalized Bloch waves in one dimension. The top figure shows the periodic function $u_k(x)$, whereas the bottom figure depicts the real part of the Bloch wave $\mathrm{Re}[\phi_k(x)]$ (blue solid line) and the plane wave part $\mathrm{Re}[e^{ikx}]$ (dashed black line). b) The linear superposition of Bloch waves with amplitudes c_k causes a spatial localization of the shallow acceptor 1s wavefunction Ψ. c) Disorder-induced potential modulations of strength ΔV. d) For zero disorder ($\Delta V = 0$), all states within the energy band of width B are spatially extended (gray shaded area). e) If the disorder ΔV is small compared to the band width B, most states are still extended. However, states at the band edges become localized as illustrated by blue areas. f) All states are localized when the disorder is large ($\Delta V/B > 1$). The subfigures c) - f) are drawn after Klingshirn [36].

at distances $|r - r_0|$ away from its origin r_0:

$$\phi^{\mathrm{loc}}(r) \propto \exp\left(-\frac{|r - r_0|}{L_{\mathrm{loc}}}\right). \tag{2.16}$$

The localization length L_{loc} determines the degree of localization and for strong disorder $\Delta V/B > 1$, all states become localized (see Fig. 2.10f).

Up to now, only 3D systems have been regarded. It can be shown that the dimensionality of the system has an enormous impact on the effect of disorder-induced localization. For dimensions $d \leq 2$, even a vanishingly weak disorder leads to a localization of all states [160–162]. However, localization lengths arising from very weak disorder can become very large. If L_{loc} is on the order of the sample size or larger, the strict statement about $d \leq 2$ is a rather theoretical concept than of practical relevance. Nevertheless, it still demonstrates the strong dimensionality dependence.

2.3.2 Carbon Nanotubes

Next, a short review of spatial localization in single-wall carbon nanotubes is provided. The relevance of surplus charge carrier localization is a key question of this thesis, and the literature concerning carrier localization is presented in chapter 5.

Here, the more intensely studied but conceptually similar spatial localization of excitons is summarized. In the framework of a perfect crystal, not only electrons but also free excitons of the Wannier-Mott type are fully delocalized over the whole crystal [159]. However, recent experiments on SWNTs suggest that exciton localization is frequently observed [163, 164,

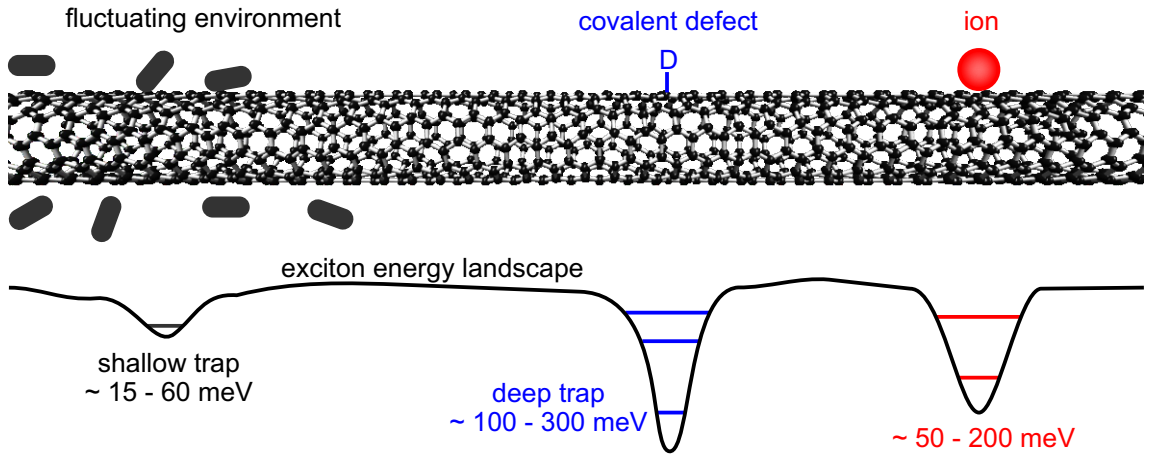

Figure 2.11: Effect of environmental disorder [163–165] and covalent defects [166] on the exciton energy landscape. Drawn after Högele *et al.* [167].

166–168].

Low-level covalent functionalization changes the hybridization of SWNT carbon atoms from sp^2 to sp^3. These defects give rise to new emission features at energies below the S_1 exciton energy [166]. For the (6,5) chirality, the redshift can even exceed 200 meV [166, 169]. Furthermore, excitons are spatially localized at the sp^3-defect site within a few nanometers [166]. The energetic redshift of the emission band serves as a rough estimate of the exciton trap depth (see Fig. 2.11) [166, 170]. For deeper traps, smaller localization lengths were observed [166].

Mechanistically, it was suggested that the mobile S_1 exciton diffuses along the SWNT axis and gets trapped at the defect site where redshifted emission occurs [166, 168]. Experimental confirmation of exciton localization at the defect site was obtained by photoluminescence imaging. Hartmann *et al.* showed that native S_1 exciton PL and defect-induced redshifted PL originate from different locations along the same SWNT [168].

Exciton localization is not limited to defective SWNTs but also occurs in pristine ones, as shown by Georgi *et al.* using near-field PL microscopy with a spatial resolution of 15 nm [163]. The room-temperature experiments revealed spatially confined exciton traps of 15 meV depth and an axial exciton energy modulation of more than 2 meV/nm. The energy fluctuations along the SWNT can be understood by the fact that all nanotube atoms are surface atoms. Consequently, exciton energies are very sensitive to external perturbations in the environment (see Fig. 2.7b). Such perturbations can arise from adsorbed species, trapped charges or variations in the local dielectric function [163].

Exciton localization by the environmental disorder has also been studied at cryogenic temperatures with conventional confocal PL microscopy by Hoffmann *et al.* leading to consistent conclusions [171].

Similar to Georgi *et al.*, Schilling *et al.* found in an ultrafast hole burning study that exciton energies differ along the SWNT axis due to electrostatic fluctuations in the environment [164].

The situation of spatially varying exciton energy is comparable to Fig. 2.10c and causes an inhomogeneous broadening of the S_1 exciton absorption band. Therefore, the exciton energy fluctuations on the order of 60 meV could be inferred from the inhomogeneous linewidth of the S_1 absorption band. Local energy minima act as shallow traps and can readily be overcome for the diffusing exciton at room temperature ($kT = 25\,\text{meV}$). However, at 17 K ($kT \approx 1.4\,\text{meV}$) S_1 excitons become trapped in the low energy sites acting as deep traps [164].

Potential energy fluctuations arising from an inhomogeneous environment experienced by excess charge carriers cannot be estimated as easily as for excitons using optical spectroscopy. However, it is expected that the spatial variations in energy are even larger if charge carriers are regarded. This can be assumed since charge-charge or charge-dipole interactions are typically stronger than interactions of charges or dipoles with charge-neutral entities like excitons. Therefore, the sensitivity of 1D SWNTs to environmental perturbations might not only result in exciton localization but also in charge carrier localization for the same physical reasons, especially if the temperature is lowered.

2.4 Intraband Absorption of Free and Localized Carriers

If not cited otherwise, the following content is based on the textbooks *Optical Properties of Solids* by Fox [159] and *Electrodynamics of Solids* by Dressel and Grüner [172].

Interband and intraband processes

In an intrinsic semiconductor, the VB is fully occupied, and the CB is empty. Fig. 2.12a depicts this situation for a direct semiconductor like gallium arsenide or semiconducting SWNTs. The only possibility to excite electrons from an occupied to an unoccupied energy level is across the band gap, *i.e.*, from the VB to the CB. Such a process is called an interband absorption because two different energy bands are involved. The optical generation of free-carriers, excitons or trions as discussed in section 2.2.3 are examples of interband absorption processes. If dielectric screening is strong and many-body effects are negligible, no absorption below the band gap energy occurs. According to Fermi's golden rule [173]

$$\Gamma \propto |M|^2 \times \text{JDOS}(E), \tag{2.17}$$

the transition rate Γ depends on the transition matrix element M and the joint density of states JDOS.

The rate of band gap absorption in an indirect semiconductor (for example silicon) is largely reduced because of momentum conservation. The photon momentum is close to zero, and therefore, transitions are quasi-vertical with $\Delta k \approx 0$ (see Fig. 2.12b). For band gap absorption, this necessitates the simultaneous absorption of a photon and absorption/emission of a phonon to provide the missing crystal momentum $p = \hbar\Delta k$.

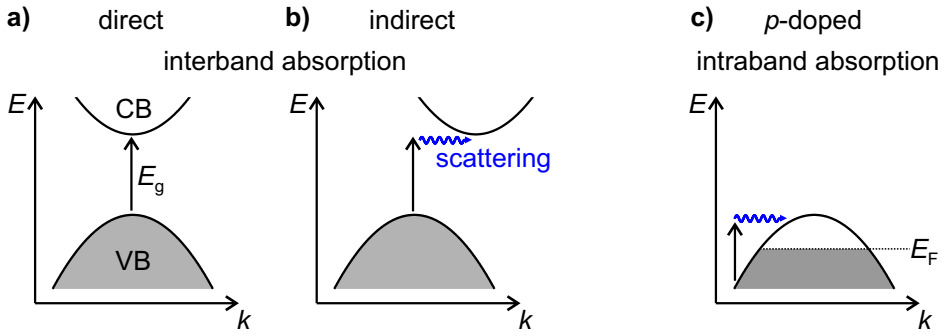

Figure 2.12: Schematic illustration of interband and intraband absorption processes. a) Interband absorption in a direct band gap semiconductor and b) an indirect semiconductor. For the latter phonon scattering is necessary to fulfill momentum conservation. c) Intraband absorption in a p-doped semiconductor.

Additional transitions are possible upon doping. Fig. 2.12c shows the energy dispersion in the case of p-doping, which leads to empty states in the vicinity of the VB edge. Electronic excitation from filled states below the Fermi energy E_F to empty states above E_F is now possible. If only states from one energy band are involved, such a process is called an intraband absorption, which is Pauli-forbidden in an intrinsic semiconductor. Similar to band gap absorption in intrinsic indirect semiconductors, scattering is necessary to conserve crystal momentum.

Next, different models describing the frequency dependence of intraband absorption and the role of scattering processes are discussed.

2.4.1 Drude and Drude-Sommerfeld Model

The simplest model of intraband absorption is the Drude model. It was developed at the beginning of the twentieth century to describe the frequency dependence of the conductivity observed in metals. Conducting electrons with mass m are treated as a classical ideal gas with a thermal velocity distribution in each dimension of standard deviation $v_\mathrm{th} = \sqrt{kT/m}$. In the absence of an electric field, the average velocity $\langle v(t) \rangle$ is zero, and no electric current can be detected. If an electric field with field strength $E(t)$ is applied, the electrons are accelerated according to the equation of motion:

$$m\frac{d\langle v(t)\rangle}{dt} + \frac{m\langle v(t)\rangle}{\tau} = -eE(t), \tag{2.18}$$

where $-e$ is the electron charge and τ is a phenomenological scattering or relaxation time constant. Electrons are assumed to be on average scattered after a time interval τ which randomizes their velocities (see Fig. 2.13a).

Fig. 2.13b illustrates the implication of the relaxation time constant τ on the electric current. If the electric field is suddenly switched off, the current density $J(t)$ exponentially decays

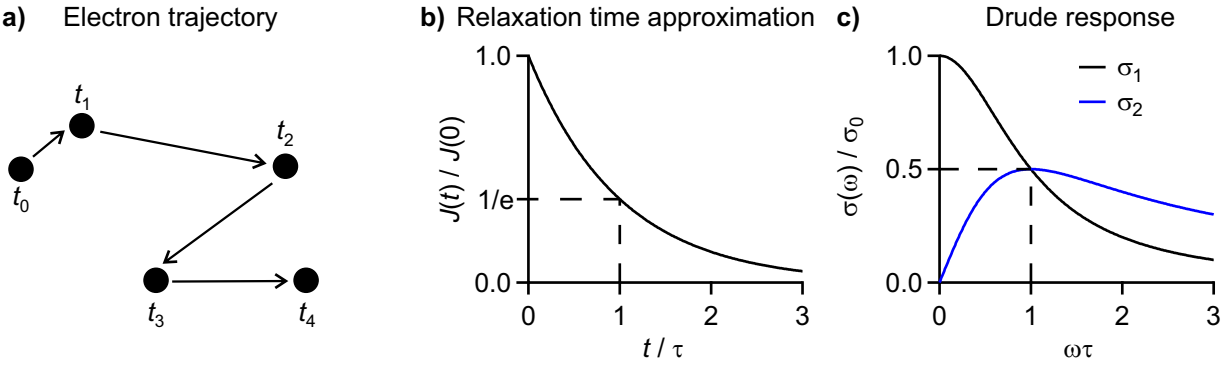

Figure 2.13: Illustration of the Drude model. a) Example trajectory of a single electron. After a time $\Delta t = t_{i+1} - t_i$ the momentum is changed due to scattering. The average value of Δt regarding many electrons and scattering events is called relaxation time τ. b) The approximation of a constant relaxation time τ leads to an exponential decay of the current density after switching off the electric field. c) Complex optical conductivity in the Drude model. The black line is the real part σ_1 and the blue line is the imaginary part σ_2.

to zero with a time constant τ. The time-dependent current density can be related to the electric field strength by

$$J(t) = \sigma E(t), \tag{2.19}$$

where the proportionality factor σ is the conductivity. After Fourier transformation of equation (2.19), the frequency dependence of the conductivity is obtained, and $\sigma(\omega)$ becomes a complex function:

$$\sigma(\omega) = \frac{\sigma_0}{1 - i\omega\tau} = \sigma_1 + i\sigma_2, \tag{2.20}$$

where the direct current (DC) conductivity $\sigma_0 = ne^2\tau/m$ is proportional to the charge density n.

The quantity $\sigma(\omega)$ is often referred to as complex optical conductivity. The optical conductivity can be related to the relative dielectric permittivity ϵ_r by:

$$\epsilon_r(\omega) = 1 + \frac{i\sigma(\omega)}{\omega\epsilon_0} = [n(\omega) + i\kappa(\omega)]^2, \tag{2.21}$$

where ϵ_0 is the free-space permittivity, n is the refractive index and κ is the extinction coefficient. Both dielectric function and optical conductivity contain the same and full information about the interaction of a material with electric fields. Another way to characterize the light-matter interaction are the frequency-dependent refractive index $n(\omega)$ and extinction coefficient $\kappa(\omega)$. The functions n and κ themselves are connected by Kramers-Kronig relations such that upon determination of one quantity over the whole spectral region $0 \leq \omega \leq \infty$ the other quantity and also the dielectric function or optical conductivity can be calculated [174].

A material having a frequency-dependence of the optical conductivity σ according to equation (2.20) shows a Drude response of free carriers (see Fig. 2.13c). The real part σ_1 of the

optical conductivity is a Lorentzian with its maximum at $\omega = 0$. The imaginary part σ_2 is positive and peaks at the angular frequency $\omega = 1/\tau$, at which real and imaginary parts intersect.

The classical Drude model implies that all free electrons contribute to the current but move with relatively small drift velocities. This picture is in stark contrast to quantum mechanics. According to quantum mechanics, only electrons in the vicinity of the Fermi level can contribute to the electric current, but they travel with much larger velocity v_F, called the Fermi velocity. Sommerfeld reconsidered the Drude model in 1927 after the advent of quantum mechanics [175]. Instead of a classical ideal gas with a Maxwell-Boltzmann velocity distribution, he used a Fermi gas, *i.e.* still non-interacting electrons but which obey Fermi-Dirac statistics [176]. This is the so-called free electron model. For parabolic bands, it can be shown that the free electron model predicts the same conductivity as the Drude model. As a consequence, equation (2.20) is still applicable, but effective electron or hole masses should be used instead of the free electron mass [172, 177, 178]. Although macroscopically the same results are obtained, microscopically both models strongly differ. For the classical Drude model, the mean free path is given by $l_\mathrm{mean} = v_\mathrm{th}\tau$ and is strongly temperature-dependent. In the low-temperature limit, the mean free path approaches zero. In contrast, the Drude-Sommerfeld model predicts $l_\mathrm{mean} = v_\mathrm{F}\tau$, which is hardly temperature-dependent.

2.4.2 Modifications due to Localization

In the Drude and Drude-Sommerfeld model, charge carriers are assumed to be free, *i.e.* they do not feel any restriction in their motion except the velocity randomizing scattering after a mean scattering time τ. Due to the presence of disorder or structural defects, this idealized description of free carriers is often not appropriate, and carriers are better described to be bound and localized.

The microscopic nature of charge carrier motion and the possible influence of localization on charge transport properties can be estimated by comparing three important length scales: the mean free path l_mean, the localization length L_loc and L_ω, the distance a carrier travels within an optical period $T_\omega = 2\pi/\omega$. If charge transport is regarded over length scales much smaller than the mean free path, charge carrier motion is ballistic with velocity v. Over a length scale much larger than l_mean, charge transport becomes diffusive. In the case of ballistic transport it follows $L_\omega = vT_\omega \propto v/\omega$, whereas in the diffusive regime $L_\omega \approx \sqrt{D/\omega}$, where D is the diffusion constant [179]. The influence of carrier localization on charge transport naturally arises if the localization length is comparable to or smaller than the mean free path $L_\mathrm{loc} \lesssim l_\mathrm{mean}$. The same is true for $L_\mathrm{loc} \lesssim L_\omega$. The latter implies that localization has the most pronounced effect on the optical conductivity $\sigma(\omega)$ at low frequencies ω where carriers can travel greater distances during an optical cycle.

In the following, two descriptions based on the Drude(-Sommerfeld) model are presented, which account for a localized and bound nature of carriers: The Drude-Smith model and the

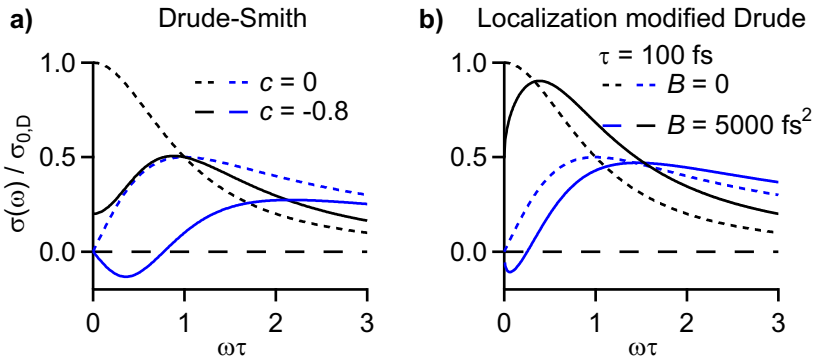

Figure 2.14: Illustration of carrier localization in the Drude-Smith and localization modified Drude model. a) Optical conductivity in the Drude-Smith and b) localization modified Drude model. Black lines correspond to σ_1 and blue lines to σ_2. The dashed lines show the Drude behavior of free carriers for comparison.

localization modified Drude model.

The Drude-Smith (DS) model considers possible backscattering of charge carriers, for example, at grain boundaries [179–181]. Mathematically, the conductivity is then described by [181]:

$$\sigma(\omega) = \frac{\sigma_{0,\mathrm{D}}}{1 - i\omega\tau}\left[1 + \sum_{n=1} \frac{c_n}{(1 - i\omega\tau)^n}\right], \tag{2.22}$$

where $\sigma_{0,\mathrm{D}}$ is the Drude DC conductivity and $-1 \leq c_n \leq 0$ is a parameter, which describes the persistence of the carrier's original velocity after the n^{th} collision.

Typically, only the first backscattering event ($n = 1$) is retained, and the index '1' can be omitted:

$$\sigma(\omega) = \frac{\sigma_{0,\mathrm{D}}}{1 - i\omega\tau}\left[1 + \frac{c}{1 - i\omega\tau}\right]. \tag{2.23}$$

Fig. 2.14a shows the Drude-Smith response for a parameter $c = -0.8$ as an example (solid lines). For comparison, the Drude model, which is obtained for $c = 0$, is shown as dotted lines. The DC conductivity in the Drude-Smith model ($\sigma_{0,\mathrm{DS}} = \sigma_{0,\mathrm{D}}[1 + c]$) is largely reduced due to backscattering. In contrast to the Drude model, the real part σ_1 does not peak at zero frequency, indicating a certain degree of carrier localization. For $c = -1$ the DC conductivity becomes zero and the carriers are fully localized such that long-range transport is suppressed.

The localization modified Drude model is based on weak localization due to disorder [174, 182, 183]. A correction to the Drude model gives the real part σ_1 of the optical conductivity:

$$\sigma_1(\omega) = \sigma_{1,\mathrm{D}}\left[1 - \frac{C}{(k_{\mathrm{F}} l_{\mathrm{mean}})^2}\left(1 - \frac{l_{\mathrm{mean}}}{L_\omega}\right)\right], \tag{2.24}$$

where C is a constant of order unity, k_{F} is the Fermi wavevector, and L_ω is the distance over which a carrier can diffuse within a period of the incident radiation. By using definitions of the mean free path and carrier diffusion coefficient, the real and imaginary parts σ_1 and σ_2

can be rewritten as [184, 185]:

$$\sigma_1(\omega) = \sigma_{1,\mathrm{D}} \left[1 - \frac{B}{\tau^2}\left(1 - \sqrt{3\omega\tau}\right)\right] \tag{2.25}$$

$$\sigma_2(\omega) = \sigma_{2,\mathrm{D}} \left[1 - \frac{B}{\tau^2}\left(1 + \sqrt{\frac{3}{\omega\tau}} - \sqrt{6}\right)\right], \tag{2.26}$$

where $B = C/(k_\mathrm{F} v_\mathrm{F})^2$ is a constant. Fig. 2.14b shows the calculated optical conductivity for $\tau = 100\,\mathrm{fs}$ and $B = 5000\,\mathrm{fs}^2$. Similar to the Drude-Smith model, a σ_1 drop-off towards zero frequency can arise. At the same time, the imaginary part σ_2 can become negative, both signatures of charge carrier localization.

2.4.3 Monte-Carlo Simulations

Using the Drude approach and treating charge carriers as a classical ideal gas of non-interacting particles, the effect of spatial localization and backscattering on the optical conductivity can be studied by Monte-Carlo (MC) simulations. Cocker *et al.* used such simulations for weak 2D confinement within a square box of length L and reflective boundaries [179]. The same approach is used in this thesis in a slightly modified version to study charge transport in 1D. The results of the MC simulations are shown in chapter 5.4 to demonstrate the effect of different localization lengths on the optical conductivity spectra.

Basis of all MC simulations are the outcomes of a large number of identical random experiments. In this particular case, the motion of a single charge carrier under the influence of an oscillating electric field is simulated, and the simulation is repeated for a large number of particles N_part. Localization of charge carriers is introduced – similar to Cocker *et al.* – by restricting carrier motion within a 1D box of localization length L_loc using perfectly reflecting boundaries (see Fig. 2.15). In the following, the MC algorithm used for the simulations is explained.

Initialization

Two variables describe each particle p entering the simulation: the position x and the velocity v in x-direction. At $t = 0$ the particle is initialized with a velocity v_0, which is randomly taken from a Gaussian distribution with zero mean and v_th^2 variance. The thermal velocity $v_\mathrm{th} = \sqrt{kT/m^*}$ is the root mean square value of the Gaussian velocity distribution following the ideal gas theory. The initial position x_0 is randomly chosen with equal probability to be within $-L_\mathrm{loc}/2 \leq x \leq +L_\mathrm{loc}/2$.

Scattering processes

The simulations take into account two different types of scattering events: velocity randomizing scattering and backscattering.

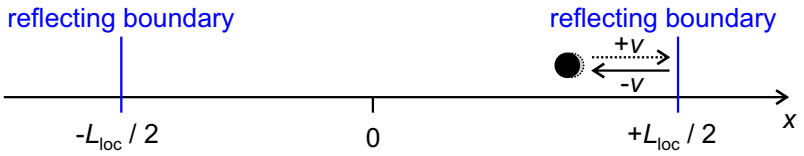

Figure 2.15: Illustration of a moving charge carrier particle (black circle) inside a 1D box of length L_{loc}. The boundaries of the 1D box have a reflectivity of 100 %. If a particle hits one of the boundaries, backscattering changes its velocity from v to $-v$.

Using the relaxation time approximation, the probability W that a carrier gets scattered after a time interval Δt is $W = \Delta t/\tau$. If scattering occurs, the velocity of the particle is again randomly reinitialized as described above. The time interval Δt is here associated with the time step size of the simulation and should be considerably smaller than τ.

Possible backscattering at the reflecting boundaries at $x = \pm L/2$ is implemented such that particles crossing the boundaries during the time step Δt change their velocity from v to $-v$.

Frequency-dependent conductivity

The conductivity as a function of driving field frequency f is obtained by separate simulations for each frequency. An oscillating electric field is applied in the x-direction and the particle velocity v is recalculated at each time step q according to

$$v(t = q\Delta t) = v_q = v_{q-1} + \frac{eE_0\Delta t}{m^*}\cos(2\pi f \times q\Delta t), \tag{2.27}$$

where E_0 is the maximum amplitude of the electric field and m^* is the effective carrier mass.

In order to obtain the current density $J(t)$ in the time-domain, the velocities of all N_{part} individual particles p are averaged:

$$\langle v(t)\rangle = \frac{1}{N_{\mathrm{part}}}\sum_{p}^{N_{\mathrm{part}}} v_p(t). \tag{2.28}$$

The current density is then simply related by $J(t) = n\langle v(t)\rangle e$ with $n = N_{\mathrm{part}}/V$ being the charge density and V the unit volume.

For the calculation of the frequency-dependent conductivity $\sigma(\omega)$, the relationship

$$\sigma(\omega) = J(\omega)/E(\omega) \tag{2.29}$$

is utilized. This equation can be rewritten by expressing $J(\omega)$ and $E(\omega)$ by their Fourier transforms:

$$\sigma(\omega) = \frac{\int_{-\infty}^{\infty} J(t)\exp(i\omega t)\,\mathrm{d}t}{\int_{-\infty}^{\infty} E(t)\exp(i\omega t)\,\mathrm{d}t}. \tag{2.30}$$

Because a discrete sampling is performed, a conversion of the integrals into sums is possible:

$$\sigma(\omega) = \frac{\sum_{j=1}^{T} J(t_j)[\cos(\omega t_j) + i\sin(\omega t_j)]}{\sum_{k=1}^{T} E_0 \cos(\omega t_k)[\cos(\omega t_k) + i\sin(\omega t_k)]}. \tag{2.31}$$

Here, the identity $\exp(i\omega t) = \cos(\omega t) + i\sin(\omega t)$ was used and T is the total number of time steps in the simulation.

In practice, the lower summation index is shifted corresponding to a time $t = 5\tau$ to avoid transient effects that accompany the turn-on of the electric field.

As the last step, $\sigma(\omega)$ is divided by the DC value of the Drude model $\sigma_{0,\mathrm{D}} = ne^2\tau/m^*$.

Input parameters

From a physical point of view, the main two input parameters of interest are the average scattering time τ and the localization length L_{loc}.

Other input parameters – mainly determining the accuracy and signal-to-noise ratio of the simulations – are the time step size Δt, the number of particles N_{part} and time steps T per driving frequency and the peak amplitude E_0 of the electric field. For the simulations $\Delta t = 0.2\,\mathrm{fs}$ is chosen as a time step size. The number of time steps is $T = 10^5$ such that the total simulated time after the turn-on of the electric field is $T\Delta t = 20\,\mathrm{ps}$. The driving frequencies are $f \geq (20\,\mathrm{ps})^{-1} = 0.05\,\mathrm{THz}$ to ensure that at least one period of the driving frequency is contained in all simulations. The number of particles used for each frequency is $N_{\mathrm{part}} = 8 \times 10^4$, which was found for a peak amplitude $E_0 = 1\,\mathrm{kV/cm}$ of the electric field to be a good compromise between signal-to-noise ratio and computation time. The peak electric field strength $E_0 = 1\,\mathrm{kV/cm}$ is approximately at the end of the linear response regime but clearly below the saturation field strength of $\approx 5 - 10\,\mathrm{kV/cm}$ reported for carbon nanotubes [186, 187].

3 Experimental Methods

The following chapter describes the preparation of the nanotube samples and the spectroscopic and electrochemical methods, which were used for their investigation.

3.1 Sample Preparation

3.1.1 Selective Dispersion of (6,5)-SWNTs

Organic (6,5)-SWNT dispersions in toluene were prepared either by sonication or shear force mixing.

Sonication

(6,5)-SWNT dispersions in toluene (analytical reagent grade, Fischer Chemicals) were produced by sonication of 0.5 mg/mL CoMoCAT® raw material (SWeNT SG 65, Southwest Nano Technologies Inc.) and 1.0 mg/mL poly[(9,9-dioctylfluorenyl-2,7-diyl)-alt-co-(2,6-bi-pyridine)] (PFO-BPy, American Dye Source) for 7 h following the description of Ozawa *et al.* [15]. During sonication, the mixture was cooled using an ice bath. Subsequently, the resulting dispersions were benchtop centrifuged (Biofuge 15, Heraeus) for 4 min at 14000 rpm, and the supernatant was collected. This procedure resulted in dispersions of purple color (see Fig. 3.1a) and a peak absorbance of $\approx 1.5 - 3$ at 1.24 eV. Fig. 3.1b shows the chemical structure of the wrapping polymer PFO-BPy.

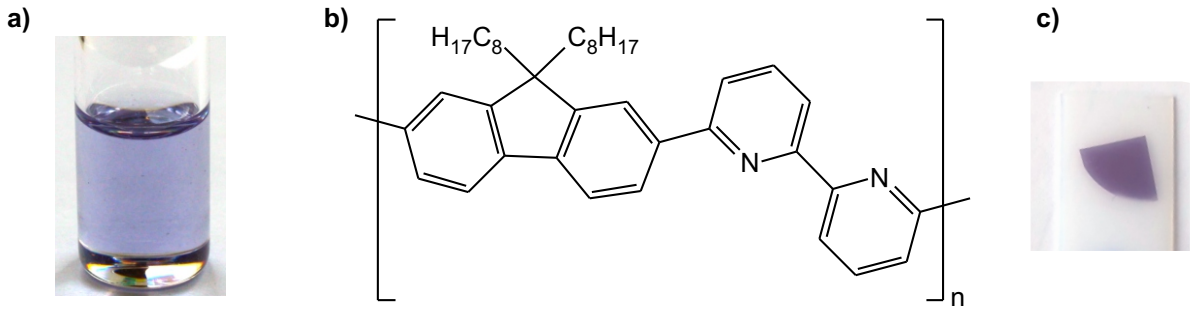

Figure 3.1: a) Purple-colored SWNT dispersion highly enriched in (6,5) chirality. b) Chemical structure of the wrapping polymer PFO-BPy. c) SWNT thin-film obtained by vacuum filtration on a semi-transparent polyethylene substrate.

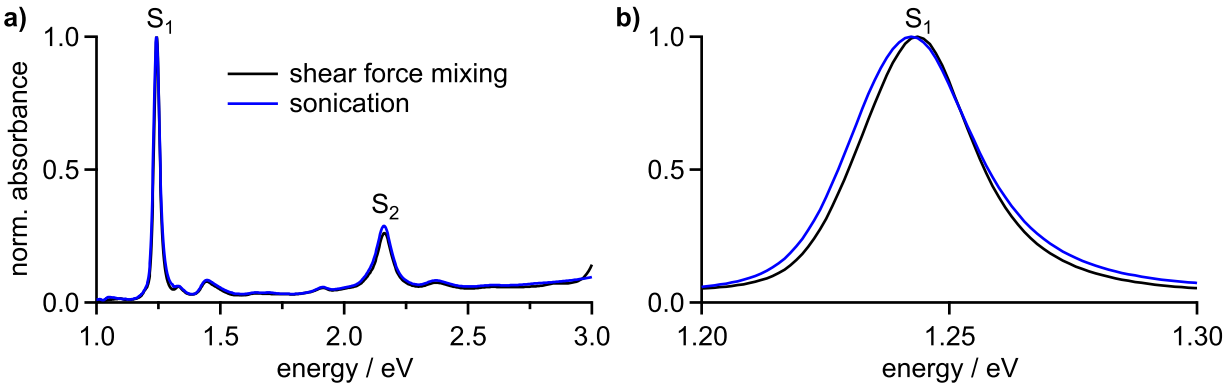

Figure 3.2: a) Comparison of normalized absorption spectra for SWNT samples prepared by shear force mixing or sonication. Hardly any differences can be observed, showing that both methods are equally suited for the selective dispersion of (6,5)-SWNTs. b) Enlarged view on the spectral region around the S_1 exciton resonance. Shear force mixing typically results in a slightly smaller S_1 exciton linewidth, which is indicative of less defective nanotubes.

Shear force mixing

(6,5)-SWNT dispersions in toluene were fabricated by Florian Oberndorfer who kindly shared his samples for spectroscopic experiments. Following the description of Graf *et al.* [17], (6,5)-SWNT dispersions in toluene (analytical reagent grade, Fischer Chemicals) were prepared by shear force mixing 0.38 mg/mL CoMoCAT® raw material (SWeNT SG 65i, Southwest Nano Technologies Inc.) and 0.76 mg/mL PFO-BPy (American Dye Source) for 12 h. In the next step, the resulting dispersions were benchtop centrifuged, and the supernatant was collected. Fig. 3.2a illustrates that shear force mixing and sonication give rise to very similar absorption spectra. However, shear force mixing is less harsh and results in longer and less defective tubes with a slightly narrower S_1 absorption band (see Fig. 3.2b) [17]. To study the doping-induced changes in optical properties, and for possible (opto-)electronic applications, high purity of semiconducting SWNTs is crucial [8, 16]. Polymer stabilization using PFO-BPy not only highly enriches the (6,5)-chirality (> 90 %) [15], but also nearly excludes all metallic nanotubes. A purity of semiconducting nanotubes of more than 99.98 % has been reported by Brady *et al.* [8].

3.1.2 Preparation of SWNT Films

The fabrication of SWNT films involved either a vacuum filtration step or SWNT deposition by drop-casting.

Vacuum filtration

Thin-films of (6,5)-SWNTs were prepared by vacuum filtration of the SWNT dispersion through cellulose acetate filter membranes (MF-Millipore VCWP, Merck Millipore) with 100 nm pore size. After filtration, the filter cake was washed with 10 mL toluene to remove

excess PFO-BPy polymer, and the filter cake was dried. The films on the filter membranes were deposited in a Petri dish with the filter membrane placed downwards. Subsequently, the filter membranes were dissolved in an acetone bath. The freely swimming SWNT films were lifted off the acetone bath by different substrates (microscope glass slides, sapphire, 500 µm thick polyethylene, intrinsic silicon or a Pt mesh electrode) and were dried. Fig. 3.1c shows a representative picture of a purple-colored SWNT thin film on a polyethylene substrate. Thickness measurements of thin films on flat substrates (microscope glass slides or sapphire) were performed with a Dektak 150 (Veeco Instruments Inc.) profilometer in collaboration with Michael Auth in the research group Dyakonov.

Drop-casting

For film preparation by drop-casting, SWNT dispersions needed to be more concentrated than dispersions directly obtained by sonication of shear force mixing (see section 3.1.1). Therefore, SWNTs in toluene were vacuum filtrated and the filter membrane dissolved in acetone. The remaining SWNT nanotube network films were redispersed in a small volume of chlorobenzene. This procedure resulted in dispersions with a peak absorbance between ≈ 50 and 150 at 1.24 eV. The highly concentrated SWNT dispersions were mixed with PFO-BPy solutions (in chlorobenzene) such that a polymer excess with PFO-BPy/SWNT mass ratio of 50 or 1000 was obtained (for details see PhD thesis of Späth [188]). Drop-casting of the resulting dispersion on glass or sapphire substrates led to SWNTs embedded in a PFO-BPy polymer matrix. If the polymer matrix films are immersed in solvent, as in the case of redox doping experiments, it is recommended to use high molecular weight PFO-BPy as matrix material. This results in less film material loss due to slower dissolution.

3.1.3 Redox Chemical Doping of SWNT Samples

SWNTs were redox chemically doped using the strong oxidants gold(III) chloride ($AuCl_3$, $> 99.99\,\%$ purity, Sigma-Aldrich) or triethyloxonium hexachloroantimonate (OA, Sigma-Aldrich). For *p*-doping of SWNTs in dispersion, the polymer wrapped nanotubes in toluene were mixed with acetonitrile ($> 99.9\,\%$ CHROMASOLV for HPLC, Sigma-Aldrich) to obtain a volume ratio of 10:1 (toluene:acetonitrile). Stepwise addition of oxidant solution in the same solvent mixture, *i.e.* redox titration, caused *p*-doping of the semiconducting SWNTs.

The addition of acetonitrile was necessary to ensure sufficient oxidant solubility but results in less stable nanotube dispersions. Therefore, only a small amount (one part in 11) of acetonitrile was chosen.

Doping of SWNT film samples was achieved by immersion of the films for 5 - 15 min in an oxidant solution (volume ratio toluene:acetonitrile 5:1) of a certain concentration and subsequent drying of the films.

3.2 Steady-State Spectroscopy

3.2.1 UV-VIS-NIR Absorption Spectroscopy

Absorption spectra in the ultraviolet (UV), visible (VIS) and near infrared (NIR) spectral regions were recorded using a Cary-5000 (Varian) spectrometer in transmission mode. SWNT dispersions were typically investigated in quartz cuvettes of 10 mm path length. In contrast, liquid samples prepared for pump-probe experiments were measured in 1 mm or 2 mm path length cuvettes due to their higher necessary SWNT concentrations. Solid film samples were fixed in the light path using tape and an appropriate sample holder. All absorption spectra were referenced to spectra of samples containing no SWNTs, *i.e.*, the pure solvent in the case of liquid samples and the empty substrate for film samples.

3.2.2 Fourier-Transform Infrared Spectroscopy

Fourier-transform infrared spectra of SWNT thin films on 500 µm thick polyethylene substrates or intrinsic silicon were measured at two different spectrometers in transmission mode. Transmission spectra in the mid-infrared ($\geq 400\,\mathrm{cm}^{-1}$) were mainly recorded at an FT/IR-4100 (Jasco) spectrometer using a high-intensity ceramic IR light source, a Ge/KBr beam splitter and a triglycine sulfate detector.

The KBr beam splitter transmittance drops severely in the far infrared at wavenumbers $< 400\,\mathrm{cm}^{-1}$. Therefore, transmission spectra in the far infrared were recorded using an IFS120HR spectrometer (Bruker) with a globar light source, a Mylar beam splitter and a triglycine sulfate detector.

3.2.3 Photoluminescence Excitation Spectroscopy

Photoluminescence (PL) spectroscopy and photoluminescence excitation (PLE) spectroscopy was performed at a custom-built setup. Here, only a brief description of the setup is given. A full description of a very similar setup is found in the PhD thesis of Hain [189].

A fiber-based supercontinuum laser SuperK Extreme EXR-15 (NKT Photonics) produces a broad spectrum ranging from ≈ 400 - 2400 nm, which can be used as the excitation light source (see Fig. 3.3). Narrow parts of the supercontinuum spectrum are selected by the filter unit SuperK Varia (NKT Photonics) acting as a variable bandpass filter. The narrowband light was used for excitation of the SWNTs in the visible spectral region. For liquid samples, a 10 mm path length cuvette was placed in the excitation laser focus. Solid thin-film samples were measured on their transparent substrates and placed in the focus using an appropriate sample holder. The NIR PL was collected in a 90° geometry and separated from scattered excitation light using a 900 nm longpass filter. The PL was spectrally dispersed by a Shamrock SR-303i (Andor) grating spectrograph (150 lines/mm) and detected by a cooled InGaAs array (iDus PDA DU491A-1.7, Andor).

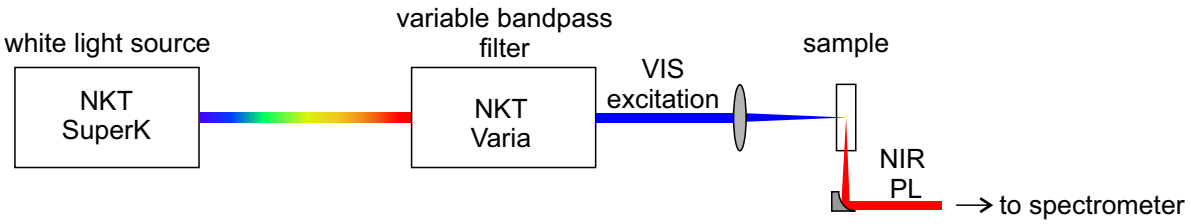

Figure 3.3: Schematic illustration of the PLE setup with restriction to the most relevant elements. The sample was either a 10 mm path length cuvette filled with a nanotube dispersion or a solid SWNT film on a transparent substrate.

3.3 Time-Resolved Spectroscopy

During this thesis, transient absorption (TA) spectroscopy was used to investigate the nonlinear optical response of intrinsic and doped SWNTs. In the following, the experimental setup for measurements in Würzburg is described. Whenever appropriate, the reader is referred to the PhD theses of Stich, Schilling and Mann for a more detailed description [96, 190, 191]. The TA setup in Würzburg is capable of experiments at probe photon energies 1.13 eV $\leq E_{\mathrm{pr}} \leq$ 2.58 eV. Measurements at lower probe photon energies were performed in Madrid in cooperation with Lüer and Abudulimu. A description of the TA setup in Madrid is found in the PhD thesis of Abudulimu [192].

3.3.1 The Femtosecond Laser System

The femtosecond transient absorption experiment is based on a commercially available laser system manufactured by *Coherent Inc.* Fig. 3.4 depicts the different laser system components. In the following the so-called chirped pulse amplification is explained. A Vitesse oscillator generates femtosecond pulses with 1.55 eV (800 nm) central energy and a repetition rate of 80 MHz using a titanium-sapphire crystal as the amplification medium. However, resulting pulse intensities are too low for TA experiments, which necessitates further amplification. Before the amplification of the pulses in a RegA 9050 regenerative amplifier, the pulses are temporally stretched in an EC 9150 stretcher/compressor unit. The temporal elongation is achieved by the introduction of a chirp. The RegA 9050 amplifier is pumped by a 10 W Nd:YVO_4 continuous-wave diode laser (Verdi V10) with a photon energy of 2.33 eV (532 nm). The time-averaged output power of the amplifier is 1.6 W at a reduced repetition rate of 250 kHz. A second passage through the stretcher/compressor unit compresses the amplified but still chirped and temporally long pulses. This results in 50 fs short pulses and a time-averaged output power of 1.1 W. Using a 70:30 beamsplitter, 30 % of the power is used for white light generation, whereas the remaining 70 % of the power is coupled into an optical parametric amplifier (OPA 9450). More detailed descriptions of the regenerative amplifier and the optical parametric amplifier can be found in the PhD theses of Stich, Schilling and Mann [96, 190, 191].

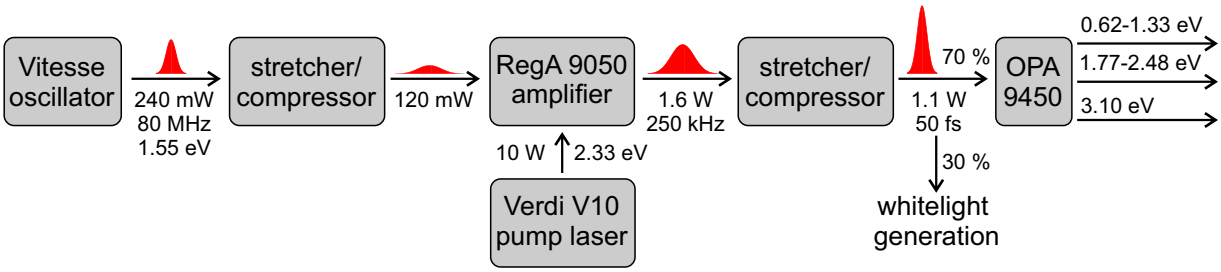

Figure 3.4: Schematic description of the femtosecond laser system sold by *Coherent Inc.*

3.3.2 The Transient Absorption Setup

Fig. 3.5 shows a simplified description of the transient absorption setup. As already noted, the output power of the compressor was divided in the ratio 70:30 with 70 % being used for the generation of frequency converted pump pulses in the OPA.

The OPA process always amplifies two photon energies. The higher energy pulses are called signal and the lower energy pulses are called idler pulses. For the experiments described in this thesis, the 1.55 eV (800 nm) input pulses were – after frequency doubling – either converted to visible signal pump pulses with central energies of 2.16 eV (574 nm) and 2.06 eV (600 nm) or NIR idler pump pulses at central energies of 1.24 eV (1000 nm) and 1.06 eV (1170 nm). Remaining 1.55 eV light and unwanted signal/idler contributions were filtered out using appropriate longpass or shortpass filters.

Within the OPA the laser pulses are transmitted through several dispersive optics leading to a chirp and a temporal elongation of the pump pulses. Therefore, the pump pulses in the visible were compressed using a single-prism compressor (SPC) as described by Akturk *et al.* [193]. A detailed description of this particular prism compressor and the theory behind prism compressors in general can be found in the PhD theses of Stich and Schilling [96, 190]. The temporal duration of the VIS pump pulses was optimized using an autocorrelator (PulseScope, APE Angewandte Physik und Elektronik GmbH) based on second harmonic generation (SHG). For NIR pump pulses the prism compressor was not used due to a less intense chirp compared to the VIS pump pulses.

A mechanical chopper (MC1000A, Thorlabs Inc.) periodically blocks on average every second pump pulse. The beam profile of the pump pulses was optimized by spatial filtering to a nearly Gaussian beam profile. The linear polarization relative to the probe pulse polarization was adjusted by a half-wave plate and a linear polarizer. Finally, a $f = 250\,\text{mm}$ or $f = 300\,\text{mm}$ lens focused the pump pulses into the sample and an aperture blocked them after the sample.

The remaining 30 % of the compressor output power was used for generation of white light probe pulses. First, a delay line (M-521, Physik Instrumente) was passed, which temporally delays the probe pulses relative to the pump pulses. White light generation was achieved by focusing the $\approx 50\,\text{fs}$ short 1.55 eV pulses into a sapphire plate using a $f = 50\,\text{mm}$ lens. The strong spectral broadening (supercontinuum generation) is mainly caused by self-phase

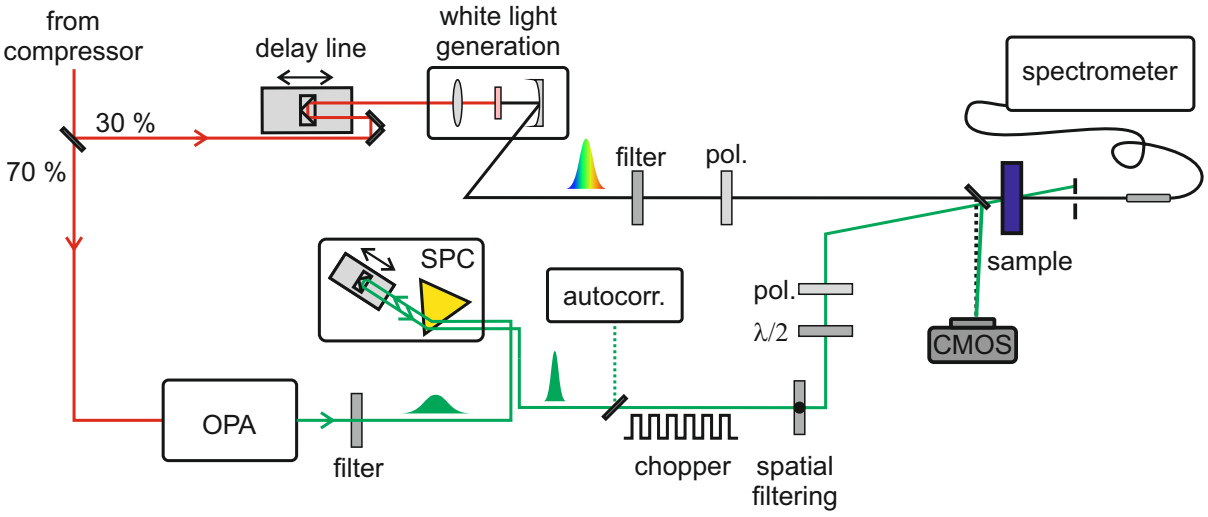

Figure 3.5: Schematic illustration of the transient absorption setup.

modulation and Raman processes [194]. Remaining 1.55 eV light was filtered out by appropriate color glass filters. In the case of probing the VIS spectral region, a BG38 (Schott AG) shortpass filter was used. For NIR probing an RG1000 (Schott AG) longpass filter sufficiently reduced the light intensity around 1.55 eV.

After passing a linear polarizer, the white light probe pulses were focused into the sample with a $f = 200\,\text{mm}$ spherical mirror and were coupled into a Shamrock SR-303i (Andor) grating spectrograph via a multimode glass fiber of 50 µm or 200 µm core diameter. A 2D silicon CCD camera (Newton DU 920P-BR-DD, Andor) operating in full vertical binning mode was used as the detector. For the determination of the spatial beam profile and spatial pump-probe overlap, a flip mirror in front of the sample reflected the pump and probe pulses onto a CMOS camera (DMK 72BUC02, The Imaging Source) with $2.2 \times 2.2\,\mu\text{m}^2$ pixel size.

The sample was, depending on the specific experiment, either a 1 mm or 2 mm path length cuvette filled with nanotube dispersion, a nanotube film on a transparent substrate, the electrochemical cell described in section 3.4.1 or a 200 µm path length flow-through cuvette (see section 8) connected to a flow-electrolysis cell.

3.3.3 Data Acquisition and Measurement Principle

The tunability of the pump pulses (see Fig. 3.4) on the one hand and the detectable white light intensity on the other hand limit the experimentally accessible spectral region. Fig. 3.6 shows measured white light spectra in the VIS and NIR. The spectrally accessible region is limited at high photon energies of $\approx 2.58\,\text{eV}$ (480 nm) by the supercontinuum generation process itself and at low photon energies of 1.13 eV (1100 nm) by the detector efficiency of the silicon CCD camera. The drop in white light intensity towards 1.55 eV is due to the BG38 and RG1000 color glass filters used for removal of excess 1.55 eV laser light. In order to

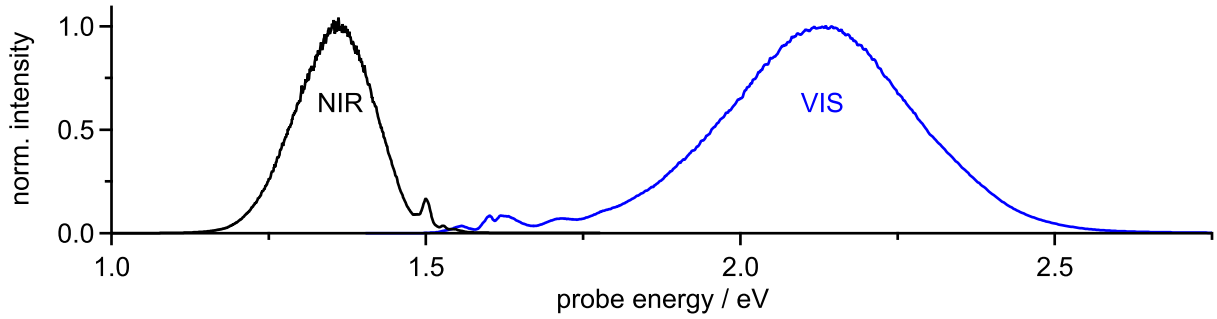

Figure 3.6: White light spectrum in the NIR and VIS spectral region.

measure the transient absorption spectrum of the sample under investigation, two separate white light transmission spectra have to be recorded. This is illustrated in Fig. 3.7. One spectrum is the reference spectrum with no pump intensity at the sample $I_{\text{off}}(E)$. The other spectrum is measured with pump intensity $I_{\text{on}}(E, \tau)$. The modulation of the pump intensity with a frequency $f/2 = 250\,\text{Hz}$ is achieved by the mechanical chopper. Since the silicon CCD camera is read out at a frequency $f = 500\,\text{Hz}$, a spectrum with pump intensity is followed by a spectrum without pump intensity and *vice versa*. It has to be noted that each spectrum is composed of a pulse train of 500 probe pulses due to the laser repetition rate of 250 kHz. The transient absorption spectrum at a certain time delay τ is calculated as:

$$\Delta A = -\log\left(\frac{I_{\text{on}}}{I_{\text{off}}}\right), \tag{3.1}$$

where ΔA is the pump-induced change in absorbance A. Alternatively, the differential transmission $\Delta T/T$ is given by:

$$\frac{\Delta T}{T} = \frac{I_{\text{on}} - I_{\text{off}}}{I_{\text{off}}}. \tag{3.2}$$

The following relationship interconverts the two quantities:

$$\frac{\Delta T}{T} = 10^{-\Delta A} - 1. \tag{3.3}$$

Caution has to be paid when transient absorbance and differential transmission are compared, since not only the absolute signal intensities change (see equation (3.3)) but also the signs of the different signal contributions (see Fig. 3.7c and d). Steady-state absorption spectra are typically shown as absorbance, and consequently, ΔA seems more beneficial than $\Delta T/T$ for a direct comparison of transient and steady-state absorption spectra. In this thesis experimental data are always shown as the negative transient absorbance $-\Delta A$ such that the signal contributions have the same sign for $\Delta T/T$ and $-\Delta A$.

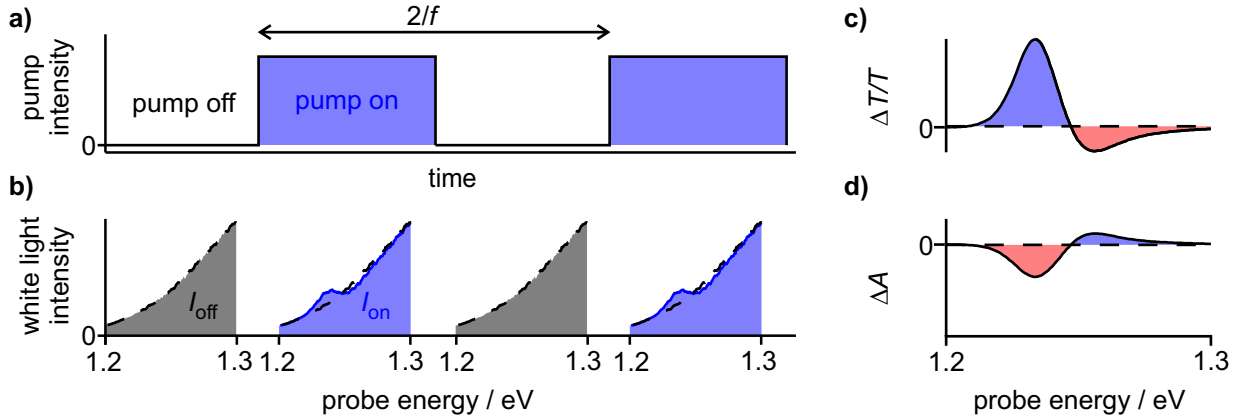

Figure 3.7: a) Illustration of the pump intensity modulation with frequency $f/2$ by the mechanical chopper. b) Experimentally measured white light intensity transmitted through a typical organic (6,5)-SWNT dispersion with strong S_1 absorption at 1.24 eV. The spectra are either without (I_{off}, black dashed line) or with pump intensity (I_{on}, blue solid line) at the sample. c) Calculated differential transmission $\Delta T/T = (I_{on} - I_{off})/I_{off}$ and d) transient absorbance $\Delta A = -\log(I_{on}/I_{off})$.

Signal contributions

Fig. 3.8 explains the different signal contributions composing a typical transient absorption spectrum. In transient absorption spectroscopy a short pump pulse excites the system of interest from the electronic ground state (GS) to an electronically excited state E_1. This leads to a reduction of ground state population and an increase in E_1 population (Fig. 3.8b). Compared to the situation of no pump intensity at the sample (Fig. 3.8a) the probe pulse measures a reduced absorption from the ground state to the excited states E_1 and E_2. Such a signal contribution is called a photobleach (PB) in this thesis and has a positive sign ($-\Delta A > 0$). Additionally, stimulated emission can occur from E_1 to the ground state GS, which has a positive sign, too. For SWNTs, the Stokes shift is less than 5 meV [17] and much smaller than the typical PB linewidth on the order of several ten meV. Therefore, PB and stimulated emission signals can often not be distinguished. A third signal contribution arises from the excitation from E_1 to higher-lying electronic states like, for example, E_2. This process is called photoabsorption (PA) and has a negative sign ($-\Delta A < 0$).

Sensitivity of the transient absorption experiment

The sensitivity of the transient absorption experiment is closely related to the fluctuations in measured white light intensity. A possibility to increase the sensitivity is to average over many spectra. The readout frequency of the CCD camera is 500 Hz, which means that for 1 s integration time 250 white light spectra with and 250 without pump intensity are averaged. However, typically an integration time of 10 s per transient absorption spectrum was chosen such that the sensitivity was further enhanced. A simple sensitivity estimate is obtained by taking many transient absorption spectra $\Delta A(E)$ without a sample and calculating the probe energy dependent standard deviation $\sigma(E)$. Fig. 3.8c shows the standard deviation for

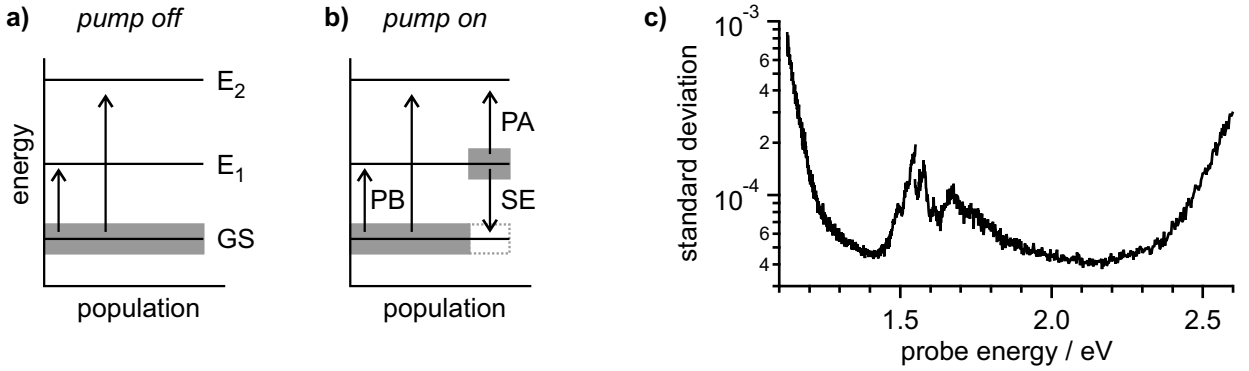

Figure 3.8: Illustration of the different signal contributions in a TA experiment and the sensitivity of the setup. a) Situation when the sample is not excited by a pump pulse. The probe pulse measures the ground state (GS) absorption spectrum of the sample. b) Situation when the sample has been excited by a pump pulse. Three signal contributions arise due to reduced ground state population and the increased excited state E_1 population: Photobleach (PB), stimulated emission (SE) and photoabsorption (PA). c) Standard deviation of $\Delta A(E)$ for 10 s integration time and a total number of 116 transient absorption spectra. The standard deviation can be taken as a measure of the sensitivity of the TA setup.

an integration time of 10 s per spectrum and a total number of 116 spectra. The standard deviation is less than 2×10^{-4} in the energy window 1.2 - 2.5 eV. This standard deviation is an estimate of the maximum sensitivity of the transient absorption setup [190]. However, it has to be noted that this is an upper bound, and for typical SWNT samples, the sensitivity can be reduced. This is especially the case for strongly scattering SWNT thin-film samples [96].

3.3.4 Laser Pulse Characterization

Spatial pump-probe overlap

The spatial pump-probe overlap at their respective focal positions was adjusted using a CMOS camera (DMK 72BUC02, The Imaging Source) with $2.2 \times 2.2\,\mu m^2$ pixel size. The pump focus was at least twice as large as the probe focus with typical 1D probe spot sizes on the order of $\approx 40\,\mu m$, and pump spot sizes $\approx 120\,\mu m$ (intensity full width at half maximum, FWHM). A more detailed description and how probed photon fluences are determined can be found in the PhD theses of Stich, Schilling and Mann [96, 190, 191].

SHG autocorrelation

The time resolution in a pump-probe experiment is essentially limited by the temporal widths of the pump and probe pulses. The second harmonic generation (SHG) based autocorrelator PulseScope (Angewandte Physik & Elektronik GmbH) was used to characterize and optimize the pump pulse duration Δt. Within the autocorrelator, each pump pulse is split into two identical pulses by a beam splitter. An interferometer delays the two replicas by a time τ relative each other. Subsequently, both pulses are spatially overlapped by focusing into a

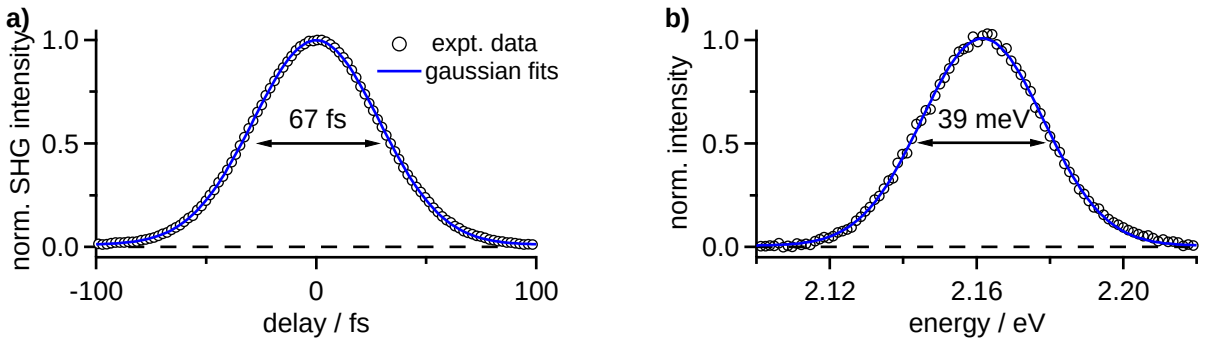

Figure 3.9: a) Autocorrelation curve for 2.16 eV pump pulses and b) the corresponding spectrum.

BBO crystal. The autocorrelation signal $A_{\mathrm{AC}}(\tau)$ in dependence of the time delay τ is given by the intensity of the SHG in the BBO crystal. If the temporal shape of the pump pulses is known, the pump pulse duration can be extracted from the autocorrelation signal. In this thesis the pump pulses are always assumed to be of Gaussian type:

$$I(t) \propto \exp\left(-\frac{4\ln 2\, t^2}{\Delta t^2}\right), \tag{3.4}$$

where Δt is the FWHM.
For Gaussian pump pulses, the autocorrelation signal is itself a Gaussian but with a $\sqrt{2}$ larger FWHM:

$$A_{\mathrm{AC}} \propto \exp\left(-\frac{2\ln 2\, \tau^2}{\Delta t^2}\right). \tag{3.5}$$

Fig. 3.9a shows the SHG autocorrelation curve for pump pulses with central energy of 2.16 eV. The SHG autocorrelation intensity is well described by a Gaussian of 67 fs FWHM. This translates into a pump pulse durations of $\Delta t = 47$ fs. The extracted pulse duration can be compared to the duration expected from a bandwidth-limited pulse. The bandwidth limit correlates the temporal width Δt and the bandwidth $\Delta\nu$ or ΔE:

$$\Delta\nu\Delta t = 0.441 \text{ or } \Delta E\Delta t = 1.82\,\mathrm{eV\,fs}. \tag{3.6}$$

Fig. 3.9b shows the spectrum of the pump pulses with a bandwidth of 39 meV. The calculated value $\Delta E\Delta t = 1.83$ eV fs obtained from the experimentally determined pulse duration and bandwidth shows that the pump pulses can be compressed close to the bandwidth limit using the single-prism compressor.

Time resolution

The time resolution is not only limited by the pump pulse duration. More precisely, the cross-correlation of pump and probe determines the time resolution. In order to experimentally measure the time resolution, the coherent artifact in pure solvent or in a pure transparent substrate can be used [195]. According to Lorenc *et al.*, the coherent artifact contains

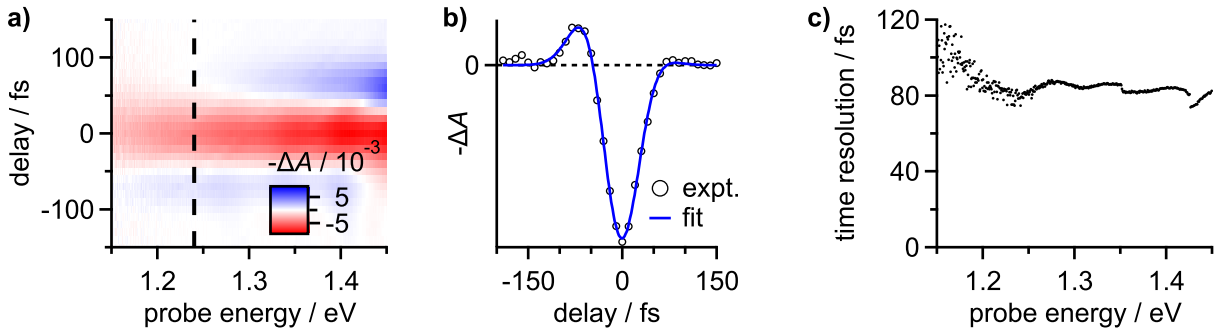

Figure 3.10: a) Transient absorption map in the NIR, showing the coherent artifact upon nonresonant excitation of pure tetrahydrofuran at 2.16 eV. b) Transient at 1.24 eV and fit using a linear combination of a Gaussian and its first and second derivative. c) Probe energy-dependent time resolution given by the FWHM of the Gaussian used for the fits.

contributions from cross-phase modulation, stimulated Raman amplification and two-photon absorption [196]. A fit of the probe energy dependent coherent artifact with a linear combination of a Gaussian and its first and second derivative allows determining the probe energy dependent time resolution [197, 198], which is here defined as the FWHM of the Gaussian profile. This is illustrated in Fig. 3.10 for nonresonant excitation of tetrahydrofuran with 2.16 eV pump pulses using the thin-layer spectroelectrochemical cell described in section 3.4.1.

Fig. 3.10a shows the transient absorption map, where a TA signal is only observed close to time zero. The spread to negative and positive delay times is a manifestation of the pump-probe cross-correlation, *i.e.* time resolution. A vertical cut at 1.24 eV probe energy, resonant with the first subband exciton absorption in (6,5)-SWNTs, is shown in Fig. 3.10b. The transient is well described by a fit using a linear combination of a Gaussian and its first and second derivative. Fig. 3.10c shows the extracted time resolution, which is about 80 fs at 1.24 eV.

An alternative estimate of the time resolution can be obtained by fitting transients with a convolution of a Gaussian instrument response function and a model decay. The FWHM of the Gaussian instrument response function then equals the time resolution.

3.3.5 Post Measurement Corrections

White light chirp correction

Traveling through transparent dispersive optics, the broadband probe pulses become chirped. This causes a probe energy dependent time delay. However, if the chirp is known, a numerical correction can be performed. In this thesis, the white light chirp was determined using the coherent artifact in pure solvent or in a transparent substrate without sample. For each pixel, corresponding to a specific probe energy, a transient is evaluated and the time at which the coherent artifact shows a minimum ($-\Delta A < 0$) was taken as the probe energy dependent time zero. Fig. 3.11a displays the same data as in Fig. 3.10a but before chirp correction.

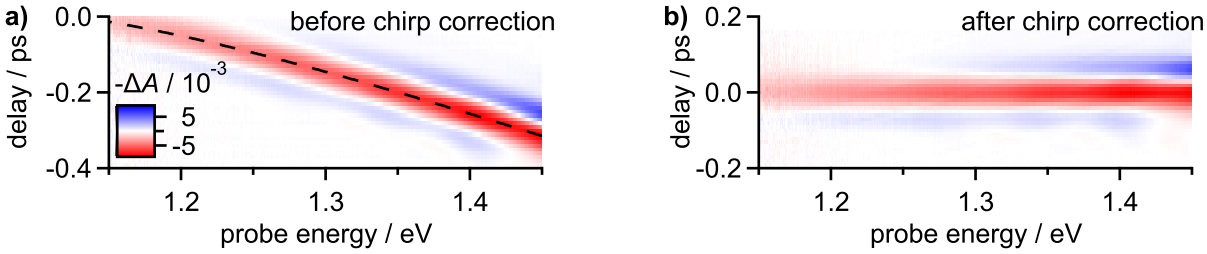

Figure 3.11: a) Transient absorption map of pure tetrahydrofuran upon nonresonant excitation with 2.16 eV pump pulses. The coherent artifact and probe energy dependent time zero caused by the white light chirp are clearly visible. The black dashed line is a curve used for chirp correction. b) Result of a successful chirp correction indicated by the probe energy independent time-zero.

The black dashed line is a polynomial fit to the time zero determination at each pixel and is used for the numerical chirp correction. The successful chirp correction with a probe energy independent time zero is shown in Fig. 3.11b.

Correction of time zero

The very accurate determination of time zero was not critical for the experiments in this thesis. Therefore time zero was adjusted after the measurement such that it reflects the temporal position at which a transient has reached half of its maximum value. This procedure is in accordance with the excited state population after pulsed but incoherent excitation [199].

Correction of background signals

The transient absorption maps were corrected by subtraction of a transient absorption spectrum measured at negative time delays of several picoseconds. This procedure corrects for constant, *i.e.* pump-probe delay independent signals like, for example, signals arising due to scattering light hitting the detector.

3.4 Spectroelectrochemistry

3.4.1 Thin-Film Spectroelectrochemistry

For spectroelectrochemical experiments at SWNT thin-films, an electrochemical cell based on a quartz cuvette (EF-1362, Bioanalytical Systems, Inc.) with 500 µm path length was used (see Fig. 3.12a). The electrochemical cell consists of a semi-transparent platinum mesh working electrode (WE) allowing to measure spectra in transmission mode. Platinum wires served as counter and quasi-reference electrodes. All electrochemical measurements were performed using 0.1 M tetrabutylammonium hexafluorophosphate ($TBAPF_6$) in dry and degassed tetrahydrofuran as an electrolyte. To further guarantee the exclusion of water and oxygen, the experiments took place in an argon inert gas atmosphere using the sample holder depicted in Fig. 3.12b. More detailed information about the preparation of the electrolyte solution and

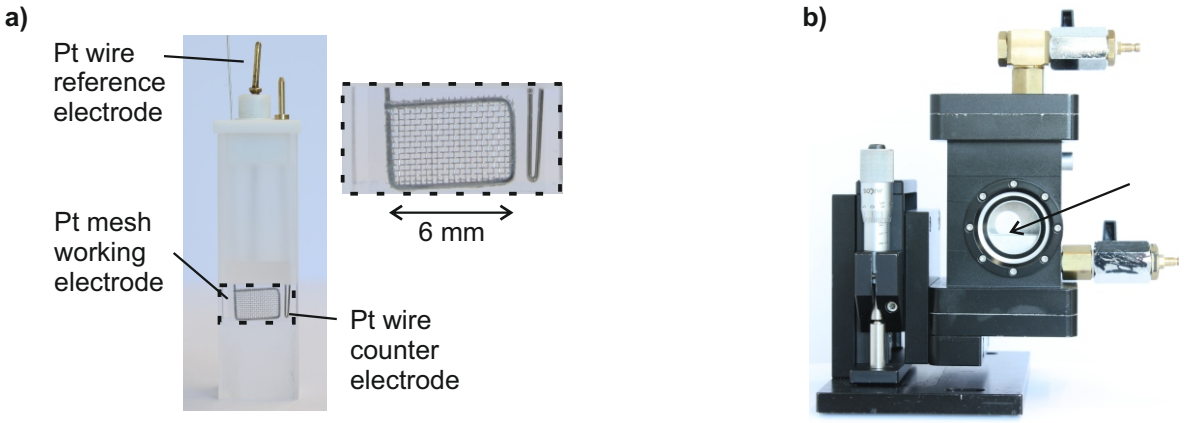

Figure 3.12: a) Electrochemical cell used for time-resolved spectroelectrochemistry at SWNT thin films. The SWNT thin-films (not shown) were deposited on a semi-transparent platinum mesh working electrode. b) Inert gas containing sample holder in which the electrochemical cell is placed during the experiment. The arrow marks the position of the electrochemical cell (not shown). Two windows allow the transmission of (laser) light through the sample holder and the electrochemical cell.

the sample holder can be found in the PhD thesis of Hartleb [200]. For time-resolved spectroelectrochemical experiments, the sample holder containing the electrochemical cell was placed in the transient absorption setup such that spatial pump-probe overlap occurred at the SWNT thin-film deposited on the platinum mesh working electrode. Control of the working electrode potential was achieved using an EG&G Model 363 potentiostat and a LabView software written by Hartleb [200].

3.4.2 Spectroelectrochemistry in Solution

Spectroelectrochemical experiments in solution were performed using a flow-electrolysis cell HX-301 (Hokuto Denko Co.). The flow-electrolysis cell was connected at the solution inlet to a micro annular gear pump mzr-4605 (HNP Mikrosysteme) using Teflon tubings. At the solution outlet, the flow-electrolysis cell was connected to a flow-through cuvette with 200 µm path length (48-Q-0.2, Starna Cells Inc.). For spectroelectrochemistry in transmission mode, the flow-through cuvette was either placed in the steady-state absorption spectrometer or in the transient absorption setup. For time-resolved spectroelectrochemical experiments, the solution passing the flow-through cuvette is reused and pumped in a cycle. This procedure saves sample volume over extended measurement times. The working electrode potential was controlled using an SP-50 potentiostat (Bio-Logic Science Instruments) and commercial software. Further descriptions of the flow-electrolysis cell can be found in chapter 8.1.

4 Comparison of Electro- and Redox Chemical Doping Schemes

Bulk semiconductors such as silicon are commonly doped by the introduction of substitutional impurities [34, 41, 201, 202]. In contrast, semiconductor nanostructures are typically doped by means of redox chemistry, electrochemistry or using electric fields in a field-effect transistor (FET) [18, 39, 203–209]. In this work, both electro- and redox chemical doping of single-wall carbon nanotubes was performed.

In order to check if both doping schemes lead to identical results, Fig. 4.1 contrasts two series of absorption spectra for either electro- or redox chemical doping. The absorption spectra for electrochemical doping were reproduced from reference [18] and were recorded by Holger Hartleb. Successive *p*-doping is realized by an incremental increase of the working electrode (WE) potential. The SWNTs, prepared as a thin-film, are in direct contact with the working electrode (see section 3.4.1).

For redox chemical doping, successive *p*-doping of the SWNTs in dispersion is achieved by a variation of the gold(III)-chloride oxidant concentration. No significant differences between the absorption spectra for both doping schemes are observed except from the S_1 (and to a lesser extent S_2) exciton linewidth in the spectra of intrinsic nanotubes shown as black lines. The discrepancy can be explained by the intertube coupling in the case of the thin-film samples used for electrochemical doping. This coupling increases the inhomogeneous exciton linewidth compared to the individually dispersed SWNTs used for redox chemical doping in dispersion [67]. Apart from that, little differences most likely arise from slight variations in

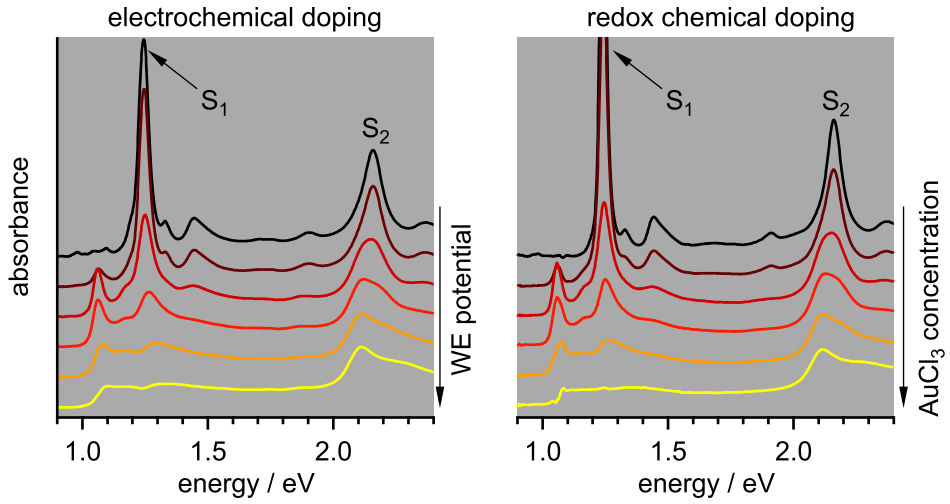

Figure 4.1: Comparison of absorption spectra of electrochemically or redox chemically *p*-doped SWNTs. The absorption spectra for the electrochemical doping were reproduced from [18].

charge density between the two directly compared absorption spectra.

4.1 Thermodynamical Considerations

The similarity between spectra for both doping schemes can be understood by thermodynamical considerations. The electrochemical potential $\bar{\mu}$ of a species describes how much energy is needed to add one additional particle of that species and is expressed by:

$$\bar{\mu} = \mu^{\ominus} + kT \ln(c) + z\,e\,\Phi, \tag{4.1}$$

where $\mu^{\ominus}$ is the chemical potential at standard conditions and c is the concentration normalized to the standard concentration $c^{\ominus}$. The term $z\,e\,\Phi$ describes the dependence of the electrochemical potential on the electric potential Φ, where z is the number of charges, and e is the elementary charge.

In the discussed p-doping of SWNTs, electron transfer from the SWNT to other systems is the essential process. Therefore, the electron's electrochemical potential $\bar{\mu}_e$ in SWNTs and in the system in contact with the SWNTs is of most interest. The relative magnitudes of the electrochemical potential $\bar{\mu}_{e,i}$ in different phases i determine if electron transfer from one phase to another is thermodynamically favorable. In the following, the subscript e for electrons is omitted because electrochemical potentials of electrons are regarded throughout the text. Using alternative terminology, which is more common in solid-state physics, the electrochemical potential of electrons is also called the Fermi energy E_{F}:

$$E_{\mathrm{F}} = \bar{\mu}. \tag{4.2}$$

Next, electro- and redox chemical doping of SWNTs are put on the same physical ground as discussed by means of Fig. 4.2. Fig. 4.2a shows the (redox) potential U vs. standard hydrogen electrode (SHE), which is commonly used to describe working electrode potentials and redox potentials alike. Additionally, the electron energy E referenced to the vacuum level (see section 2.1.3) is depicted, which is a common scale for energy levels in solid state systems. Note that U increases from top to bottom whereas the opposite is true for E. Equation (4.1) predicts that a variation of the electrostatic potential Φ alters the electron's ($z = -1$) electrochemical potential $\bar{\mu}$. This field-effect provides a thermodynamic incentive for electron transfer in an electrochemical experiment but also in frequently used FET based doping. In electrochemistry, the electrochemical potential $\bar{\mu}_{\mathrm{WE}}$ of the WE is controlled by the application of a defined WE potential U_{WE}. The working electrode potential U_{WE} is measured against a reference electrode (RE) and can be related to the difference of electrochemical potentials of the WE and RE by:

$$U_{\mathrm{WE}} = \frac{\bar{\mu}_{\mathrm{RE}} - \bar{\mu}_{\mathrm{WE}}}{e}. \tag{4.3}$$

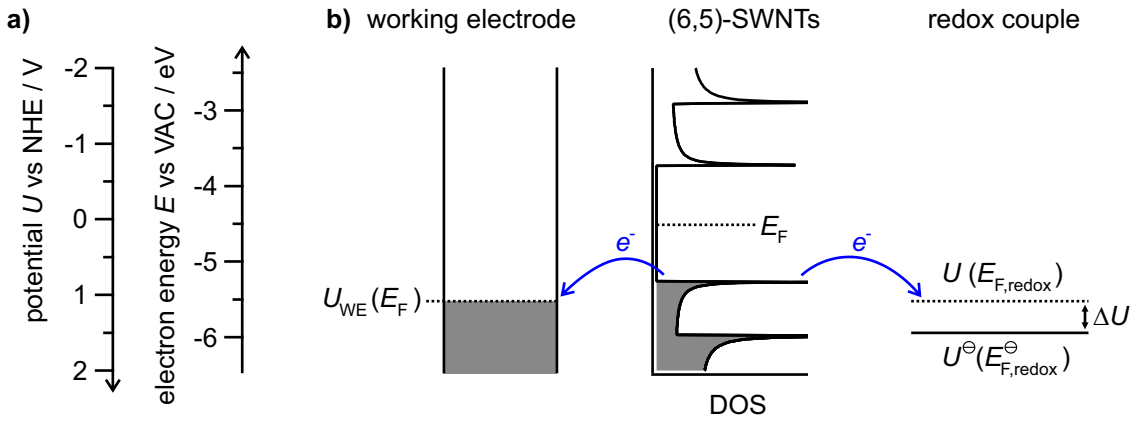

Figure 4.2: a) Comparison of the potential U used in electro- and redox chemistry with the electron energy E used in solid state physics. b) Electrochemical and redox chemical p-doping of (6,5)-SWNTs. Electrons are transferred from the nanotube to the WE for a sufficiently positive applied WE potential U_{WE}. Redox chemical p-doping of nanotubes is achieved by using $AuCl_3$. Stepwise addition of $AuCl_3$ solution, *i.e.* redox titration, controls the redox potential U.

Upon application of a sufficient positive WE potential, electrons are transferred from the SWNT to the WE, *i.e.* SWNT p-doping occurs, as shown in Fig. 4.2b. Electron transfer proceeds until $\bar{\mu}_{\mathrm{SWNT}} = \bar{\mu}_{\mathrm{WE}}$, which allows controlling the nanotube Fermi level by the applied WE potential U_{WE}.

Fig. 4.2b is also used to illustrate redox chemical doping of SWNTs. Differences in redox potentials U between two redox pairs provide the driving force of electron transfer in redox chemistry. According to the Gerischer model (see section 2.1.3), the redox potential U of a redox pair can again be associated with the electrochemical potential of the electron $\bar{\mu}_{\mathrm{redox}}$ (or $E_{\mathrm{F,redox}}$). The redox potential U follows the Nernst equation, which describes the dependence of U on the concentration of species in their oxidized (Ox) and reduced (Red) state as well as the standard potential $U^{\ominus}$. Control of U (and therefore also of the electrochemical potential $\bar{\mu}_{\mathrm{redox}}$) is achieved by altering the respective concentrations, here by successive addition of the oxidant $AuCl_3$. The standard potential $U^{\ominus}_{\mathrm{Au^{3+}/Au^0}} = 1.5\,\mathrm{V}$ (in aqueous medium) [210] is highly positive such that electron transfer from the SWNTs to the redox couple system is easily achieved, even for small ratios of $c_{\mathrm{ox}}/c_{\mathrm{red}}$. In contact with the nanotubes and in thermodynamic equilibrium, the electrochemical potential are equal ($\bar{\mu}_{\mathrm{SWNT}} = \bar{\mu}_{\mathrm{redox}}$). This allows adjusting the nanotube Fermi level by a variation of the concentration of redox-active molecules.

Since both electro- and redox chemical doping control the SWNTs Fermi level, it appears clear why the absorption spectra in Fig. 4.1 are hardly distinguishable. However, the electronic and optical properties of SWNTs, possessing only surface atoms, strongly depend on the environment. The similarity of absorption spectra upon electro- and redox chemical doping suggests that the interaction of doped SWNTs with the electrolyte or the $AuCl_3$ solution is either negligibly small or similarly strong. Chapter 5 further discusses the interaction of

SWNT excess charges with counterions, which are always present in both doping schemes.

4.2 Quantification of Doping Levels

In Fig. 4.1 absorption spectra of electro- and redox chemical doping were contrasted by simple visual inspection of spectra and finding pairs which look almost identical. However, for a quantitative comparison of different experiments, a quantification of the doping level by the charge density n is more desirable. Unfortunately, charge densities in carbon nanotubes or low-dimensional semiconductors in general are not easily determined. Chapter 7 investigates how absorption spectroscopy of the S_1 exciton can be used for a model-based determination of charge densities. Fig. 4.1 showed that the S_1 absorption decreases monotonically with increasing working electrode potential or $AuCl_3$ concentration. Therefore, the renormalized S_1 oscillator strength f_{S_1} ($0 \leq f_{S_1} \leq 1$) referenced to the oscillator strength $f_{S_1,0}$ in intrinsic SWNTs provides a good measure for the nanotube charge density n. It is reasonable to conclude that the charge density n is a monotonous function of the renormalized S_1 oscillator strength f_{S_1}. For practical reasons, in the following f_{S_1} or the exciton bleach $\chi = 1 - f_{S_1}$ instead of n is used for the definition of the doping degree or for comparison of different experiments. This is done because the oscillator strength f_{S_1} (or the bleach χ) is an experimentally easily accessible and model-independent quantity. In the following, the subscript 'S_1' is omitted ($f_{S_1} \rightarrow f$), and f is associated with the renormalized S_1 exciton oscillator strength unless stated otherwise.

5 Spectroscopy in the Moderate Doping Regime – Evidence for Charge Localization

The presented experiments deal with semiconducting carbon nanotubes over a broad range of doping levels, from intrinsic over moderately to heavily doped. In the following, these qualifiers will be defined.

From the viewpoint of electron transport, moderate doping can be defined for impurity concentrations at which the impurity atoms are decoupled, and the material becomes insulating at low temperatures [33]. In the 3D case, the transition from moderate to heavy doping then happens when distances $d \propto n^{-1/3}$ ($n =$ impurity concentration) between impurities become so small that the impurity wavefunctions start to overlap. For high enough impurity concentrations, the discrete impurity energy levels merge into impurity bands and conduction takes place even at low temperature [33]. Mott discussed this insulator-metal transition with the critical concentration n_c in 3D depending on the impurity Bohr radius a_B by $a_B\, n_c^{1/3} \approx 0.24$ [33, 211].

Hertel [44] classified the different doping regimes in the context of carbon nanotube spectroscopy by taking into account the nanotube length and exciton related length scales like the exciton coherence length or exciton size.

In this work, a more pragmatic classification is chosen. The doping regimes are divided roughly into three categories:

- *intrinsic*: no intentional doping with the only impurities resulting from the synthesis, sample preparation and ambient conditions
- *moderate doping*: low concentrations of intentionally introduced impurities such that the S_1 exciton oscillator strength is reduced but the absorption band is not fully bleached yet
- *heavy doping*: doping levels exceeding the previous definitions with nearly or fully suppressed S_1 absorption

Most spectroscopic studies on doped carbon nanotubes are performed in the moderate doping regime with existent exciton and trion absorption bands. The following section presents an overview of previous investigations.

5.1 State of the Art

Spectroscopy of doped single-wall carbon nanotubes has been carried out in numerous studies. Here, only a subset of these publications can be presented. Therefore, mainly studies

with samples and spectroscopic techniques comparable to the ones used in this thesis are considered. It will be focused on nearly monochiral SWNT dispersions or thin films doped electro- or redox chemically. The interested reader finds some experimental work on devices or spectroscopy of doped SWNTs on the single tube level in the following references: [32, 212–219]. Moreover, *n*-type doping is also not discussed here because spectroscopic behavior is nearly identical as for *p*-doping in (6,5)-SWNTs. This originates from the almost perfect electron-hole symmetry in near-armchair carbon nanotubes [152, 220, 221], resulting in very similar positive and negative trion energies [30, 200].

Zheng and Diner first investigated the redox chemistry of highly enriched (6,5)-SWNTs in 2004 [111]. They found that redox titration of dispersed SWNTs with K_2IrCl_6 leads to electron transfer from SWNTs to the Iridium complex. Increasing concentrations of the redox agent caused a strong absorption intensity reduction of the first subband exciton S_1 and a weaker reduction of the second subband exciton S_2. Alongside with the exciton bleach, a new redshifted and doping-induced absorption band at 1.06 eV (1170 nm) was observed. This spectral feature was later assigned to a charged exciton or trion X_1^+ by Matsunaga *et al.* [28] and Santos *et al.* [27]. In 2008 Frank *et al.* made similar observations regarding the S_1 and S_2 exciton absorption intensities upon electrochemical doping of (6,5)-SWNT enriched thin-films [222]. They found that the bleaching of both exciton absorption bands is accompanied by a spectral redshift.

Semiconducting carbon nanotubes were not only investigated regarding the doping-induced absorbance changes. Moreover, the dynamical properties of excitons, measured via photoluminescence (PL) or time-resolved spectroscopy, were of much interest. Hartleb *et al.* reported in an electrochemical doping study that the stationary S_1 PL is even more sensitive to doping than absorbance [18, 200]. Similar results have been reported by Kimoto *et al.* [223] for redox chemical doping using the hole-dopant F_4TCNQ. Time-resolved spectroscopy showed that the nonradiative decay of S_1 excitons becomes strongly accelerated upon doping [112, 143, 145, 224, 225]. Hence, increasing nonradiative decay rates provide a plausible explanation for the steady-state PL results.

Doping of SWNTs is frequently discussed in terms of band filling assuming that the charge density is fully delocalized over the whole nanotube crystal [18, 226–232]. However, this assumption is challenged by experimental studies suggesting that charge carrier localization might play a larger role than previously believed. A detailed discussion about this topic is also found in the book chapter *Optical Spectroscopy of Doped Carbon Nanotubes* by Hertel [44].

In a theoretical work, Adamska *et al.* calculated that surplus charges localize even in SWNTs in vacuum due to self-trapping (polaron formation) with a 30-60 meV binding energy [233]. Due to the high sensitivity of SWNTs to external perturbations, a further stabilization might arise from the electrostatic interaction of SWNT excess charges with opposite charges or dipoles in the environment. In another theoretical study, Veiga and Miwa calculated that charges on the SWNT, induced by redox chemical *p*-doping with TCNQ, are localized at the

SWNT/TCNQ contact region [234].

Experimental evidence for carrier localization has been reported by Mouri *et al.* by temperature-dependent PL [144]. The lack of a clear temperature dependence of trion PL was attributed to trion localization which in turn suggests a charge carrier localization. In contrast, the exciton PL follows the $T^{-1/2}$ temperature dependence expected for free and delocalized 1D excitons [144, 235]. Santos *et al.* used intense irradiation to produce electrons and holes via exciton-exciton annihilation and study all-optical trion generation [27]. The excitation fluence dependence and lineshape of the trion emission suggest that the trion and the associated charges are localized (trapped). This interpretation was further strengthened by pump-probe experiments showing long charge carrier recombination lifetimes probed by the trion photoabsorption signal. Lifetimes on the order of several hundred picoseconds are indicative of electron and hole trapping, which slows down recombination [27, 135].

In aqueous media or under ambient conditions, the oxygen/water redox couple causes *p*-doping for many SWNT chiralities [110, 111]. This is especially the case at low pH (acidic conditions), because of more favorable redox potentials [44, 110, 111, 236]. Upon addition of sulfuric acid, Cognet *et al.* observed a reversible stepwise quenching of exciton PL from single nanotubes [114]. This PL reduction in steps of discrete height indicates the local character of the induced charge, which acts as an efficient quencher of the diffusing exciton [98, 114].

Crochet *et al.* further demonstrated the local nature of PL quenching by photoluminescence imaging of an SWNT before and after addition of gold(III)-chloride, a strong *p*-type dopant also mainly used in this thesis [237]. The PL was found to be locally reduced by $\approx 60\,\%$ due to the formation of a localized hole on the SWNT. Investigations by Kim *et al.* and Choi *et al.* showed that treatment of SWNTs with gold(III)-chloride leads to a reduction of Au^{3+} to elementary gold Au^0, which forms at the nanotube surface [238–240]. The chlorine anions were suggested to be adsorbed on the nanotube surface counterbalancing the positive SWNT charges and were found to play a decisive role in the observed doping and dedoping phenomena [239].

5.2 Doping-Induced Changes in Interband Absorption

From a molecular perspective, steady-state absorption spectroscopy is ideally suited to determine the concentration of distinct species participating in an electron transfer reaction of the form

$$A^n + m\,e^- \rightarrow A^{n-m}. \tag{5.1}$$

This is the case because reactants and products typically possess strongly different absorption properties, and the Beer-Lambert law dictates that absorbance is proportional to the species concentration. In contrast, extended solid-state systems like carbon nanotubes can take up many charges with only gradual changes in their optical properties. Nevertheless, steady-state absorption is a valuable tool since the exciton bleach χ is directly related to the electron

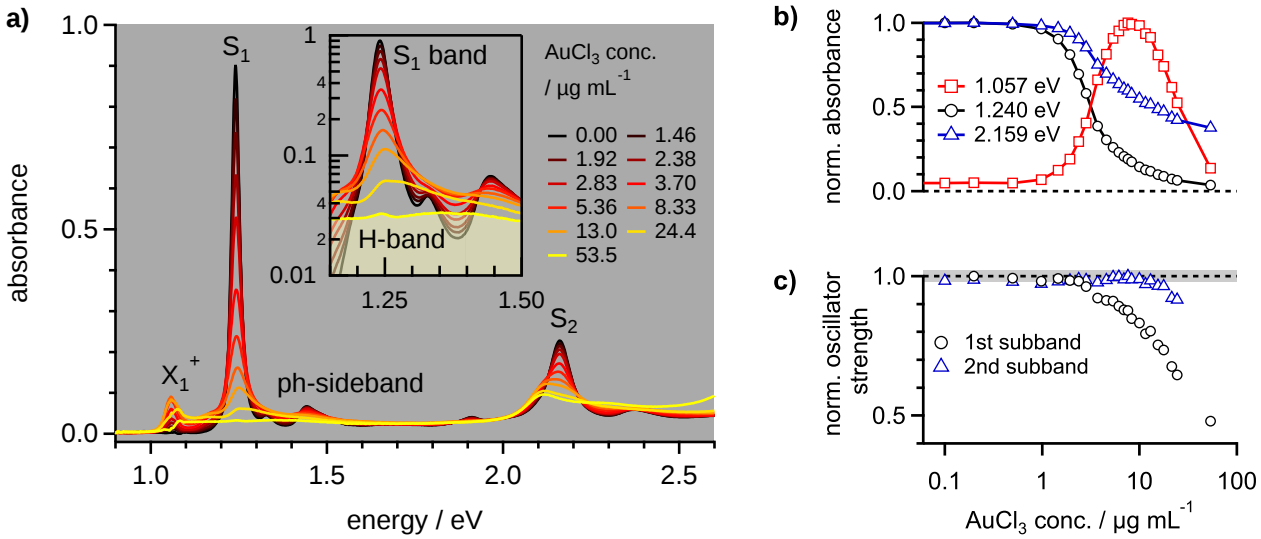

Figure 5.1: a) Series of nanotube absorption spectra at different $AuCl_3$ concentrations. The inset shows the S_1 absorption band on a logarithmic axis. b) Normalized S_1 exciton (black), S_2 exciton (blue) and X^+ trion absorbance (red) as a function of $AuCl_3$ concentration. c) Doping level dependence of the normalized first and second subband oscillator strength. Relative oscillator strengths were obtained by integration of the absorption spectrum from 0.95 eV to 1.85 eV and 1.95 eV to 2.50 eV, respectively. The gray shaded region displays the range 1±0.02.

and hole distribution functions $f_{e,h}(k)$ in the system by [92] (see chapter 7.2 for details):

$$\chi \propto \sum_k [f_e(k) + f_h(k)]\, \Psi(k), \tag{5.2}$$

where $\Psi(k)$ is the exciton wavefunction in k-space. Further valuable information can be obtained by spectral changes besides simple intensity variations. Excitonic transition energies strongly depend on the dielectric environment due to screening effects. Hence, spectral shifts provide additional insight into doping-induced changes in electronic structure.

The spectroscopic investigation of doped SWNTs is initiated by steady-state absorption experiments in the VIS and NIR spectral region. Fig. 5.1a shows a selection of absorption spectra for redox titration of (6,5)-SWNTs in dispersion with $AuCl_3$. The spectrum of intrinsic nanotubes (black line) is dominated by the excitonic S_1 and S_2 resonances at 1.24 eV and 2.16 eV [23–25, 67] as well as a phonon sideband of the K-momentum dark exciton at 1.44 eV [76–78, 80, 241]. The following spectral changes are observed for increasing $AuCl_3$ concentration, *i.e.* enhanced p-doping: The S_1 exciton and the phonon sideband gradually lose absorption intensity and become completely bleached for the highest $AuCl_3$ concentration. A spectral blueshift accompanies the S_1 exciton bleach. At 1.06 eV a new signal rises up to a $AuCl_3$ concentration of 8 µg/mL and decreases in intensity for higher $AuCl_3$ concentrations. Fig. 5.1b shows the quantitative concentration dependence on a logarithmic $AuCl_3$ concentration axis. The new 1.06 eV signal is caused by X_1^+ trion absorption [27, 28].

The S_2 absorption intensity in the VIS at 2.16 eV also gradually decreases with higher $AuCl_3$

concentrations. However, the resonance seems not completely bleached as in the case of the S_1 exciton. In contrast to the S_1 blueshift, the position of the peak maximum in the VIS spectral region shifts to lower energies.

Fig. 5.1c shows the changes in the total oscillator strength f of first subband and second subband transitions. The relative oscillator strength f_{1st} of first subband transitions was calculated by integration from 0.95 eV to 1.85 eV, whereas the integration limits for the second subband transitions (f_{2nd}) were 1.95 eV and 2.50 eV. The spectral window between 1.85 eV and 1.95 eV was left out because of cross-polarized E_{12} absorption between first and second subbands [26, 242, 243]. Moreover, photon energies exceeding 2.50 eV were excluded because of increasing gold-chloride absorption overlapping with the SWNT absorption. Upon doping, f_{1st} is reduced due to phase space filling by as much as 50 %, whereas f_{2nd} is hardly affected. This can be explained by the absence of phase space filling in the second subbands. For the highest p-doping level, both S_1 exciton and X^+ trion absorption are completely bleached, and a nearly 1 eV broad and featureless absorption band remains. This band has previously been identified and called H-band [18] indicating the heavy ('H') doping regime. The regime of heavily doped SWNTs with a fully bleached band-edge exciton is further investigated in chapter 6.

Next, the spectral changes of the S_1 and S_2 exciton band are discussed in more detail.

5.2.1 First Subband Exciton

For higher p-doping levels, the S_1 absorption band increasingly overlaps with the contribution of the nonresonant H-band absorption (see inset of Fig. 5.1a). For a detailed analysis, the pure exciton absorption spectrum has to be extracted. A fit of the exciton band with a symmetric line profile like a Lorentzian, Gaussian or Voigt profile is not possible due to the increasing asymmetry of the exciton band.

Therefore, a simple linear background subtraction was performed. The linear background is defined by the absorbances at $E_1 = 1.19$ eV and $E_2 = 1.51$ eV. Fig. 5.2 shows the results of the background correction as normalized spectra. The subtraction procedure separates the exciton absorption band well from the nonresonant, constant H-band absorption but not from the phonon sideband. However, the relative spectral weight of the phonon sideband in the background corrected spectra is less than ≈ 5 %, and the introduced error seems acceptable. As already mentioned, the S_1 exciton band experiences four deformations upon doping: a bleach, a blueshift, a broadening and an increasing asymmetry.

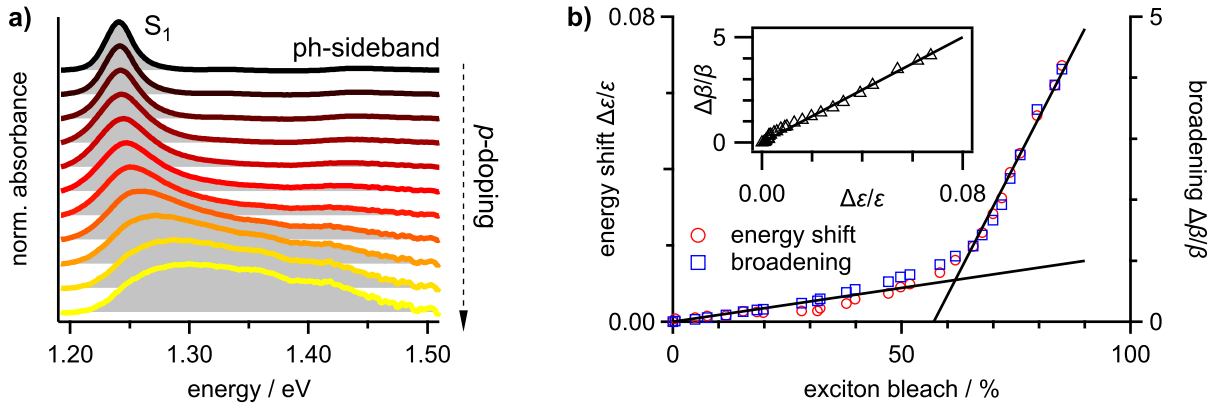

Figure 5.2: a) Background corrected and normalized SWNT absorption spectra in the spectral region 1.19 eV $\leq E \leq$ 1.51 eV for successive $AuCl_3$ mediated doping. b) Relative energy shift $\Delta\epsilon/\epsilon$ and broadening $\Delta\beta/\beta$ as a function of the exciton bleach χ. The inset shows a strong correlation of broadening and energy shift.

To quantify the exciton bleach and blueshift, an analysis after Langlois *et al.* [244] was performed:

$$f = \int_{E_1}^{E_2} A(E)\,\mathrm{d}E \tag{5.3}$$

$$\epsilon = f^{-1} \int_{E_1}^{E_2} E \times A(E)\,\mathrm{d}E, \tag{5.4}$$

where f is proportional to the oscillator strength and the average exciton energy ϵ is obtained by weighting each photon energy E with the absorbance $A(E)$. The broadening of the absorption band is described by the integral breadth β, which is given by the ratio of the absorption band integral to the peak height. For example, the integral breadth is related to the full width at half maximum (FWHM) of the symmetric Gaussian line profile by $\beta \approx 1.064 \times \mathrm{FWHM}$. The advantage of the integral breadth over the FWHM is that β is also well suited to describe asymmetric line profiles like the ones observed upon SWNT doping.

The following equations describe how relative changes were calculated:

$$\chi = \frac{f_0 - f}{f_0} \tag{5.5}$$

$$\frac{\Delta\epsilon}{\epsilon} = \frac{\epsilon - \epsilon_0}{\epsilon_0} \tag{5.6}$$

$$\frac{\Delta\beta}{\beta} = \frac{\beta - \beta_0}{\beta_0}, \tag{5.7}$$

where χ is the exciton bleach and the subscript '0' denotes the properties of the intrinsic nanotubes. Fig. 5.2b shows the relative energy shift $\Delta\epsilon/\epsilon$ and relative broadening $\Delta\beta/\beta$ as a function of the exciton bleach χ. For $\chi < 50\,\%$ both the relative energy shift and broadening are moderate and approximately linear in χ. For stronger p-doping with $\chi > 70\,\%$ both

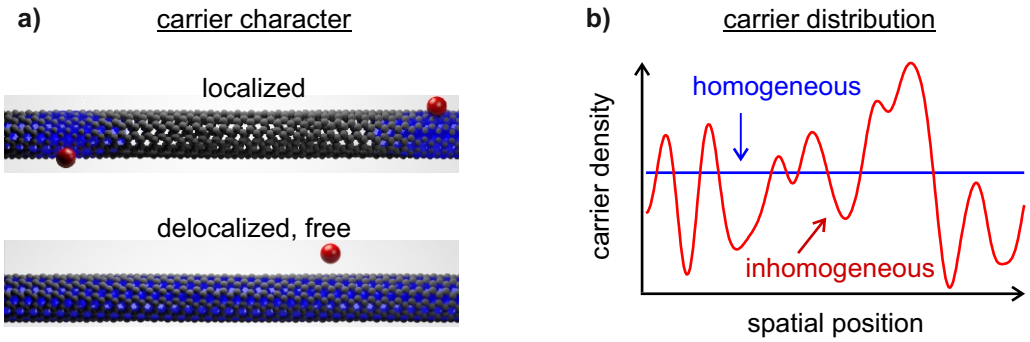

Figure 5.3: a) The two limiting cases of localized and delocalized carriers. The charge density is shaded in blue, whereas the red spheres are counterions which are always present in electrochemical and redox chemical doping schemes. b) Idealized case of a homogeneous carrier distribution and an inhomogeneous distribution caused by spatial potential energy fluctuations.

quantities are again approximately linear in the exciton bleach, however, with a much bigger slope. Interestingly, the exciton energy shift and the relative broadening show a strong correlation over the whole doping range. This suggests that the microscopic origin of both spectral changes is closely linked.

To better understand this microscopic origin is one of the key motivations of this thesis. Fig. 5.3 illustrates the two main questions, which are addressed in the following:

- Are charge carriers localized or delocalized?
- Are the carriers homogeneously or inhomogeneously distributed?

Chapter 2.1.2 and 2.3 introduced possible mechanisms for charge carrier and exciton localization. In both electro- and redox chemical doping schemes, the presence of counterions can not be prevented. Due to the strong sensitivity of SWNTs to external perturbations, the Coulomb interaction of SWNT excess charges with adsorbed counterions might provide a mechanism for charge localization.

Estimation of field-induced charge localization

If field-induced hole localization is relevant for p-doped (6,5)-SWNTs is estimated using the model illustrated in Fig. 5.4a. The electrostatic potential $V(z)$ between an adsorbed negative counterion and an SWNT excess hole is given by:

$$V(z) = -\frac{e^2}{4\pi\epsilon_0\epsilon_r\sqrt{d^2+z^2}}, \tag{5.8}$$

where ϵ_r is the relative dielectric constant, d is the counterion distance from the nanotube axis and z is the axial displacement. Solving the one-dimensional stationary Schrödinger equation

$$H\Psi = E\Psi \tag{5.9}$$

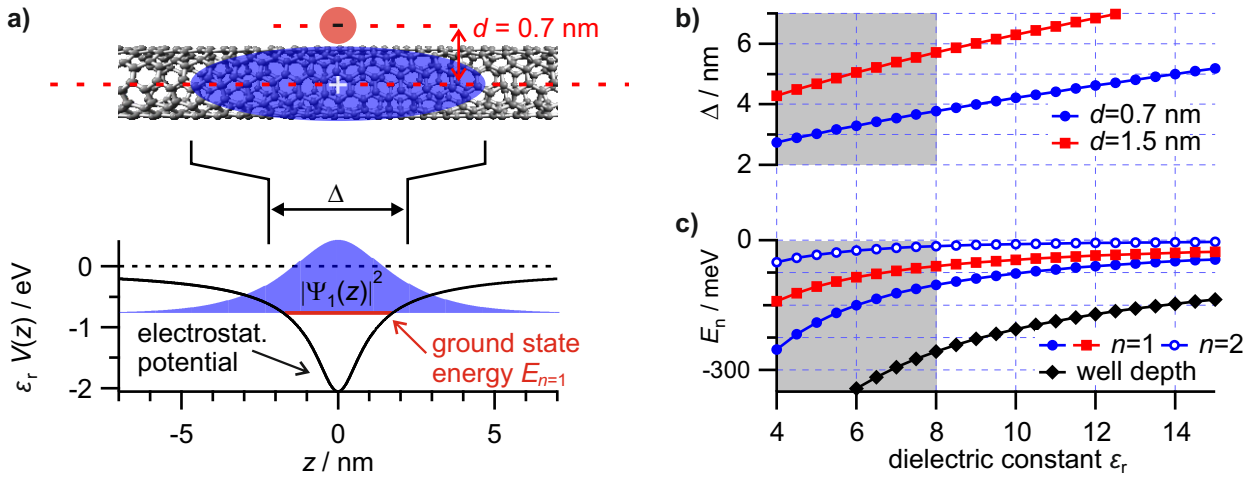

Figure 5.4: a) Coulomb interaction between an adsorbed negatively charged counterion and an SWNT hole at distance d. The electrostatic potential $V(z)$ describes the electrostatic interaction. By solving the 1D Schrödinger equation, the eigenenergy E_n and the charge distribution $|\Psi_n(z)|^2$, characterized by its FWHM Δ, were obtained . The displayed ground state charge distribution $|\Psi_1(z)|^2$ and the ground state energy E_1 was calculated for $d = 0.7\,\mathrm{nm}$ and $\epsilon_r = 8$. b) Localization length Δ and c) eigenenergy E_n as a function of the relative dielectric constant for two counterion distances $d = 0.7\,\mathrm{nm}$ and $d = 1.5\,\mathrm{nm}$. The grey region highlights the range of relevant dielectric constants.

with the Hamiltonian $H = -\hbar^2\nabla^2/(2\,m^*) + V(z)$ yields the eigenenergies E_n and the corresponding wavefunctions $\Psi_n(z)$. The effective hole mass is $m^* = 0.07\,m_e$ as reported by Hartleb *et al.* [18]. For the calculation two counterion distances $d = 0.7\,\mathrm{nm}$ and $d = 1.5\,\mathrm{nm}$ were used. The smaller distance is the approximate ion distance for bare SWNTs, whereas the larger distance corresponds to polymer-coated SWNTs [112]. The relative dielectric constant was estimated to range from $\epsilon_\mathrm{r} = 4$ used for bare SWNTs [51, 112, 241] to about $\epsilon_\mathrm{r} = 6$ for the solvent mixture toluene:acetonitrile in the volume ratio 10:1 (redox chemical doping) [245] or to about $\epsilon_\mathrm{r} = 8$ for tetrahydrofuran (electrochemical doping).

Fig. 5.4b and c show the results of the calculations. For directly adsorbed counterions, the $n = 1$ eigenstate binding energy $E_\mathrm{b} = -E_\mathrm{n}$ ranges from 253 meV to 103 meV for the relevant dielectric constant range $4 \leq \epsilon_\mathrm{r} \leq 8$. The charge localization length Δ is here defined as the FWHM of the charge carrier distribution $|\Psi_1(z)|^2$ and varies between 2.7 and 3.8 nm (average $\bar{\Delta} = 3.28\,\mathrm{nm}$) within the same dielectric constant range. The binding energy of the excited $n = 2$ state is $14\,\mathrm{meV} \leq E_{n=2} \leq 51\,\mathrm{meV}$ and is consequently too small to trap charges persistently at room temperature. Therefore, the excited states $n \geq 2$ are neglected in the following. The population of the $n = 1$ ground state can be estimated using Boltzmann statistics and a phase space factor on the order of 1/90. This factor corresponds to the charge localization length Δ compared to the length $l \approx 300\,\mathrm{nm}$ of an otherwise intrinsic tube. For the localized $n = 1$ ground state to be occupied $\geq 90\,\%$ of the time, the binding energy needs to exceed 170 meV, which is roughly given for dielectric constants of six and lower. The calculations show that charge carrier localization due to poorly screened Coulomb interaction

between excess charges and counterions adsorbed at the SWNT surface is likely.

Influence of carrier localization on excitons

Next, the expected influence of localized charges on exciton properties is discussed before experimental evidence is provided. Spatial localization of charge carriers distorts the crystal periodicity, which potentially influences both the energetics and dynamics of excitons in carbon nanotubes. This is explained in more detail using Fig. 5.5. Localized charges represent local perturbations of the band structure and create an impedance mismatch between intrinsic and charged SWNT regions [44, 112]. Therefore, they are expected to act as barriers for excitons and potentially as conduits for nonradiative exciton decay [108]. The barriers can be imagined as borders of the particle in a box, whereas the spacing between two neighboring charges determines the box width w.

Increasing doping levels are accompanied by a bleach, a spectral blueshift, broadening and increasing asymmetry of the exciton absorption band. A good model, therefore, needs to account for all of these four characteristic changes. For the blueshift, this is done by allowing the exciton energy to increase due to axial confinement, as previously discussed for ultrashort length-sorted SWNTs [246]. The ground state energy of a particle in a 1D box of width w is given by:

$$E_{\mathrm{GS}}(w) = \pi^2 \hbar^2 (2Mw^2)^{-1}, \tag{5.10}$$

where the exciton translational mass $M = m_e^* + m_h^*$ is the sum of electron and hole effective masses $m_{e/h}^*$ in the effective mass approximation [247]. The broadening and asymmetry can be accounted for by a random distribution of localized charges causing an exponential distribution (Poisson form) $p_{\overline{w}}(w)$ of barrier spacings w [248]:

$$p_{\overline{w}}(w) = \overline{w}^{-1}\, \mathrm{e}^{-w/\overline{w}}, \tag{5.11}$$

where $\overline{w}$ is the average distance between charge carriers. The line shapes of the intrinsic nanotube segments are assumed to follow a Gaussian profile with the shape function $f_w(E)$. Depending on the barrier spacing w, the band center needs to be shifted by the appropriate zero-point energy $E_{\mathrm{GS}}(w)$. With this in mind, the exciton line profile in doped samples can be calculated by weighting the individual absorption bands:

$$I_{\overline{w}}(E) = \overline{w}^{-1} \int_0^\infty p_{\overline{w}}(w')\, w'\, f_{w'}(E)\, \mathrm{d}w'. \tag{5.12}$$

The factors w and $\overline{w}^{-1}$ were introduced to weight the spectral contribution of a single SWNT segment by its length and to normalize the weighting function in order to conserve the total oscillator strength. Within this model, the parameter $\overline{w}$ mainly determines the shape of the absorption band.

Exciton bleaching is included when the barriers are assigned to a certain width Δ, which

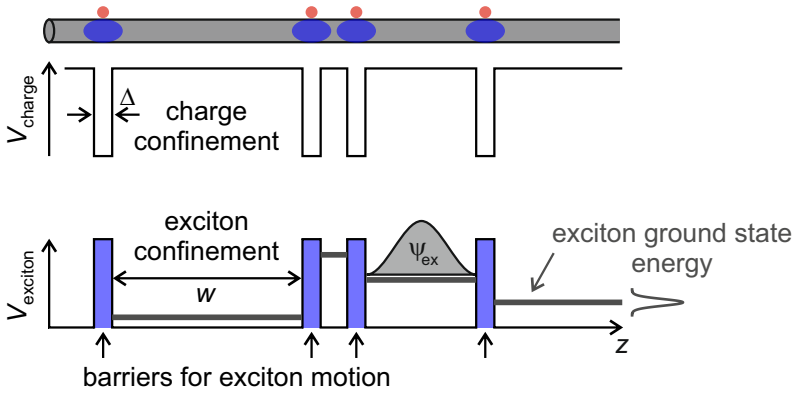

Figure 5.5: Schematic illustration of the spatially varying potential energy $V(z)$ experienced by SWNT charges and excitons. The counterion-induced localization of charges confines the exciton wavefunction Ψ_{ex} to intrinsic regions between neighboring charges due to an impedance mismatch between intrinsic and charged SWNT regions. The axial confinement of excitons leads to an increase in exciton ground state energies analogous to the particle in a 1D box.

effectively reduces the total length of intrinsic segments, where exciton absorption occurs. For this purpose, the distribution function $p_{\overline{w}}(w)$ can be replaced by $p_{\overline{w},\Delta}(w) = \overline{w}^{-1}\,\mathrm{e}^{-(w+\Delta)/\overline{w}}$ with the additional adjustable parameter Δ. In a previous study, such an analysis has already been performed for electrochemically doped SWNTs and gave a value $\Delta \approx 4\,\mathrm{nm}$ in good agreement with the calculations, if Δ is associated with the FWHM of the spatial charge carrier distribution $|\Psi(z)|^2$ [112].

Fig. 5.6a shows fits of the confinement model to the normalized S_1 absorption band using an exciton translational mass $M = m_e^* + m_h^* \approx 2\,m_c^* = 0.14\,m_e$ [18]. The fits reproduce the trend of increasing blueshift and asymmetry solely by the average impurity spacing $\overline{w}$ as fit parameter. However, it has to be mentioned that the overall width of the Gaussian shape function was allowed to increase up to 60 meV, a value found for the inhomogeneous broadening in intrinsic individualized surfactant-coated nanotubes in a gelatine matrix [164]. The introduction of an additional fit parameter was necessary because for doping levels up to a 30 % exciton bleach, the exciton band center hardly shifts but already a significant broadening of the absorption band occurs for SWNTs in dispersion. Microscopically, this can be explained by doping-induced but non-confinement related inhomogeneous broadening. This effect is more pronounced for nanotubes in organic solution with a comparably small intrinsic inhomogeneous linewidth $\Gamma = 28\,\mathrm{meV}$ (inferred from the overall linewidth [164]) than for nanotube thin-films used for electrochemical doping with $\Gamma = 50\,\mathrm{meV}$. Fig. 5.6b shows the extracted average impurity spacings $\overline{w}$ and the corresponding impurity concentrations $n = \overline{w}^{-1}$. According to this analysis, a maximum impurity density $n = 0.48\,\mathrm{nm}^{-1}$ is obtained. A more detailed discussion about the quantification of charge carrier densities using the exciton confinement model is provided in chapter 7.1.

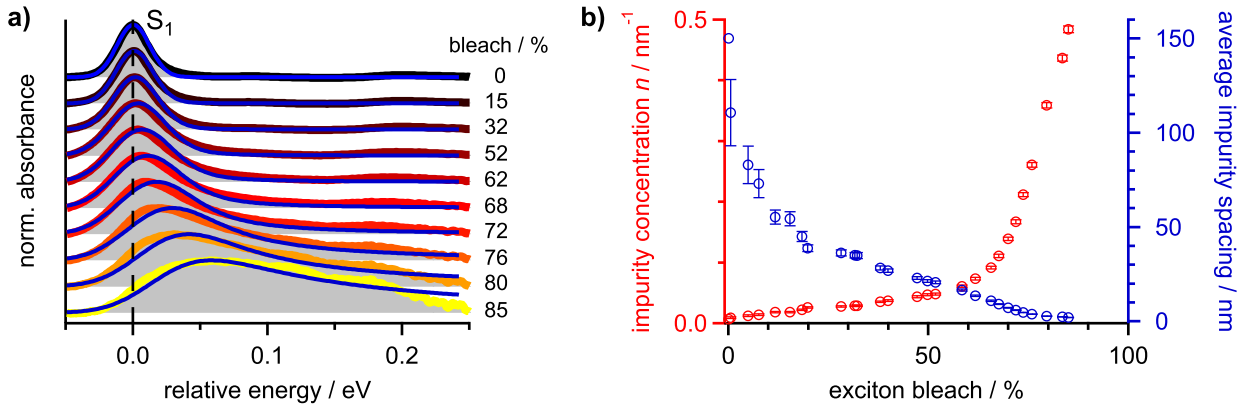

Figure 5.6: a) Fits (blue lines) of the confinement model to the normalized S_1 absorption bands for different doping levels. The average impurity spacing $\overline{w}$ as fit parameter controls the blueshift, asymmetry and large parts of the broadening. b) Average impurity spacing $\overline{w}$ (blue markers) and impurity concentration $n = \overline{w}^{-1}$(red markers) as a function of the S_1 exciton bleach. The error bars indicate the standard deviation obtained from the fit. For the intrinsic SWNTs, $n = 2/(300\,\text{nm})$ was assumed, which corresponds to one impurity per tube end and an average SWNT length of 300 nm.

5.2.2 Second Subband Exciton

Fig. 5.7a shows the spectral region around the absorption band of the second subband S_2 exciton. To facilitate comparison, the absorbance is normalized to the S_1 peak absorbance of the intrinsic SWNTs. The spectrum of the intrinsic nanotubes (black curve) features three prominent resonances in the spectral window from 1.8 eV to 2.6 eV:

- the E_{12} exciton at 1.91 eV with the transition moment perpendicular to the nanotube axis
- the S_2 exciton at 2.16 eV
- a phonon sideband at 2.37 eV.

Upon hole doping, all three absorption bands lose intensity. The E_{12} band and the phonon sideband appear to be fully bleached at the highest doping degree. In contrast, doping-induced modifications of the S_2 absorption band are more complicated. The S_2 resonance of intrinsic SWNTs is well described by a single symmetric Lorentzian with an FWHM of ≈ 75 meV. In the absence of other dephasing mechanisms, the linewidth corresponds to an excited state population lifetime of ≈ 9 fs. This lifetime is consistent with fast internal conversion of S_2 excitons to the S_1 exciton band in less than 40 fs [94, 95, 97].

Hole doping leads to a decrease of the peak intensity and seemingly to a redshift of the S_2 resonance (see Fig. 5.7b) at simultaneously increasing asymmetry. However, careful inspection of the spectrum highlighted in blue color shows that a shoulder evolves slightly blueshifted to the S_2 resonance in intrinsic nanotubes. For comparison, the blue spectrum corresponds to a doping level of nearly maximized trion absorbance, as shown in the inset of Fig. 5.7b. The appearance of a shoulder in the VIS indicates the superposition of two absorption bands. One

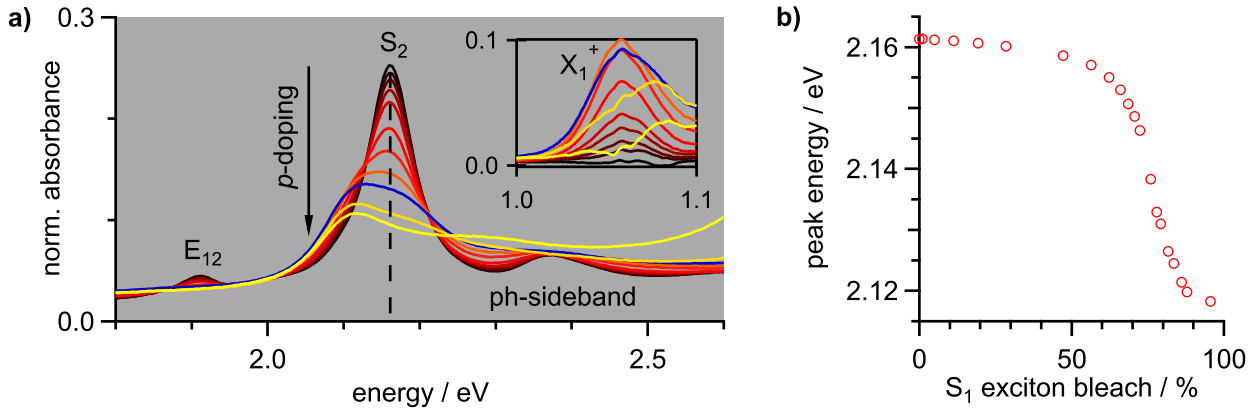

Figure 5.7: a) Series of absorption spectra in the VIS spectral region normalized to the peak S_1 absorbance in the intrinsic SWNT sample (black line). The inset shows the NIR region around the X_1^+ trion absorption band. b) Peak energy in the VIS as a function of the S_1 exciton bleach.

absorption band seemingly shifts to higher energies and the other to lower energies relative to the S_2 resonance energy in intrinsic SWNTs.

Within the picture of charge localization and the distribution of doped and intrinsic segments along an individual nanotube, the higher energy resonance could be associated with the S_2 resonance in intrinsic segments. The lower energy resonance, here called X_2^+, is attributed to interband absorption between the second valence and conduction subbands in doped segments.

Pump energy dependent photobleaching

Next, this assignment is confirmed by time-resolved spectroscopy. If the neutral S_1/S_2 excitons and the charged X_1^+/X_2^+ states are localized on different segments of the same carbon nanotube as hypothesized, the neutral and charged exciton states are expected to be decoupled. This hypothesis is validated with pump energy dependent transient absorption (TA) spectroscopy using NIR pump pulses and broadband VIS probe pulses. The idea is to excite the charged X_1^+ trion or neutral S_1 exciton selectively and look for the instantaneous photobleach (PB) signal of the two overlapping spectral features in the VIS. In order to achieve a high temporal resolution in such a two-color pump-probe experiment, the sample thickness should be very thin. Unfortunately, resonant S_1 excitation leads to notoriously weak TA signals associated with higher-energy states $S_{n>1}$. For example, the PB signal at the S_2 resonance in intrinsic nanotubes was found to be more than an order of magnitude less than at the S_1 resonance [244]. Both minimum sample thickness and weak S_2 PB signals make highly concentrated doped samples in solution necessary. However, for high nanotube concentrations, the dispersions in toluene/acetonitrile 10:1 volume ratio are not stable and nanotubes tend to aggregate. Therefore, SWNTs were individualized in a PFO-BPy polymer matrix with a 1000-fold polymer mass excess as described by Späth [188]. Doping of the SWNT/PFO-BPy matrix film was achieved by immersion into a 50 µg/mL $AuCl_3$ solution (see section 3.1.3 for details).

Fig. 5.8a shows the absorption spectra of the intrinsic and doped films. Doping reduced the peak S_1 absorbance by about 70 % and the doping level stayed constant for at least one month (see inset of Fig. 5.8a). The further characterization of the doped film using PLE spectroscopy is shown in Fig. 5.8b. The majority of emitted photons originates from trion recombination, but S_1 exciton emission still occurs. Fig. 5.8c illustrates the pump-probe schemes of two different pump energy dependent TA experiments. In the first experiment, the 1.06 eV excitation pulses were resonant with the X_1^+ transition, whereas the pulses were resonant with the S_1 transition at 1.24 eV in the second experiment. Broadband VIS probe pulses covered the spectral region of the two overlapping signals found in steady-state absorption. These signals were tentatively assigned to the S_2 exciton absorption in intrinsic and the X_2^+ absorption in charged nanotube segments. Fig. 5.8d presents the results of the two TA experiments. Excitation of the first subband trion X_1^+ causes a PB signal at early pump-probe delay times centered at 2.10 eV and a weaker bleach at 2.17 eV. Conversely, S_1 excitation leads to the main PB at 2.17 eV and a weaker bleach at 2.10 eV. The selective photobleaching upon excitation with different photon energies confirms that the lower energy feature in the VIS spectral region is associated with an optical transition localized on charged segments. The 2.17 eV bleach signal, on the other hand, belongs to the neutral S_2 transition in uncharged SWNT segments.

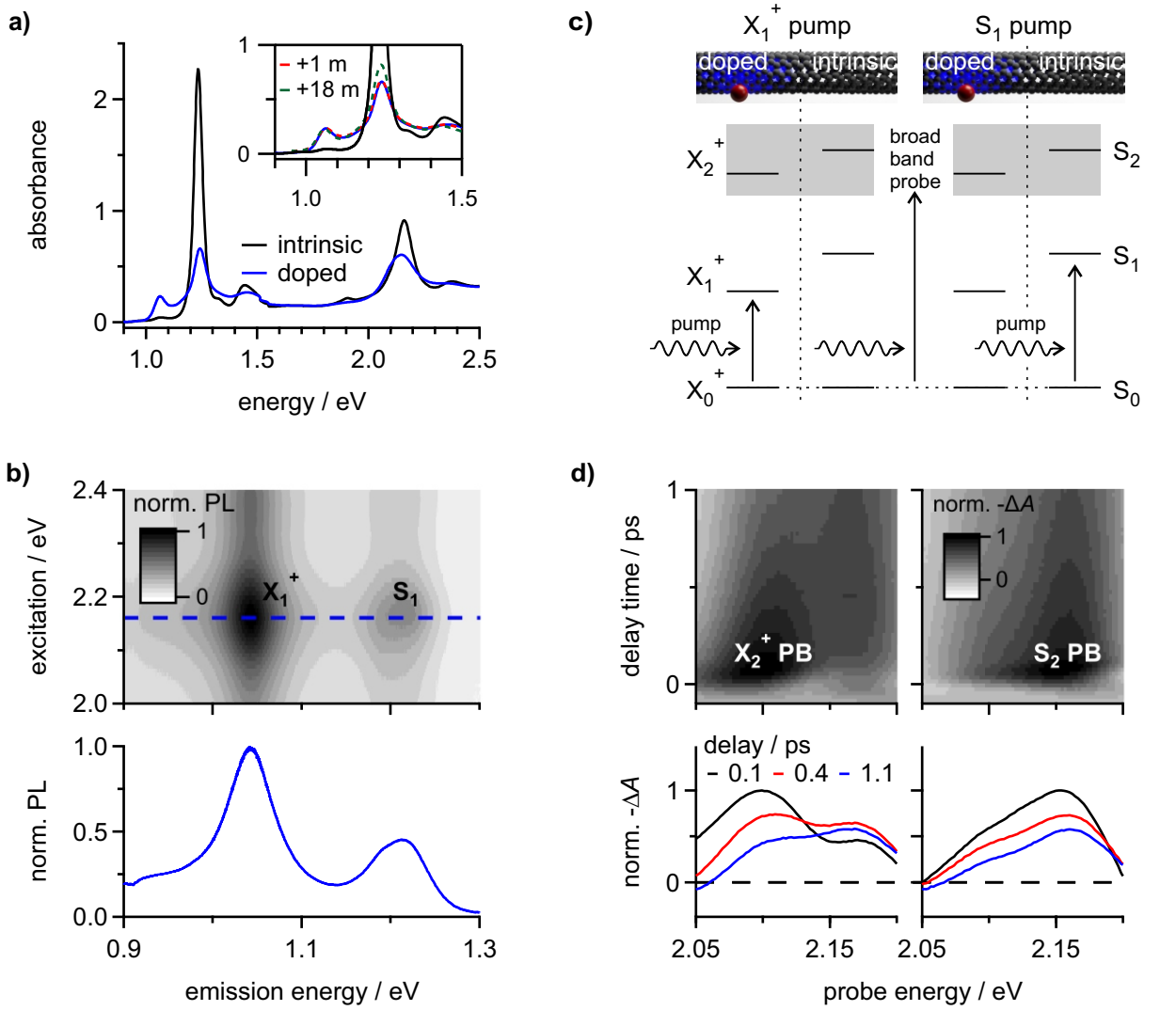

Figure 5.8: a) Absorption spectra of (6,5)-SWNTs embedded in a PFO-BPy polymer matrix before and after $AuCl_3$ mediated *p*-doping. The inset shows the long-term doping stability. After one month the absorption spectra were still identical, whereas a weak dedoping occurred within 18 months. b) PLE map of the doped SWNTs and PL spectrum at 2.16 eV excitation energy. c) Pump-probe scheme for pump energy dependent TA. The NIR excitation pulses were centered at 1.06 eV for resonant X_1^+ excitation and at 1.24 eV for resonant S_1 excitation. d) Resulting TA maps upon X_1^+ trion (left) and S_1 exciton excitation (right) and TA spectra at 0.1 ps (maximum signal intensity), 0.4 ps and 1.1 ps.

Quantification of the S_2 energy shift

After the confirmation of the spectral assignment regarding the two overlapping signal contributions in the VIS spectral region, a quantification of the doping-induced S_2 energy shift is desirable. Spectral deconvolution of the overlapping absorption bands with a double peak fit was not possible, most likely due to the asymmetric nature of the absorption bands. For an approximate quantification of the S_2 exciton blueshift, the second derivatives of the spectra were calculated and searched for minima [20, 249–251].

Fig. 5.9a shows the normalized absorbance A around the S_2 resonance for a set of spectra, whereas Fig. 5.9b depicts the second derivatives $\mathrm{d}^2A/\mathrm{d}E^2$. The second derivatives clearly show the appearance of a double minimum structure corresponding to an additional peak in the absorption spectrum. The position of the higher-energy minimum was taken as the approximate spectral position of the S_2 peak. Fig. 5.9c shows the resulting S_2 energies along with the doping level dependence of the S_1 energy, which was directly obtained from the absorption spectra. Both exciton energies have a similar doping level dependence, which strengthens the assumption that localized charges act as barriers to the S_1 and S_2 excitons wavefunctions and therefore increase the exciton ground state energies.

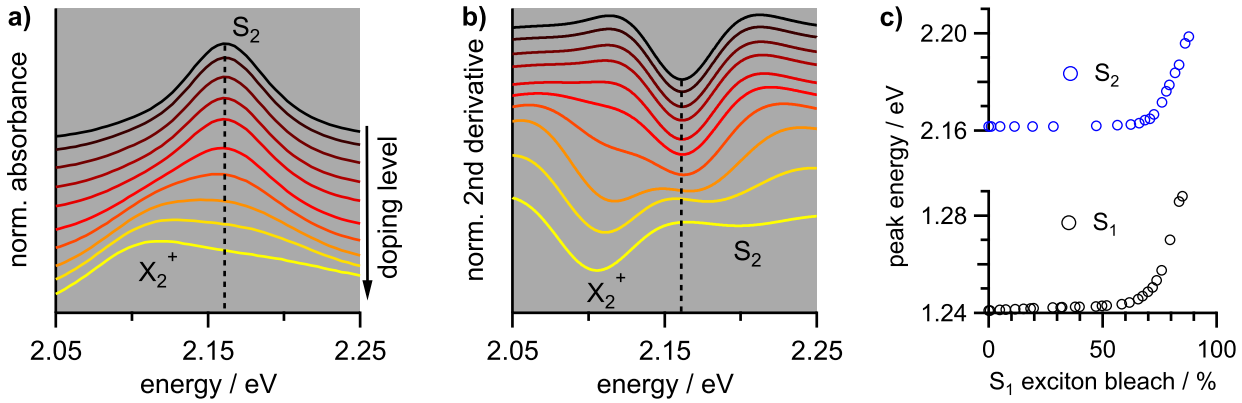

Figure 5.9: a) Normalized absorption spectra $A(E)$ and b) the second derivative spectra $\mathrm{d}^2A(E)/\mathrm{d}E^2$ in the VIS spectral region for successive p-doping (from top to bottom). c) Doping-induced blueshift of the S_2 resonance extracted from the second derivative spectra and blueshift of the S_1 resonance. A qualitative agreement between both excitons is obtained, whereas slight discrepancies possibly arise due to the usage of two different data sets.

5.2.3 Discussion of Doping-Induced Absorbance Changes

The doping-induced spectral changes of (6,5)-SWNTs were presented, and the first evidence of charge carrier localization was found in the absorption spectra. In the following, the results are compared to other experimental and theoretical studies on doped SWNTs. Later, a comparison with quasi-2D systems puts the spectral changes into a wider context.

Comparison with previous studies on doped SWNTs

The experimentally observed bleaching of the S_1 absorption band and the simultaneous blueshift is in good agreement with many experimental studies [18, 19, 200, 223]. In addition to the S_1 exciton blueshift, a similar blueshift of the S_2 exciton was observed, which has not been reported in the literature so far.

As mentioned in section 5.1, some studies discussed the possible localization of charge carriers in doped SWNTs. However, most studies regard the doping of SWNTs in terms of band filling and fully delocalized carriers. Using many-body *ab initio* calculations, Spataru and Léonard calculated the electronic and optical properties of an electrostatically doped (10,0)-SWNT, which has a similar diameter d as the (6,5)-SWNT ($d_{(10,0)}/d_{(6,5)} = 1.05$) [231, 232]. Upon band filling, doping with a charge carrier density $n = 0.6\,\mathrm{nm}^{-1}$ reduces the fundamental band gap by 0.8 eV to almost 50 % of its intrinsic value. This band gap renormalization (BGR) is caused by dynamical screening effects and is a manifestation of delocalized carriers. At the same time, the S_1 oscillator strength is reduced to about 1/6 of its intrinsic value.

Steady-state absorption spectroscopy can hardly measure the BGR in SWNTs because of a nearly complete transfer of oscillator strength from free electron-hole pairs to excitons. Kimoto *et al.* used two-photon PLE spectroscopy on redox-chemically doped (7,5)-SWNTs to determine the effect of BGR [223]. They observed a BGR of $\approx 5\,\mathrm{meV}$ for a somewhat lower but comparable amount of S_1 bleaching. This BGR corresponds to only 0.3 % of the intrinsic band gap, in stark contrast to the theoretical studies by Spataru and Léonard. The discrepancy might indicate the charge carrier's tendency to localize upon redox chemical doping due to the presence of counterions.

Interestingly, Spataru and Léonard also observed, that both the S_1 and S_2 excitons bleach and their energies simultaneously increase on the order of 0.1 eV in agreement with the experiments presented in this thesis. Unfortunately, the calculations so not provide the shape of the exciton absorption bands. Therefore, it is not clear if band filling also leads to a simultaneous broadening and asymmetry of the S_1 absorption band.

In this work, the doping-induced broadening and asymmetry of the S_1 absorption band was interpreted as the result of an increasing inhomogeneous broadening caused by the inhomogeneous carrier distribution and the confinement of excitons between neighboring localized charges. For homogeneous doping with delocalized carriers (band filling), the broadening of the exciton absorption band is more likely interpreted in terms of homogeneous linewidth broadening due to an increased exciton-charge carrier scattering rate. However, Konabe *et al.* calculated that such scattering is largely suppressed and leads at maximum to an additional homogeneous broadening of $\approx 5\,\mathrm{meV}$ for carrier densities below $0.3\,\mathrm{nm}^{-1}$ [252]. These theoretical predictions make a faster exciton dephasing as the main doping-induced S_1 absorption band broadening mechanism unlikely. On top of that, pure homogeneous broadening can not account for the observed increasing absorption band asymmetry.

Comparison with doped 2D materials

Besides carbon nanotubes, doping of semiconductor nanostructures recently focused mainly on quasi-2D sheet materials, which are also dominated by many-body excitations like excitons and trions. Tab. 5.1 shows a collection of the exciton and trion binding energies of (6,5)-SWNTs and diverse other low-dimensional materials. Here, the binding energies and the absolute exciton and trion energies correspond to the limit of small carrier densities.

In intrinsic (6,5)-SWNTs in dispersion, the exciton binding energy $E_{\mathrm{b,ex}}$ is on the order of 300-400 meV [18, 23, 24]. Hence, the binding energy is comparable to the ones reported for intrinsic transition metal dichalcogenide (TMD) monolayers on non-metallic substrates. The similarity of exciton binding energies indicates a similar strength of the Coulomb interaction. Both material classes have about an order of magnitude larger exciton binding energies than observed in ≈ 10 nm thick CdTe or GaAs quantum wells, which can be explained by enhanced dielectric screening in the latter materials.

The energetic separation $E_{\mathrm{ex}} - E_{\mathrm{tr}} = 183$ meV between exciton and trion absorption in (6,5)-SWNTs is exceptionally large. On an absolute energy scale, the energy separation is much larger than in all other quasi-2D materials. For a better comparison, a relative energy scale $(E_{\mathrm{ex}} - E_{\mathrm{tr}})/E_{\mathrm{b,ex}}$ is introduced. The relative energy scale takes into account the differences in Coulomb interaction and dielectric screening between the materials due to normalization by the respective exciton binding energy $E_{\mathrm{b,ex}}$ in the intrinsic material. Also on the relative energy scale, the exciton-trion energy separation $(E_{\mathrm{ex}} - E_{\mathrm{tr}})/E_{\mathrm{b,ex}} \approx 50\,\%$ is strongly enhanced for 1D (6,5)-SWNTs.

Next, (6,5)-SWNTs are compared to a modulation-doped 10 nm thick cadmium telluride (CdTe) quantum well [22] and a gate-doped monolayer of tungsten disulfide (WS_2) [20] in terms of the doping-induced changes in the linear susceptibility. Fig. 5.10 shows a series of spectra for each material. The doping level (charge density) increases from the top (black line) to the bottom (yellow line). Note that for (6,5)-SWNTs and the CdTe quantum well absorption spectra are presented, whereas for the WS_2 monolayer the reflectance contrast is shown. Again, the relative energy axis is used to simplify comparison.

Table 5.1: Comparison of exciton binding energies $E_{\mathrm{b,ex}}$ and energetic exciton-trion separation $E_{\mathrm{ex}} - E_{\mathrm{tr}}$ in different low-dimensional materials.

material	dim.	$E_{\mathrm{b,ex}}$ / meV	$[E_{\mathrm{ex}} - E_{\mathrm{tr}}]$ / meV	$\frac{E_{\mathrm{ex}} - E_{\mathrm{tr}}}{E_{\mathrm{b,ex}}}$ / %
(6,5)-SWNTs	1D	310[18], 370[24], 420[23]	183 [this work]	44-59
WS_2 monolayer	2D	320[253], 240[254]	23[20]	7-10
MoS_2 monolayer	2D	421[255]	20[21]	5
WSe_2 monolayer	2D	240[254], 370[256]	21-35[257]	6-15
10 nm CdTe quantum well	2D	18[22]	2[22]	11
9.1 nm GaAs quantum well	2D	12[258]	2[258]	17

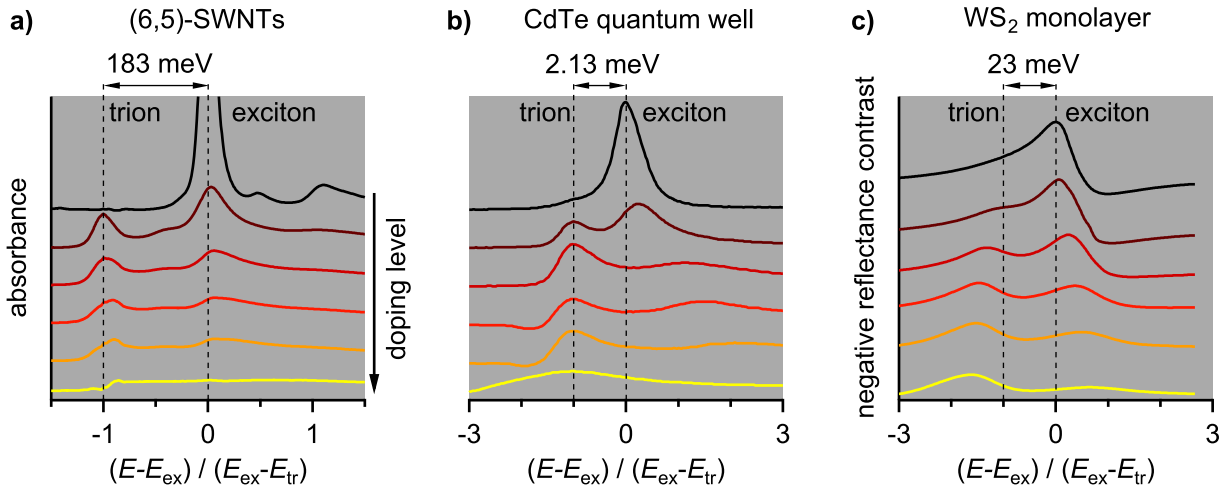

Figure 5.10: a) Absorption spectra of a (6,5)-SWNT dispersion for $AuCl_3$-mediated p-doping at room temperature. The exciton and trion energies marked by a dashed line correspond to the low-doping limit. b) Absorption spectra of a modulation n-doped 10 nm thick CdTe quantum well at temperature $T = 2\,\mathrm{K}$. c) Negative reflectance contrast of a n-type gate-doped WS_2 monolayer at $T = 50\,\mathrm{K}$. The spectra of the CdTe quantum well and the WS_2 monolayer are taken from references [22] and [20].

The energetic origin corresponds to the exciton energy in the intrinsic materials, whereas the relative energy is expressed in terms of the energetic exciton-trion separation in the limit of small charge densities. For all three materials, the exciton band decreases in intensity and blueshifts upon doping. An increase in trion oscillator strength accompanies the reduction in exciton oscillator strength. For the highest depicted doping levels (yellow lines), the trion band in (6,5)-SWNTs and in the CdTe quantum well merges into a broad and featureless absorption band.

Besides these similarities, there are also differences between the three materials. The trion band in (6,5)-SWNTs blueshifts at the highest doping levels, whereas no such shift can be resolved for the CdTe quantum well. For the WS_2 monolayer a redshift is observed.

The similarity between the doping-induced changes in the exciton absorption band of (6,5)-SWNTs and quasi-2D materials calls the carrier localization-based 1D confinement model developed in section 5.2.1 into question. Therefore, additional spectroscopic evidence for charge localization is necessary and will be presented in the following.

5.3 Dynamical Properties of Excitons and Trions

5.3.1 PL Spectroscopy

Not only the absorption properties of (6,5)-SWNTs are influenced by additional charges, but also the nanotube fluorescence. Fig. 5.11a shows a series of normalized PL spectra of (6,5)-

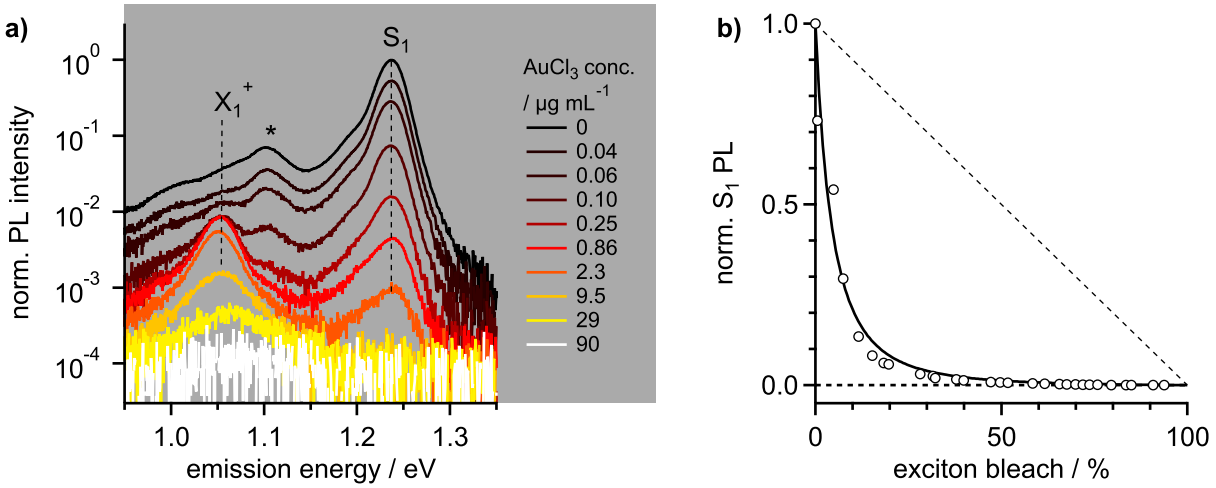

Figure 5.11: a) NIR emission of (6,5)-SWNTs for increasing $AuCl_3$ concentrations. b) The spectrally integrated S_1 emission as a function of the exciton bleach χ is highly nonlinear. The dashed line highlights the one to one correspondence between the exciton PL and exciton bleach.

SWNTs in dispersion for increasing $AuCl_3$ concentration. The excitation energy of 2.155 eV was resonant with the S_2 transition in intrinsic SWNTs. The PL intensity shows a large dynamic range of four orders of magnitude. The spectra were corrected for doping-dependent absorption at the excitation energy of 2.155 eV. Furthermore, they were corrected for different acquisition times and excitation powers, which were necessary to cover the large dynamic range with an acceptable signal-to-noise ratio.

The S_1 exciton emission at 1.237 eV dominates the PL in intrinsic SWNTs and was set to unity. Another emission band at 1.102 eV (denoted with an asterisk) with a peak intensity of 7 % belongs to a phonon sideband [76, 78]. Weak residual emission at energies below 1.05 eV possibly originates from emission at defect sites deep in the band gap [169, 259–261]. Upon hole-doping, the S_1 PL intensity sharply decreases and a new emission band at 1.055 eV gains intensity due to radiative X_1^+ trion recombination. For $AuCl_3$ concentrations exceeding 0.4 µg/mL, the trion emission intensity decreases again, and for the highest $AuCl_3$ concentration (90 µg/mL, white spectrum) the NIR emission is fully quenched to the noise level.

S_1 PL energetics

Before the doping level dependence of S_1 and X_1^+ PL intensity is discussed in more detail, the S_1 PL signal is investigated for doping-induced changes in energetics. Fig. 5.12a shows a comparison of normalized PL and absorption spectra in intrinsic and doped SWNTs. In intrinsic SWNTs (exciton bleach $\chi = 0\,\%$), the S_1 PL almost perfectly mirrors the S_1 absorbance with a small Stokes shift of 3.8 meV, in good agreement with published results [17]. The same graph shows the normalized absorption and emission spectra of samples doped with 2.3 µg/mL and 4.5 µg/mL $AuCl_3$. The exciton bleach χ has increased to 70 % and 76 %, whereas the peak PL dropped to 0.1 % and 0.03 % of its intrinsic value. For even higher dop-

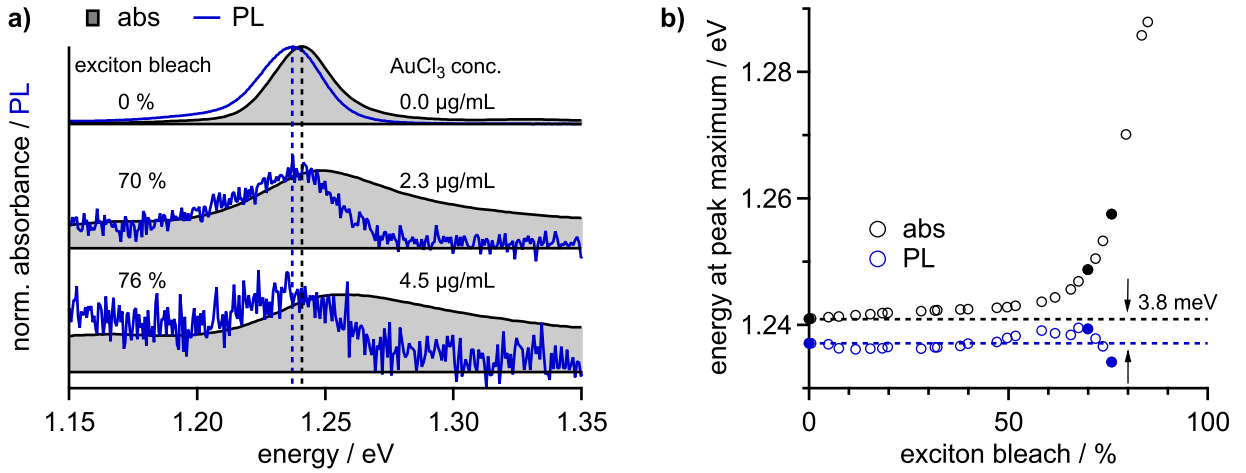

Figure 5.12: a) Normalized S_1 exciton absorption and emission in intrinsic and doped SWNTs. b) Energetic position of the S_1 peak absorbance or peak PL as a function of the exciton bleach. The full circle symbols correspond to the spectra shown in a).

ing levels, the S_1 PL could not be distinguished from the noise anymore, albeit trion emission is still detectable. The energy at the absorbance peak maximum has blueshifted in the two doped sample by $\approx 8\,\text{meV}$ and $\approx 17\,\text{meV}$ compared to the intrinsic sample. In contrast, the energetic variation of the peak PL is only $\approx 2\,\text{meV}$. This can be seen more clearly in Fig. 5.12b, where the energy at both peak maxima is shown as a function of the bleach. Peak energies were determined by Gaussian fits over the spectral region around the peak maximum. The S_1 energy obtained from absorption monotonically rises with more pronounced shifts for doping levels $\chi \gtrsim 65\,\%$, whereas the PL peak energy stays rather constant. Interestingly, S_1 PL in doped samples does not at all mirror the S_1 absorption band, but seems to originate mainly from the low-energy part of the absorption band. This implies that the shape of the absorption spectrum of doped SWNTs is – like in intrinsic SWNTs [164] – mainly caused by inhomogeneous broadening effects as already discussed in section 5.2.1. In turn, doping is very likely inhomogeneous as well. The constancy of the PL peak energy and the absence of PL from high-energy regions of the S_1 absorption band can be taken as further evidence for the charge localization and the resulting hard segmentation of nanotubes.

Within this model and assuming diffusion-limited exciton quenching [98] at localized charges, the PL intensity in an individual segment of length w is proportional to $1/w^2$. Therefore, S_1 PL should originate primarily from the larger intrinsic segments in which exciton absorption and emission hardly blueshifts due to negligible confinement energies. Since the confinement related exciton blueshift for a particle in a box is itself proportional to $1/w^2$, it can be estimated how severe this effect is.

For an illustration, the PL of an intrinsic segment of length $w_0 = 150\,\text{nm}$, corresponding to one quenching defect in the middle of a 300 nm long SWNT, and the PL of five intrinsic segments of length $w = w_0/5 = 30\,\text{nm}$ is compared. In the latter case, the PL drops by a factor of $5^2 = 25$ relative to the PL in the 150 nm segment. The exciton ground state energy is only

raised by 3 meV due to axial exciton confinement (see equation (5.10)) assuming an effective exciton mass of $M = 0.14\,m_e$ [18] as done in section 5.2.1. This simple example demonstrates that PL from smaller segments is effectively suppressed within the model, which can explain the measured PL spectra upon doping.

PL intensity changes

In the following, the doping-induced PL intensity changes are regarded in more detail. The total S_1 PL for the i-th spectrum $\mathrm{PL}_{i,\mathrm{S}_1}$ was determined by summation over the pixels within the energy range 1.18 eV and 1.35 eV. Fig. 5.11b shows the S_1 PL as a function of the S_1 exciton bleach. The dependence is highly nonlinear, highlighting the strong sensitivity of the exciton PL intensity to additional charges.

In order to disentangle the trion PL from the overlapping phonon sideband and defect PL, a subtraction procedure was performed. From each spectrum $I_i(E)$ the spectrum of the intrinsic sample $I_0(E)$ weighted with the relative S_1 PL was subtracted:

$$I_{i,\mathrm{corr}}(E) = I_i(E) - \frac{\mathrm{PL}_{i,\mathrm{S}_1}}{\mathrm{PL}_{0,\mathrm{S}_1}} I_0(E). \tag{5.13}$$

Fig. 5.13a displays the subtraction-corrected spectra in the energy range in which trion emission occurs ($0.95\,\mathrm{eV} \leq E \leq 1.15\,\mathrm{eV}$). Again, like in steady-state absorption, the rise and decline of the trion signal are observable. The deconvolution of trion PL from overlapping phonon sideband and defect emission bands allows evaluating the different PL contributions as a function of doping level. Fig. 5.13b presents the resulting doping level dependences. The total PL was obtained by summation over all pixels in the range energy [0.95-1.35 eV], whereas S_1 PL belongs to the range [1.18-1.35 eV]. The residual PL contains contributions from the phonon sideband, the trion and defect emission and is the difference of total and S_1 PL. The pure trion PL was calculated by summation over the pixels in the subtraction-corrected spectra (see Fig. 5.13a) in the range [0.95-1.15 eV]. For an S_1 exciton bleach up to $\chi \approx 20\,\%$, the S_1 PL dominates the whole NIR emission and trion emission continuous to increase. For higher doping levels up to $\chi \approx 60\,\%$, the trion emission is nearly constant with a relative PL quantum yield (PLQY) of 1.3 % of the total PL or 1.7 % of the S_1 PL in the intrinsic sample. A hardly changing trion PL intensity over a broad charge density range has also been observed for quasi-2D TMD monolayers [21, 262]. When the exciton bleach exceeds 60 %, the decreasing trion PL dominates the whole spectrum. Next, the relative S_1 PLQY is analyzed with two different models to obtain a deeper understanding of the microscopic mechanism of doping-induced S_1 emission quenching. Such mechanistic models rely on a precise knowledge of the charge density, which however is not accurately known. Here, simple phase space filling (PSF) arguments are used to approximate the charge carrier density n by the exciton bleach χ. PSF predicts the fairly simple linear relationship $\chi = n/n_\mathrm{s}$, where n_s is the saturation density [93].

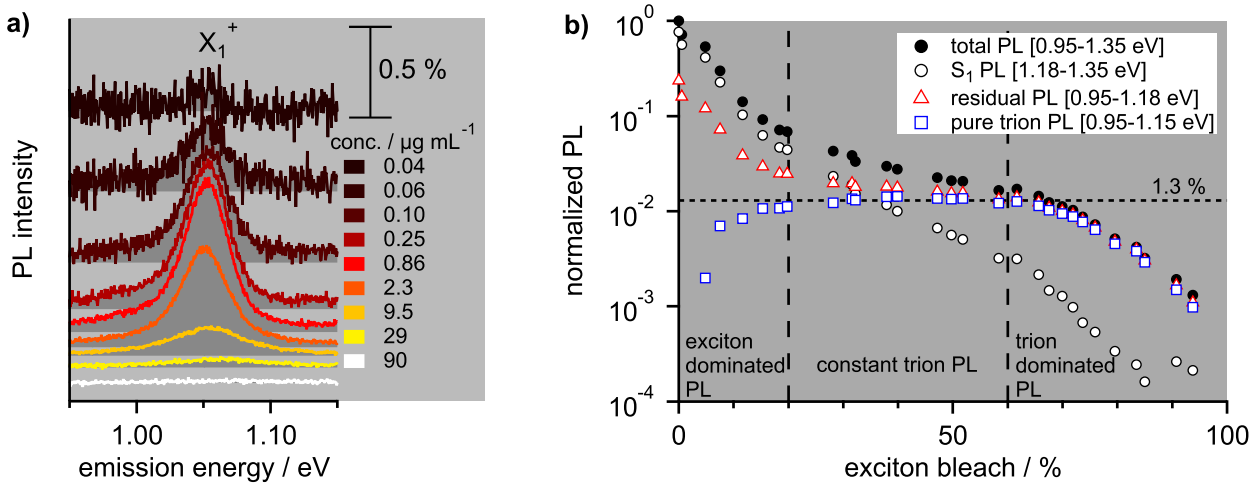

Figure 5.13: a) Trion emission for different $AuCl_3$ concentrations. The scale bar indicates 0.5 % of the S_1 peak intensity in the intrinsic sample. b) Detailed analysis of the different PL contributions in dependence of the S_1 exciton bleach. Three different regimes are observed: exciton dominated PL at low doping levels, nearly constant trion PL at intermediate doping and trion dominated PL at high doping levels.

For band filling (BF) and in the absence of doping-induced screening effects, the normalized S_1 exciton PLQY is expressed as (see appendix 11.1):

$$\mathrm{PLQY}^{\mathrm{BF}}(\chi) = \frac{1-\chi}{1+A\cdot\chi}, \tag{5.14}$$

where the only fit coefficient $A \approx k_{\mathrm{nr}}(\chi = 100\,\%)/k_{\mathrm{nr},0}$ describes the ratio of nonradiative decay rates k_{nr} for a fully quenched S_1 absorption band compared to the intrinsic sample. Within this theoretical framework, the doping-induced nonradiative decay rate is linear in charge density n or exciton bleach χ, respectively. A linear n-dependence is in agreement with the n-dependence predicted for the phonon-assisted indirect exciton ionization (PAIEI) mechanism at moderate doping [108] (see chapter 2.2.3).

In contrast, diffusion-limited contact quenching at localized charges leads to a nonradiative decay rate, which is approximately proportional to n^2 [98]. For the sake of simplicity, the distances w between localized charges (LC) are assumed to be constant. The normalized S_1 PLQY can then be described by (see appendix 11.1):

$$\mathrm{PLQY}^{\mathrm{LC}}(\chi) = (1-\chi)\left[1+\frac{d_0}{\Delta}\chi\right]^{-2}, \tag{5.15}$$

where d_0/Δ is the only fit coefficient. Here, d_0 is the exciton diffusion length in intrinsic SWNTs and Δ is the localization length of a charge carrier. Fig. 5.14a shows the normalized S_1 PLQY as a function of the exciton bleach along with the best fits of the band filling and localized charge model. The best fits were obtained for $A = 34 \pm 4$ and $d_0/\Delta = 11 \pm 1$. The localized charge model with the approximate n^2 dependence of the nonradiative de-

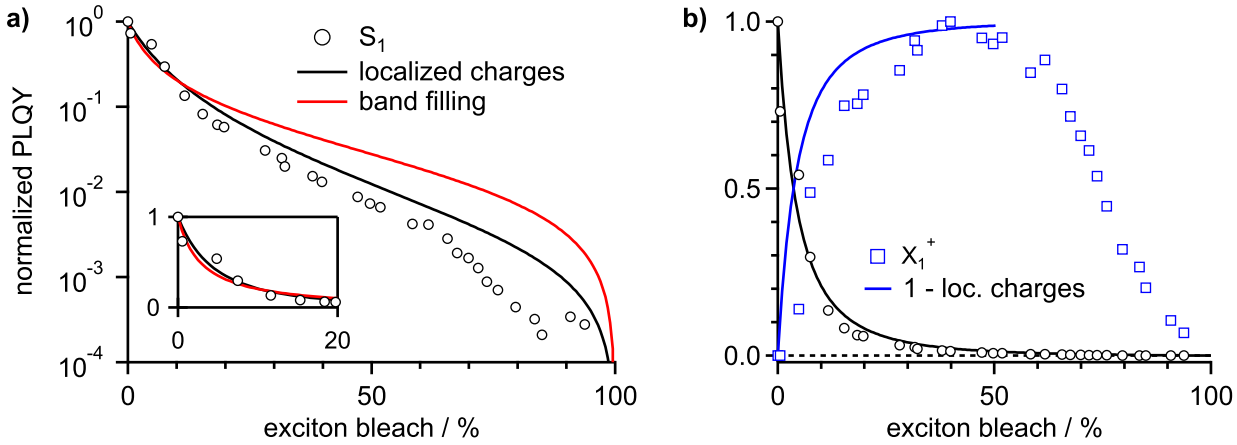

Figure 5.14: a) Dependence of the normalized S_1 PLQY on the exciton bleach on a log-lin plot. Agreement of the localized charge model with the experimental data is slightly better than for the band filling model. The inset shows the data on linear axes up to a doping level of $\chi \leq 20\,\%$. b) Comparison of normalized exciton and trion PLQY.

cay rate describes the data slightly better than the band filling model. For a diffusion length $d_0 \approx 100\,\mathrm{nm}$ in intrinsic samples [114, 117], the resulting carrier localization length is $\Delta \approx 9\,\mathrm{nm}$. This Δ-value is somewhat larger but comparable to the localization lengths obtained by calculations in section 5.2.1 ($\Delta \approx 3 - 4\,\mathrm{nm}$) and previous experiments of our group ($\Delta \approx 4\,\mathrm{nm}$) [112].

However, two additional facts have to be noted:

- For band filling also a mechanism called multiparticle exciton ionization with an n^2-dependence of the nonradiative decay rate has been predicted and could describe the experimental data as well [263].
- A model based on diffusion-limited quenching loses its validity if the (average) distance between quenching centers w becomes smaller than the exciton coherence length l_c.

For $w < l_c$, transport to quenching centers is no longer diffusive but coherent. Experimentally, the exciton coherence length has been determined to be on the order of 10 nm [102]. Calculated coherence lengths $l_c = \pi\hbar/\sqrt{2M\Gamma_h}$ [264] are somewhat larger and on the order of $l_c = 20\,\mathrm{nm}$. For the calculation, the effective exciton mass $M = 0.14\,m_e$ [18, 112] and homogeneous linewidth $\Gamma_h = 2\hbar/T_2 = 6.4\,\mathrm{meV}$, corresponding to a dephasing time $T_2 = 205\,\mathrm{fs}$ [113], were used. The coherence length sets the validity of the diffusive quenching to at least $\chi < \Delta/l_c \approx 50\,\%$. Therefore, diffusive exciton quenching at localized charges is best probed at very low carrier concentrations.

A simple nonradiative decay mechanism of the scheme $S_1 + h^+ \rightarrow X_1^+$ suggests that the relative decrease in S_1 PL intensity mirrors exactly the relative increase in X_1^+ PL intensity. Fig. 5.14b shows that this is not the case. The trion PL increase is somewhat 'delayed' compared to the S_1 PL decrease. In terms of band filling, this could be a manifestation of a more complicated dependence of the delocalized trion's radiative and nonradiative lifetimes on

the charge density n. On the other hand, ESR studies on $AuCl_3$ doped SWNTs showed that charges become localized as unpaired spins (radicals) for a very low S_1 exciton bleach [236]. The lack of a quantitative agreement between the decline of S_1 PL and the rise of trion PL might suggest that unpaired, localized charges mainly act as exciton quenching centers whereas spin-paired charges act as both, exciton quenching centers and trion emission sites.

In conclusion, the doping level dependence of the S_1 PL could be reasonably well described and the PL might be used to determine carrier concentrations in nanotubes. Due to its high sensitivity to additional charges, the detection of carrier density variations of less than one charge per average tube length seems possible. However, modeling the doping level dependence of the S_1 PL does not allow a clear statement about the microscopic mechanism of nonradiative exciton decay in doped SWNTs. Nevertheless, discrimination between a mechanism based on band filling and a diffusive quenching mechanism is possible using time-resolved ultrafast spectroscopy. For band filling, the probability for exciton decay does not depend on the exciton position since charge carrier density is spatially uniform for fully delocalized excess charges. The nonradiative decay rate k is therefore constant in time, and exciton decay should be unimolecular, *i.e.* $\mathrm{d}[S_1]/\mathrm{d}t = k[S_1]$. If exciton decay, however, is limited by diffusion to quenching sites, the nonradiative decay rate is time-dependent, *i.e.* $\mathrm{d}[S_1]/\mathrm{d}t = k(t)[S_1]$. According to Hertel *et al.*, the exciton dynamics is then described by a stretched-exponential decay [98].

5.3.2 Time-Resolved Spectroscopy

$AuCl_3$-doped SWNTs in dispersion were characterized by transient absorption (TA) to distinguish band filling from charge localization. TA experiments, especially for non-degenerate pump and probe, should be performed in samples of small path length to guarantee high temporal resolution. Here, a 1 mm cuvette was used instead of the 10 mm cuvette used for steady-state absorption and PL. Consequently, higher SWNT concentrations and also higher $AuCl_3$ concentrations were necessary to achieve an S_1 peak absorbance of 0.22 in the intrinsic sample and a similar doping effect for the doped samples. Fig. 5.15a shows the absorption spectra of nine samples with increasing $AuCl_3$ concentration. The samples were excited with VIS pump pulses (2.15 eV central energy), resonant with the S_2 transition. Probed photon fluences of $3 \times 10^{12}\,\mathrm{cm}^{-2}$ per pulse were used. The pump pulses had a bandwidth of ≈ 40 meV and were sub-50 fs long as determined by fitting of the intensity autocorrelation SHG signal with a Gaussian profile. Temporal resolution of ≈ 190 fs was estimated by fitting the initial rise of the S_1 photobleach (PB) signal in the intrinsic sample with a Gaussian instrument response function, whose FWHM was taken as the time resolution. All steady-state absorption and TA spectra were corrected for dilution caused by the addition of $AuCl_3$ solution.

The TA spectra of the nine samples at an early delay time of 0.32 ps are shown in Fig. 5.15b. Increasing $AuCl_3$ concentrations monotonically reduce the peak photobleach (PB) signal. The signal reduction can partly be explained by the bleaching of the S_1 transition in steady-state

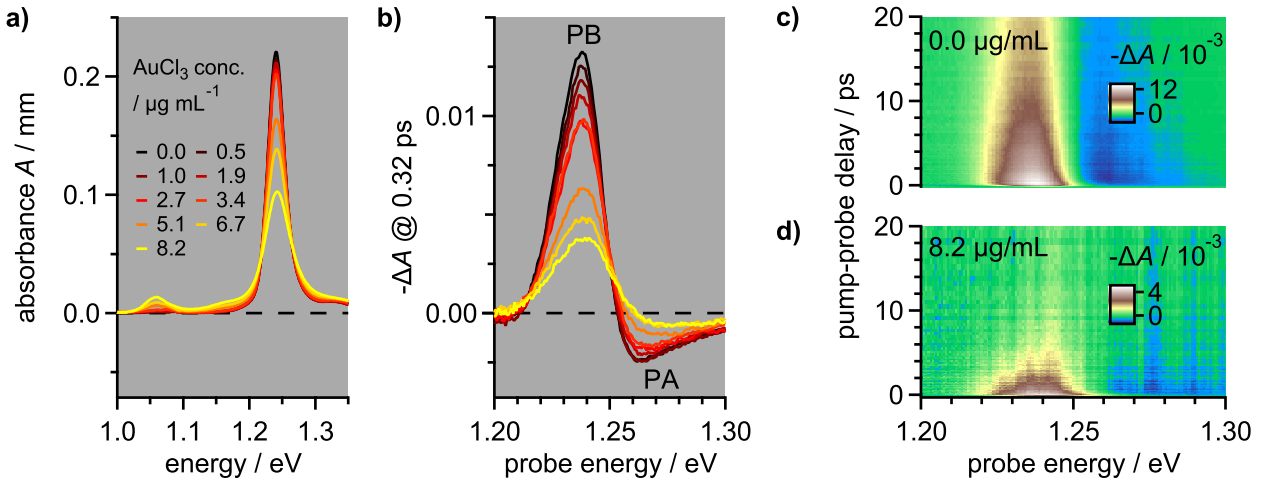

Figure 5.15: a) Absorption spectra of doped SWNT dispersions in a 1 mm path length cuvette. b) Corresponding TA spectra at a pump-probe delay time of 0.32 ps. c) TA map of intrinsic SWNTs and d) SWNTs doped with 8.2 µg/mL $AuCl_3$.

absorption. However, peak PB signals are somewhat more reduced than the peak absorbance. This indicates that already considerable decay occurs during the first 320 fs, especially for the more strongly doped samples. The TA maps of the intrinsic sample (Fig. 5.15c) and the sample doped with 8.2 µg/mL $AuCl_3$ (Fig. 5.15d) clearly visualize the accelerated dynamics.

Kinetic analysis

In the following, the decay dynamics is investigated in more detail. Fig. 5.16a shows transients at 1.235 eV probe energy for the intrinsic sample, the sample with the highest doping level and for two intermediate $AuCl_3$ concentrations. Doping causes a strong acceleration of the S_1 PB decay. For a semi-quantitative analysis, a line at which the signal has decayed to 1/e of its peak value is also drawn. The time, at which the signal has decayed to 1/e is constantly decreasing from $\approx$ 22 ps to $\approx$ 3 ps. In terms of a monoexponential decay $\Delta A(t) = \Delta A(0)\,\exp(-t/\tau)$, this time could be associated with the characteristic time constant τ. However, Fig. 5.16b shows in a log-lin plot that the decay is strongly non-exponential for all samples. For a monoexponential decay, a linear relationship between $\ln(-\Delta A)$ and t is expected, which is not observed.

A non-exponential power-law decay has been frequently observed for intrinsic SWNTs [88, 190, 244, 265] and was interpreted as a diffusion-limited reaction in one dimension. One decay mechanism causing a power-law decay is a diffusion-limited exciton-exciton annihilation reaction of the kind $S_1 + S_1 \rightarrow S_0 + S_1$ [188, 244, 266]. However, for the low excitation fluences used, only a minority of SWNTs has more than one exciton within twice the exciton diffusion length, and therefore such a decay mechanism can be neglected. Another more plausible mechanism assumes the reaction of the kind $S_1 + Q \rightarrow S_0 + Q$, where Q is a stationary quenching site at which the S_1 exciton can rapidly decay nonradiatively [98, 188, 267, 268].

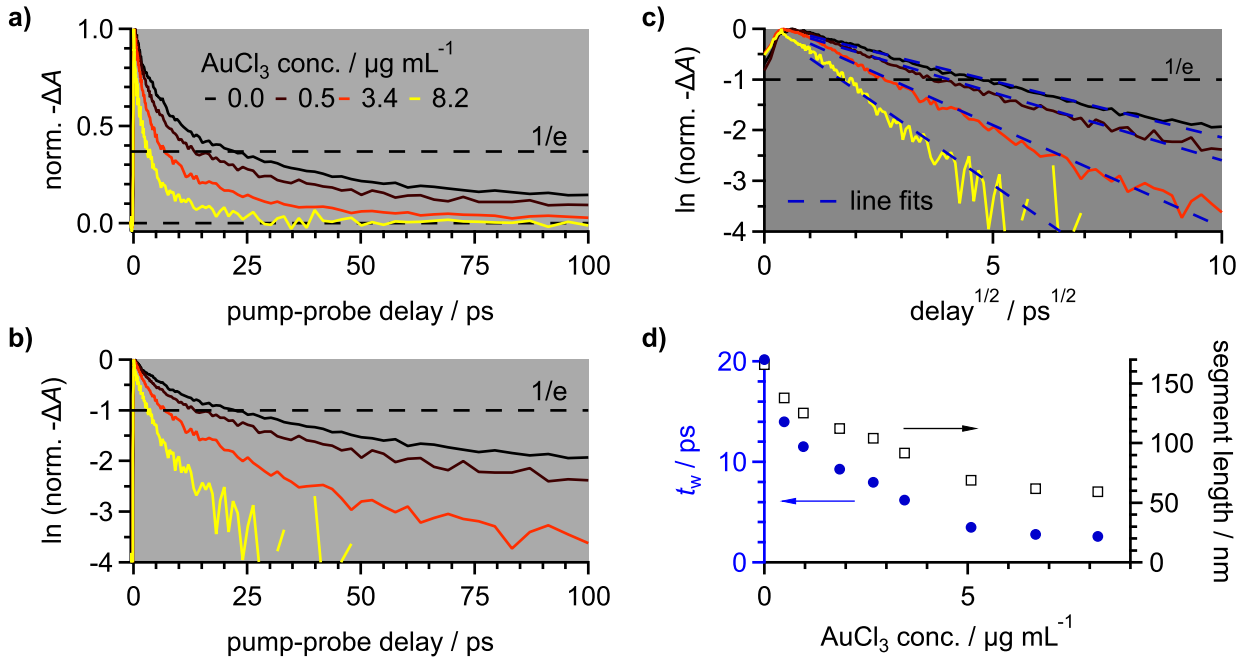

Figure 5.16: a) S_1 photobleach dynamics on a linear x- and y-axis. The exciton decay is strongly accelerated upon doping. b) Same data in a log-lin plot showing that all samples exhibit a strongly non-exponential decay. c) The linear relationship in the $\ln(-\Delta A)$ vs $\sqrt{t}$ plot indicates a diffusion-limited decay in one dimension. Line fitting (blue lines) is performed for delay times $1\,\text{ps} \leq t \leq 100\,\text{ps}$. d) Diffusion time constants t_w obtained from the line fits and calculated segment lengths using an exciton diffusion constant of $D = 10.7\,\text{cm}^2/\text{s}$ [98].

Hertel *et al.* described that the S_1 population P for diffusion-limited contact quenching (DLCQ) can be expressed as [98, 269]:

$$P(t) = P_0 \exp\left[-\sqrt{t/t_w}\right], \tag{5.16}$$

where $t_w = \pi w^2/(4D)$ is a characteristic diffusion time constant. The time constant t_w is determined by is the average distance w between quenching sites and the exciton diffusion constant D. Fig. 5.16c shows a plot of the PB decay according to the natural logarithm applied to equation (5.16):

$$\ln(P(t)) = \ln(P_0) - \sqrt{t/t_w}. \tag{5.17}$$

The PB decay of the intrinsic SWNT sample is linear on this $\ln(-\Delta A)$ vs $\sqrt{t}$ plot suggesting that DLCQ governs the S_1 exciton PB decay at immobile defects like the SWNT ends. However, the DLCQ mechanism describes not only the decay in the intrinsic sample but also in all doped samples as indicated by the linear relationship. The remarkable agreement with the DLCQ model implies that:

- excess charges indeed act as conduits for nonradiative S_1 exciton decay
- excitons need to diffuse to the charges to decay nonradiatively

The latter statement is in clear disagreement with homogeneously distributed and delocalized charges and provides strong evidence for the localized nature of excess charges in moderately doped SWNTs. The same decay characteristics were also found in SWNT samples of varying sp^3-defect concentration introduced by diazonium chemistry [61]. Such functionalization clearly produces localized and immobile quenching sites due to covalent bonds.

Nevertheless, a linear relationship between $\ln(-\Delta A)$ and $\sqrt{t}$ does not necessarily mean that the quenchers have to be immobile, but they can be diffusing themselves [270, 271]. For mobile quenchers, the effective diffusion constant is given by the sum of the exciton and quencher diffusion constants and is therefore increased compared to the case of immobile quenchers. In general, the diffusion constant of a charged particle is expected to be lower than that of a charge-neutral particle like an exciton, because charges polarize their environment, which in turn reduces their mobility [272]. In contrast to the diffusion-limited exciton PB decay, monoexponential trion dynamics with decay constants of 0.5-2 ps has been found, demonstrating the localized and immobile nature of charged trions [143–145, 225, 273]. Therefore, diffusion of charged particles is neglected in the following.

The line fits in Fig. 5.16c were used to extract the characteristic time scales $t_w = 1/m^2$, where m is the slope. Fig. 5.16d shows t_w as a function of $AuCl_3$ concentration. Up to a concentration of $c_{AuCl_3} = 3.4\,\mu g/mL$, the characteristic diffusion time t_w sharply decreases from the intrinsic value of 20 ps. In terms of S_1 exciton bleaching, this corresponds to only 5 %. For higher $AuCl_3$ concentrations and therefore stronger bleaching, t_w saturates and equals 2.6 ps for the sample with the highest $AuCl_3$ concentration.

The diffusion time t_w can be used to calculate the average segment length between two quenchers if the exciton diffusion constant is known. Fig. 5.16d shows the average segment length w obtained from this analysis using an exciton diffusion constant $D = 10.7\,cm^2/s$, according to Hertel *et al.* [98].

Comparison of PL and TA

Next, the S_1 PB dynamics from time-resolved TA spectroscopy are compared to steady-state PL experiments. The steady-state PL intensity I_{S_1} reflects the time-integrated S_1 population $P(t)$ via:

$$I_{S_1} \propto \int_0^\infty P(t)\,dt. \tag{5.18}$$

For a normalized stretched-exponential of the form $P(t) = \exp\left(-\sqrt{t/t_w}\right)$ the integral is exactly solvable with $\int_0^\infty P(t)\,dt = 2t_w$. Therefore, the relative PLQY as a function of the exciton bleach χ could also be obtained from the S_1 dynamics (see appendix 11.1):

$$\mathrm{PLQY}(\chi) = \frac{t_w(\chi)}{t_w(\chi = 0)}(1 - \chi), \tag{5.19}$$

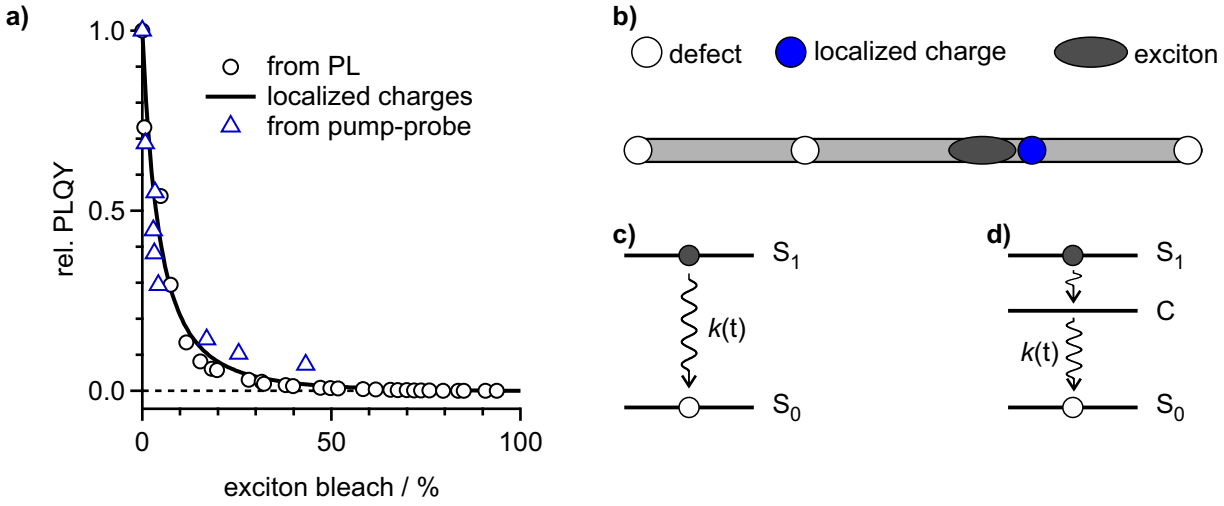

Figure 5.17: a) Comparison of the relative PLQY as determined by direct steady-state PL measurement and by analysis of the S_1 PB dynamics obtained in the pump-probe experiment. The solid line is a fit to the PL data with the localized charge (LC) model. b) Illustration of the diffusion-limited contact quenching model. In intrinsic SWNTs, mainly the tube ends act as defects at which the S_1 exciton can decay nonradiatively very quickly. Localized charges introduced by doping also act as conduits for nonradiative decay and increase the effective quencher concentration. c) In a two-level system S_0 ground state recovery dynamics and S_1 population dynamics are the same whereas this is not the case for the three level system shown in d).

where the factor $(1 - \chi)$ accounts for the reduced oscillator strength besides the purely dynamical changes. Fig. 5.17a shows the calculated relative PLQYs using the results of the TA decay analysis along with the relative PLQY directly obtained by PL measurements. For a small doping-induced exciton bleach up to 5 %, both experiments show a qualitative agreement. The S_1 PB signal is therefore assumed to be approximately proportional to the S_1 population. In this very weak doping regime, the pump-probe data were well described by the diffusion-limited contact quenching of S_1 excitons as illustrated in Fig. 5.17b. For a hypothetical two-level (S_0, S_1) system (see Fig. 5.17c), the dynamics of ground state recovery, as mainly measured by pump-probe, mirrors the S_1 population dynamics as measured by time-resolved photoluminescence.

The situation strongly changes for higher doping levels. The agreement of the PLQY from PL measurements and from the S1 PB dynamics becomes worse. For the three pump-probe data points at the highest doping-induced exciton bleach, the relative disagreement between the pump-probe analysis and the PL data rises from roughly a factor of two to already one order of magnitude. For these doping levels, the S_1 PB dynamics does clearly not follow the S_1 population dynamics, but rather describes the ground state recovery in a system with more than two energy levels.

Fig. 5.17d illustrates how a stretched-exponential PB decay can still occur in a three-level system. If decay from S_1 to a third state C is fast and C decays via diffusion-limited contact quenching, the ground state recovery follows a stretched-exponential decay. However, the S_1

PB signal then rather measures the population in C than in the emissive S_1 state.

5.4 Intraband Absorption of Charge Carriers

Up to now, this work only regarded electronic interband transitions in the VIS and NIR spectral region. For doped semiconductors, additional intraband transitions in the far infrared or terahertz regime are possible due to free-carrier absorption [159, 172, 209]. Apart from that, impurity absorption in substitutionally doped semiconductors [43], polaron absorption in doped semiconducting polymers [274] or plasmon resonances typically occur at energies far below the band gap energy [159, 272]. The different IR absorption processes can be characterized and discriminated by their distinct spectral signatures [272]. These spectral signatures in the IR possibly also allow the discrimination of localized and delocalized charges in SWNTs.

Electrical four-point-probe direct current (DC) measurements on ensembles of redox chemically doped SWNTs have been performed by Chandra *et al.* [206], Ferguson *et al.* [230] and others [275]. For such experiments, SWNT thin-film samples are used. Hence, DC measurements probe the electrical properties of the film over distances of the four-point-probe tip spacing, which is typically on the order of millimeters. As a consequence, not the intrinsic charge transport properties of individual SWNTs are revealed but rather the intertube conductivity of the percolation network.

In contrast, alternating current measurements probe charge transport on a smaller length scale approximately given by the distance the carrier moves within one cycle of the electric field. The following example estimates the probed length scale l_{probe} at an angular frequency $\omega = 3\,\mathrm{THz}$ for a metallic nanotube. Using the Fermi velocity $v_F \approx 10^6\,\mathrm{m/s}$ [276] and assuming ballistic transport results in $l_{\mathrm{probe}} \approx v_F/\omega = 300\,\mathrm{nm}$. This length scale is comparable to typical SWNT lengths.

5.4.1 Broadband Transmission Spectroscopy

This work investigates the interaction of *p*-doped (6,5)-SWNT with electromagnetic fields ranging from the UV to the far infrared down to $6\,\mathrm{meV} \approx 1.5\,\mathrm{THz}$ by transmission spectroscopy.

All spectra in the IR region are shown as the negative logarithm $-\log(T)$ of the transmission T to avoid the somewhat misleading quantity absorbance $A = -\log(T)$. This should remind the reader that a reduced transmission can be caused by both absorption and reflection. For negligible reflection, $-\log(T)$ describes the absorption and the Beer-Lambert law is valid. However, as will be shown in chapter 6, the Beer-Lambert law is not valid anymore for heavily doped thin-films. Below specific photon energy, free carriers cause reflection [277] like it is the case in conventional metals like, for example, silver [159].

This chapter intends to answer the following questions:

- How 'intrinsic' are the nanotubes before intentional treatment with hole dopants?
- Can doping-induced IR intraband absorption be correlated with changes in NIR interband absorption?
- Does the IR response support the hypothesis of localized charge carriers?

Fig. 5.18a shows the transmission spectrum of an intrinsic (6,5)-SWNT thin-film between 0.05 eV and 4.5 eV on a logarithmic energy scale. Besides the already discussed excitonic transitions and their phonon sidebands in the VIS and NIR, a strong peak in the UV at ≈ 3.5 eV is visible. This absorption band belongs to the interband absorption of the wrapping polymer PFO-BPy and overlaps with the third subband exciton (S_3) absorption of the SWNTs [200]. In the IR region, there is essentially just a flat baseline very close to zero. The negligible absorption in the IR region indicates the high quality of the as-prepared intrinsic SWNTs. Metallic SWNTs show strong IR absorption due to free carriers [277–280], which suggests that metallic SWNT content in the PFO-BPy wrapped SWNT samples is very low. The low metallic content is consistent with the findings of Brady *et al.* who report a semiconducting purity of $> 99.98\,\%$ [8, 16]. Apart from the low amount of metallic SWNTs, the absence of IR absorption also indicates that the as-prepared thin-films have a very low charge density due to unintentional doping at ambient conditions, for example, caused by the oxygen/water redox couple [110, 111, 236, 281].

Fig. 5.18b depicts the influence of additional charge carriers on the broadband transmission of SWNT films as a color map. Doping was achieved by immersing the SWNT thin-films for 5 min in a triethyloxonium hexachloroantimonate (OA) solution (toluene/acetonitrile 5:1) of varying concentration (0-1000 µg/mL) and subsequent drying of the film. Doping with the hole dopant $AuCl_3$ was found to show no apparent difference to doping with OA. The absorption in the IR region rises for increasing OA concentration, which is accompanied by the changes of SWNT interband absorption (S_1, S_2, X_1^+, phonon sidebands) in the NIR-VIS spectral region (see section 5.2). Fig. 5.18c shows the same data on a logarithmic energy scale from the IR to the UV region. The wrapping-polymer related peak at 3.5 eV loses intensity upon doping. For the highest doping level (yellow spectrum) with completely bleached S_1 absorption, an additional peak is apparent at ≈ 3 eV. This new absorption band has previously been attributed to hole polaron absorption in the doped polymer PFO-BPy [19, 282]. Interestingly, polymer doping was not observed for electrochemical doping [18, 200] or ionic liquid gating [283] of (6,5)-SWNT films wrapped with PFO-BPy.

Control experiments

To investigate the influence of the polymer doping on IR absorption, a thin-film of pure PFO-BPy was prepared by drop-casting of a PFO-BPy solution on a 500 µm thick polyethylene substrate. Fig. 5.18d shows the broadband transmission spectrum of the polymer film before and after doping. The *p*-doping was again achieved by immersion of the intrinsic polymer film

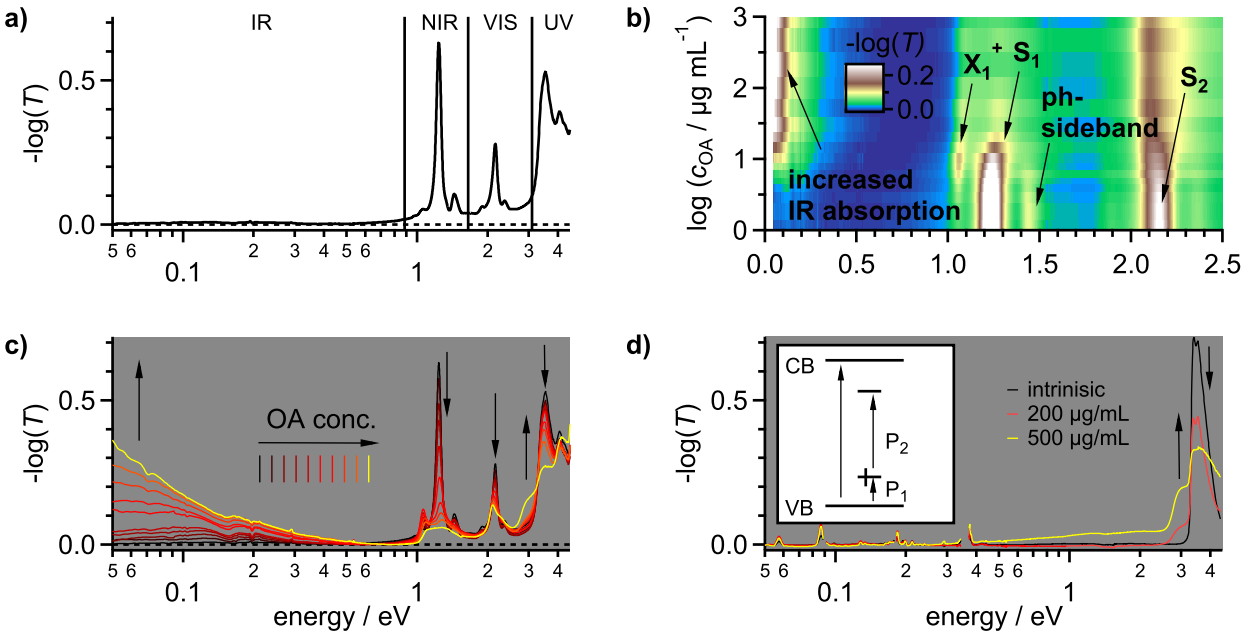

Figure 5.18: a) Broadband transmission spectrum of a (6,5)-SWNT/PFO-BPy thin-film on a logarithmic energy axis. IR absorption in the energy range 0.05 eV-0.89 eV is negligible compared to the SWNT and polymer interband absorption from the NIR to the UV. b) Transmission as a function of OA hole dopant concentration illustrated as a color map on a linear energy axis. c) Same data as in b) using a logarithmic energy axis. OA concentrations increase from 0.0 µg/mL (black) to 1000 µg/mL (yellow). d) Control experiment with a pure PFO-BPy thin-film on a polyethylene substrate. *p*-doping with OA leads to a decrease of the 3.5 eV absorption band, to an absorption increase at 3.0 eV but to no apparent changes in IR absorption.

into OA solutions with concentrations of 200 µg/mL and 500 µg/mL. This procedure leads to an increase of the 3.0 eV absorption band but to no apparent change in IR absorption.

Hole polaron formation is typically discussed to lead to stabilized states within the band gap causing two new absorption bands called P_1 and P_2 (see inset of Fig. 5.18d) [274, 284–289]. In this theoretical framework, the 3.0 eV absorption band would be ascribed to the P_2 band, but a low energy P_1 band could not be observed here.

Significant contributions from the hole dopants (OA or $AuCl_3$) or their reaction products to the IR absorption of doped SWNT thin-films can also be excluded since doping with OA or $AuCl_3$ leads to similar IR spectra with no apparent difference. Kim *et al.* reported that elementary gold nanoparticles form at the nanotube surface during $AuCl_3$-mediated doping [239]. This process can neither be neglected nor confirmed, but the influence of possible gold nanoparticles on the low energy IR absorption seems negligible. These control experiments lead to the conclusion that changes in IR absorption originate almost exclusively from excess charge carriers on SWNTs.

The mutual dependence of IR oscillator strength and nanotube NIR oscillator strength further corroborates this finding (see Fig. 5.19a and b). Oscillator strengths were determined by integration over distinct regions of the spectrum. In the IR region, the lower integration

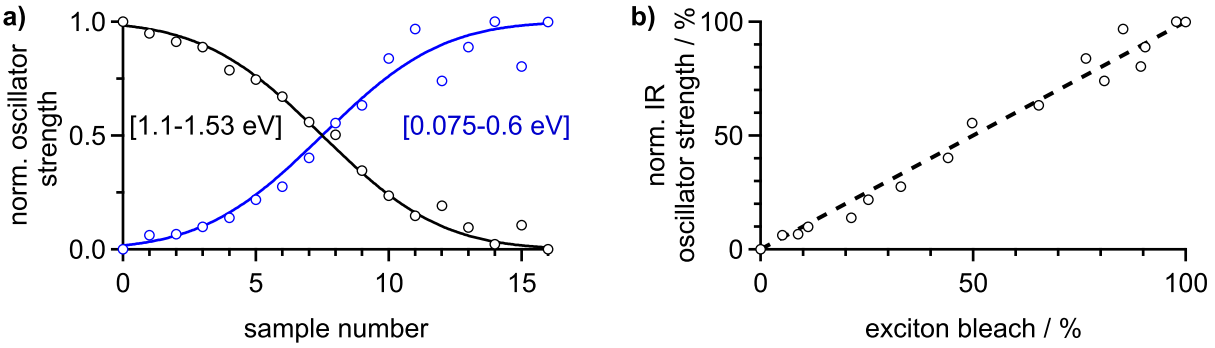

Figure 5.19: a) Normalized oscillator strengths in the exciton spectral region between 1.10 eV and 1.53 eV and in the IR region between 0.075 eV and 0.60 eV as a function of the sample number. OA concentrations increase with sample number from 0 to 1000 µg/mL. The lowest oscillator strength values were taken as reference and equal zero. b) Same data with the NIR oscillator strength converted to the exciton bleach. The dashed line illustrates the 1:1 correspondence between the exciton bleach and the doping-induced absorption in the IR.

limit was 0.075 eV because the Beer-Lambert law seems to lose validity at lower energies (see chapter 6). The upper integration limit was set to 0.6 eV because this is approximately the energy below which doping-induced IR absorption starts to increase. For the NIR region, the integration limits were 1.10 eV and 1.53 eV in order to span the spectral region of the S_1 absorption in intrinsic and doped SWNTs. The IR and NIR oscillator strengths were further referenced to the lowest values, *i.e.* IR absorption of intrinsic SWNTs and NIR absorption of heavily doped SWNTs. Subsequently, the relative oscillator strengths were normalized to cover a range between 0 and 1. Fig. 5.19a shows the normalized oscillator strengths in the IR and NIR region for the 17 measured samples with increasing OA concentration. The two solid lines, whose sum equals one, are guides to the eye. The excitonic NIR oscillator strength decreases for higher sample numbers, whereas the IR absorption increases. Interestingly, the exciton bleach and the doping-induced IR absorption show an almost one to one correspondence (see also Fig. 5.19b). From this finding, two conclusions are drawn. First, since the IR oscillator strength originates from the absorption of excess charge carriers, the integrated IR absorption should be proportional to the charge concentration (charge density) according to the Beer-Lambert law. Second, the one to one correspondence of increasing IR oscillator strength and exciton bleach suggests that the exciton bleach is also approximately linear in charge density. A linear relationship between charge density and exciton bleach is in good agreement with the phase space filling model [93]. In turn, this agreement suggests that rather phase space filling than screening effects dominate the exciton oscillator strength reduction in moderately doped SWNTs.

Doping-induced changes in energetics

It was demonstrated how relative charge densities might be estimated by spectral changes in the NIR or IR region. However, changes in oscillator strength alone do not allow drawing

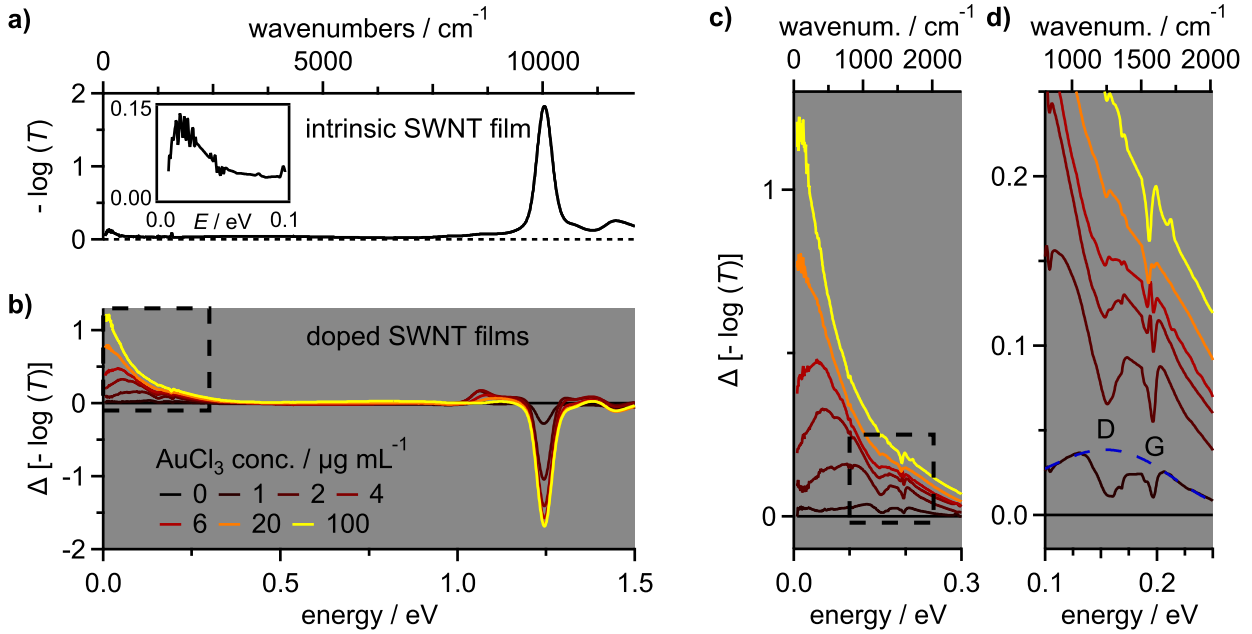

Figure 5.20: a) Broadband transmission spectrum of an intrinsic SWNT thin film used for $AuCl_3$-mediated doping experiments. The inset shows an enlarged view of the low energy part. The observed, low energy oscillating signal is most like a spectrometer artifact. b) Difference spectra for various $AuCl_3$ concentrations using the intrinsic film ($c_{AuCl_3} = 0$) as reference. The spectral region marked with a dashed box is enlarged and shown in c). d) Closer view on the D- and G-band antiresonances. The dashed blue line is a guide to the eye and illustrates how the carrier absorption band potentially looks like without antiresonances.

a conclusion about the character of charges, being either delocalized or localized. Therefore, the reduced transmission in the IR is further investigated for its exact spectral shape or energetics. In order to do so, the spectral region in the IR should extend to energies as low as possible. Therefore, absorption spectra covering the spectral range from 6 meV up to the NIR were recorded. The additional energy range from 6 to 50 meV compared to the OA doping series shown above was covered by a second Fourier-transform infrared spectrometer (see section 3.2.2). The cooperation partner Florian Hirsch from the research group of Prof. Fischer performed the infrared measurements. SWNT thin-films on polyethylene substrates were charged using the hole dopant $AuCl_3$. The observed spectral changes were very similar to the results of OA doping presented in Fig. 5.18a, which suggests that transmission changes in the IR are not related to the hole dopant but indeed to the SWNT excess charges. Fig. 5.20a shows the transmission spectrum of the intrinsic, as-prepared SWNT thin-film on a linear energy scale. IR absorption is again almost negligible except a small asymmetric and oscillating signal centered at ≈ 18 meV (see inset of Fig. 5.20a). This signal contribution was present in all spectra of the doping series and its origin is not exactly known. Most likely it is a spectrometer artifact. In order to remove this artifact, difference spectra were calculated with the intrinsic spectrum as reference. Since the interest is on doping-induced changes and not on absolute signals, a subtraction procedure is also acceptable in the case

of a non-artificial signal. Fig. 5.20b shows the results of the subtraction procedure for doped SWNT films. The S_1 exciton absorption again decreases for higher dopant concentration (more negative signals in the difference spectra), and the IR absorption increases (more positive signals). However, not only the IR intensity changes but also the spectral shape. To show this more clearly, Fig. 5.20c depicts an enlarged view of the energy region between 0 eV and 0.3 eV. At low $AuCl_3$ concentrations $c < 20\,\mu g/mL$, the spectra seem to be composed of multiple asymmetric absorption bands. In contrast, for dopant concentrations exceeding 20 mg/mL the signal intensity constantly rises towards decreasing photon energies and peaks at the lowest measured photon energy.

D-band antiresonance

However, the IR spectra at low doping levels could also be interpreted as showing only one broad absorption band and two dips at ≈ 196 - 197 meV (1580 - 1590 cm^{-1}) and ≈ 155 - 156 meV (1250 - 1260 cm^{-1}), which was suggested by Lapointe *et al.* [129]. They used SWNTs films made from aqueous nanotube dispersions stabilized by sodium cholate and containing a mixture of semiconducting and metallic SWNTs. Upon redox chemical doping, the two dips were observed and were ascribed to SWNT Raman bands. Following Lapointe *et al.*, the high energy dip is assigned to the so-called G-band, and the lower energy dip is assigned to the localized defect-induced D-band [60, 123, 125, 129].

With this in mind, the following two questions arise:

- Why do Raman-allowed and IR-forbidden vibrational modes become IR-active upon doping?
- Why do the vibrational bands show up as dips instead of peaks in the spectrum?

For a vibrational mode to be IR-allowed, the dipole moment needs to change during the vibration. Because of symmetry reasons, this is not the case for the G- and D-mode in SWNTs [126]. However, the polarizability changes during the vibration and the modes can be observed in the Raman spectrum.

Doping-induced IR activation of Raman-active modes (having even-parity) is well known in the research field of semiconducting polymers, and the modes are called IR-active vibrations (IRAV) [286, 290]. The IR-activation can be understood as follows: Doping-induced localized charges, called polarons in semiconducting polymers, act like 'defects' and break the local symmetry [125]. Therefore, IR-forbidden and Raman-allowed modes become IR-active [291, 292]. For similar reasons, the localization of charge carriers in doped (6,5)-SWNTs could also be responsible for the IR-activation of Raman-active phonon bands.

However, the G- and D-phonon bands do not produce peaks but dips in the absorption spectrum. This phenomenon can be explained by a so-called Fano antiresonance [293] and has – among many other systems [294–296] – also been observed in doped semiconducting polymers [284, 286, 287, 297]. An antiresonance can occur whenever there is a coupling and destructive interference between transitions to a discrete state and to a broadband continuum

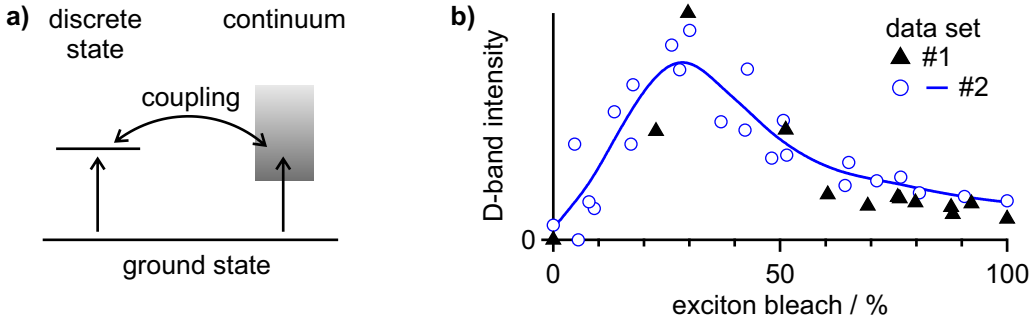

Figure 5.21: a) Illustration of the Fano resonance model. The coupling strength between the discrete state and the continuum of states determines if an antiresonance is observed. b) Approximated intensity of the D-band antiresonance as a function of the exciton bleach for two different data sets. Data set #1 corresponds to the spectra shown in Fig. 5.20. The solid line is a guide to the eye obtained by smoothing the experimental data points from data set #2.

(see Fig. 5.21a) [293]. In the case of doped SWNTs, the absorption to a discrete state belongs to the G- and D-phonon transitions embedded in a broad electronic continuum absorption band due to charge carrier absorption.

Lapointe *et al.* demonstrated an enhancement of the D-band antiresonance in doped SWNTs and doped graphene by the intentional introduction of sp^3-defects [128, 129]. The redox chemical doping with OA or $AuCl_3$ in this work obviously does not produce additional sp^3-defects. Therefore, the increase in D-band antiresonance intensity upon doping might be explained by an increase of localized charges, producing localized energy levels in the band gap and behaving similarly to covalently attached defects.

It should be stressed that a broadband continuum absorption due to free carriers alone is not sufficient to observe the D-band antiresonance. This can be seen in the literature by the absence of the antiresonance for samples containing metallic SWNTs without intentional doping [129, 277, 280].

Fig. 5.20d shows the doping level dependence of the D-band antiresonance. The depth of the D-band antiresonance first seems to increase and later to decrease again. For the highest doping levels ($c_{AuCl_3} \geq 20\,\mu g/mL$), the antiresonance becomes again almost negligible. A quantitative determination of the D-band antiresonance intensity was not possible because the exact shape of the pure continuum absorption without antiresonance can not be determined. However, for a qualitative determination of the doping level dependence, the D-band antiresonance intensity was approximated as the difference between the absorption value at the antiresonance minimum position and the next maximum position at higher photon energies. Fig. 5.21b shows the obtained antiresonance intensity as a function of the exciton bleach. Two different data sets, both obtained upon $AuCl_3$-mediated doping of SWNT thin films, are presented, whereas data set #1 belongs to the spectra shown in Fig. 5.20. For direct comparison, the signal intensities were normalized to the number of SWNTs in the films. Despite the large scatter in this plot, it is evident that the signal intensity upon doping first

increases up to an exciton bleach of $\approx 30\,\%$ and then decreases again. Although it is not known how the antiresonance intensity scales with the continuum absorption intensity and defect density, this qualitative doping level dependence is interpreted as follows: First, the signal intensity rises because of the introduction of an increasing number of localized charges acting similar to defects. For doping levels beyond $\chi \approx 30\,\%$, the number of localized charges decreases because of an increasing degree of delocalization. This behavior is very similar to results obtained by ESR spectroscopy of $AuCl_3$-doped SWNT dispersions. In these experiments, the number of spins associated with localized charges first increases at higher $AuCl_3$ concentrations and then decreases due to spin-spin interaction at smaller charge distances (higher doping levels) [236].

For heavily doped SWNTs (fully bleached S_1 absorption) the D-band antiresonance almost completely vanishes. Since the D-band antiresonance is also not observable for samples containing metallic SWNTs without intentional doping [129, 277, 280], it is concluded that heavily doped SWNTs behave similarly to metallic SWNTs. Microscopically, this suggests that the degenerate doping regime is reached and the Fermi energy has been shifted within an energy band, just like for metallic SWNTs. Charge carriers in heavily doped SWNTs are then better described as free and delocalized Bloch waves.

5.4.2 Transition from Localized to Delocalized Carriers

In the following, the hypothesis of a transition from carrier localization to delocalization is corroborated. Evidence is obtained by a more detailed analysis of the IR spectral changes. As could be seen in Fig. 5.20c, the peak of the continuum absorption shifts to lower energy values for higher doping levels. For heavily doped SWNTs (yellow spectrum), the peak position can not be determined anymore and is below the experimentally accessible spectral region of $> 6\,\mathrm{meV}$. The infrared absorption bands of doped SWNT films have frequently been discussed in terms of plasmon resonance [278, 298, 299]. Since the plasmon resonance blueshifts [298, 300, 301] (instead of redshifts) for higher charge densities, plasmons are a rather unlikely explanation for the increased IR absorption upon doping. Additionally, 1D plasmon energies are proposed to be inversely proportional to the SWNT length [299, 302], a quantity which is not changed by doping.

In order to unravel the origin of the redshifting IR peak position, the broadband transmission spectra were converted into optical conductivity spectra by the Kramers-Kronig relation and under the thin-film approximation as described by Zhang *et al.* [278]. An SWNT film thickness $h_{\mathrm{film}} = 531 \pm 26\,\mathrm{nm}$ was used as obtained by profilometer measurements (see chapter 6.5.1 for details). Fig. 5.22 shows the optical conductivity spectra calculated from the broadband transmission spectra shown in Fig. 5.20 for 2, 4 and 100 µg/mL $AuCl_3$ concentration. Optical conductivity spectra are presented as difference spectra $\Delta\sigma(E)$ with the spectrum of the intrinsic sample being the reference. For the 2 µg/mL and 4 µg/mL samples, the real part $\Delta\sigma_1$ drops towards lower energies. Additionally, the imaginary part $\Delta\sigma_2$ becomes negative at

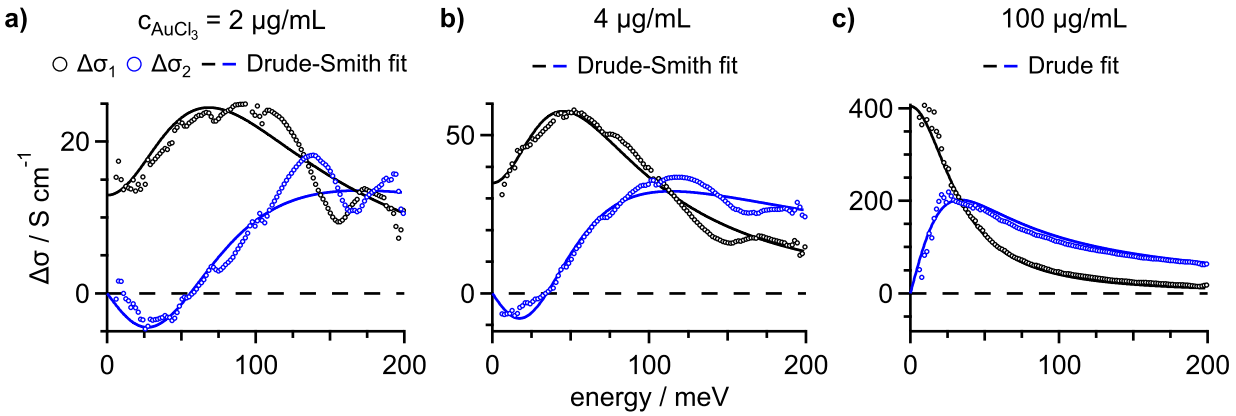

Figure 5.22: Difference spectra of the optical conductivity $\Delta\sigma$ obtained from the broadband transmission spectra for $AuCl_3$ concentrations of a) 2 µg/mL, b) 4 µg/mL and c) 100 µg/mL. In the case of the two lower concentrations, the experimental data are fitted with the Drude-Smith model whereas the Drude free carrier response well describes the spectrum of heavily doped SWNTs (100 µg/mL).

low energies. Both signatures indicate the localization of charge carriers (see chapter 2.4.2). The effect of localization becomes evident if the length scale L_ω of charge migration during a cycle of the oscillating driving field is comparable to the carrier localization length L_{loc}. Consequently, the real part $\Delta\sigma_1$ drops at low photon energies, corresponding to long oscillating periods and large charge migration length scales L_ω. A particularly simple, empirical model to describe the phenomenon of localization is the so-called Drude-Smith model, a modification of the classical Drude model [181]. The Drude-Smith model assumes that the charge carriers are fairly free but can be backscattered at reflecting barriers. The optical conductivity in the Drude-Smith model is given by:

$$\sigma(\omega) = \frac{\sigma_0}{1 - i\omega\tau}\left(1 + \frac{c}{1 - i\omega\tau}\right), \tag{5.20}$$

where σ_0 is the DC conductivity in the absence of backscattering, τ is the average scattering time leading to momentum randomization, and c is a constant describing the degree of localization. The constant c takes values between zero and minus one with $c = 0$ meaning that the barriers are fully transmissive, *i.e.* no localization, and $c = -1$ means that the barriers are perfectly reflecting, *i.e.* strong localization. The two optical conductivity spectra in Fig. 5.22a and b can qualitatively be described by this model using localization parameters $c = -0.68$ and -0.73. The agreement with the Drude-Smith model indicates that carriers in moderately doped SWNTs suffer substantially from localization. Significant discrepancies between the model and the experimental data arise, for example, from the D-band antiresonance at ≈ 150 meV, which is evident in the experimental data but not covered by the fit.

The shape of the optical conductivity spectrum is entirely different for the highest doping level ($c_{AuCl_3} = 100$ µg/mL) at which the S_1 resonance is completely bleached (see Fig. 5.22c). In this case, neither the real part $\Delta\sigma_1$ drops at low energies nor the imaginary part $\Delta\sigma_2$ becomes

negative. A Drude-Smith fit (not shown) gives a localization parameter $c = -0.05$ indicating that the carriers are largely delocalized. A fit to the Drude model, which is obtained from the Drude-Smith model for $c = 0$, agrees remarkably well with the experimental data for fit parameters $\sigma_0 \approx 400\,\mathrm{S\ cm^{-1}}$ and $\tau \approx 20\,\mathrm{fs}$.

The good agreement between the experimental data and the classical Drude model or the quantum mechanical Drude-Sommerfeld model, respectively (see section 2.4.1 for details), seems at first glance very surprising. The optical conductivity is expected to be modified in structures with strong quantum confinement like 1D SWNTs [174, 272]. Nevertheless, the Drude model was also found by other researchers to describe the intraband absorption in metallic or heavily doped 1D SWNTs [303] as well as the 2D parent material graphene [128, 209, 304, 305].

Monte-Carlo simulations

Due to its simplicity and good agreement with the experimental data, the classical Drude approach was used to perform Monte-Carlo simulations of charge transport. The simulations intend to describe how different charge carrier localization lengths modify the optical conductivity spectrum. Fig. 5.20c showed that the IR peak position shifts to lower energies for increasing doping levels. The doping level dependent peak position in the broadband transmission spectra is also observed in the real part of the optical conductivity and has not been discussed so far. Therefore, the simulations focus on changes in peak position as a function of charge carrier localization length L_{loc}. A description of the Monte-Carlo simulations is found in section 2.4.3. For the simulations, an effective charge carrier mass $m^* = 0.07\,m_e$ [18] and an average scattering time $\tau = 20\,\mathrm{fs}$ (as determined from the Drude fit in the heavily doped sample) was used. The simulations were validated by setting the localization length L_{loc} to infinity. In this case, no localization occurs, and the Drude response of free carriers is expected to be retrieved. Fig. 5.23a shows that this is indeed the case because simulated data points and the Drude model (solid lines) are in good agreement. For heavily doped SWNT thin-film samples, the good agreement of the optical conductivity spectrum with the Drude model suggests that the real conductivity peaks at $\omega = 0$. However, this is probably not the case since long-range charge transport in thin-films is not determined by intratube transport but rather by intertube charge transfer acting as a bottleneck. In order to illustrate this effect, Fig. 5.23b shows a simulation for a localization length $L_{\mathrm{loc}} = 200\,\mathrm{nm}$, comparable to average tube lengths. Agreement with the Drude model (solid lines) is still remarkable for energies larger than 6 meV. Therefore, the limited experimental data range $E \geq 6\,\mathrm{meV}$ does not allow drawing conclusions regarding intertube charge transfer. Nevertheless, it is reasonable to assume that charge carriers are delocalized along the whole nanotube in heavily doped SWNTs.

Next, the dependence of the σ_1 peak position on localization length L_{loc} is regarded in more detail. Fig. 5.23c shows simulations for different localization lengths in the range between 5

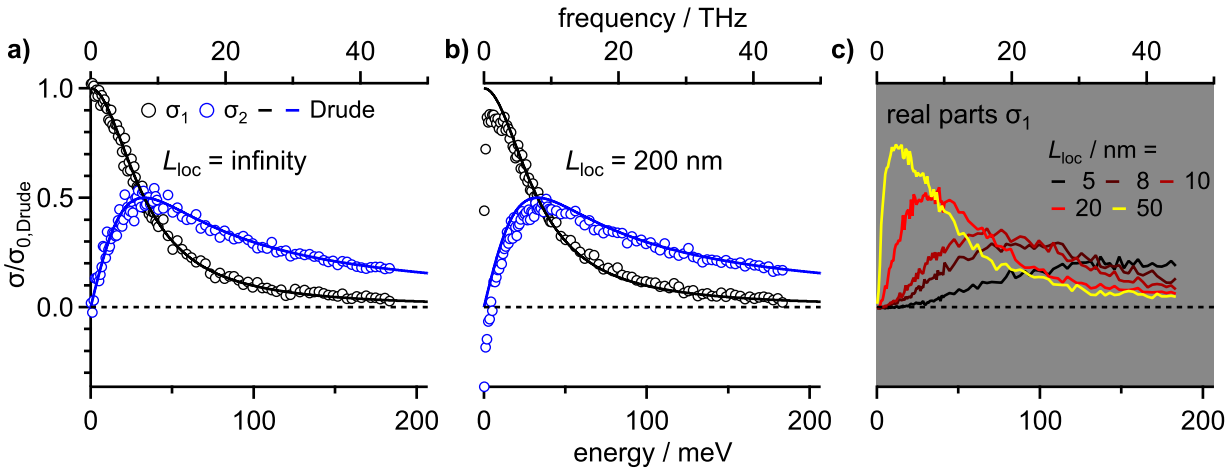

Figure 5.23: Monte Carlo simulation of the optical conductivity for different localization lengths L_{loc}. a) For $L_{\mathrm{loc}} = \infty$ the simulation reveals the expected Drude response whereas b) slight variations occur for $L_{\mathrm{loc}} = 200\,\mathrm{nm}$ at low photon energies. c) Real part of the optical conductivities σ_1 for L_{loc} ranging from 5 nm to 50 nm.

and 50 nm. The peak position shifts to lower energies for larger localization lengths L_{loc}. The energetic peak positions are obtained by fitting a Gaussian profile in the vicinity of the peak maximum. Fig. 5.24a presents the inverse of the energetic peak positions E_{max}^{-1} as a function of the localization length. A linear relationship between both quantities is given by:

$$L_{\mathrm{loc}} = c\, E_{\mathrm{max}}^{-1}, \tag{5.21}$$

where $c = 691\,\mathrm{meV\,nm}$ is a constant. This relationship can be used to correlate experimentally observed peak positions in broadband transmission spectra with the approximate localization lengths experienced by the charge carriers. Fig. 5.24b presents the obtained localization lengths for the spectra shown in Fig. 5.20. As discussed before, the IR peak position decreases for higher charge densities. For a 1 µg/mL $AuCl_3$ concentration, corresponding to $\approx 20\,\%$ exciton bleach, the peak position is at $E_{\mathrm{max}} = 127\,\mathrm{meV}$. However, due to an overlap with the D-band antiresonance, the real peak position of the charge carrier continuum absorption is probably somewhat higher. Therefore, the peak position at 127 meV is taken as a lower bound, and the calculated carrier localization length $L_{\mathrm{loc}} = 5.5\,\mathrm{nm}$ is an upper bound for the low doping limit. This upper bound is consistent with the calculated average localization length $L = 3.3\,\mathrm{nm}$ in chapter 5.2.1 and $L \approx 4\,\mathrm{nm}$ determined by an analysis of the S_1 absorption band in electrochemically doped (6,5)-SWNTs [112]. At higher $AuCl_3$ concentrations the localization length increases.

Within this data set, the last spectrum exhibiting a clear peak was at an $AuCl_3$ concentration of 10 µg/mL ($\chi \approx 70 - 80\,\%$). The IR peak position at 26 meV suggests a localization length of $L_{\mathrm{loc}} = 26\,\mathrm{nm}$. For the highest doping levels ($\chi = 100\,\%$), corresponding to heavily doped SWNTs, no peak could be observed in the limited spectral range $\geq 6\,\mathrm{meV}$. Nevertheless, it can roughly be estimated that the peak position has to be smaller than $\approx 10\,\mathrm{meV}$ to be not

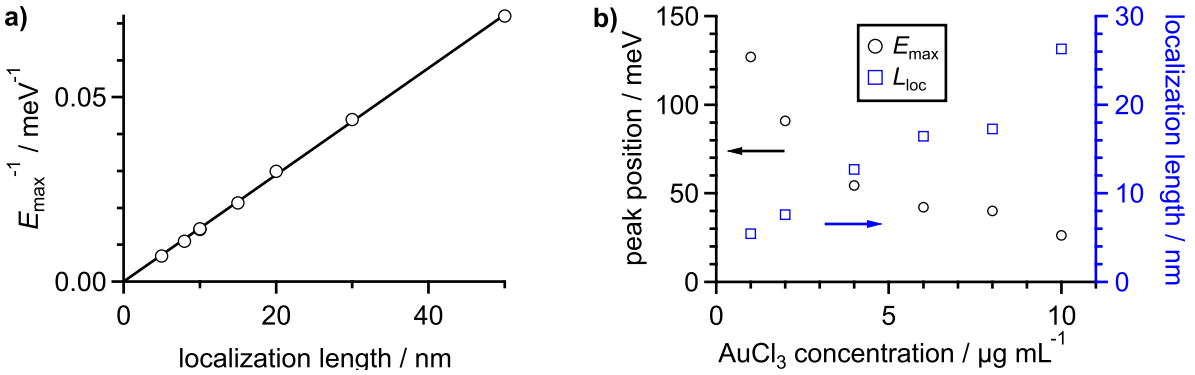

Figure 5.24: a) Inverse peak position of the real parts of the simulated optical conductivity spectra as a function of localization length. b) Experimentally determined IR peak positions and calculated localization lengths using equation (5.21).

observed. From equation (5.21), it follows that charge carriers are delocalized more than 70 nm.

5.5 Metal-Insulator Transition Model

Broadband transmission spectroscopy, transient absorption and PL spectroscopy revealed that surplus charges in redox chemically doped SWNTs tend to localize at low carrier concentrations. At low temperatures $T \ll E_b/k$, at which the charge carrier binding energy E_b strongly exceeds the thermal energy kT, semiconducting SWNTs are therefore expected to behave like poor conductors or insulators. In contrast, charge carriers were found to be delocalized in the heavy doping or degenerate regime. The degenerate doping regime was evidenced by the remarkable agreement between the experimentally determined optical conductivity with the Drude response of free carriers. Hence, heavily doped SWNTs behave more like good conductors with metallic-like properties.

A good model of SWNT doping needs to explain most of the experimental findings in chapter 5.2 to 5.4 as well as the transformation from a low-temperature insulator with localized carriers to a metal-like system. Section 5.2.1 already explained the microscopic mechanism behind charge carrier localization in the dilute limit by Coulomb interaction with counterions adsorbed at the SWNT surface. The spatial extent of charge carrier delocalization was estimated to be on the order of 3 - 4 nm as given by the FWHM of the charge carrier distribution $|\Psi(z)|^2$.

The following qualitative model explains how an increase in oxidant concentration, *i.e.* a higher SWNT hole density, influences the charge carrier properties in terms of localization. Fig. 5.25a shows the 1D density of states (DOS) and a simplified band diagram of intrinsic SWNTs. In the absence of any impurities, the SWNT Fermi level E_F is located close to the middle of the band gap because of the nearly symmetric valence and conduction bands. If an oxidant Ox like $AuCl_3$ or OA is added, the SWNT Fermi level aligns to the Fermi level

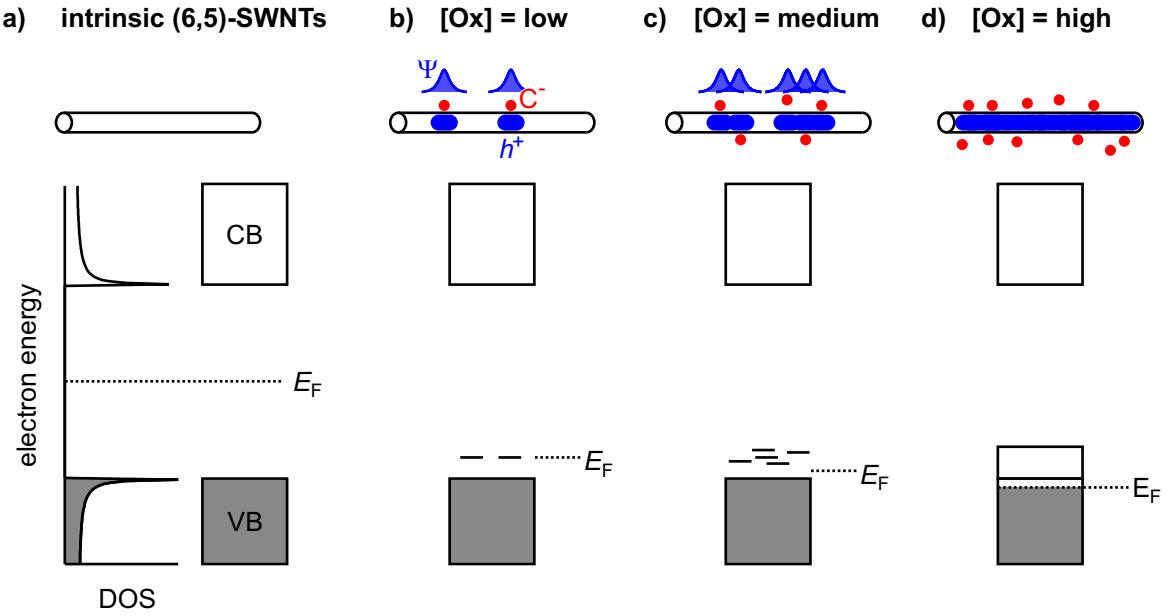

Figure 5.25: a) DOS and simplified band diagram of intrinsic SWNTs. b, c, and d) Schematic influence of the oxidant concentration [Ox] on the SWNT Fermi level E_F, the number of (localized) states in the band gap and on the localization lengths of excess holes h^+ (blue areas). b) At low oxidant concentrations, causing dilute excess charge carriers, the holes are spatially localized by C^- counterion adsorption and do not interact with each other. c) At intermediate oxidant concentrations, charge carrier wavefunctions Ψ start to overlap and localization lengths increase. d) For high oxidant concentrations, a new energy band might be formed and the Fermi level is shifted into this band or the native VB.

$E_{F,redox}$ of the redox couple Red/Ox according to the Gerischer model [53–55]. Addition of Ox decreases the redox couple's Fermi energy $E_{F,redox}$. Consequently, the Fermi level alignment shifts the SWNT Fermi level towards the valence band (VB), which is illustrated in Fig. 5.25b for a low concentration [Ox] of added oxidant and only a few excess charges per SWNT. As described in section 5.2.1, the Coulomb interaction between excess holes on the SWNT and adsorbed counterions localizes the hole with a binding energy $E_b \approx 100 - 250\,meV$. Therefore, localized hole states are split off the VB and are located $\approx E_b$ above the VB edge. If average distances between localized charges are much larger than the extent of the charge carrier wavefunction Ψ no interaction occurs and the states are degenerate. The charge carrier localization lengths are small and on the order of a few nm. The situation changes if the oxidant concentration is further increased and the Fermi level shifts closer to the valence band as depicted in Fig. 5.25c. Distances between localized charges on the order of their spatial wavefunction extent lead to an interaction between charge carriers, which causes the degenerate energy levels to split. Thereby, the localization lengths are increased as indicated by the enlarged spatial charge carrier distribution drawn as blue areas. A further increase in oxidant concentration (Fig. 5.25d) and the resulting enhanced overlap of charge carrier wavefunctions might lead to an energy band comparable to impurity bands found in heavily

doped bulk semiconductors [33, 34, 41, 45, 46]. Furthermore, if the Fermi level is shifted into this newly formed energy band or in the already present valence band, excess charge carriers are better described as delocalized Bloch waves. In this heavy or degenerate doping regime, the SWNTs have metal-like properties.

5.6 Summary

This chapter discussed the modifications of (6,5)-SWNT photophysics upon *p*-doping. The spectroscopic investigations focused on UV to IR absorption and NIR emission changes as well as variations of the ultrafast exciton dynamics following electronic excitation.

Doping-induced changes in the S_1 and S_2 absorption intensities and their energetics dominate the VIS and NIR interband absorption. Both exciton resonances bleach and blueshift upon doping. Moreover, the S_1 absorption band experiences increasing broadening and asymmetry. All spectral changes could be understood in terms of inhomogeneous doping and charge carrier localization induced by adsorbed counterions. The carrier localization leads to axial confinement of exciton wavefunctions and an increase in exciton energy, whereas the inhomogeneous carrier distribution causes the broadening and asymmetry of the absorption band.

Counterions are inevitable companions of electrochemical and redox chemical doping schemes. The poorly screened Coulomb interaction between SWNT excess charges and adsorbed counterions was identified as a probable reason for spatial charge carrier localization. Quantum mechanical model calculations suggest that field-induced carrier localization is characterized by trap depths exceeding 100 meV, which makes localization possible even at room temperature. Additionally, the calculations revealed the spatial extent of the charge carrier distribution on the order of 3 - 4 nm.

SWNT doping also has profound implications on exciton dynamics. The exciton PLQY is drastically reduced by more than four orders of magnitude upon addition of excess charges and is a lot more sensitive than the exciton bleach. For small carrier densities, which is equivalent to a small exciton bleach, the drastic PLQY reduction can be modeled by localized excess charge carriers acting as efficient exciton quenching sites. The exciton decay can then be assumed to be limited by diffusional exciton transport to the quenching centers.

Femtosecond transient absorption spectroscopy provided further evidence for the localized nature of charge carriers in doped SWNTs. A stretched-exponential decay with an exponent of one half well describes the ground state recovery dynamics in intrinsic and weakly doped SWNTs. Such decay behavior is indicative of a diffusion-limited reaction in one dimension and supports the hypothesis of diffusion-limited exciton quenching at localized charges. Pump-energy dependent measurements revealed a different response in the VIS spectral region after selective excitation of the S_1 exciton or X_1^+ trion. The distinct response corroborated that trions are colocalized to charges in charged SWNT regions and excitons are more likely localized to intrinsic SWNT regions.

Infrared transmission spectroscopy provided the most direct evidence of carrier localization. Infrared activation of the dipole-forbidden and defect-induced D-band upon doping suggests that charges become localized and act as perturbations to the band structure similar to spatially localized sp^3-defects. Detailed analysis of the optical conductivity spectra further showed that the charge carrier localization length increases with higher charge densities. This trend was explained by the spatial overlap of localized carrier wavefunctions if distances between charges become comparable to their spatial extent. The tendency of increasing delocalization continues to exist up to the limit of heavy doping with completely bleached S_1 absorption bands. In the heavy doping regime, the optical conductivity matches a Drude free-carrier response, which indicates that the SWNT Fermi level is shifted into the valence band. Heavily doped SWNTs, therefore, behave more like conductors than semiconductors. Charge carriers are then better classified as homogeneously distributed and delocalized over the whole SWNT.

The findings of this chapter suggest that doping of SWNTs is more complex than previously believed. The poorly screened Coulomb interaction in quasi-1D SWNTs facilitates charge carrier localization and hampers the introduction of mobile charge carriers in the moderate doping regime. The model of field-induced localization by counterion adsorption implies that carrier localization might be prevented for larger-diameter SWNTs in environments of high dielectric constant.

6 Heavy or Degenerate doping

In chapter 5 various spectroscopic techniques were applied to moderately doped SWNTs. Spectroscopic properties defined moderate doping as a regime in which the S_1 absorption band has decreased compared to the intrinsic sample but is not fully bleached yet. Charge carriers were found to be spatially localized but experience a continuous transition to larger delocalization for increasing doping levels.

This chapter focuses on heavily doped SWNTs, spectroscopically defined by the absence of many-body (exciton and trion) interband transitions in the absorption spectrum. As briefly discussed at the end of chapter 5, charge carriers in the degenerate or heavy doping regime are considered delocalized over the whole SWNT and can be described as Bloch waves in terms of conventional band structure theory. Since sharp absorption resonances of band gap excitons and trions are absent and PL quantum yields are less than $\approx 10^{-5}$ - 10^{-6}, the literature about optical spectroscopy of heavily doped SWNTs is scarce.

6.1 State of the Art

In the following, a literature overview of the spectroscopy of heavily doped SWNTs is presented. Since chirality-enriched SWNT samples are beneficial to avoid spectral congestion, the review of published results focuses on experiments with samples of a small nanotube diameter distribution.

Zheng and Diner performed the first redox chemical doping experiments on (6,5)-enriched aqueous SWNT dispersions in combination with VIS-NIR absorption spectroscopy [111]. The hole dopant K_2IrCl_6 was used in a redox titration experiment. At high dopant concentrations, the S_1 absorption peak was found to be nearly bleached, and a broad and almost featureless absorption band ranging from ≈ 1.05 to 1.7 eV could be observed.

The characteristics and the microscopic origin of this flat absorption band were not discussed until 2015 when Hartleb *et al.* published their research on electrochemically doped (6,5)-SWNT thin-films [18, 200]. At largely positive working electrode potentials (*p*-doping) the broad and featureless absorption band was again observed and called H-band to indicate that SWNTs are heavily doped. The authors showed, using tight-binding calculations, that even in the presence of band gap renormalization single-particle excitations are a rather unlikely explanation of the H-band absorption. In the single-particle picture, the lowest possible transition energy between the first valence and conduction subbands was calculated to be ≈ 1.6 - 1.7 eV. From the discrepancy of the experiment (≈ 1.06 eV) and the single-particle calculations (≈ 1.6 - 1.7 eV), it was concluded that many-particle interactions and strong elec-

tronic correlations prevail even in the heavy doping regime [18].

Even higher doping levels were obtained by Avery *et al.* [19], Norton-Baker *et al.* [282] and Berger *et al.* [283] using redox chemical doping or ionic liquid gating. The further increase in carrier density leads to a successive bleaching of the H-band. For the highest *p*-doping levels, also the transitions between the second valence and conduction subband can be bleached [19, 282]. This indicates that the Fermi level is shifted within the second valence subband. Nevertheless, a conclusive microscopic picture about the origin of the H-band was not presented and is still missing.

Doping levels beyond the regime of existent H-band absorption can not only suppress existing absorption bands but also new absorption bands can emerge. Using ionic liquid gating in combination with aligned thin-films of small diameter SWNTs, Yanagi *et al.* showed that an absorption band arises due to intersubband plasmons [306]. The authors used polarization-dependent absorption experiments, revealing a perpendicular transition dipole moment of intersubband plasmons relative to the SWNT axis.

6.2 H-band in Linear Absorption Spectroscopy

In the following, the linear absorption of the H-band is reconsidered, and its microscopic origin is discussed. Fig. 6.1 shows three absorption spectra of intrinsic, moderately and heavily doped SWNTs in dispersion using $AuCl_3$ as a hole dopant. For the moderate doping regime, the spectrum with maximized trion absorbance was chosen. The intrinsic S_1 peak absorbance is $A_{S_1} = 0.9$, whereas the maximum trion peak absorbance in moderately doped SWNTs is $A_{X_1^+} = 0.09$, *i.e.* only 10 % of the exciton peak absorbance. The H-band in the heavily doped sample has a nearly constant absorbance $A_H \approx 0.03$, which is 3.3 % of the exciton peak absorbance. At first glance, the H-band absorption seems negligible compared to the S_1 exciton absorbance in intrinsic SWNTs. However, S_1 absorption bands in intrinsic SWNT dispersions prepared by shear force mixing are very narrow, and the H-band absorption is very broad.

Therefore, a better comparison is via oscillator strengths determined by the areas under the absorption bands. Oscillator strengths of the S_1 band in the intrinsic sample and the trion band in the moderately doped sample were obtained by Voigt fits. The Voigt profile describes the resonances considerably better than pure Gaussian or Lorentzian profiles due to both, inhomogeneous and homogeneous broadening. In the case of the H-band, the absorption spectrum was integrated between 1.00 eV and 1.95 eV. The ratio of trion oscillator strength $f_{X_1^+}$ and intrinsic S_1 oscillator strength f_{S_1} is $f_{X_1^+}/f_{S_1} = 15\,\%$. For the H-band, a value of $f_H/f_{S_1} = 77\,\%$ was obtained, highlighting that the H-band oscillator strength is not negligible but indeed very high.

Since the H-band absorption is almost constant in a broad spectral region, the absorption can be compared to the universal absorption $\theta \approx 2.3\,\%$ of a single graphene sheet [209]. The

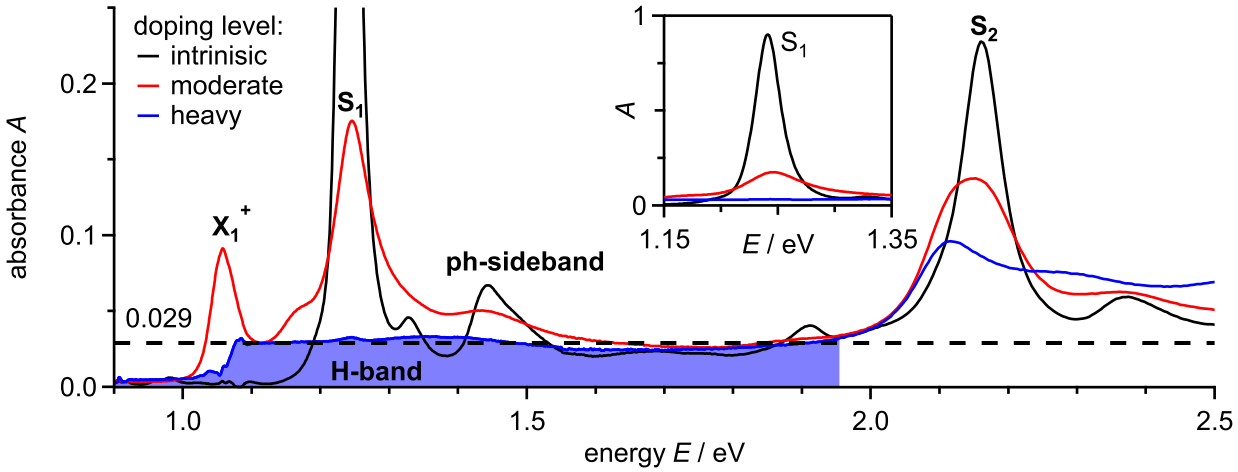

Figure 6.1: Absorption spectra of intrinsic, moderately and heavily doped SWNTs in dispersion. $AuCl_3$ was used for doping with concentrations of 0.0 µg/mL (intrinsic), 7.6 µg/mL (moderately doped) and 54 µg/mL (heavily doped). The inset shows the spectral region around the S_1 exciton up to an absorbance of one.

absorption cross-section σ of a single graphene layer is given by the Beer-Lambert law [307]:

$$-\ln(1-\theta) = \sigma N d \tag{6.1}$$

where N is the volumetric density of carbon atoms and d is the thickness of a graphene monolayer. The product $N \times d \approx 3.85 \times 10^{15}\,\mathrm{cm}^{-2}$ can be calculated using the hexagonal unit cell area $0.052\,\mathrm{nm}^2$, which contains two carbon atoms. Hence, a value $\sigma_{\mathrm{gr}} = 6.0 \times 10^{-18}\,\mathrm{cm}^2$ per carbon atom results for the absorption cross-section of graphene.

The absorption cross-section of the H-band is estimated by comparison with the absorption cross-section σ_{S_2} at the peak of the S_2 absorption band in intrinsic samples. The absorption cross-section at the peak of the S_2 exciton is itself revealed by comparison with the S_1 and S_2 peak absorbances in the publication of Schöppler *et al.* with $A_{S_1}/A_{S_2} \approx 3$. By using the reported absorption cross-section at the S_1 exciton peak maximum of $\sigma_{S_1} = 1.7 \times 10^{-17}$ per carbon atom, the absorption cross-section at the S_2 peak is determined to be roughly the same as for graphene [307].

The absorption cross-section of the H-band relative to graphene can then be estimated as the ratio of constant H-band absorbance $A_{\mathrm{H}} \approx 0.03$ to S_2 peak absorbance $A_{S_2} = 0.20$ in the intrinsic SWNT sample as obtained by Lorentzian peak fitting:

$$\frac{\sigma_{\mathrm{H}}}{\sigma_{\mathrm{gr}}} \approx \frac{A_{\mathrm{H}}}{A_{S_2}} = 15\,\%. \tag{6.2}$$

The relative absorption cross-section of 15 % is a factor of two smaller than estimated by Hartleb *et al.*, who reported $\sigma_{\mathrm{H}}/\sigma_{\mathrm{gr}} = 30\,\%$ through comparison of the H-band absorbance with the S_1 peak absorbance in electrochemically doped samples [18]. It should be stressed

here that a comparison with reported absorption cross-sections of the S_1 resonance is less accurate than with the S_2 resonance. S_1 absorption bands are mainly inhomogeneously broadened and the linewidth strongly depends on sample type [96, 164]. S_2 absorption bands, on the other hand, are largely homogeneously broadened [95] and do not differ as much between different sample types.

So far, only the intensity of the H-band plateau was regarded. A closer look on the H-band energetics should provide additional information. The exact onset-energy of the H-band absorption on the higher energy side can not be determined from the absorption spectrum due to overlap with absorption bands related to second subband transitions. However, the 1.07 eV onset-energy in the NIR, here defined as the energy at which absorbance has increased to half of the constant H-band value, is easily extracted. The H-band onset-energy is almost isoenergetic to the trion energy of 1.06 eV.

Another interesting fact is that the H-band seems to merge right into the background absorption of the intrinsic sample. Vialla *et al.* studied this background absorption and termed it 'nonresonant background' [308]. Similar to the microscopic H-band origin, the origin of the nonresonant background in intrinsic SWNT samples has not been sufficiently clarified so far. However, Vialla *et al.* argued that the nonresonant background absorption most likely corresponds to free-carrier interband transitions [308].

6.3 Nonlinear Optical Response

Doping of (6,5)-SWNTs was found to have a profound influence on the many-body states in linear absorption spectroscopy. In this part of the thesis, nonlinear transient absorption (TA) spectroscopy is used to gain insight into the temporal and spectral response of intrinsic and doped carbon nanotubes after excitation with femtosecond laser pulses.

Doping level dependence

Fig. 6.2a shows a series of TA spectra at 0.1 ps pump-probe delay for an electrochemically *p*-doped (6,5)-SWNT thin-film using 2.16 eV pump pulses. The pump pulses were resonant with the S_2 exciton absorption and had a probed photon fluence of $3.5 \times 10^{12}\,\mathrm{cm}^{-2}$ per pulse. The chosen excitation fluence largely excludes saturation effects but signal intensities are still high enough for a sufficient signal to noise ratio, especially for heavily doped SWNTs. The solid lines in Fig. 6.2a are normalized TA spectra whereas the black dashed lines correspond to the real signal amplitudes. The spectrum of the intrinsic sample (WE potential $U_{\mathrm{WE}} = -0.20\,\mathrm{V}$ vs. Pt) consists of a strong photobleach (PB), and a weaker blueshifted photoabsorption (PA) signal. The doping-induced PB changes follow the same trend as for the S_1 absorption band in linear spectroscopy, *i.e.* a reduction, blueshift, broadening and an increasing asymmetry of the PB signal.

Fig. 6.2b compares the PB intensity changes to the steady-state absorbance changes of electro-

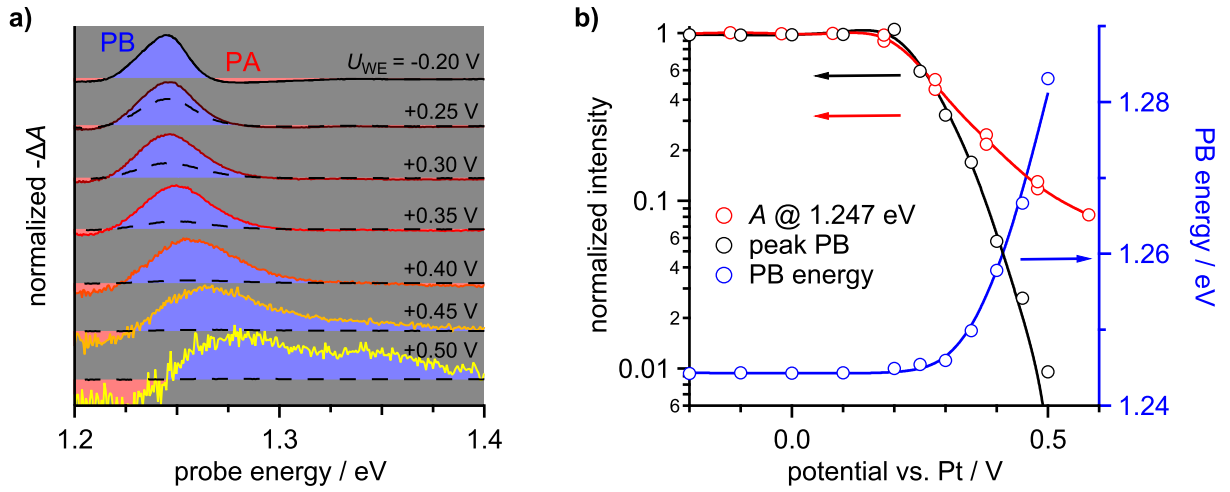

Figure 6.2: a) Normalized (solid lines) and non-normalized (dashed lines) TA spectra at 0.1 ps pump-probe delay in dependence of the applied working electrode potential U_{WE}. b) Dependence of steady-state absorbance A, peak PB, and PB energy on the applied WE potential. The solid lines are guides to the eye. For WE potentials exceeding 0.3 V, the PB shifts to higher energies and relative intensities of PB and absorbance start to differ.

chemically doped (6,5)-SWNT thin-films. Absorbance data were taken from Hartleb *et al.* [18] and horizontally shifted on the WE potential axis to match the signal drop-off at low doping levels. The absorbance was evaluated at 1.247 eV, which is the energetic position associated with the peak absorbance in the intrinsic sample. The PB signal reduction is qualitatively comparable to the absorbance reduction up to a potential of ≈ 0.3 V at which signal intensities are reduced to roughly 50 %. For higher WE potentials (higher hole densities), the PB signal amplitude and steady-state absorbance strongly deviate, which can be explained by two effects. First, for working electrode potentials > 0.3 V, the PB signal begins to blueshift and broaden significantly. Increased overlap with the photoabsorption (PA) signal reduces the peak PB intensity more strongly than the steady-state S_1 absorbance. Second, the absorbance at 1.247 eV contains an increasing amount of H-band absorption for increasing doping levels. In order to illustrate the changes in linear and nonlinear spectroscopy more clearly, Fig. 6.3a and b compare the steady-state and transient absorption spectra for the highest working electrode potentials.

The absorbance is found to be reduced by roughly 90 % of its intrinsic peak value, whereas the peak PB signal is decreased by 99 %. Interestingly, although the H-band is dominant in linear spectroscopy of heavily doped SWNTs, the nonlinear signal is exclusively composed of the small residual S_1 exciton contribution. No PB signal of the H-band could be observed in the limited silicon detector range > 1.13 eV. The fact that the H-band is indeed TA silent was confirmed using other samples and varying the probed pump pulse fluence up to 1.4×10^{14} cm^{-2}, which is a factor of 40 higher than in the experiment presented here. Moreover, pump energies were tuned to resonant H-band excitation at 1.77 eV to exclude a dependence on pump

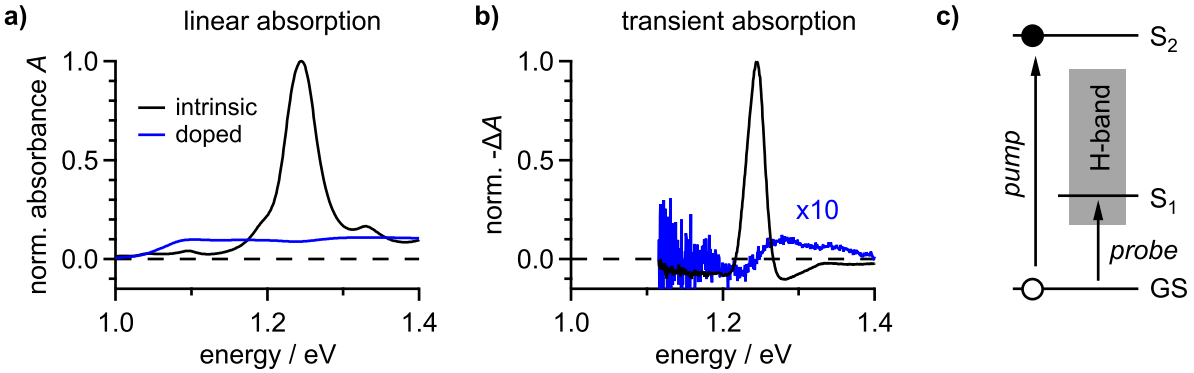

Figure 6.3: a) Steady-state and b) transient absorption spectra of intrinsic and heavily doped SWNTs. c) Illustration of the pump-probe scheme with resonant S_2 excitation and probing the NIR spectral region around the S_1 exciton and parts of the H-band. In a molecular picture, the ground state depletion gives rise to a ground state bleach proportional to the linear absorption spectrum.

energy, but still, no nonlinear H-band signal in the NIR was observed.

From a simple molecular point of view, illustrated in Fig. 6.3c, the absence of an H-band PB signal in transient absorption is surprising. Electronic excitation reduces the SWNT ground state population and consequently a ground state bleach signal proportional to steady-state absorbance should be observed [267]. However, for multi-chromophoric molecules or extended solid-state systems like SWNTs, which can support more than one electronic excitation, the situation is more complicated.

The presence of already created electronic excitation, for example excitons, alters the linear absorption spectrum due to the interaction between excitons beyond simple ground state bleach, excited state absorption, or stimulated emission bands discussed for monochromophoric molecules. The complex linear susceptibility χ of the exciton is given by [92]:

$$\chi = \frac{f_0}{E - E_0 + i\Gamma_0}, \tag{6.3}$$

where f_0, E_0 and Γ_0 are the oscillator strength, energy and width of the resonance. A nonlinear optical response arises if the optical excitation alters at least one of these three quantities.

6.3.1 Intrinsic SWNTs

For intrinsic SWNTs and other low-dimensional excitonic semiconductors, the nonlinear optical response has been described by three excitation density dependent modifications of the exciton absorption bands resulting from many-body effects [92, 93, 244]:

- oscillator strength reduction (OSR) $\Delta f/f_0$ due to phase space filling
- energy shifts $\Delta E/E_0$
- broadening $\Delta\Gamma/\Gamma_0$ due to exciton-exciton scattering.

Langlois *et al.* showed – using intrinsic SWNTs in aqueous dispersion – that all three modifications of the exciton bands are linear in S_1 exciton density N upon resonant S_1 excitation [244]. Furthermore, they found that the nonlinear optical response of the S_2 exciton is almost exclusively caused by the energetic blueshift and broadening of the resonance. In order to understand the nonlinear optical response of heavily doped SWNTs better, a solid understanding of the nonlinear optical response of intrinsic SWNTs is inevitable.

The results of an analogous pump-probe experiment as performed by Langlois *et al.* are presented and discussed in the following. In contrast to Langlois *et al.*, an organic SWNT dispersion in a 2 mm path length cuvette was used. Moreover, much lower excitation densities were used in this work with probed pump pulse fluences below $1 \times 10^{13}\,\mathrm{cm}^{-2}$. The bandwidth (FWHM) of the 1.24 eV excitation pulses was 30 meV, which is very close to the FWHM of the inhomogeneously broadened S_1 absorption band. Therefore, dominant contributions from spectral hole burning to the TA spectrum can be excluded.

Fig. 6.4a and b present the linear absorption spectrum in the NIR and VIS spectral region together with transient absorption spectra for a pump-probe delay of 0.2 ps. Note that the spectra were multiplied by different factors for better visibility and easier comparison of relative intensities. Fig. 6.4c and d show the corresponding transient absorption maps in the NIR and VIS spectral regions. Contributions close to the S_1 and S_2 resonance dominate the TA signals but the overall signal intensities in the VIS are much smaller, as indicated by the multiplication factor of 40. For better quantification, the OSR $\Delta f/f_0$ is calculated by integration over the steady-state and transient absorption spectra:

$$f_0 \propto \int_{E_1}^{E_2} A(E)\,\mathrm{d}E \tag{6.4}$$

$$\Delta f(\tau) \propto \int_{E_1}^{E_2} \Delta A(E,\tau)\,\mathrm{d}E. \tag{6.5}$$

In the NIR spectral region, the integration limits $E_1 = 1.18\,\mathrm{eV}$ and $E_2 = 1.35\,\mathrm{eV}$ were chosen. Beyond these limits, S_1 absorbance and transient absorption signals were found to be negligible. For the VIS region the integration limits are $E_1 = 1.95\,\mathrm{eV}$ and $E_2 = 2.55\,\mathrm{eV}$ for similar reasons.

A simple integration over the steady-state absorption spectrum in the VIS, measured in transmission mode, can lead to significant errors if no background correction is performed. In order to separate SWNT absorption signals from other contributions like reflection or scattering, a PLE spectrum of the same SWNT dispersion diluted by a factor of 20 was recorded. Fig. 6.4e shows the PLE spectrum at 1.236 eV emission energy together with the steady-state absorption and TA spectrum. A PLE spectrum mirrors the absorption (not absorbance) if the photoluminescence quantum yield is independent of the excitation energy (Kasha-Vavilov rule [309]). That this is the case for SWNTs has been confirmed by Vialla *et al.*, who used pump-energy dependent transient absorption spectroscopy and found, independent of excitation energy, an extremely fast and efficient relaxation to the emissive S_1

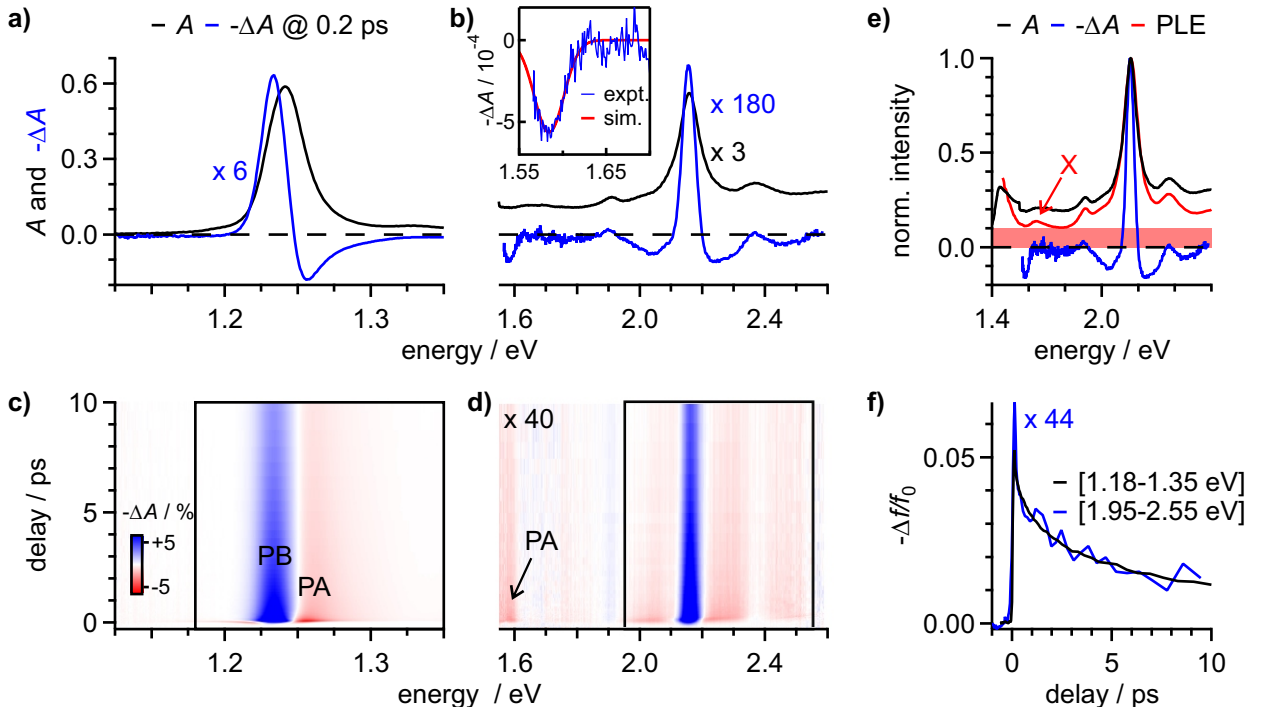

Figure 6.4: a) Linear absorption and transient absorption at 0.2 ps pump-probe delay in the NIR and b) VIS spectral regions. The inset shows an enlarged view on the weak PA feature at 1.59 eV and a simulation taking into account a BGR $\Delta E_g = -1.1$ meV. c) and d) Corresponding TA maps. Note the multiplication factor 40 in the VIS region. The black boxes indicate the spectral regions used for the analysis of pump-induced OSR. e) Comparison of steady-state absorption with TA and PLE. The red shaded area highlights the nonresonant background absorption, and the X marks a peak most likely associated with free-carrier transitions. f) Oscillator strength reduction $-\Delta f/f_0$ in the NIR and VIS spectral region.

state [308].

The linear absorption spectrum has a higher background signal than the PLE spectrum. For the evaluation of f_0, a constant offset was subtracted from the steady-state absorption spectrum such that the shape of the absorption spectrum matched the PLE spectrum. Here, it was used that absorption α as measured by PLE and absorbance $A = -\log(1-\alpha)$ are approximately proportional for the small regarded absorbances. Fig. 6.4f shows the oscillator strength reduction $\Delta f/f_0$ in the NIR and VIS as a function of pump-probe delay. The presence of S_1 excitons leads to a strong OSR in the NIR of 5 % at early delay times and a subsequent signal decay because of S_1 exciton deactivation. In the VIS spectral region, $\Delta f/f_0$ is much smaller, but the NIR decay can be matched by multiplying the signal intensity by a factor 44. Small discrepancies in the NIR and VIS at early delay times result most likely from a short-lived transient S_2 population due to S_1 exciton-exciton annihilation [244].

The molecular picture predicts a factor of four between the NIR and VIS OSR signal intensities. A factor of two arises because an S_1 population causes a bleach in the NIR not only due to ground state depletion but also due to an occupation of the final S_1 state [267]. Stimulated

emission, which has the same sign as the ground state bleach, doubles the signal finally a second time [90, 310].

The experimentally determined factor $\frac{\Delta f/f_0^{\mathrm{NIR}}}{\Delta f/f_0^{\mathrm{VIS}}} = 44$ is an order of magnitude larger than expected from the molecular picture. The absence of a sizable $\Delta f/f_0$ contribution for the S_2 exciton in the VIS can be understood in terms of phase space filling (PSF). A transient S_1 population reduces the available electron and hole states in the first valence and conduction subbands v_1, c_1. Since the S_2 exciton wavefunction is composed of electron and hole states of the second valence and conduction subbands v_2, c_2, the S_2 oscillator strength is not affected by the S_1 population. This finding is in good agreement with the experiments by Langlois *et al.* [244]. A similar effect was observed in chapter 5.2, where a doping-induced (instead of pump-induced) depletion of the first valence subband v_1 caused an OSR of the first subband related interband transitions $v_1 \rightarrow c_1$ but not for $v_2 \rightarrow c_2$ transitions.

Interestingly, the nonresonant background in the VIS, as marked by the red area under the PLE spectrum in Fig. 6.4e, is completely TA-silent. This is analogous to the H-band in heavily doped SWNTs which seems to merge into the nonresonant background absorption. The fact that both featureless absorption bands are TA silent makes a common origin very likely. The absence of a nonlinear H-band signal in heavily doped SWNTs and the nonresonant background in intrinsic SWNTs could have two reasons:

- both are not affected by phase space filling or
- their nonlinear optical response is orders of magnitude smaller than for S_1 excitons.

Vialla *et al.* described that the nonresonant background in intrinsic SWNTs results most likely from absorption into the free-carrier continuum [308], whereas Kimoto *et al.* showed that the small peak marked with an X in the PLE spectrum (Fig. 6.4e) can be roughly associated with the continuum absorption onset energy [223]. It can be speculated that the asymmetric X peak is a small remnant of the Van Hove singularity in the joint density of states of a 1D system or results from higher-lying exciton Rydberg states.

The TA spectra show a weak PA signal just below the X peak, which is tentatively interpreted as the result of a small but measurable band gap renormalization (BGR) caused by the optical generation of S_1 excitons. Fig. 6.4b shows a simulation of the PA signal based on the hypothesis of photo-induced BGR. For the simulation, the continuum absorption onset energy was set to $\approx 1.59\,\mathrm{eV}$, and a Gaussian broadening of 40 meV was applied to the rectangular continuum absorption band [68]. The constant continuum absorbance $A = 0.02$ was estimated from a comparison of the PLE and linear absorption spectrum. Within this theoretical framework, the intensity of the PA signal is mainly determined by the pump-induced amount of BGR. Good agreement of the simulation with the TA spectrum at 0.2 ps was obtained for a small BGR $\Delta E_{\mathrm{g}} \approx -1.1\,\mathrm{meV}$.

At first glance, a BGR caused by neutral excitons seems unlikely. Typically, BGR is associated with screening by charged particles like free-carriers. However, the large S_1 exciton size $\xi = 13\,\mathrm{nm}$ [90] gives rise to a non-negligible average spatial separation of electron and hole

$d_{e\text{-}h} = \xi/\sqrt{\pi} = 7\,\mathrm{nm}$. Therefore, a very small BGR on the order of $\Delta E_g = -1\,\mathrm{meV}$ seems not impossible for the estimated exciton density N on the order of $N = 0.01\,\mathrm{nm}^{-1}$.

6.3.2 Heavily Doped SWNTs

If the interpretation of a BGR related PA signal is correct, and the nonresonant background and H-band possess a common origin, a PA band close to the H-band onset-energy is expected in heavily doped and excited SWNT samples. The H-band onset-energy is below the detection range of the silicon camera ($E_{\min} \approx 1.13\,\mathrm{eV}$) in the pump-probe setup in Würzburg. Therefore, four samples containing (6,5)-SWNTs embedded in a PFO-BPy polymer matrix were prepared, doped by immersion in an $AuCl_3$ solution and sent to the collaboration partner Larry Lüer in Madrid. Fig. 6.5a shows the absorption spectra of the as-prepared intrinsic films. Based on the absorption spectra, the films were almost identical. However, slight variations in S_1 absorbance on the order of 20 % arise, which are most pronounced for the sample with the orange spectrum. Fig. 6.5b and c present absorption and PL spectra of the films after the doping procedure. The sample with the highest doping level ($c_{AuCl_3} = 50\,\mu\mathrm{g/mL}$) shows almost no S_1 absorption in the NIR and is mainly characterized by the H-band absorption. Fig. 6.5d - g show the corresponding TA maps. Excitation pulses at 2.16 eV were resonant with the S_2 transition, and no pump intensity dependence of the dynamics was observed. The transient absorption spectrum of the intrinsic sample (Fig. 6.5d) shows a strong PB signal close to the S_1 exciton energy and weak PA bands at lower and higher energies. The situation changes slightly for the samples moderately doped with 7.5 and 15 µg/mL $AuCl_3$. The main difference is the appearance of a PB signal corresponding to the X_1^+ trion, which is, however, still weak compared to the S_1 PB signal. For the heavily doped sample ($c_{AuCl_3} = 50\,\mu\mathrm{g/mL}$, Fig. 6.5g), the TA map exhibits a PA feature at $\approx 1.04\,\mathrm{eV}$ with a signal intensity comparable to the residual S_1 PB.

A possible correspondence between the H-band onset and the PA feature in heavily doped samples is further discussed using Fig. 6.6. The absorption spectrum of the heavily doped SWNT film is presented in Fig. 6.6a. The shape of the H-band and especially the onset were modeled by a broadened rectangular absorption band (grey shaded area) of constant absorbance $A = 41.5/10^{-3}$ and an onset-energy $E_{\mathrm{onset}} = 1.042\,\mathrm{eV}$. Broadening was included by convolution of the rectangular absorption band with a Gaussian profile (FWHM = 45 meV).

Fig. 6.6b and c show selected TA spectra and the corresponding TA map. After a delay time of $\approx 1 - 2\,\mathrm{ps}$, the H-band absorption onset-energy matches well the energetic position of the PA band observed in the TA map. At earlier delay times, the PA band position seemingly shifts to higher energies and is strongly distorted by spectral overlap with the X_1^+ trion PB band. The decay dynamics at 1.04 eV and at the S_1 PB band (1.25 eV) strongly disagree for delay times less than 1 ps due to this overlap effect but are in good agreement after 1 ps (see Fig. 6.6f).

Next, the optical nonlinear response of the H-band, *i.e.* the PA band at the onset-energy

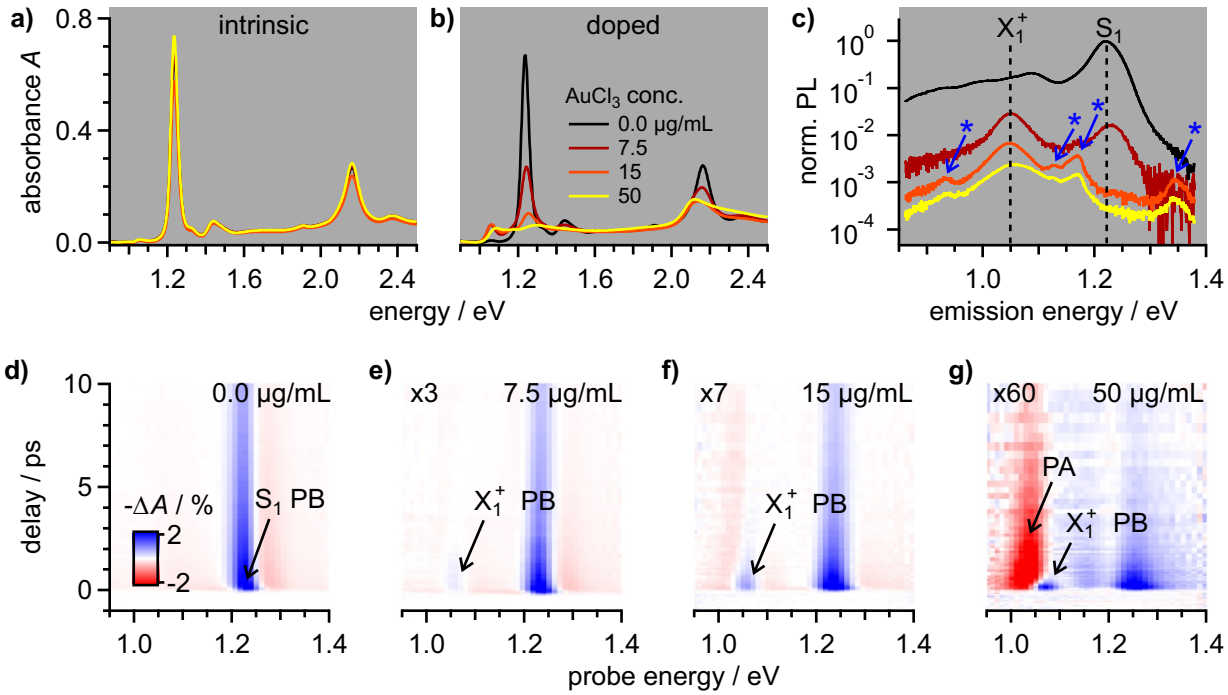

Figure 6.5: a) Absorption spectra of (6,5)-SWNTs embedded in a PFO-BPy matrix before and b) after doping. c) PL spectra of the doped samples obtained by excitation at 2.17 eV. The blue asterisks mark signals due to weak fluorescence of the glass substrate. TA maps of the samples doped by immersion in an $AuCl_3$ solution of d) 0.0 µg/mL, e) 7.5 µg/mL, f) 15 µg/mL and g) 50 µg/mL. Note that the maps in e) - g) are scaled by different factors for easier comparison.

and no TA signal elsewhere, is tried to be qualitatively understood. For this purpose, the exciton and continuum absorption optical nonlinearities are discussed on the same footing. As outlined above, exciton nonlinearities arise from OSR, an energetic shift or broadening of the exciton absorption band. For a weak, nearly 1 eV broad and practically constant continuum absorption band, the effects of a small broadening $\Delta\Gamma$ are negligible everywhere except the absorption band edges. An energy-independent OSR results in a weak and constant PB signal, whereas energetic shifts ΔE produce PB/PA bands at the onset-energies and no TA signal in between. In the following, broadening and OSR effects are neglected, and only energetic shifts are regarded.

Fig. 6.6d illustrates the effect of an energy shift on the H-band absorption. If the pump pulses are blocked by the chopper (pump off), the absorption spectrum of the H-band equals the linear absorption spectrum (black line). The absorption of pump photons (pump on) might cause an energetic redshift, here illustrated for a very strong shift of $\Delta E = -20$ meV. A TA spectrum is the difference spectrum $\Delta A = A_{\text{on}} - A_{\text{off}}$. Fig. 6.6e shows the experimental TA spectrum at a delay of 1.9 ps and a simulated TA spectrum by taking into account an energetic shift of the H-band. The shape and height of the H-band for the 'pump off' situation was already independently modeled using the linear absorption spectrum with $E_{\text{onset}} = 1.042$ eV and an absorbance $A = 41.5/10^{-3}$. Therefore, the only free parameter for the simulation is

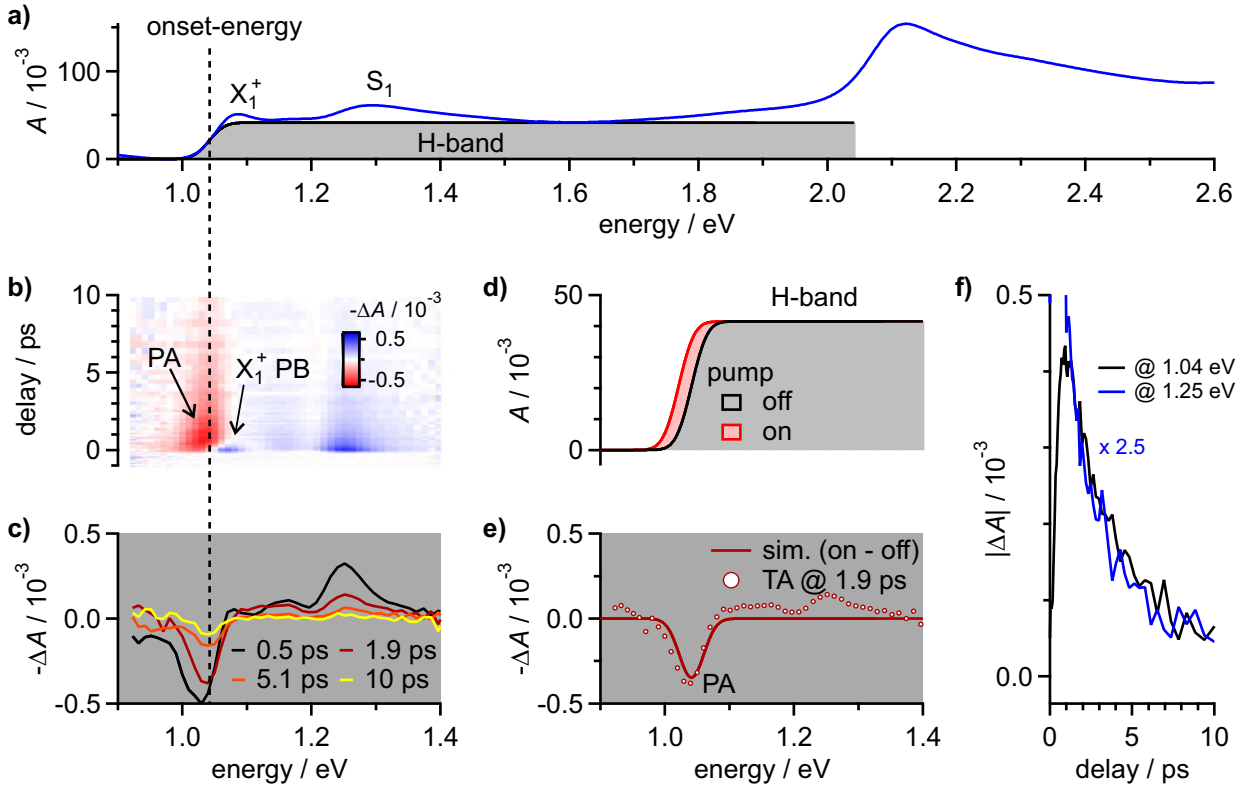

Figure 6.6: a) Steady-state absorption spectrum, b) TA map and c) TA spectra of a heavily doped SWNT film. d) Illustration of a pump-induced energetic redshift $\Delta E = -20\,\text{meV}$ of the H-band. e) Experimental TA spectrum at a pump-probe delay of 1.9 ps and simulated PA band for $\Delta E = -0.5\,\text{meV}$. f) Decay dynamics at the PA band (1.04 eV) and at the S_1 PB signal (1.25 eV).

ΔE, which mainly determines the signal intensity. Here, a reasonable agreement between experiment and simulation is obtained for $\Delta E = -0.5\,\text{meV}$.

Microscopically, the energy shift ΔE could again – like in the case of intrinsic SWNTs – be interpreted in terms of BGR, as long as the H-band absorption belongs to free-carrier intraband transitions. In this case, ΔE equals the amount of BGR ΔE_g.

The observation that tentatively assigned free-carrier transitions show much weaker nonlinear optical signals compared to excitonic transitions is not limited to SWNTs. Scheidt *et al.* reported a transient absorption study on $CsPbBr_3$ perovskite films, which show a similar nonlinear optical response [311]. Although the steady-state absorbance of the weakly bound exciton and the free-carrier continuum are comparable in the perovskite films, the TA spectrum seems fully dominated by the nonlinear optical response of the exciton.

6.4 Discussion of the Microscopic Origin of the H-band

Fig. 6.7 shows a comparison of linear absorption spectra of heavily doped SWNTs and other low-dimensional semiconductors doped to the extent that exciton and trion bands seem to have vanished. Like in chapter 5, the (6,5)-SWNTs are compared to a 10 nm thick CdTe

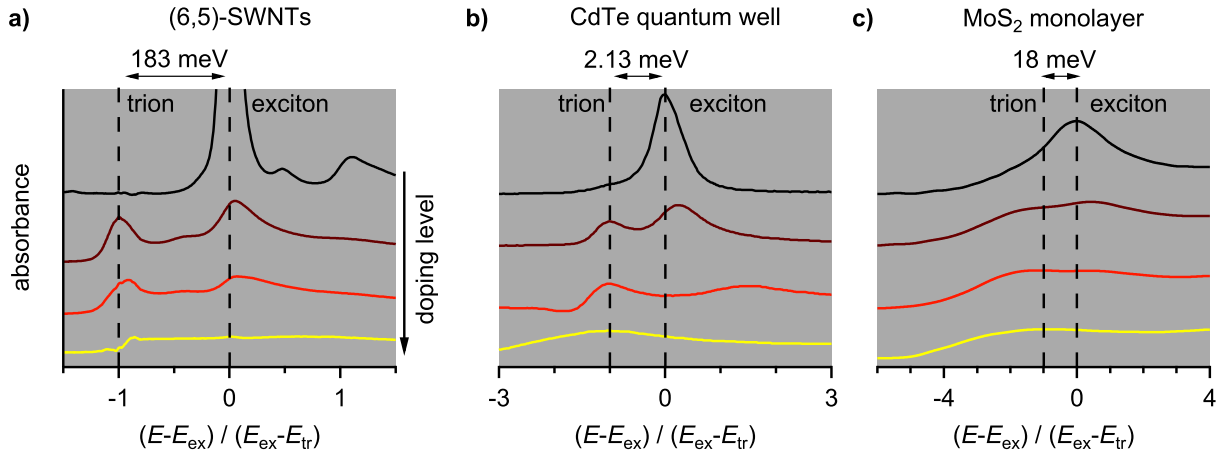

Figure 6.7: Comparison of absorption spectra of a) (6,5)-SWNTs with b) a 10 nm thick CdTe quantum well [22] and c) a MoS_2 monolayer [21] at different doping levels. Upon doping, qualitatively similar trends occur with broad absorption bands in the case of heavy doping (yellow spectra). Note that trion energies are given in the limit of low doping levels. Especially for the MoS_2 monolayer, the trion energy seems to considerably redshift upon doping.

quantum well structure and a TMD monolayer material (MoS_2) on a relative energy scale. The absorption spectra of all three materials with the highest doping levels (yellow spectra) are rather broad and show only little structure. The similarity indicates that flat absorption bands are a more general feature of heavily doped degenerate semiconductors and are not limited to (6,5)-SWNT samples.

At first glance, this is not surprising since theory predicts that the free-carrier continuum absorption in 1D, 2D and 3D is almost constant with an onset-energy given by the single-particle band gap [68, 312, 313]. So, it seems obvious to interpret the spectra of these degenerate semiconductors in terms of doping-induced screening effects reducing the exciton binding energy to values less than the thermal energy. In this case, the exciton oscillator strength becomes negligible, and only the free-carrier continuum absorption with its energetic onset close to the exciton energy is observed. Gao *et al.* theoretically predicted such a behavior for doped MoS_2 monolayers [314].

However, this interpretation seems to be too simple for (6,5)-SWNTs, but also for the 2D materials. The disagreement between theory and experiment is evident because the energetic onset of the broad and featureless absorption band in the heavy doping regime does not at all match the exciton energy. For all three materials, the exciton energy is blueshifting upon doping, but the onset-energy of the featureless absorption band is even clearly below the exciton energy in the intrinsic samples. The discrepancy might be resolved if the blueshift of the exciton resonance is mainly caused by confinement effects as discussed in section 5.2.1.

For nanotubes, the H-band onset-energy is rather well described by the trion energy although it is about 5 - 10 meV higher than the trion energy in the low doping limit. Nevertheless, since the trion energy moderately blueshift towards the H-band onset-energy for high doping levels,

it is reasonable to ascribe the H-band onset-energy to the trion energy in the high doping limit.

Linear absorption spectroscopy showed that the H-band in heavily doped SWNTs merges into a broad absorption band already existing in intrinsic SWNTs, which was termed 'nonresonant background' [308]. This was taken as evidence that both absorption bands share a common origin.

Nonlinear spectroscopy revealed that the nonresonant background in intrinsic SWNTs and the H-band are both TA-silent. This means that their nonlinear optical response has to be orders of magnitude weaker than the S_1 exciton response. An exception to this rule was observed at the H-band onset-energy and possibly also at the onset-energy of the nonresonant background, where photoabsorption occurs. Despite some discrepancies outlined above, the most plausible microscopic origin of both the H-band and the nonresonant background absorption are free-carrier interband transitions across the band gap.

Next, the implications of this hypothesis are elucidated. For this, it needs to be reconsidered how the excitonic and free-carrier wavefunctions are related. The S_1 exciton wavefunction can be described as a coherent superposition of single-particle electron and hole states with the largest amplitudes for states with momentum $k_{e/h}$ close to zero (see chapter 7.2 for details). Single-particle transitions at $k = 0$ are associated with the band gap in intrinsic SWNTs. Therefore, the generation of S_1 excitons in a pump-probe experiment is expected to produce a PB signal at the band gap energy due to phase space filling. Similarly, in the case of heavily doped SWNTs, fast relaxation to the bottom of the H-band would also be expected to produce a PB signal at the H-band onset. Experimentally, no such PB bands were observed. Therefore, PSF effects on the H-band and on the nonresonant background seem to be very small. In contrast, PA bands were found at the H-band onset-energy and probably also at the onset-energy of the nonresonant background absorption. An energetic redshift represents a simple deformation of the flat linear absorption bands causing only a PA band at its onset-energy. Microscopically, a small pump-induced BGR explains the redshift and strengthens the hypothesis of a free-carrier continuum absorption as the microscopic origin of both the H-band in heavily doped SWNTs and the nonresonant background in intrinsic SWNTs.

Nevertheless, in order to confirm this hypothesis and elucidate the exact microscopic origin of the H-band, further theoretical and experimental investigations are necessary. Recent theoretical investigations seriously question the existence of a three-particle trion [153, 157]. Instead, the doping-induced low energy absorption is interpreted as the optical generation of an attractive exciton-polaron, *i.e.* an exciton dressed by the excess carriers of the Fermi sea [154–158]. Further theoretical investigations into this direction might explain why H-band onset energy and trion energy are identical for semiconducting SWNTs.

6.5 Interaction of Degenerately Doped SWNTs with IR Radiation

Section 5.4 showed that the mid and far infrared absorption of heavily doped SWNTs – in contrast to moderately doped SWNTs – can be well understood by the intraband absorption of free carriers. This was demonstrated by the excellent agreement of the experimentally obtained optical conductivity with the Drude free-carrier response. In the following, the results of the Drude analysis are discussed more quantitatively.

6.5.1 Extended Drude Analysis

One goal of this thesis is to determine charge carrier densities by optical spectroscopy. For conventional bulk semiconductors, carrier densities are typically obtained by electrical methods. A simple DC conductivity measurement provides the product of charge density n and mobility μ:

$$\sigma = n\,\mu\,e, \tag{6.6}$$

where e is the elementary charge. The separate determination of the mobility, for example by a Hall measurement, allows extracting the carrier density n. For SWNTs in dispersion, this procedure is obviously not possible. However, also the mobility determination using SWNT thin-films has some pitfalls due to the percolated SWNT network morphology. Therefore, the results of Hall measurements are at least questionable [315]. Even if mobilities are determined in field-effect transistors (FET), they are often limited by intertube charge transfer acting as a bottleneck to the measured charge transport [316].

Thus, the determination of charge densities and mobilities using alternating current frequencies, at which intertube charge transport can be neglected, is highly desirable. In turn, this should allow studying the intratube charge transport properties of doped nanotubes even in film samples. Fig. 6.8a shows the optical conductivity spectrum and Drude fit of a highly doped SWNT film in the IR region (see chapter 5.4 for details). At the top axis, angular frequencies are plotted to simplify conversion into the time domain. The DC conductivity σ_0 and the scattering time τ are adjustable parameters of the Drude fit:

$$\sigma(\omega) = \frac{\sigma_0}{1 - i\omega\tau} = n\,\mu(\omega)\,e. \tag{6.7}$$

Equation (6.7) is equivalent to equation (6.6) but with a complex mobility $\mu(\omega)$ describing the frequency dependence. For the heavily doped film displayed in Fig. 6.8a, the values $\sigma_0 = 405\,\mathrm{S\ cm^{-1}}$ and $\tau = 19.3\,\mathrm{fs}$ were obtained. The dashed line marks the scattering rate $\gamma = 1/\tau$, which equals the frequency at which the real and imaginary parts intersect.

In the classical Drude model, the scattering time τ and the effective carrier mass m^* fully determine the DC mobility $\mu_0 = e\tau/m^*$. For an effective hole mass $m^* = 0.07\,m_e$ in (6,5)-SWNTs [18], a mobility value $\mu_0 \approx 500\,\mathrm{cm^2\,V^{-1}\,s^{-1}}$ is obtained. This hole mobility is much larger than the mobilities obtained by FET measurements of SWNT thin-films with

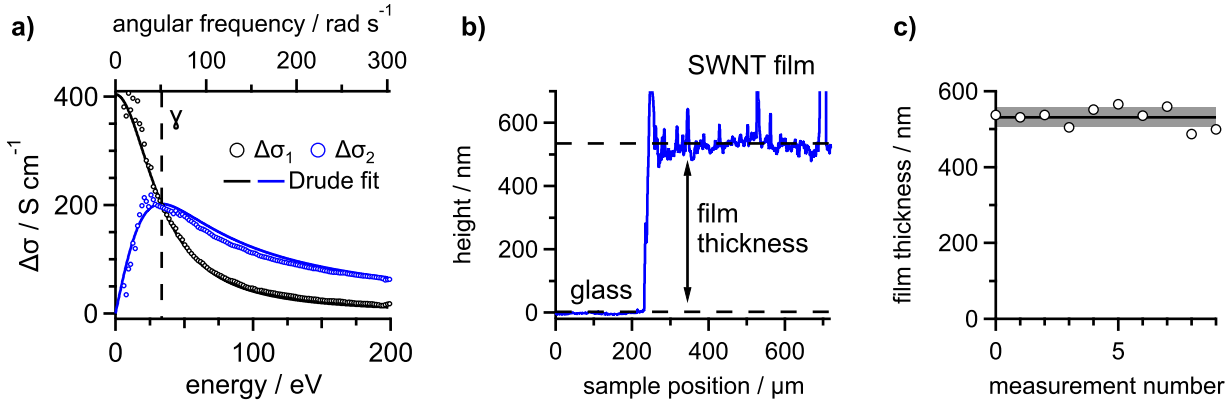

Figure 6.8: a) Drude fitting of the experimentally obtained optical conductivity. The real part $\Delta\sigma_1$ is shown in black, whereas the imaginary part $\Delta\sigma_2$ is shown in blue. b) Representative profilometer measurement of an SWNT thin-film on a glass substrate. c) Ten different measurements give an average film thickness $h_{\text{film}} = 531 \pm 26\,\text{nm}$. The solid line shows the average value and the shaded region displays the standard deviation.

channel lengths of several micrometers. In this case, the mobilities typically vary between $1\text{-}20\,\text{cm}^2\,\text{V}^{-1}\,\text{s}^{-1}$ [316–319]. The discrepancy between the long channel FET mobilities and the mobility extracted from the Dude fit is easily explained. In FET structures with channel lengths much larger than the average SWNT length, charge transport is highly suppressed by intertube charge transfer and not limited by intratube transport. However, the Drude mobility $\mu_0 \approx 500\,\text{cm}^2\,\text{V}^{-1}\,\text{s}^{-1}$ compares well to FET mobilities for short channel lengths $< 300\,\text{nm}$ ranging from 320 to $410\,\text{cm}^2\,\text{V}^{-1}\,\text{s}^{-1}$ as reported, for example, by Brady *et al.* [16]. For such short channel lengths, the intertube resistance can be neglected and diffusive intratube transport determines the mobility.

The charge density $n = \sigma_0 \mu_0^{-1} e^{-1}$ is obtained by reversing equation (6.6). Here, n is the volumetric charge density $n_{3\text{D}}$ in nm^{-3} but can be converted into a 1D SWNT charge density n_{SWNT} by multiplication with the (6,5)-SWNT cross-sectional area $A_{\text{SWNT}} = 0.454\,\text{nm}^2$. SWNTs occupy only a fraction of the thin-film volume V_{film}, and therefore, the fill factor $\theta = V_{\text{SWNT}}/V_{\text{film}}$ is needed for the analysis. The SWNT charge density is finally expressed by:

$$n_{\text{SWNT}} = n_{3\text{D}}\, A_{\text{SWNT}}/\theta. \tag{6.8}$$

The SWNT fill factor was determined by measuring the thin-film thickness h_{film} with a profilometer and by absorption spectroscopy revealing the number of SWNT carbon atoms in the film [307]. Multiplication of the film thickness with the known film cross-sectional area provides the film volume V_{film}, whereas the number of SWNT carbon atoms is easily converted into an SWNT volume V_{SWNT}.

Fig. 6.8b and c show a representative profilometer measurement performed by Michael Auth and the resulting film thicknesses of ten measurements. The average film thickness of 531 nm translates into a SWNT fill factor $\theta = 2.0\,\%$. A detailed calculation is found in the ap-

pendix 11.2. The remaining 98.0 % of the film volume is either void or occupied by the excess polymer. The fill factor θ is a factor of five smaller than reported by Namal [320], although the vacuum filtration process is identical. However, Namal used SWNT dispersions prepared by sonication, whereas $\theta = 2.0\,\%$ was obtained for vacuum filtration of dispersions obtained by shear force mixing. Shear force mixing results in longer SWNTs [17] and also presumably longer PFO-BPy chains. This could cause a less efficient removal of the excess polymer through the 100 nm filter pores, which is in agreement with the observation of strongly reduced filtration speeds for dispersions obtained by shear force mixing compared to sonication.

Using equation (6.8), an SWNT charge density $n_{\mathrm{SWNT}} = 0.11\,\mathrm{nm}^{-1}$, or a charge every 9 nm results. In order to check if this value is reasonable, the obtained charge density is compared to the S_1 exciton size $\xi = 13\,\mathrm{nm}$ [90]. Since the exciton resonance is predicted to be bleached when there is roughly one charge per exciton size [93], a charge density of $n = (9\,\mathrm{nm})^{-1}$ seems plausible for a heavily doped SWNT film with a fully bleached S_1 absorption band. In chapter 7, other methods for the carrier density determination by optical spectroscopy are presented. The charge density $n_{\mathrm{SWNT}} = 0.11\,\mathrm{nm}^{-1}$ for heavily doped SWNTs is slightly lower but within the order of magnitude of values determined by different methods and analyses.

Another quantity, which can be extracted from the Drude model, is the so-called plasma frequency ω_{p}, below which the material becomes a good reflector:

$$\omega_{\mathrm{p}} = \sqrt{\frac{n_{\mathrm{3D}} e^2}{\epsilon_{\mathrm{r}} \epsilon_0 m^*}} = \sqrt{\frac{\sigma_0}{\epsilon_{\mathrm{r}} \epsilon_0 \tau}}. \tag{6.9}$$

Using the values of the DC conductivity σ_0 and scattering time τ from above and a relative dielectric constant ϵ_{r} between 4 and 8, the plasma frequency $\omega_{\mathrm{p}} = 17\text{ - }24\,\mathrm{rad\,THz}$ is obtained. In other units, this range is 11 - 16 meV or 90 - 127 cm^{-1}. In the following, it is attempted to check the predicted plasma frequency experimentally.

6.5.2 Infrared Reflectivity

Free charge carriers do not only cause IR absorption and high conductivity but also lead to reflection of light by the surface of a conductor [159]. This can be seen by the empirical Hagen-Rubens relationship which connects the far infrared reflectivity R of metals to their DC conductivity [321]:

$$R(\omega) \approx 1 - \sqrt{8\epsilon_0 \omega / \sigma_0} \tag{6.10}$$

Therefore, good conductors are expected to be also good reflectors at low frequencies. The physical reason for the good reflectivity is that an electric field can not sustain inside materials with a large density of free carriers.

The optical conductivity of heavily doped SWNTs is well described by a Drude free-carrier response, which is indicative of metallic properties and that the SWNTs are degenerately doped. The broadband transmission measurements of doped SWNT thin-films do not distinguish be-

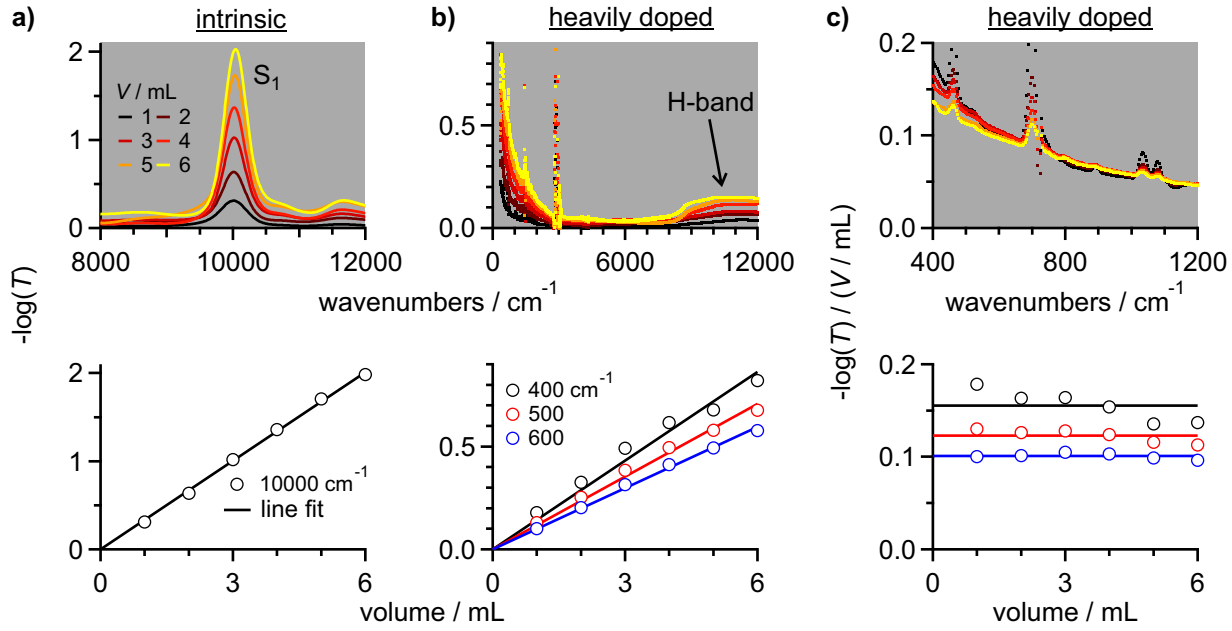

Figure 6.9: Transmission spectra of a) intrinsic and b) doped SWNT films depending on the filtrated volume V. The Beer-Lambert law is valid in intrinsic SWNTs as shown by the linear relationship of V and $-\log T$ at the S_1 exciton resonance. c) Same data as in b) but normalized to the filtrated volume V and zoomed into the low wavenumber region. For wavenumbers $\tilde{\nu} \lesssim 600\,\mathrm{cm}^{-1}$, the Beer-Lambert law continuously loses validity.

tween light absorption or reflection because both processes lead to reduced transmission T. In order to disentangle reflection and absorption, a combined measurement of broadband transmission spectroscopy and broadband reflection spectroscopy is desirable but was not possible during this work.

However, if the reduced IR transmission of doped SWNTs has a significant contribution from reflection can also be checked differently. In order to do so, the validity of the Beer-Lambert law was examined in the infrared region for heavily doped SWNT thin films. The Beer-Lambert law considers only the light attenuation due to absorption and states that the absorbance $A = -\log T \propto c\,d$ is proportional to the product of the concentration c and sample thickness d. Hence, if the negative logarithm of the transmission is proportional to $c\,d$, reflection at surfaces can be neglected.

The validity of the Beer-Lambert law was checked using six SWNT thin-films of different thickness prepared by vacuum filtration. All films were fabricated using the same SWNT dispersion. Different sample volumes, ranging from one to six milliliters, were used for filtration in order to obtain different film thicknesses. Fig. 6.9a shows the transmission spectra of the intrinsic thin-films in the NIR spectral region around the S_1 exciton resonance. A direct proportionality between $-\log T$ at the S_1 resonance ($10000\,\mathrm{cm}^{-1}$) and the filtrated volume V is observed as indicated by the good agreement with the line fit through the origin. The six thin-films were heavily doped by immersion in a 50 µg/mL $AuCl_3$ solution for 15 min and the transmission spectra are shown in Fig. 6.9b. The S_1 absorption at $10000\,\mathrm{cm}^{-1}$ is fully

quenched and replaced by the broad H-band absorption. Additionally, $-\log T$ increases in the IR spectral region due to free carriers. The bottom graph shows the dependence of $-\log T$ at 400, 500 and 600 cm^{-1} on the filtrated volume V. For all three wavenumbers, a nearly linear relationship is obtained, but the agreement between experimental data and the line fits becomes worse at lower wavenumbers. Fig. 6.9c illustrates the discrepancy more clearly. Here, the transmission spectra were normalized to the filtrated volume. All six curves agree quite well for wavenumbers above $\tilde{\nu} \approx 650\,\mathrm{cm}^{-1}$. For lower wavenumbers, a clear trend is observable, indicating that thinner films (less filtrated volume) show higher nomalized $-\log T$ values. The bottom graph again shows $-\log T$ at 400, 500 and 600 cm^{-1} normalized to the filtrated volume. For 400 cm^{-1}, it is evident that the data points do not fall onto a constant value as predicted by the Beer-Lambert law. The increased influence of reflection best explains the violation of the Beer-Lambert law at lower photon wavenumbers (or photon energies). Based on the experimental results, the plasma wavenumber $\tilde{\nu}_\mathrm{p}$ is estimated to lie somewhere around 500 cm^{-1}. The plasma wavenumber $\tilde{\nu}_\mathrm{p} \propto \sqrt{n}$ rises with charge density n. Therefore, transmission measurements of doped SWNT thin-films with carrier densities below the heavy doping regime are dominated by charge carrier *absorption* as long as wavenumbers $\tilde{\nu} \gtrsim 600\,\mathrm{cm}^{-1}$ (photon energies $E \gtrsim 75\,\mathrm{meV}$) are regarded.

This finding has implications for the determination of charge carrier concentrations by integration over the IR absorbance if measured in transmission mode. Only if $-\log T \propto c\,d$, the integral over $-\log T$ is proportional to the charge density. Therefore, the lower integration limit should exceed 600 cm^{-1} (75 meV).

Next, the experimentally approximated plasma wavenumber is compared to the prediction by the Drude model when the volumetric charge density n_3D is taken into account. The predicted plasma wavenumber ($\approx 100\,\mathrm{cm}^{-1}$) is a factor ≈ 5 lower than the experimentally estimated value ($\approx 500\,\mathrm{cm}^{-1}$). The Drude model was developed for homogeneous, isotropic conducting media. Therefore, the disagreement between the experiment and predictions by the Drude model for anisotropic SWNT thin-films containing mostly weakly conducting PFO-BPy is not too surprising. However, a better agreement between theory and experiment could be obtained if the local volumetric charge density $n_\mathrm{3D}^\mathrm{SWNT}$ in the vicinity of the SWNT instead of the averaged volumetric charge density n_3D of the whole film is regarded. This would increase the predicted plasma wavenumber by a factor $\sqrt{\theta^{-1}} \approx 7$, where $\theta = 2.0\,\%$ is the SWNT filling fraction, in reasonable agreement with the experimental value.

6.6 Summary and Outlook

The optical properties of heavily doped SWNTs were investigated using linear and nonlinear absorption spectroscopy. In the VIS-NIR spectral region, heavily doped SWNTs are characterized by a nearly 1 eV broad and featureless absorption band (H-band), which consumes almost 80 % of the S_1 exciton oscillator strength in intrinsic SWNTs. In contrast, S_1 exciton

and X_1^+ trion absorption bands are efficiently bleached. The absorption cross-section σ_H of the H-band was estimated by comparison with reported absorption cross-sections of the S_1 and S_2 absorption of intrinsic SWNTs. A value $\sigma_H \approx 0.9 \times 10^{-18}\,\mathrm{cm}^2$ per carbon atom could be obtained, which is $\approx 15\,\%$ of the absorption cross-section of a graphene monolayer. Linear absorption spectroscopy further showed that the H-band seems to merge into a featureless absorption band already present in intrinsic SWNTs, called nonresonant background [308].

For both H-band and nonresonant background, hardly any signal in the transient absorption spectrum was detected. This showed that the nonlinear optical response of SWNTs can not be interpreted in terms of a simple molecular picture where the ground state depletion leads to a photobleach signal proportional to the steady-state absorption spectrum. The only observed nonlinear signals of the H-band and the nonresonant background were weak photoabsorption bands located at the H-band ($\approx 1.04\,\mathrm{eV}$) and nonresonant background ($\approx 1.59\,\mathrm{eV}$) onset-energies. A weak photo-induced band gap shrinkage on the order of 1 meV or less could reasonably well describe the photoabsorption signals.

Consequently, the most likely microscopic origin of the H-band in heavily doped SWNTs and the nonresonant background in intrinsic SWNTs is free-carrier absorption. A comparison with the absorption spectra of other low-dimensional materials revealed that broad and featureless absorption bands are more common for heavily doped semiconductor nanostructures and not limited to semiconducting SWNTs.

Moreover, the interaction of IR radiation with SWNT was investigated. Broadband transmission spectroscopy at frequencies in the THz regime allowed studying the intratube charge transport properties of heavily doped SWNT thin-films. An analysis of the Drude response in the optical conductivity spectrum revealed an average scattering time constant $\tau \approx 20\,\mathrm{fs}$. The intratube hole mobility was estimated as $\mu_0 \approx 500\,\mathrm{cm}^2\,\mathrm{V}^{-1}\,\mathrm{s}^{-1}$, in good agreement with reported FET mobilities in short channel length transistors [16]. The Drude analysis suggests that the SWNT charge density n, which is necessary for a complete bleaching of the S_1 absorption band, is on the order of one charge every 9 nm.

Finally, film thickness dependent transmission measurements explored the reflection properties of heavily doped SWNT thin-films. A deviation from the Beer-Lambert law at wavenumbers below approximately $500\,\mathrm{cm}^{-1}$ was identified to be caused by the increasing influence of light reflection induced by free-carriers.

In the future, experiments on SWNT samples with even higher charge densities are desirable. Such doping levels could be achieved by ionic-liquid gating and using larger-diameter SWNTs with smaller band gaps. The changes in H-band absorption for further increasing charge densities might confirm the hypothesis of free-carrier transitions as the microscopic H-band origin. Due to Pauli blocking, a gradual blueshift of the H-band onset-energy would be expected. Studies on heavily doped aligned SWNT films could provide additional insight in the plasmon coupling, which strongly enhances plasmon absorption signals as already shown in pioneering works by Yanagi *et al.* [306] and Chiu *et al.* [298].

7 Quantifying Doping in CNTs Using Absorption Spectroscopy

In order to understand and optimize doping processes, the ability to quantify charge densities is inevitable. For bulk semiconductors, a quantification of free carrier concentrations is achieved by combined conductivity and mobility measurements. Mobilities in thin-film semiconductors are typically determined by Hall measurements or in a field-effect transistor (FET). Both methods have some drawbacks when applied to SWNTs as explained by Blackburn, Ferguson and Reid [315].

FET measurements can provide mobilities of nominally intrinsic SWNTs. The gate voltage introduces mobile carriers, and the transistor is in its 'on' state, where mobilities can be extracted. Heavily doped samples are already in their 'on' state, and the gate voltage is ineffective in altering the charge density. This ineffectiveness restricts the determination of the carrier mobility [315].

Charge transport in SWNTs is highly anisotropic due to their 1D geometry. Mobility measurements using the Hall effect, however, rely on isotropic conductors. In this case, a magnetic field perpendicular to the electric field leads to a measurable and predictable Hall voltage, which can be related to the carrier mobility [315].

Another drawback of all electrical measurements is that only free carrier concentrations can be determined and localized carriers, which do not contribute to the electric current, are overseen. This chapter discusses how doping-induced absorbance changes in combination with band structure calculations can provide estimates of the total, *i.e.* free and localized carrier concentration in SWNTs. As outlined before, a spectroscopic determination of carrier concentrations has some advantages over frequently used electrical measurements. First, no electrical contacts are necessary, *i.e.* it is non-invasive, and even individualized SWNTs in dispersion can be investigated. Second, spectroscopic measurements on SWNT thin-film samples do not depend on intertube contact resistances, like in the case of electrical measurements. Therefore, the results of spectroscopic experiments are less prone to variations in film morphology or nanotube fill factor.

7.1 Exciton Confinement Model

In chapter 5.2.1, exciton confinement effects rationalized the doping-induced blueshift, broadening and the increasing asymmetry of the S_1 absorption band. Randomly distributed localized charges, acting as barriers, confine the exciton wavefunction between two neighboring charges. This confinement is analog to the particle in a box as long as the barriers are suffi-

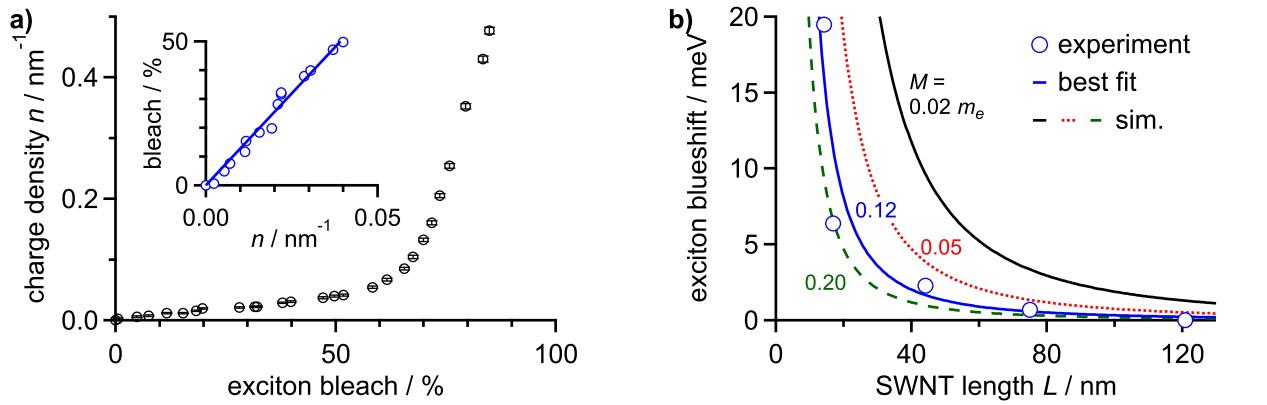

Figure 7.1: a) Carrier density $n = \overline{w}^{-1}$ as a function of the S_1 exciton bleach χ using the exciton confinement model. The inset shows the linear dependence of χ on small carrier densities as predicted by the phase space filling model. b) Exciton blueshift in ultra-short SWNTs depending on the SWNT length L. Experimental data points were taken from Gao *et al.* [246], whereas the lines are simulations and a fit (blue) using the particle in a box model with variable exciton mass M.

ciently high (for details, see chapter 5.2.1). A fit of the confinement model to the background corrected S_1 absorption band provides the average distance $\overline{w}$ between barriers and can be related to the carrier concentration $n = \overline{w}^{-1}$.

Fig. 7.1a shows the resulting carrier concentration as a function of the S_1 bleach. For moderate doping with an exciton bleach $\chi < 50\,\%$ the charge density is linear in χ. The linear relationship is in agreement with phase space filling (PSF) theory, which predicts for small charge densities n [93]:

$$\chi = n/n_s, \tag{7.1}$$

where n_s is the saturation charge density.

The inset of Fig. 7.1a shows the dependence of the exciton bleach on small carrier densities. Additionally, a line fit through the origin according to equation (7.1) is shown. The slope $m = 12.8\,\text{nm}$ translates into a saturation density $n_s = 1/(12.8\,\text{nm})$, which is in good agreement with reported exciton sizes of 13 nm [90] and the theoretical prediction that the exciton absorption band is fully bleached when there is approximately one charge per exciton size [93]. A more detailed treatment of the PSF effect is found in the next section, where charge densities are directly determined from the relative exciton bleaching.

The linear dependence between χ and n breaks down for exciton bleaching exceeding approximately 50 %. In this regime, saturation effects and higher orders of n might start to play a role. Despite the qualitative agreement between the PSF predictions and carrier concentrations determined by the exciton confinement model,a few disadvantages of the exciton confinement model have to be noted. First, the assumption of localized carriers loses validity for increasing charge density because of considerable carrier wavefunction overlap (see chapter 5.5). This limits the model to small exciton bleaches. Second, the determination of exact absolute charge densities furthermore relies on a precisely known translational exciton mass

M, which enters the formula of the particle in a box. Here, $M \approx 2\,m^* = 0.14\,m_e$ [247] was used, where the effective electron and hole mass $m^* = 0.07\,m_e$ was obtained from curvature-corrected tight-binding band structure calculations [18].

Gao *et al.* reported on blueshifts of the exciton absorption band for ultra-short and length-sorted SWNTs. The blueshift upon reduction of the SWNT length was interpreted as a confinement effect and was modeled by the 1D particle in a box, analog to the exciton confinement between localized charges. Average SWNT lengths of different samples were determined by atomic force microscopy and photothermal microscopy. Fig. 7.1b shows the blueshift as a function of SWNT length L (the experimental data were taken from reference [246]). The black, red and green lines are simulations according to the particle in a box model with

$$\Delta E = \frac{\hbar^2 \pi^2}{2ML^2}, \tag{7.2}$$

and the blue line is the best fit. The best agreement is obtained for an exciton mass $M = (0.12 \pm 0.02)\,m_e$, which is close to the value obtained from the band structure calculation and suggests the validity of the used exciton mass M. It has to be noted, that the carrier density n scales only with the square root of M within the exciton confinement model, and therefore, minor errors in M do not have a big influence on the extracted charge density.

The exciton confinement model mainly concerns the exciton energetics. In the following, two models are presented, which correlate the exciton absorption intensity to the charge density.

7.2 Phase Space Filling Model

The phase space filling (PSF) model has frequently been used to quantify the pump-induced exciton bleach observed in transient absorption experiments [90–93, 322, 323]. The physical basics of the PSF model are briefly described in the following. Subsequently, this model is used to predict the doping-induced S_1 exciton bleach.

The excitonic oscillator strength f_0 is proportional to the probability to find electron and hole at the same position, *i.e.*, $f_0 \propto |\Psi(x = 0)|^2$ [92]. Here, $x = x_e - x_h$ is the distance between electron and hole and $\Psi(x)$ is the envelope of the 1D exciton relative motion orbital wavefunction in real space [91]. According to Capaz *et al.*, the envelope can be approximated by a Gaussian [50, 90, 91]

$$\Psi(x) = \xi^{-\frac{1}{2}} \pi^{-\frac{1}{4}} \exp\left(-\frac{x^2}{2\xi^2}\right), \tag{7.3}$$

where ξ is the so-called exciton size, which is related to the average electron-hole distance $\bar{x}$ by $\xi = \sqrt{\pi}\,\bar{x}$. In the following, real space is abandoned, and k-space is entered.

According to Huang *et al.* [324] and Elliott [325], the exciton state is described as a linear combination of free electron and hole states, where the amplitudes $\Psi(k)$ are given by the

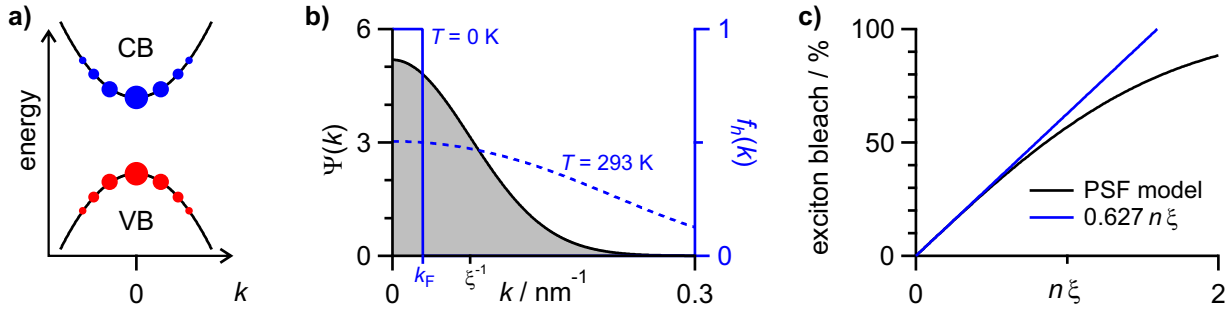

Figure 7.2: a) Exciton wavefunction as a linear combination of single-particle electron and hole Bloch states. The sizes of the blue and red circles illustrate the amplitudes of the electron and hole states given by $\Psi(k)$. b) k-space exciton wavefunction $\Psi(k)$ (grey shaded area, left axis) for an exciton size $\xi = 13\,\mathrm{nm}$ [90]. The blue lines (right axis) show the Fermi-Dirac distribution function $f_h(k)$ at $T = 0\,\mathrm{K}$ and $T = 293\,\mathrm{K}$. A Fermi wavevector $k_\mathrm{F} = 0.03\,\mathrm{nm}^{-1}$ and an effective hole mass $m^* = 0.07\,m_e$ [18] were used. c) Dependence of the exciton bleach χ on the product of charge density n and exciton size ξ in the low-temperature limit.

Fourier transform of $\Psi(x)$:

$$\Psi(k) = 2^{\frac{1}{2}}\xi^{\frac{1}{2}}\pi^{\frac{1}{4}}\exp\left(-\frac{1}{2}k^2\xi^2\right). \tag{7.4}$$

This is illustrated in Fig. 7.2a and b and $\Psi(k)$ will be called the k-space exciton wavefunction in the following. With the definition of the k-space exciton wavefunction, the oscillator strength can also be expressed by

$$f_0 \propto |\Psi(x=0)|^2 = \Psi(x=0)\sum_k \Psi(k), \tag{7.5}$$

where the Fourier transform $\Psi(x) = \sum_k \Psi(k)\,\mathrm{e}^{ikx}$ was used.

Although excitons are composite bosons, the Pauli exclusion principle acts on the fermionic electrons and holes, which compose the exciton. The presence of excitons reduces the number of available electron and hole states. This state reduction is called phase space filling and renormalizes the exciton oscillator strength f in the limit of small changes to:

$$f \propto \Psi(x=0)\sum_k [1 - f_e(k) - f_h(k)]\Psi(k), \tag{7.6}$$

where $f_{e,h}(k)$ are the electron and hole distribution functions accounting for the reduction of available states.

For optical excitation, it was shown that the exciton bleach χ is given by [90, 91]:

$$\chi = \frac{f_0 - f}{f_0} = \frac{\sum_k [f_e(k) + f_h(k)]\Psi(k)}{\sum_k \Psi(k)} = \frac{N}{N_\mathrm{s}}, \tag{7.7}$$

where N is the exciton density and $N_\mathrm{s} = (2.05\,\xi)^{-1}$ is the saturation exciton density. Provided that the exciton density is precisely determined, the exciton size ξ can be calculated from the exciton bleach measured in a pump-probe experiment [90, 91].

In the following, the same theoretical framework is used to predict the doping-induced – instead of pump-induced – exciton bleach. Doping only affects electron or hole states and consequently for p-doping $f_e(k)$ can be disregarded. Therefore, equation (7.7) is rewritten:

$$\chi = \frac{\int_{-\infty}^{\infty} f_h(k)\Psi(k)\,\mathrm{d}k}{\int_{-\infty}^{\infty} \Psi(k)\,\mathrm{d}k} = 2c^{-1}\int_0^{\infty} f_h(k)\Psi(k)\,\mathrm{d}k, \tag{7.8}$$

where integrals replaced the sums, $f_h(k)$ is the Fermi-Dirac distribution function for holes in the valence band (VB) and $c = 2\,\xi^{-\frac{1}{2}}\pi^{\frac{3}{4}}$ is the solution of the denominator integral. The factor of two on the right-hand side reflects the symmetry of the remaining integral, whose lower integration limit was shifted from $-\infty$ to zero.

7.2.1 Low-Temperature Limit

In the low-temperature limit $T \to 0$ an analytical solution of equation (7.8) exists. At zero temperature, the Fermi function $f_h(k) = \Theta(k - k_\mathrm{F})$ is the Heaviside step function Θ, which changes from one to zero at the Fermi wavevector k_F (see Fig. 7.2b). This allows expressing equation (7.8) by

$$\chi = 2c^{-1}\int_0^{k_\mathrm{F}} \Psi(k)\,\mathrm{d}k = \mathrm{erf}\left(2^{-\frac{1}{2}}\xi k_\mathrm{F}\right). \tag{7.9}$$

The Fermi wavevector k_F is related to the charge density n by $k_\mathrm{F} = \pi n/4$ [232], where the factor of four accounts for the two-fold spin and K, K' valley degeneracies. The exciton bleach as a function of charge density n is therefore

$$\chi(n) = \mathrm{erf}\left(2^{-\frac{5}{2}}\xi\pi n\right). \tag{7.10}$$

Fig. 7.2c shows this function as a black line. In the limit of a small exciton bleach, the low-temperature result of the PSF model can be well approximated by a linear relationship $\chi = 0.627\,n\,\xi$ depicted as a blue line. In terms of equation (7.1), this correlates to a the saturation density $n_\mathrm{s} = (0.627\,\xi)^{-1}$ and is in agreement with the prediction that the exciton resonance is bleached when there is roughly one charge per exciton size [93].

Next, the saturation charge density $n_\mathrm{s} = (0.627\,\xi)^{-1}$ is compared to the saturation exciton density $N_\mathrm{s} = (2.05\,\xi)^{-1}$. By taking into account that an exciton is composed of two charges, a bound charge in an exciton is a factor $n_\mathrm{s}/(2\,N_\mathrm{s}) \approx 1.6$ more effective in exciton bleaching than a doping-induced charge. This somewhat surprising effect results from the K, K' valley degeneracy, which doubles the charge density for a given Fermi wavevector. For a 1D semiconductor without valley degeneracy, bound charge in an exciton would be slightly less effective (≈ 0.8 times) than a doping-induced charge.

7.2.2 Arbitrary Temperatures

The temperature dependence of exciton bleaching on charge density is expressed by:

$$\chi(n,T) = 2c^{-1} \int_0^\infty f_h(k,n,T)\Psi(k)\,\mathrm{d}k. \tag{7.11}$$

This integral has no analytical solution and has to be solved numerically.

For practical reasons, two separate calculations were performed. The first calculation quantifies $\chi(E_\mathrm{F},T)$, *i.e.*, the dependence of the exciton bleach on the Fermi level E_F. The second calculation provides the carrier density n as a function of the Fermi level, which is obtained by an integration over the product of the density of states DOS and the Fermi-Dirac function [44]. In 1D, the density of states DOS(k) as a function of k is constant, such that it results:

$$n(E_\mathrm{F},T) = \frac{4}{\pi} \int_0^\infty f_h(k,E_\mathrm{F},T)\,\mathrm{d}k\,. \tag{7.12}$$

The Fermi level $E_\mathrm{F}(k)$ in the effective mass approximation depends on the effective carrier mass m^*. For the calculations $m^* = 0.07\,m_e$ [18] and an exciton size $\xi = 13\,\mathrm{nm}$ [90] were used as input parameters.

Fig. 7.3a shows the exciton bleach χ as a function of charge density at different temperatures. For small χ, the relative exciton bleaching is linear in n, *i.e.*, $\chi = n/n_\mathrm{s}$, where n_s^{-1} is the slope. The temperature dependence was quantified by the evaluation of n_s in the limit of vanishing carrier densities $n \to 0$. Fig. 7.3b shows the saturation density n_s as a function of temperature. Charges at low temperatures are about twice as effective in exciton bleaching as charges at room temperature. This effect can be rationalized by the width of the Fermi edge, which at room temperature ($T = 293\,\mathrm{K}$) significantly exceeds the range of electron and hole k-momenta contributing to the exciton wavefunction $\Psi(k)$ (see Fig. 7.2b).

In the following, the temperature dependence is neglected, and the theoretical predictions focus on room temperature, at which the spectroscopic experiments were conducted. According to the PSF model, room temperature carrier concentrations can be described by $n = n_\mathrm{s}\,\chi$, where $n_\mathrm{s} = 0.27\,\mathrm{nm}^{-1}$. This means that the exciton resonance fully bleaches for about one charge every 4 nm, which is in good agreement with reported values of Hertel [44] and of a previous work [112] using a band filling analysis and the exciton confinement model for electrochemically doped SWNTs.

The PSF model can not only be used to estimate charge densities when the exciton size and effective carrier masses are known but also allows estimating exciton sizes if carrier densities are evaluated precisely.

Although the PSF model provides seemingly reasonable carrier densities, there are some drawbacks. First, the model relies on the fact that PSF is the dominant exciton bleaching mechanism. For 1D systems, where screening effects are weak compared to 3D systems [93], this assumption is quite reasonable. Second, the input parameters ξ and m^* have to be

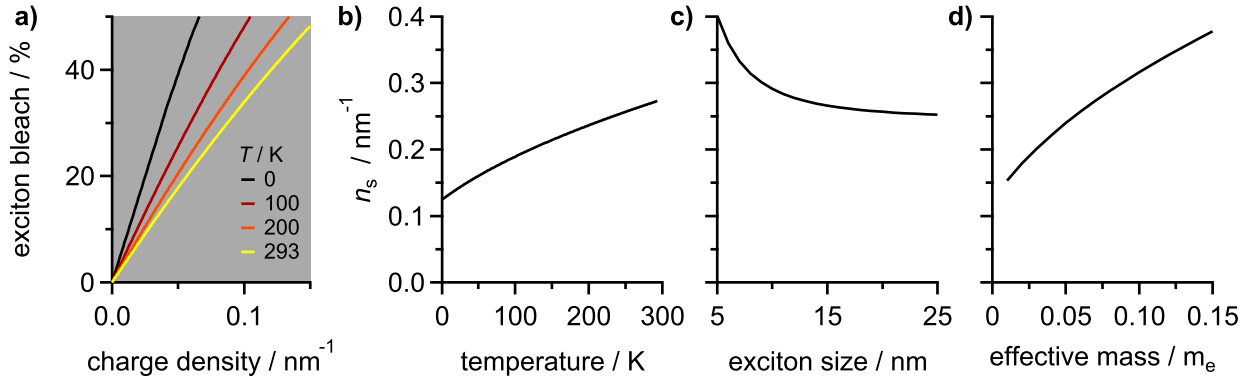

Figure 7.3: a) Exciton bleaching as a function of the carrier density n for different temperatures. A nearly linear relationship is observed for a small exciton bleach χ. Input parameters: $\xi = 13\,\mathrm{nm}$ and $m^* = 0.07\,m_e$. b) Temperature dependence of the saturation density n_s as obtained from the initial slopes of χ vs. n. c) Dependence of the saturation density on exciton size ξ for constant temperature $T = 293\,\mathrm{K}$ and effective hole mass $m^* = 0.07\,m_e$. d) Effective mass dependence of the saturation density for constant temperature $T = 293\,\mathrm{K}$ and exciton size $\xi = 13\,\mathrm{nm}$.

precisely known in order to avoid errors. Fig. 7.3c and d show that the dependences of the saturation density n_s on the exciton size ξ and the effective hole mass m^* are not negligible. Third, the PSF model relies on a detectable exciton bleach. As for the exciton confinement model, this ultimately limits the usability of the model to doping levels at which the exciton resonance has not yet been completely bleached. Higher charge densities are as such not accessible. However, the validity of the PSF model is anyway limited to small χ values [92], and otherwise, larger errors have to be expected.

This limitation of non-accessibility towards higher charge densities might be overcome by regarding not only the change in S_1 oscillator strength but in the whole first subband related oscillator strength.

7.3 First Subband Analysis

In intrinsic 1D direct gap semiconductors, free-carrier transitions are typically weak. Strong exciton binding energies in low dimensions cause a redistribution of oscillator strength from free-carrier transitions to excitonic resonances [67]. The Thomas-Reiche-Kuhn sum rule states that the total oscillator strength f_tot is conserved and is proportional to the number of electrons N_e participating in the transitions under consideration [67]:

$$f_\mathrm{tot} \propto N_e. \tag{7.13}$$

As a further example, chapter 5.4 showed that doping leads to a redistribution of oscillator strength from the NIR spectral region to lower-energy intraband transitions.

In the single-particle picture, the doping-induced renormalization of interband oscillator

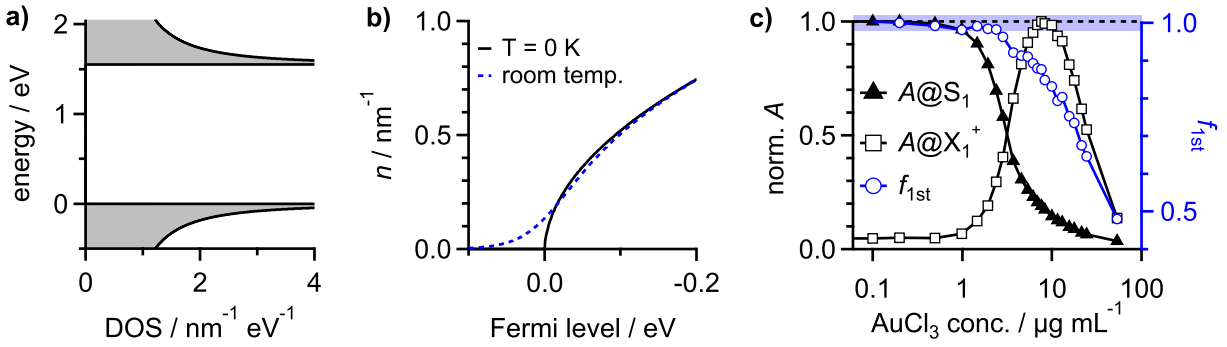

Figure 7.4: a) 1D DOS in the effective mass approximation. b) Hole density as a function of the Fermi level position at zero temperature (black line) and thermally broadened (blue line). c) Normalized exciton absorbance at 1.240 eV and normalized trion absorbance at 1.057 eV depending on the gold(III) chloride concentration. Additionally, the concentration dependence of the normalized integrated first subband oscillator strength f_{1st} between 0.95 eV and 1.85 eV is shown.

strength $\Delta f/f$ over a certain energy range can be associated with a relative loss of electrons $\Delta N_e/N_e$ participating in the transitions over this energy range. The same should be true, when excitonic transitions are included as long as the regarded energy range is large enough to cover the excitonic absorption band and most of the free e-h pair transitions, which transferred oscillator strength to the exciton.

Fig. 7.4a shows the density of states of (6,5)-SWNTs in the effective mass approximation. An effective electron and hole mass of $m^*_{e,h} = 0.07\,m_e$ and a band gap of $E_g = 1.55$ eV [18] was used for the calculation. The density of states is given by [18]:

$$\mathrm{DOS}(E) = a\sqrt{m^*}\,(|E - E_{c,v}|)^{-\frac{1}{2}}\,, \tag{7.14}$$

where $a\sqrt{m^*} = 3.25\sqrt{m^*/m_e}$ nm^{-1} eV$^{-1/2}$ is a constant. $E_v = 0$ eV and $E_c = 1.55$ eV are the energies of the valence and conduction band edges. Fig. 7.4b shows the hole density $n(E_F)$ as a function of the Fermi level position, which was obtained by:

$$n(E_F) = \int_{-\infty}^{E_v} \mathrm{DOS}(E) f_h(E, E_F, T)\,\mathrm{d}E, \tag{7.15}$$

where f_h is the Fermi-Dirac distribution function of holes.

Fig. 7.4c compares the exciton and trion absorbance with the first subband related oscillator strength f_{1st}. The data were reproduced from Fig. 5.1 in chapter 5.2. The first subband related oscillator strength f_{1st} was obtained by integration over the absorption spectrum between $E_1 = 0.95$ eV and $E_2 = 1.85$ eV and subsequent normalization.

Therefore, it covers the spectral range of the trion, exciton, and large parts of the nonresonant background and H-band absorption associated with transitions between the first valence and conduction subband. A larger upper integration limit would cause errors due to the inclusion of cross-polarized E_{12} exciton absorption involving a second valence/conduction subband [26,

242, 243].

Fig. 7.4c illustrates that f_{1st} starts to drop approximately at the same $AuCl_3$ concentration at which trion absorbance starts to increase and S_1 absorbance decreases. However, it has to be noted that changes in f_{1st} are small for very low doping levels, *i.e.*, on the order of 1 %, and therefore very prone to errors.

Provided that the integration limits are sufficient to cover most of the first subband related oscillator strength f_{1st}, the doping-induced loss in f_{1st} can be related to the loss of electrons participating in the interband transitions. The number of electrons per unit length participating in transitions up to $E_2 = 1.85\,\text{eV}$ in intrinsic tubes can be obtained analog to equation (7.15) by

$$n^0_{1st} = n([E_g - E_2]/2) = n(-0.2\,\text{eV}) = 0.74\ \text{nm}^{-1}. \tag{7.16}$$

If band gap renormalization is neglected, the doping-induced charge density n directly reflects the loss in participating electrons and is related to the normalized oscillator strength f_{1st} by:

$$n = (1 - f_{1st}) \cdot n^0_{1st}. \tag{7.17}$$

A nearly complete S_1 exciton quenching and fully developed H-band is obtained for $f_{1st} \approx 50\,\%$. This 50 % bleaching corresponds in this analysis to a hole density $n = 0.37\,\text{nm}^{-1}$, which is slightly more than one charge every 3 nm. In terms of the Fermi energy, it corresponds to $E_F = -60\,\text{meV}$. The charge density and Fermi level are in good agreement with a detailed analysis of the potential drop between the working electrode and the SWNTs in electrochemical doping experiments by Hertel [44].

7.4 Comparison of the Models

Next, the results of the three presented models are compared. Fig. 7.5a shows the extracted charge densities according to the exciton confinement model (ECM) and the analysis of the first subband oscillator strength (FSA). Additionally, the predictions by the phase space filling model (PSF) are depicted. For a small exciton bleach χ, the ECM and FSA model give similar charge densities, which are approximately linear in the bleach. When the bleach exceeds 50 %, the charge densities increasingly deviate from the initial linear behavior. In this doping level range, disagreement between both models increases and is on the order of a factor of two. The phase space filling model predicts considerably larger carrier densities than the other two models with an initial slope that is approximately 3 - 4 times higher.

In conclusion, the exact determination of absolute carrier densities via optical spectroscopy is hard, and it can not be finally clarified which model provides the most realistic charge densities. However, it was shown that relative carrier densities are quite similar within all models for $\chi < 50\,\%$, as indicated by the linear dependence of n on χ. This suggests that the

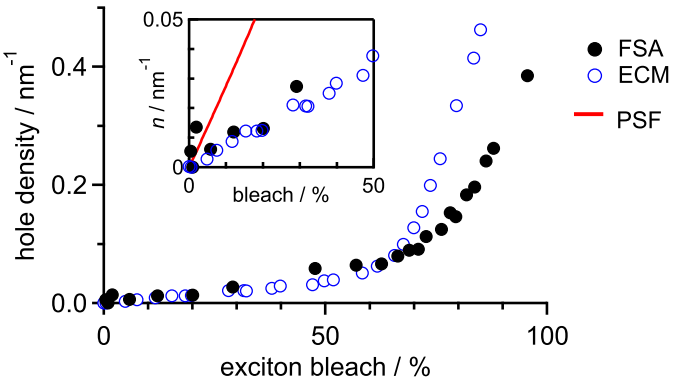

Figure 7.5: Comparison between the different models used for the estimation of carrier densities: the exciton confinement model (ECM), the first subband oscillator strength analysis (FSA) and the phase space filling (PSF) model. The PSF simulation is performed for $T = 293\,\mathrm{K}$, $m^* = 0.07\,m_e$ and $\xi = 13\,\mathrm{nm}$.

exciton bleach is a good measure for carrier densities at least up to $\chi \approx 50\,\%$. For stronger exciton bleaching, all models predict a nonlinear dependence of the charge density on χ and care has to be taken when correlating the exciton bleach to relative charge densities.

If different experiments are compared regarding their degree of doping, it is recommended to use model-free quantities, which are easily accessible with optical spectroscopy and are monotonic functions in carrier density. Such quantities are the S_1 exciton bleach, the doping-induced S_1 blueshift or the relative integrated oscillator strength including all first subband transitions. Although the trion oscillator strength might be proportional to n for low carrier densities, it is not a monotonic function in carrier density and therefore only of limited use.

If absolute carrier densities are necessary, for example for comparison with other low-dimensional doped materials, the relationship between carrier density and integrated first subband related oscillator might be of most practical use. In this case, carrier densities are easily extracted without the need for modeling. Furthermore, the simple linear relationship between the loss in first subband related oscillator strength and carrier density has a solid physical basis with the Thomas-Reiche-Kuhn sum rule, and neither many assumptions nor input parameters have to be used. On top of that, the carrier density extraction using $f_{1\mathrm{st}}$ should also be possible for doping levels exceeding the ones studied here. That this is of practical relevance was shown by other researchers, which found that for increasing doping levels also the H-band can be bleached and $f_{1\mathrm{st}}$ is further reduced [19, 282, 283].

7.5 Summary and Outlook

This chapter aimed to develop a methodology to extract carrier densities from absorption spectra. In order to correlate carrier densities to doping-induced spectral changes, three different models have been developed.

The first model is based on exciton confinement caused by localized charge carriers. The carrier density was found to be linearly related to the exciton bleach χ up to $\chi \approx 50\,\%$. For stronger exciton bleaching, the relation between charge density and exciton oscillator strength becomes strongly nonlinear.

The second model uses phase space filling to predict the doping-induced exciton bleaching. An analytical expression for χ could be derived in the low-temperature limit with $\chi = 0.627\, n\, \xi$, where n is the charge density and ξ is the exciton size. At low temperatures, the K, K' valley degeneracy in SWNTs causes a doping-induced charge to be slightly less effective in exciton bleaching than a bound charge in an optically generated exciton. For an exciton size $\xi = 13\,\mathrm{nm}$ [90], the exciton bleaching efficiency of doping-induced charges further decreases at room temperature by a factor of ≈ 2. This can be explained by the width of the Fermi edge at room temperature, which exceeds the energies of relevant k-states composing the exciton wavefunction. Future temperature-dependent absorption experiments on doped SWNTs could check the predicted temperature dependence.

The third model is based on the Thomas-Reiche-Kuhn sum rule and uses the normalized integrated oscillator strength $f_{1\mathrm{st}}$ associated with all first subband related transitions (exciton, trion, free e-h pairs) between 0.95 eV and 1.85 eV. Within this model, a doping-induced loss in oscillator strength is linearly related to the loss of electrons participating in the transitions. Density of states calculations based on the effective mass approximation correlated the absolute carrier density n and the loss of integrated oscillator strength (1-$f_{1\mathrm{st}}$) by:

$$n = 0.74 \cdot (1 - f_{1\mathrm{st}})\,\mathrm{nm}^{-1}. \tag{7.18}$$

The exciton confinement model and the analysis of the first subband related oscillator strength gave qualitatively similar results, whereas charge densities predicted by phase space filling were about a factor of 3 - 4 higher. The validity of the exciton confinement and phase space filling models is limited to smaller exciton bleaching, whereas the usage of equation (7.18) should be possible even for doping levels exceeding a complete S_1 exciton bleaching.

In order to check the predicted dependence of the carrier density on certain spectroscopically accessible quantities, an independent determination of the carrier concentration is desirable. This could be done in a spectroelectrochemical experiment, in which larger amounts of SWNT material are deposited on the working electrode, and the flowing current is constantly recorded. SWNT charge densities could be obtained from the transferred charges calculated by temporally integrating the faradaic current. The simultaneous acquisition of absorption spectra provides the link between charge densities and absorbance changes.

8 Time-Resolved Spectroelectrochemistry in Solution

Electrochemistry can reveal the thermodynamics and kinetics associated with an electron transfer reaction. However, neither the chemical nor the electronic structure of the involved species can be determined by electrochemistry alone. This limitation is circumvented by the combination of electrochemistry with spectroscopic methods, commonly termed spectroelectrochemistry [326, 327].

The probably most frequently used spectroelectrochemical methods are based on steady-state absorption spectroscopy in the UV-VIS-NIR [328, 329] or IR spectral region [330] for the determination of electronic and vibrational transitions. However, the methodology is not limited to absorption spectroscopy and consequently, other techniques like Raman, ESR, and fluorescence-based spectroelectrochemistry have been developed [327].

Coupling electrochemistry to time-resolved spectroscopy allows studying excited state properties. Chapter 6.3 demonstrated how femtosecond TA spectroscopy is used to *in-situ* monitor the transient absorption changes of (6,5)-SWNTs depending on the applied working electrode (WE) potential in an electrochemical cell. In this case, the (6,5)-SWNTs were prepared as a thin-film in direct contact with a transparent WE, and the pump and probe pulses were focused on the same sample spot during the whole experiment. Similar time-resolved spectroelectrochemistry experiments have been performed by Scheidt *et al.* for $CsPbBr_3$ perovskite films attached to a transparent fluorine tin oxide working electrode [311].

Both experiments, on nanotubes and $CsPbBr_3$ perovskite, conducted without a continuous exchange of sample volume in the laser focus, were only possible due to the high photostability of the investigated systems. In contrast to these inorganic crystals, many organic molecules rapidly degrade during irradiation with intense femtosecond light pulses in the UV or VIS. This necessitates a continuous and rapid exchange of the probed sample volume.

During the last four years, an experimental setup was realized which integrates a flow-electrolysis cell for continuous *in-situ* generation of electrolyzed species into a femtosecond transient absorption spectrometer. In the meantime, the flow-electrolysis cell has also been successfully integrated into a coherent 2D electronic spectroscopy setup of the collaborating research group AK Brixner.

8.1 Description of the Flow-Electrolysis Cell

For the rapid electrochemical generation of molecular species, the commercially available flow-electrolysis cell (FEC) HX-301 (Hokuto Denko Co.) was used with slight modifications. The modifications facilitated the liquid flow through the cell by removing a bottleneck at the solution inlet and allowed the usage of a leakless Ag/AgCl reference electrode. Fig. 8.1a shows a schematic illustration of the FEC. The cell is based on a three-electrode geometry. The central element of the cell is the working electrode (WE) compartment, which consists of carbon fibers densely packed into a Vycor glass tube of 50 mm length, 4.8 mm inner diameter and a wall thickness of 1.1 mm. The Vycor glass is porous with an average pore size of $\approx$ 4 nm. The percolating network of pores makes the migration of ions between the WE and counter electrode (CE) through the glass wall possible, which is necessary for the flow of electric current. A large scale diffusional exchange between molecules in the CE and WE compartments is, however, prevented by the small pore size. A glassy carbon rod electrically contacts the densely packed carbon fibers inside the Vycor tube, which act as a porous WE material making fast electrolysis possible. The platinum wire CE is wrapped around the Vycor tube, and an Ag/AgCl electrode is used as a reference electrode (RE). The sample solution is pumped through the Vycor glass tube along the densely packed carbon fibers by a micro annular gear pump. A flow-through cuvette after the HX-301 FEC solution outlet is used for the spectroscopic investigation of the electrolyzed solution (see Fig. 8.1b). In order

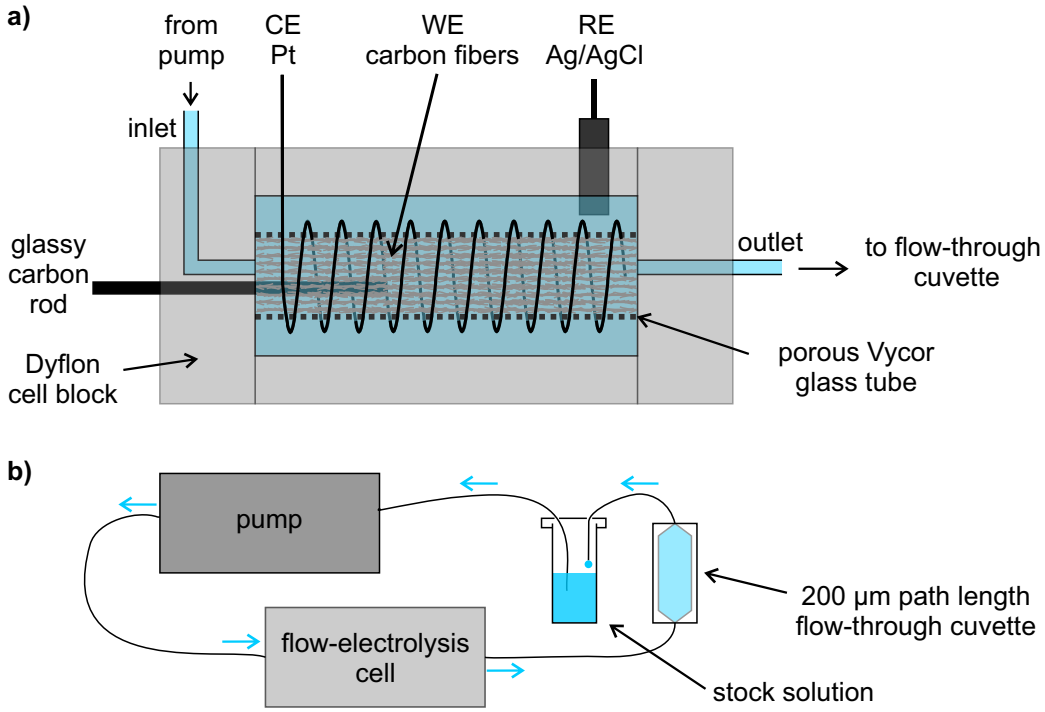

Figure 8.1: a) Schematic illustration of the flow-electrolysis cell HX-301. Screws, sealings and some openings are omitted for clarity. b) Illustration of the flow cycle between the stock solution, micro annular gear pump, the flow-electrolysis cell HX-301 and the flow-through cuvette with d =200 µm path length. The solution is transferred via Teflon tubings between the four elements.

to save sample volume during extended measurement times in a time-resolved spectroscopic experiment, the solution is pumped in a cycle. For steady-state absorption experiments, fresh sample volume is inserted into the FEC, and the solution which has passed the flow-through cuvette is discarded.

8.2 Electrochemical Characterization

In the following, the FEC is investigated for its ability to electrolyze the sample solution rapidly. For fast electrolysis, the charge transfer between the WE and molecules in the solution must not be limited by slow diffusional transport of molecules to the electrode. Therefore, the distances between the molecules in solution and the electrode surface should be small. Since the manufacturer does not specify the exact geometry and number of the carbon fibers pressed into the Vycor tube, accurate distances can not be calculated Nevertheless, distances can be roughly estimated using the Vycor tube inner radius $r_{\mathrm{Vyc}} = 0.24\,\mathrm{cm}$ and the total working electrode surface area $A_{\mathrm{tot}} = 1000\,\mathrm{cm}^2$ as reported by the manufacturer.

The fibers are approximated as $l = 50\,\mathrm{mm}$ long rods with uniform radius r and are assumed to be closest packed into the Vycor tube (see Fig. 8.2a), *i.e.*, the centers of the cross-sectional circles are arranged in a hexagonal lattice (see Fig. 8.2b). The approximate number of rods n inside the Vycor tube is calculated via $n \approx \Theta(r_{\mathrm{Vyc}}/r)^2$, where $\Theta = \pi/\sqrt{12}$ [331] is the filling fraction in the hexagonal packing. The radius r of the rods is found by equating the surface area of n rods with the total surface area A_{tot} specified by the manufacturer ($nA_{\mathrm{rod}} = A_{\mathrm{tot}}$). This results in a rod radius $r \approx 16\,\mu\mathrm{m}$. The maximum distance $d_{\mathrm{max}} = (2/\sqrt{3} - 1)r = 2.5\,\mu\mathrm{m}$ to the nearest rod surface is calculated using the equilateral triangle shown in Fig. 8.2c. These tiny distances on the order of a few microns suggest – although only a very rough estimate and lower limit due to idealized assumptions – that fast electrolysis should be possible [328].

Experimentally, cyclic voltammetry can be used to check if the electrochemical cell behaves more like a thin-layer cell or a cell in the semi-infinite limit. In the semi-infinite limit, the

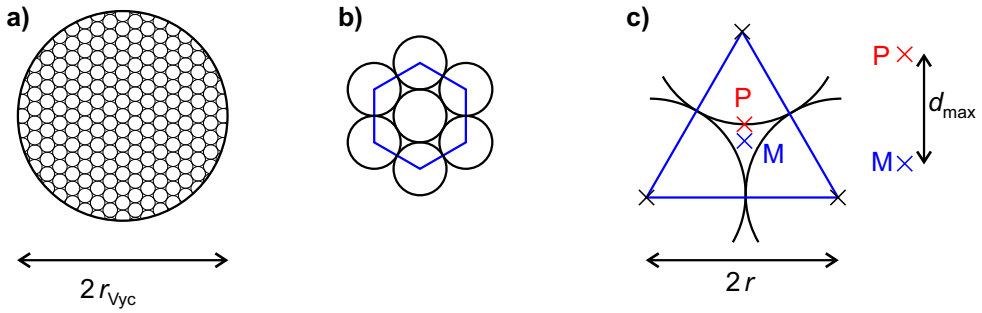

Figure 8.2: a) Cross-section of a Vycor tube packed with equal rods in the closest packing, which is described by b) the arrangement in the hexagonal lattice. c) Equilateral triangle used for the determination of the maximum distance d_{max} between the solution and the nearest rod surface. The maximum distance is given by the distance between the triangle midpoint M and the point P.

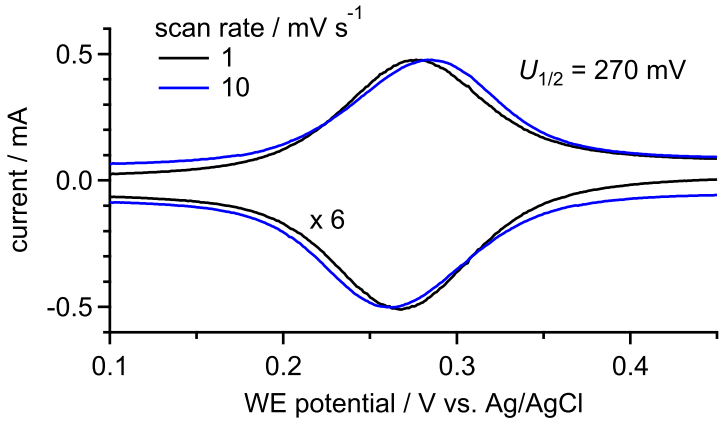

Figure 8.3: Cyclic voltammogram of 0.1 mM $K_4Fe(CN)_6$ for two different scan rates: 1 mV/s and 10 mV/s. The current obtained for the 1 mV/s scan rate was multiplied by a factor of 6 for comparison. The standard redox potential is $U_{1/2} \approx 270$ mV vs. Ag/AgCl.

faradaic current of an electrochemically reversible electron transfer reaction is limited by diffusional mass transfer [332]. The potential difference between the anodic and cathodic peaks is $\Delta U_\mathrm{p} \approx 57$ mV [333] whereas in the thin-layer limit $\Delta U_\mathrm{p} = 0$ mV results [332].

Fig. 8.3 shows two cyclic voltammograms of an aqueous solution of 0.1 mM $K_4Fe(CN)_6$ in 1 M KCl at different scan rates. For a scan rate of 1 mV/s, the potential difference ΔU_p between the anodic and cathodic peaks is 9 mV. The discrepancy between the experimentally measured 9 mV and the theoretically predicted 57 mV in the semi-infinite limit shows that the current is not limited by diffusional mass transport to the working electrode. The ideal case of $\Delta U_\mathrm{p} = 0$ mV in the thin-layer limit is also not reached, probably due to experimental imperfections and substantial ohmic drop $\Delta U = I R_\mathrm{u}$, where R_u is the uncompensated resistance, and I is the current flowing between WE and CE.

The effect of the ohmic drop is illustrated by an increase in the current I caused by the tenfold scan rate (10 mV/s). The current raises by a factor of six, which is expected to cause an increase in ohmic drop IR_u. The potential difference ΔU_p is found to change from 9 mV to 23 mV and is in agreement with the presence of substantial ohmic drop. Later, a more detailed quantification of the ohmic drop will be presented.

Electrolysis efficiency

Next, the electrolysis efficiency and speed are regarded more quantitatively. For highly photo-unstable molecules, a new sample volume in the laser focus per laser pulse is desirable. The needed solution flow rate $\mathrm{d}V/\mathrm{d}t$ is estimated by:

$$\frac{\mathrm{d}V}{\mathrm{d}t} = s\, f\, A, \tag{8.1}$$

where s is the one-dimensional size of the pump focus, f is the laser repetition rate, and A is the cross-sectional area of the flow-through cuvette. For typical values of $s = 100\,\mu$m,

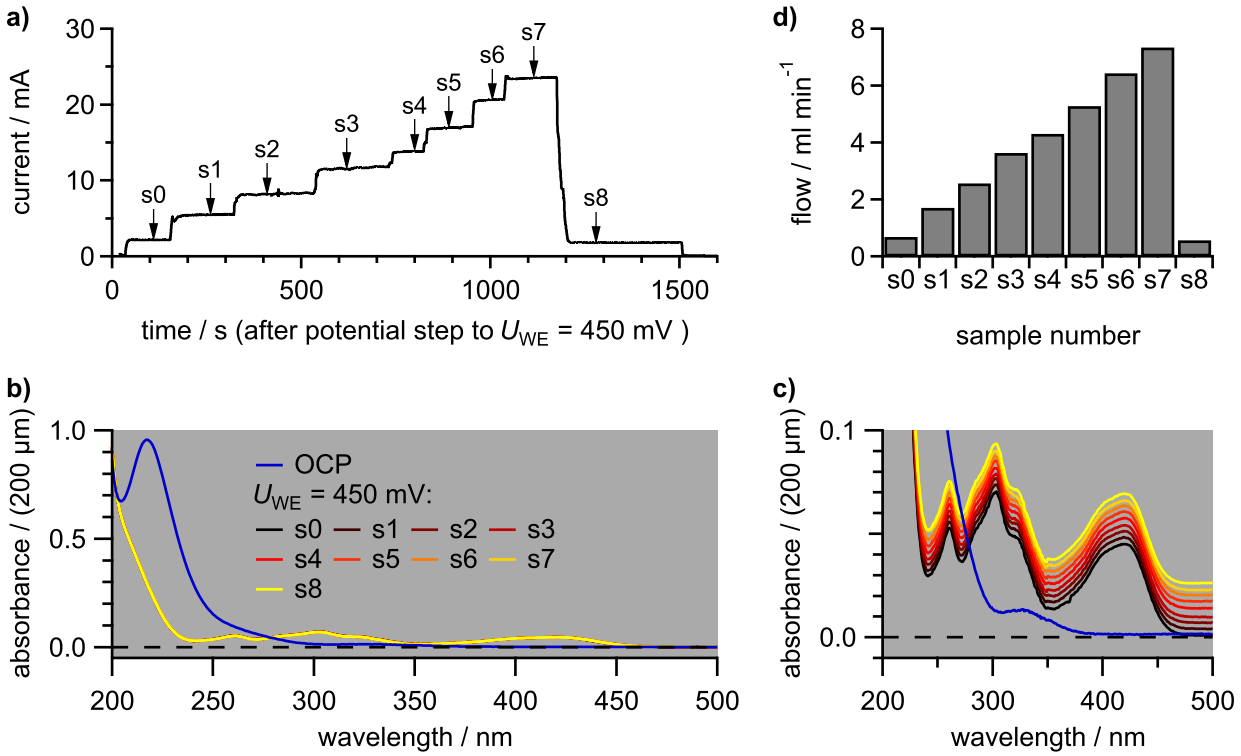

Figure 8.4: Results of a chronoamperometric flow electrolysis experiment coupled to linear absorption spectroscopy. a) Current as a function of time for nine different solution flow rates $\mathrm{d}V/\mathrm{d}t$. The arrows mark the time at which an absorption spectrum was collected. b) The absorption spectra demonstrate th the full conversion of ferrocyanide to ferricyanide at a WE potential of 450 mV for all tested flow rates. OCP = open circuit potential. c) Enlarged view on the absorption spectra at low absorbances. The spectra s0 - s8 are vertically offset for clarity. d) Calculated flow rates.

$f = 1\,\mathrm{kHz}$ and the cross-sectional area of the flow-through cuvette $A = wd = 1.6 \times 10^{-2}\,\mathrm{cm}^2$ (width $w = 0.8\,\mathrm{cm}$, path length $d = 0.02\,\mathrm{cm}$), the calculated flow rate is $\mathrm{d}V/\mathrm{d}t = 9.6\,\mathrm{mL/min}$. Here, the laser repetition rate $f = 1\,\mathrm{kHz}$ of the 2D electronic spectroscopy setup in the collaborating research group AK Brixner was chosen. This pretty high flow rate of $\approx 10\,\mathrm{mL/min}$ could be considerably lowered upon reducing the pump focus to spot sizes well below 10 µm by using a high numerical aperture objective. Furthermore, a flow-through cuvette of smaller cross-section like the commercially available cuvette Hellma 131,310-QS with a cross-section $A = (250\,\mu\mathrm{m})^2$ could be used. Both, reduction in pump focus size and cuvette cross-section, could theoretically lower the needed solution flow rate to below 0.04 mL/min.

The conversion efficiency as a function of the flow rate $\mathrm{d}V/\mathrm{d}t$ was experimentally determined by steady-state absorption spectroelectrochemistry. For this purpose, a chronoamperometric experiment with a $c = 2\,\mathrm{mM}$ $K_4Fe(CN)_6$ solution was conducted, and the results are shown in Fig. 8.4. At time $t = 0$, the WE potential was stepped from open circuit potential to 450 mV vs. Ag/AgCl, which is 180 mV more positive than the redox potential $U_{1/2}$. The Nernst equation predicts a nearly complete conversion to the oxidized species in thermodynamic equilibrium ([Ox]/[Red]$\approx 10^3$) for this WE potential. Then, the solution flow rate

was varied, and the current response, as well as the absorption spectrum, were recorded. Between each flow rate step and the measurement of the absorption spectrum, there was a sufficient waiting time to ensure that the electrolyzed solution has reached the cuvette. It has to be noted that the sample solution is not flowing in a cycle in this experiment. For each variation of the solution flow rate $\mathrm{d}V/\mathrm{d}t$, the current varies in a step-like fashion (Fig. 8.4a). Each flow rate step is marked with a sample number s0 - s8 and an arrow indicating the time at which an absorption spectrum was taken. Fig. 8.4b shows the resulting absorption spectra along with the blue spectrum of the reduced species $K_4Fe(CN)_6$, recorded at open circuit potential. The spectra at a WE potential $U_{WE} = 450\,\mathrm{mV}$ strongly differ from the spectrum taken at open circuit potential, which indicates the conversion of $K_4Fe(CN)_6$ to the oxidized species $K_3Fe(CN)_6$. The same absorption data at low absorbances are vertically offset for clarity and shown in Fig. 8.4c. The spectra s0 - s8 measured at different flow rates are identical. According to Appleby and Morton, $K_3Fe(CN)_6$ has an extinction coefficient $\epsilon(420\,\mathrm{nm}) = 1040\,(\mathrm{M\,cm})^{-1}$ [334]. For a complete conversion to $K_3Fe(CN)_6$, an absorbance $A = \epsilon\,c\,d = 42 \times 10^{-3}$ is calculated, which is close to the experimental absorbance $A = 45 \times 10^{-3}$ at 420 nm. Therefore, it can be concluded that the electrolysis efficiency is $\approx 100\,\%$ at all used flow rates. The knowledge about the complete electrolysis allows calculating the solution flow rate from the current plateaus observed after altering the power of the micro annular gear pump. For a faradaic current, the current is related to the flow rate by:

$$I = \frac{\mathrm{d}Q}{\mathrm{d}t} = c\,\frac{\mathrm{d}V}{\mathrm{d}t}\,z\,e, \tag{8.2}$$

where z is the number of electrons transferred per reaction and e is the elementary charge. The calculated flow rates, obtained by reversing equation (8.2), are shown in Fig. 8.4d for $z = 1$ and $c = 2\,\mathrm{mM}$. This analysis suggests that for flow rates up to at least $\mathrm{d}V/\mathrm{d}t = 7\,\mathrm{mL/min}$, the conversion efficiency is complete.

Error in WE potential

Next, the FEC is characterized in terms of the WE potential error arising from the uncompensated resistance R_u, which is illustrated using Fig. 8.5a. The current, which flows between WE and CE is impeded by the resistance $R = R_{Vycor} + R_s$ due to the Vycor glass tube (R_{Vycor}) and the solution resistance R_s. Part of this resistance, the so-called compensated resistance R_c, is already taken into account by the potentiostat. However, the uncompensated part R_u leads to an error between the measured and actual WE potential. Since the RE is placed outside the Vycor tube, R_u is given as the sum of R_{Vycor} and the solution resistance $R_{s,u}$ between WE and RE.

Experimentally, R_u can be determined by the current interrupt method using the pure electrolyte without analyte in the cell. The method and the results for a 1M KCl solution are illustrated in Fig. 8.5b. A constant current $I = 2.4\,\mathrm{A}$ is applied, which results from non-faradaic charging of the double layer at the WE/electrolyte interface. Simultaneously the

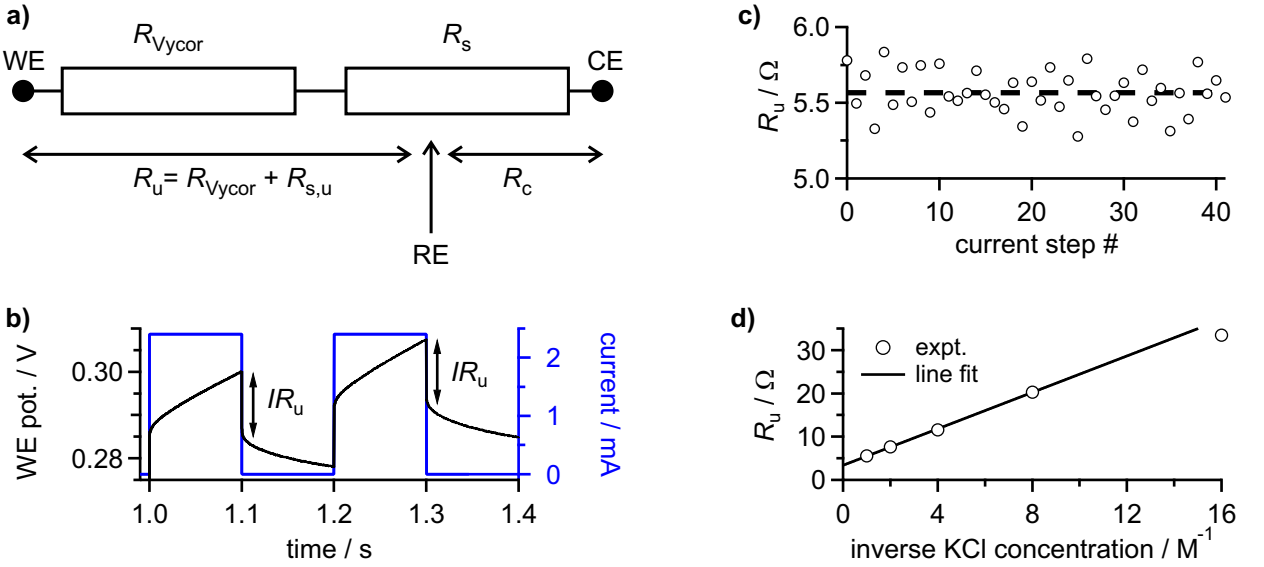

Figure 8.5: a) Equivalent circuit illustrating the uncompensated (R_u) and compensated (R_c) resistances. b) Results of a current interrupt experiment using 1 M KCl electrolyte. c) Uncompensated resistance values extracted from the ohmic drop IR_u for 42 consecutive measurements with an average of $R_u = (5.6 \pm 0.1)\,\Omega$. d) Averaged R_u values at different inverse KCl concentrations. The line fit uses the four data points with the highest KCl concentration. The slope is $(2.1 \pm 0.1)\,\Omega\,M$, and the y-intercept at infinite KCl concentration is $R_{Vycor} = (3.4 \pm 0.1)\,\Omega$.

WE potential is measured. A sudden decrease in current to zero leads to an instantaneous drop in WE potential, which equals IR_u. Fig. 8.5c shows the uncompensated resistance R_u for several current steps, which gives $R_u = (5.6 \pm 0.1)\,\Omega$. The uncompensated resistance at different electrolyte concentrations is shown in Fig. 8.5d. For higher KCl concentrations, R_u is reduced because of a decreasing solution resistance. In the limit of infinite electrolyte concentration, R_s should be negligible, and R_{Vycor} can be extracted by an extrapolation $1/c \to 0$. Such an extrapolation gives a value $R_{Vycor} \approx 3.4\,\Omega$.

8.3 Proof of Principle TA Measurements

For a proof of principle TA study, the water-soluble dye methylene blue (MB) was chosen. Fig. 8.6a shows the chemical structures of MB and its reduced, colorless form leucomethylene blue (LMB). According to Impert *et al.*, the standard redox potential of the LMB/MB^+ redox pair is $U_{1/2} \approx -0.2\,V$ vs. Ag/AgCl ($U_{1/2} \approx 0.0\,V$ vs. SHE) at pH = 7 [335]. For much more negative WE potentials than $U_{1/2}$, MB is expected to be fully converted to LMB, whereas at much more positive WE potentials MB is not electrolyzed. Fig. 8.6b - d show the steady-state absorption and TA spectra of a 0.2 mM methylene blue solution in 1 M KCl at three different WE potentials. The spectra were kindly measured and provided by Pascal Kunkel. For a WE potential of 0.0 V vs. Ag/AgCl (Fig. 8.6b), the absorption spectrum shows two broad absorption bands at 1.87 eV and 2.04 eV. The 2.04 eV band originates from

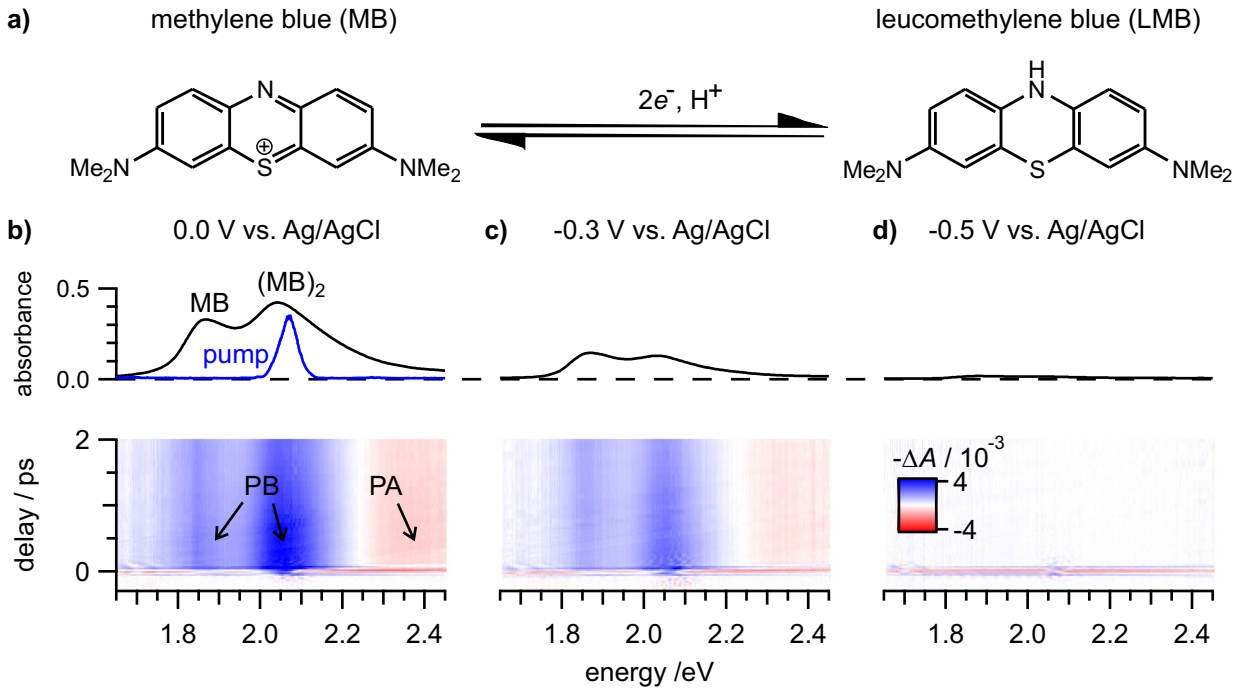

Figure 8.6: a) Redox equilibrium between MB and LMB. b) Steady-state absorption spectra and TA maps at a WE potential of 0.0 V, c) -0.3 V and d) -0.5 V vs. Ag/AgCl. All experimental data were kindly provided by Pascal Kunkel.

the absorption of the H-type $(MB)_2$ dimer, whereas the 1.87 eV band belongs to the absorption of the MB monomer [336, 337]. Pump pulses centered at 2.07 eV (blue spectrum in Fig. 8.6b) with a probed pulse fluence on the order of $10^{14}\,\mathrm{cm}^{-2}$ were used to excite the $(MB)_2$ dimer resonantly. The TA map at a WE potential $U_{\mathrm{WE}} = 0.0\,\mathrm{V}$ vs. Ag/AgCl is shown in Fig. 8.6b. Ground state depletion leads to a strong photobleach (PB) of the dimer absorption band and a weaker bleach of the monomer absorption band. Additionally, a weak photoabsorption (PA) signal at 2.36 eV is detected. The decay of the dimer PB signal happens on a sub-10 ps timescale, which is in agreement with measurements by Dean *et al.* suggesting efficient nonradiative decay [336]. Fig. 8.6c shows the linear absorption and TA spectra for a WE potential of −0.3 V vs. Ag/AgCl, which is slightly lower than the LMB/MB redox potential $U_{1/2} \approx -0.2\,\mathrm{V}$. The overall absorbance is reduced due to the formation of the colorless LMB. Additionally, the relative intensities of dimer and monomer absorption bands changed. This can be explained by the reduction of the total MB concentration, *i.e.*, monomer plus dimer, shifting the dimerization equilibrium to the monomer side. Although the dimer absorption is lower in intensity than the monomer absorption, the PB of the MB_2 dimer is still the dominant feature in TA after resonant dimer excitation. For even more negative WE potential ($U_{\mathrm{WE}} = -0.5\,\mathrm{V}$, Fig. 8.6d), only some residual absorption can be detected. This indicates a nearly complete conversion of MB to LMB. The complete conversion to LMB is also evident in the TA map where the PB signals are suppressed below the noise level. Only the coherent artifact of the electrolyte is detected.

8.4 Conclusion and Outlook

In conclusion, a flow-electrolysis cell was integrated into a transient absorption setup for time-resolved spectroelectrochemistry of molecular systems in solution. The flow-electrolysis cell was characterized in terms of its thin-layer characteristics, electrolysis efficiency, and errors in WE potential caused by the uncompensated resistance. Electrolysis efficiencies of $\approx 100\,\%$ for flow rates exceeding $7\,\mathrm{mL/min}$ could be demonstrated. The rapid electrolysis allows probing a new sample volume per laser shot for widespread $1\,\mathrm{kHz}$ laser systems, as long as pump focus sizes and cross-sectional areas of flow-through cuvettes are chosen to be small.

First time-resolved experiments using the flow-electrolysis cell HX-301 were successfully performed. The water-soluble dye methylene blue was reduced to its colorless leuco form, and transient absorption spectra at different working electrode potentials were recorded. A suppression of TA signal intensities below the noise level demonstrated the full conversion of methylene blue to leucomethylene blue.

However, many molecules cannot be dissolved or electrolyzed in aqueous electrolytes. Therefore, the setup is extended to organic electrolytes in the future. Additionally, electrolysis under an inert gas atmosphere is desirable for air-sensitive molecules or electrolysis products. The presented experiments form the basis for time-resolved spectroelectrochemistry on molecules, performed by Markus Voelckel and Julia Heitmüller. First results coupling electrochemistry in an organic electrolyte and coherent 2D electronic spectroscopy have already been obtained by Julia Heitmüller in the research group of Prof. Brixner.

9 Summary

Doping plays a decisive role for the functionality of semiconductor-based (opto-)electronic devices. Hence, the technological utilization of semiconductors necessitates control and a fundamental understanding of the doping process. However, for low-dimensional systems like carbon nanotubes, neither concentration nor distribution of charge carriers is currently well known.

The research presented in this thesis investigated the doping of semiconducting carbon nanotubes by spectroscopic methods. Samples of highly purified, intrinsic (6,5) single-wall carbon nanotubes were fabricated using polymer stabilization.

Chapter 4 showed that both electro- and redox chemical p-doping lead to identical bleaching, blueshift, broadening and asymmetry of the S_1 exciton absorption band. The similar spectral changes induced by both doping schemes suggest that optical spectra can not be used to infer what process was used for doping. Perhaps more importantly, it also indicates that the distribution of charges and the character of the charge transfer states does not depend on the method by which doping was achieved.

The detailed analysis of the doping-induced spectral changes in chapter 5 suggests that surplus charges are distributed inhomogeneously. The hypothesis of carrier localization is consistent with the high sensitivity of the S_1 exciton photoluminescence to additional charge carriers and with the stretched-exponential decay of the exciton population following ultrafast excitation. Both aspects are in good agreement with diffusion-limited contact quenching of excitons at localized charges. Moreover, localized charges act – similar to structural defects – as perturbations to the bandstructure as evidenced by a doping-induced increase of the D-band antiresonance in the mid-infrared spectrum.

Quantum mechanical model calculations also suggest that counterions play a crucial role in carrier localization. Counterion adsorption at the nanotube surface is thus believed to induce charge traps of more than 100 meV depth with a carrier localization length on the order of 3 - 4 nm. The doping-induced bleach of interband absorption is accompanied by an absorption increase in the IR region below 600 meV. The observed shift of the IR peak position indicates a continuous transition from localized to rather delocalized charge carriers. This transition is caused by the increase of the overlap of charge carrier wavefunctions at higher charge densities and was modeled by classical Monte-Carlo simulations of intraband absorption.

Chapter 6 discussed the spectroscopy of heavily (degenerately) doped nanotubes, which are characterized by a Drude-response of free-carrier intraband absorption in the optical conductivity spectrum. In the NIR spectral region, the S_1 exciton and X_1^+ trion absorption is replaced by a nearly 1 eV broad and constant absorption signal, the so-called H-band. The

linear and transient absorption spectra of heavily doped nanotubes suggest that the H-band can be attributed to free-carrier interband transitions.

Chapter 7 dealt with the quantification of charge carrier densities by linear absorption spectroscopy. A particularly good measure of the carrier density is the S_1 exciton bleach. For a bleach below about 50 %, the carrier density is proportional to the bleach. At higher doping levels, deviations from the linear behavior were observed. For doping levels exceeding a fully bleached S_1 band, the determination of the normalized oscillator strength f_{1st} over the whole first subband region (trion, exciton, free *e-h* pairs) is recommended for quantification of carrier densities. Based on the nanotube density of states, the carrier density n can be estimated using $n = 0.74\,\mathrm{nm}^{-1} \cdot (1 - f_{1st})$.

In the last part of this thesis (chapter 8), the time-resolved spectroelectrochemistry was extended to systems beyond photostable carbon nanotube films. The integration of a flow-electrolysis cell into the transient absorption spectrometer allows the investigation of *in-situ* electrochemically generated but photounstable molecules due to a continuous exchange of sample volume. First time-resolved experiments were successfully performed using the dye methylene blue and its electrochemically reduced form leucomethylene blue.

10 Zusammenfassung

Die Dotierung von Halbleitern spielt eine entscheidende Rolle für die Funktionsweise von halbleiterbasierten (opto-)elektronischen Bauteilen. Deshalb erfordert die technische Nutzbarmachung von Halbleitern die Kontrolle und ein fundamentales Verständnis des Dotierungsprozesses. Für niederdimensionale Halbleiter, wie Kohlenstoffnanoröhren, ist momentan weder die Dichte noch die Verteilung von Ladungsträgern genau bekannt.

In dieser Arbeit wurde die Dotierung von halbleitenden Kohlenstoffnanoröhren mittels spektroskopischer Methoden untersucht. Proben hochreiner, intrinsischer und einwandiger (6,5) Kohlenstoffnanoröhren wurden durch Polymerstabilisierung hergestellt.

In Kapitel 4 wurde gezeigt, dass sowohl die elektro-, als auch die redoxchemische *p*-Dotierung zu einem identischen Bleichen, einer Blauverschiebung, Verbreiterung und Asymmetrie der Absorptionsbande des S_1 Exzitons führt. Die ähnlichen spektralen Änderungen, die durch beide Dotierungsverfahren induziert wurden, legen den Schluss nahe, dass optische Spektren nicht zur Identifikation des Dotierungsverfahrens genutzt werden können. Möglicherweise wichtiger ist die Schlussfolgerung, dass die Ladungsverteilung und der Charakter der Ladungen nicht davon abhängt mittels welcher Methode die Dotierung erreicht wurde.

Die detaillierte Analyse der durch Dotierung hervorgerufenen spektralen Änderungen in Kapitel 5 deutet eine inhomogene Verteilung der Überschussladungen an. Die Hypothese der Ladungsträgerlokalisierung ist konsistent mit der hohen Sensitivität der Photolumineszenz des S_1-Exzitons auf zusätzliche Ladungen und mit dem gestreckt-exponentiellen Zerfall der Exzitonenpopulation nach ultrakurzer Anregung. Beide Aspekte sind in guter Übereinstimmung mit dem diffusionslimitierten Kontaktlöschen von Exzitonen an lokalisierten Ladungen. Weiterhin wirken lokalisierte Ladungen – ähnlich zu strukturellen Defekten – als Störungen der Bandstruktur. Dies wurde durch den dotierungsbedingten Anstieg der D-Bandenantiresonanz im mittleren Infrarot nachgewiesen.

Quantenmechanische Modellrechnungen deuten weiterhin darauf hin, dass Gegenionen eine entscheidende Rolle bei der Ladungsträgerlokalisierung spielen. Die Adsorption von Gegenionen an der Nanorohroberfläche induziert Fallenzustände für Ladungen, die mehr als 100 meV tief sind. Weiterhin ergibt sich eine Lokalisierungslänge der Ladungsträger von ungefähr 3 - 4 nm. Das dotierungsbedingte Bleichen der Interbandabsorption wird begleitet von einem Anstieg der Absorption im IR-Bereich unterhalb von 600 meV. Die beobachtete Verschiebung der IR-Peakposition deutet einen kontinuierlichen Übergang von lokalisierten zu delokalisierten Ladungsträgern an. Dieser Übergang wird durch den steigenden Überlapp der Ladungsträgerwellenfunktionen bei höheren Ladungsdichten verursacht und wurde durch klassische Monte-Carlo-Simulationen der Intrabandabsorption modelliert.

In Kapitel 6 wurde die Spektroskopie stark dotierter (entartet dotierter) Nanoröhren diskutiert. Dieses zeichnen sich durch eine Drude-Antwort der Intrabandabsorption freier Ladungsträger im Spektrum der optischen Leitfähigkeit aus. Im NIR-Spektralbereich wird die Absorption des S_1-Exzitons und des X_1^+-Trions durch ein beinahe 1 eV breites und konstantes Absorptionssignal, die sogenannte H-Bande, ersetzt. Die linearen und transienten Absorptionsspektren stark dotierter Nanoröhren legt den Schluss nahe, dass die H-Bande Interbandübergängen freier Ladungsträger zugeordnet werden kann.

Kapitel 7 beschäftigte sich mit der Quantifizierung von Ladungsträgerdichten mittels linearer Absorptionsspektroskopie. Ein besonders gutes Maß für die Ladungsträgerdichte ist das Bleichen des S_1 Exzitons. Für ein Bleichen unterhalb von ungefähr 50 % ist die Ladungsträgerdichte proportional zum Bleichen. Bei höherer Dotierung wurden Abweichungen vom linearen Verhalten beobachtet. Für Dotierungen jenseits einer vollständig gebleichten S_1-Bande wird zur Quantifizierung der Ladungsträgerdichte die Bestimmung der normierten Oszillatorstärke über den gesamten ersten Subbandbereich (Trion, Exziton, freie *e*-*h*-Paare) empfohlen. Basierend auf der Zustandsdichte der Nanoröhren kann die Ladungsträgerdichte n mittels $n = 0.74\ \mathrm{nm}^{-1} \cdot (1 - f_{1\mathrm{st}})$ abgeschätzt werden.

Im letzten Teil dieser Arbeit (Kapitel 8) wurde die zeitaufgelöste Spektroelektrochemie auf Systeme jenseits photostabiler Kohlenstoffnanoröhren ausgeweitet. Der Einbau einer Flusselektrolysezelle in das transiente Absorptionsspektrometer erlaubt die Untersuchung von elektrochemisch *in-situ* hergestellten aber photoinstabilen Molekülen durch einen kontinuierlichen Austausch des Probenvolumens. Die ersten zeitaufgelösten Experimente wurden erfolgreich anhand des Farbstoffs Methylenblau und dessen reduzierter Form Leukomethylenblau durchgeführt.

11 Appendix

11.1 Exciton PL Quantum Yield

The S_1 PL quantum yield (PLQY) as a function of the S_1 exciton bleach χ ($0\,\% \leq \chi \leq 100\,\%$) can be calculated by:

$$\mathrm{PLQY}(\chi) = \frac{k_\mathrm{r}(\chi)}{k_\mathrm{r}(\chi) + k_\mathrm{nr}(\chi)} \cdot (1-\chi) \approx \frac{k_\mathrm{r}(\chi)}{k_\mathrm{nr}(\chi)} \cdot (1-\chi), \tag{11.1}$$

where k_r and k_nr are the radiative and nonradiative decay rates. The approximation in equation (11.1) is valid for $\mathrm{PLQY} \ll 1$, which is the case even for intrinsic nanotubes. The factor $(1-\chi)$ accounts for a PL decrease due to an exciton bleach in addition to variations in exciton dynamics.

Band filling model

The exciton bleach can be caused by two effects: phase space filling and screening. Here, it is assumed that phase space filling (PSF) provides the dominant contribution. Changes in screening are neglected in the following. This means that the exciton binding energy and exciton size are independent of the doping level. In turn, this suggests a constant radiative decay rate [51, 307]:

$$k_\mathrm{r}(\chi) = k_\mathrm{r}(0) = k_{\mathrm{r},0}, \tag{11.2}$$

where the subscript '0' indicates the intrinsic quantity.

In this case, the doping-induced PL drop is mainly driven by an increase in nonradiative decay rate

$$k_\mathrm{nr}(\chi) = k_{\mathrm{nr},0} + \chi \cdot A \cdot k_{\mathrm{nr},0} \tag{11.3}$$

$$= k_{\mathrm{nr},0}[1 + A \cdot \chi], \tag{11.4}$$

where the product $A \cdot k_{\mathrm{nr},0}$ is the increase in nonradiative decay rate for a complete exciton bleaching.

Here, it was assumed that

- the nonradiative decay rate increases linearly with charge density
- charge densities are proportional to the exciton bleach χ.

The absolute PL quantum yield is given by:

$$\mathrm{PLQY}_{\mathrm{abs}}(\chi) \approx \frac{k_{\mathrm{r}}(\chi)}{k_{\mathrm{nr}}(\chi)} \cdot (1-\chi) \tag{11.5}$$

$$= \frac{k_{\mathrm{r},0}}{k_{\mathrm{nr},0}[1+A\cdot\chi]} \cdot (1-\chi) \tag{11.6}$$

$$= \frac{\mathrm{PLQY}_0}{1+A\cdot\chi} \cdot (1-\chi). \tag{11.7}$$

The relative PL quantum yield is obtained upon division by PLQY_0:

$$\mathrm{PLQY}_{\mathrm{rel}}(\chi) = \frac{1-\chi}{1+A\cdot\chi}. \tag{11.8}$$

Localized charge model

For intrinsic SWNTs, the PL quantum yield in the diffusive-limited contact quenching model is given by [98]:

$$\mathrm{PLQY}_0 = \frac{k}{(1/d_0)^2}, \tag{11.9}$$

where k is a constant and d_0 is the average distance between quenching sites.

Contact quenching at localized charges of density n is incorporated via:

$$\mathrm{PLQY}(n) = \frac{k}{(1/d_0+n)^2}. \tag{11.10}$$

Note that the charge carrier density is inversely proportional to the average distance $\overline{w} = n^{-1}$ between charges.

Next, it is assumed that each localized charge blocks a certain width Δ of the intrinsic tube length, where S_1 absorption occurs. The exciton bleach is then described by $\chi = n\Delta$. Rearranging yields $n = \chi/\Delta$, which is plugged into equation (11.10) to result in an absolute PL quantum yield

$$\mathrm{PLQY}_{\mathrm{abs}}(\chi) = \frac{k}{(1/d_0+\chi/\Delta)^2} \cdot (1-\chi), \tag{11.11}$$

where the factor $(1-\chi)$ is again introduced to account for the drop in PL quantum yield caused by a decreased oscillator strength in addition to changes in S_1 dynamics.

The relative PL quantum yield is obtained upon division by PLQY_0:

$$\mathrm{PLQY}_{\mathrm{rel}}(\chi) = \frac{(1/d_0)^2}{(\frac{1}{d_0}+\frac{\chi}{\Delta})^2} \cdot (1-\chi). \tag{11.12}$$

Expanding the fraction by d_0^2 and simplifying gives

$$\mathrm{PLQY}_{\mathrm{rel}}(\chi) = (1-\chi)\left[1+\frac{d_0}{\Delta}\chi\right]^{-2}, \tag{11.13}$$

where d_0/Δ is the only fit coefficient.

Relative PL quantum yield from time-resolved experiments

The stationary PL intensity can be related to the exciton dynamics via:

$$\mathrm{PL} \propto \int_0^\infty P(t)\,\mathrm{d}t, \tag{11.14}$$

where $P(t)$ is the time-dependent exciton population. In a pump-probe experiment, the normalized signal intensity $\Delta A(t)$ is well described by a stretched exponential decay of the form

$$\Delta A(t) = \exp\left(-\sqrt{\frac{t}{\tau_w}}\right), \tag{11.15}$$

where τ_w is a characteristic diffusion time after which the signal has decayed to 1/e. Assuming $P(t) \propto \Delta A(t)$, the steady-state PL is given by:

$$\mathrm{PL} \propto \int_0^\infty \exp\left(-\sqrt{\frac{t}{\tau_w}}\right)\mathrm{d}t \tag{11.16}$$

$$= 2\tau_w. \tag{11.17}$$

Therefore, the relative PL intensity and PLQY can be obtained from a time-resolved experiment via:

$$\frac{\mathrm{PLQY}(\chi)}{\mathrm{PLQY}_0} = \frac{\mathrm{PL}(\chi)}{\mathrm{PL}_0} = \frac{\tau_w(\chi)}{\tau_{w,0}} \cdot (1-\chi), \tag{11.18}$$

where the factor $(1-\chi)$ accounts again for a PL decrease due to a reduced exciton oscillator strength besides the variations in exciton dynamics.

11.2 Drude Analysis of Heavily Doped SWNTs

Drude response

For heavily doped SWNT films, the optical conductivity is well described by a Drude response:

$$\sigma(\omega) = \frac{ne^2\tau/m^*}{1-i\omega\tau} = \frac{\sigma_0}{1-i\omega\tau} = ne\mu(\omega), \tag{11.19}$$

where ω is the angular frequency, n is the volumetric charge density (in nm^{-3}), e is the elementary charge, τ is the average scattering time, m^* is the effective carrier mass, σ_0 is the DC conductivity, and $\mu(\omega)$ is the complex mobility.

The DC mobility ($\omega = 0$) and the volumetric carrier density are given by:

$$\mu_0 = \frac{e\tau}{m^*} \tag{11.20}$$

$$n = \frac{\sigma_0}{e\mu_0}. \tag{11.21}$$

SWNT carrier density

To obtain a one-dimensional SWNT carrier density n_{SWNT}, the volumetric charge density has to be multiplied by A_{SWNT}/θ, where $A_{\mathrm{SWNT}} = \pi(d/2)^2 \approx 0.44\,\mathrm{nm}^2$ is the nanotube cross-sectional area for a (6,5)-SWNT diameter $d = 0.75\,\mathrm{nm}$. The filling factor θ is defined as:

$$\theta = \frac{V_{\mathrm{SWNT}}}{V_{\mathrm{film}}}, \tag{11.22}$$

where V_{SWNT} is the volume occupied by SWNTs and V_{film} is the total film volume.

The SWNT volume is calculated by

$$V_{\mathrm{SWNT}} = \frac{c_{\mathrm{C}} V_{\mathrm{disp}} A_{\mathrm{SWNT}}}{N_{\mathrm{C}}}, \tag{11.23}$$

where c_{C} is the carbon atom concentration in dispersion, V_{disp} is the filtrated dispersion volume and $N_{\mathrm{C}} = 88\,\mathrm{nm}^{-1}$ is the number of carbon atoms per unit length. According to Schöppler *et al.*, the carbon atom concentration c_{C} is obtained from absorption spectroscopy [307].

The product of the cross-sectional area A_{film} and the height h_{film} of the film define the film volume V_{film}. The cross-sectional area is $A_{\mathrm{film}} = \pi(d_{\mathrm{fs}}/2)^2$, where $d_{fs} \approx 1.625\,\mathrm{cm}$ is the diameter of the filtration system and equals the SWNT film diameter. Profilometer measurements determined the height.

Results

The following values were used for the calculation:

$$\begin{aligned}
\tau &= 19.3\,\mathrm{fs} \\
m^* &= 0.07\,m_e \ \ (m_e = \text{electron mass}) \\
\sigma_0 &= 405\,\mathrm{A/(V\,cm)} \\
h_{\mathrm{film}} &= 531\,\mathrm{nm} \\
c_{\mathrm{C}} &= 7.38 \cdot 10^{16}\,\mathrm{mL}^{-1} \\
V_{\mathrm{disp}} &= 6\,\mathrm{mL},
\end{aligned}$$

where the scattering time τ and the DC conductivity σ_0 were determined from the Drude response of heavily doped SWNTs and the effective hole mass m^* was taken from reference [18].

The following results were obtained:

$$\begin{aligned} \mu_0 &= 485\,\mathrm{cm}^2/(\mathrm{V\,s}) \\ \theta &= 2.0\,\% \\ n_{\mathrm{SWNT}} &= 0.114\,\mathrm{nm}^{-1}, \end{aligned}$$

which means that there is a charge every 8.77 nm.

Bibliography

[1] J. Bardeen, W. H. Brattain, "The Transistor, A Semi-Conductor Triode", *Physical Review* **1948**, *74*, 230–231, DOI 10.1103/PhysRev.74.230.

[2] W. B. Shockley, Nobel Lecture:Transistor Technology Evokes New Physics, **1956**, https://www.nobelprize.org/prizes/physics/1956/shockley/lecture/ (visited on 06/28/2019).

[3] M. Riordan, L. Hoddeson, P. Platzman, "Crystal Fire: The Birth of the Information Age", *American Journal of Physics* **1999**, *67*, 648–650, DOI 10.1119/1.19345.

[4] A. Ozcan, "Mobile phones democratize and cultivate next-generation imaging, diagnostics and measurement tools", *Lab on a chip* **2014**, *14*, 3187–3194, DOI 10.1039/c4lc00010b.

[5] R. W. Keyes, "Physical limits of silicon transistors and circuits", *Reports on Progress in Physics* **2005**, *68*, 2701–2746, DOI 10.1088/0034-4885/68/12/R01.

[6] M. M. Shulaker et al., "Three-dimensional integration of nanotechnologies for computing and data storage on a single chip", *Nature* **2017**, *547*, 74–78, DOI 10.1038/nature22994.

[7] A. D. Franklin et al., "Sub-10 nm carbon nanotube transistor", *Nano Letters* **2012**, *12*, 758–762, DOI 10.1021/nl203701g.

[8] G. J. Brady et al., "Quasi-ballistic carbon nanotube array transistors with current density exceeding Si and GaAs", *Science advances* **2016**, *2*, e1601240, DOI 10.1126/sciadv.1601240.

[9] T. Dürkop, S. A. Getty, E. Cobas, M. S. Fuhrer, "Extraordinary Mobility in Semiconducting Carbon Nanotubes", *Nano Letters* **2004**, *4*, 35–39, DOI 10.1021/nl034841q.

[10] A. Javey, J. Guo, Q. Wang, M. Lundstrom, H. Dai, "Ballistic carbon nanotube field-effect transistors", *Nature* **2003**, *424*, 654–657, DOI 10.1038/nature01797.

[11] M. S. Arnold et al., "Recent developments in the photophysics of single-walled carbon nanotubes for their use as active and passive material elements in thin film photovoltaics", *Physical chemistry chemical physics* **2013**, *15*, 14896–14918, DOI 10.1039/C3CP52752B.

[12] I. V. Zaporotskova, N. P. Boroznina, Y. N. Parkhomenko, L. V. Kozhitov, "Carbon nanotubes: Sensor properties. A review", *Modern Electronic Materials* **2016**, *2*, 95–105, DOI 10.1016/j.moem.2017.02.002.

[13] M. S. Arnold, S. I. Stupp, M. C. Hersam, "Enrichment of Single-Walled Carbon Nanotubes by Diameter in Density Gradients", *Nano Letters* **2005**, *5*, 713–718, DOI 10.1021/nl050133o.

[14] M. S. Arnold, A. A. Green, J. F. Hulvat, S. I. Stupp, M. C. Hersam, "Sorting carbon nanotubes by electronic structure using density differentiation", *Nature Nanotechnology* **2006**, *1*, 60–65, DOI 10.1038/nnano.2006.52.

[15] H. Ozawa, N. Ide, T. Fujigaya, Y. Niidome, N. Nakashima, "One-pot Separation of Highly Enriched (6,5)-Single-walled Carbon Nanotubes Using a Fluorene-based Copolymer", *Chemistry Letters* **2011**, *40*, 239–241, DOI 10.1246/cl.2011.239.

[16] G. J. Brady et al., "Polyfluorene-sorted, carbon nanotube array field-effect transistors with increased current density and high on/off ratio", *ACS Nano* **2014**, *8*, 11614–11621, DOI 10.1021/nn5048734.

[17] A. Graf et al., "Large scale, selective dispersion of long single-walled carbon nanotubes with high photoluminescence quantum yield by shear force mixing", *Carbon* **2016**, *105*, 593–599, DOI 10.1016/j.carbon.2016.05.002.

[18] H. Hartleb, F. Späth, T. Hertel, "Evidence for Strong Electronic Correlations in the Spectra of Gate-Doped Single-Wall Carbon Nanotubes", *ACS Nano* **2015**, *9*, 10461–10470, DOI 10.1021/acsnano.5b04707.

[19] A. D. Avery et al., "Tailored semiconducting carbon nanotube networks with enhanced thermoelectric properties", *Nature Energy* **2016**, *1*, 16033, DOI 10.1038/nenergy.2016.33.

[20] A. Chernikov et al., "Electrical Tuning of Exciton Binding Energies in Monolayer WS_2", *Physical Review Letters* **2015**, *115*, 126802, DOI 10.1103/PhysRevLett.115.126802.

[21] K. F. Mak et al., "Tightly bound trions in monolayer MoS_2", *Nature Materials* **2013**, *12*, 207–211, DOI 10.1038/nmat3505.

[22] V. Huard, R. T. Cox, K. Saminadayar, A. Arnoult, S. Tatarenko, "Bound states in optical absorption of semiconductor quantum wells containing a two-dimensional electron Gas", *Physical Review Letters* **2000**, *84*, 187–190, DOI 10.1103/PhysRevLett.84.187.

[23] F. Wang, G. Dukovic, L. E. Brus, T. F. Heinz, "The Optical Resonances in Carbon Nanotubes Arise from Excitons", *Science* **2005**, *308*, 838–841, DOI 10.1126/science.1110265.

[24] J. Maultzsch et al., "Exciton binding energies in carbon nanotubes from two-photon photoluminescence", *Physical Review B* **2005**, *72*, 241402, DOI 10.1103/PhysRevB.72.241402.

[25] J. Maultzsch et al., "Excitons in carbon nanotubes", *Physica Status Solidi (b)* **2006**, *243*, 3204–3208, DOI 10.1002/pssb.200669131.

[26] J. Lefebvre, P. Finnie, "Excited Excitonic States in Single-Walled Carbon Nanotubes", *Nano Letters* **2008**, *8*, 1890–1895, DOI 10.1021/nl080518h.

[27] S. M. Santos et al., "All-Optical Trion Generation in Single-Walled Carbon Nanotubes", *Physical Review Letters* **2011**, *107*, 187401, DOI 10.1103/PhysRevLett.107.187401.

[28] R. Matsunaga, K. Matsuda, Y. Kanemitsu, "Observation of Charged Excitons in Hole-Doped Carbon Nanotubes Using Photoluminescence and Absorption Spectroscopy", *Physical Review Letters* **2011**, *106*, 037404, DOI 10.1103/PhysRevLett.106.037404.

[29] N. Akizuki et al., "Nonlinear photoluminescence properties of trions in hole-doped single-walled carbon nanotubes", *Physical Review B* **2014**, *89*, 195432, DOI 10.1103/PhysRevB.89.195432.

[30] J. S. Park et al., "Observation of Negative and Positive Trions in the Electrochemically Carrier-Doped Single-Walled Carbon Nanotubes", *Journal of the American Chemical Society* **2012**, *134*, 14461–14466, DOI 10.1021/ja304282j.

[31] M. Yoshida, A. Popert, Y. K. Kato, "Gate-voltage induced trions in suspended carbon nanotubes", *Physical Review B* **2016**, *93*, 041402, DOI 10.1103/PhysRevB.93.041402.

[32] N. Rühl, "Spektroelektrochemie an einzelnen (6,5)-Kohlenstoffnanöhren", University of Würzburg, **2014**.

[33] M. Grundmann, *The Physics of Semiconductors*, 1. ed., Springer, Berlin, Heidelberg, **2006**.

[34] M. D. McCluskey, E. E. Haller, *Dopants and Defects in Semiconductors*, 1. ed., CRC Press, Boca Raton, **2012**.

[35] A. F. Holleman, E. Wiberg, N. Wiberg, *Lehrbuch der anorganischen Chemie*, 102. ed., de Gruyter, Berlin, **2007**.

[36] C. Klingshirn, *Semiconductor optics*, 4. ed., Springer, Berlin, Heidelberg, **2012**.

[37] A. Zunger, "Practical doping principles", *Applied Physics Letters* **2003**, *83*, 57–59, DOI 10.1063/1.1584074.

[38] B. I. Shklovskii, A. L. Ėfros, *Electronic properties of doped semiconductors*, *Vol. 45*, Springer, Berlin, Heidelberg, **1984**.

[39] I. Salzmann, G. Heimel, "Toward a comprehensive understanding of molecular doping organic semiconductors (review)", *Journal of Electron Spectroscopy and Related Phenomena* **2015**, *204*, 208–222, DOI 10.1016/j.elspec.2015.05.001.

[40] S. M. Sze, K. K. Ng, *Physics of semiconductor devices*, 3. ed., John Wiley & Sons, Inc, Hoboken, **2007**.

[41] E. F. Schubert, *Physical Foundations of Solid-State Devices*, ebook, **2015**.

[42] C. Xiao, D. Yang, X. Yu, L. Xiang, D. Que, "Determination of the Boron and Phosphorus Ionization Energies in Compensated Silicon by Temperature-Dependent Luminescence", *Silicon* **2017**, *9*, 147–151, DOI 10.1007/s12633-014-9193-3.

[43] C. Jagannath, Z. W. Grabowski, A. K. Ramdas, "Linewidths of the electronic excitation spectra of donors in silicon", *Physical Review B* **1981**, *23*, 2082–2098, DOI 10.1103/PhysRevB.23.2082.

[44] T. Hertel, "Optical Spectroscopy of Doped Carbon Nanotubes" in *Handbook of Carbon Nanomaterials*, (Eds.: R. B. Weisman, J. Kono), World Scientific Series on Carbon Nanoscience vol. 9-10, pp. 191–236, World Scientific Publishing Co. Pte. Ltd, Singapore, **2019**, DOI 10.1142/9789813235465_0013.

[45] G. L. Pearson, J. Bardeen, "Electrical Properties of Pure Silicon and Silicon Alloys Containing Boron and Phosphorus", *Physical Review* **1949**, *75*, 865–883, DOI 10.1103/PhysRev.75.865.

[46] P. P. Debye, E. M. Conwell, "Electrical Properties of N-Type Germanium", *Physical Review* **1954**, *93*, 693–706, DOI 10.1103/PhysRev.93.693.

[47] A. M. Stoneham et al., "Trapping, self-trapping and the polaron family", *Journal of Physics: Condensed Matter* **2007**, *19*, 255208, DOI 10.1088/0953-8984/19/25/255208.

[48] D. Emin, "Optical properties of large and small polarons and bipolarons", *Physical Review B* **1993**, *48*, 13691–13702, DOI 10.1103/PhysRevB.48.13691.

[49] B. A. Gregg, S.-G. Chen, R. A. Cormier, "Coulomb Forces and Doping in Organic Semiconductors", *Chemistry of Materials* **2004**, *16*, 4586–4599, DOI 10.1021/cm049625c.

[50] R. B. Capaz, C. D. Spataru, S. Ismail-Beigi, S. G. Louie, "Diameter and chirality dependence of exciton properties in carbon nanotubes", *Physical Review B* **2006**, *74*, 121401, DOI 10.1103/PhysRevB.74.121401.

[51] V. Perebeinos, J. Tersoff, P. Avouris, "Scaling of Excitons in Carbon Nanotubes", *Physical Review Letters* **2004**, *92*, 257402, DOI 10.1103/PhysRevLett.92.257402.

[52] J. Deslippe et al., "Electron-hole interaction in carbon nanotubes", *Nano Letters* **2009**, *9*, 1330–1334, DOI 10.1021/nl802957t.

[53] H. Gerischer, "The impact of semiconductors on the concepts of electrochemistry", *Electrochimica Acta* **1990**, *35*, 1677–1699, DOI 10.1016/0013-4686(90)87067-C.

[54] R. Memming, *Semiconductor Electrochemistry*, 2. ed., Wiley-VCH, Weinheim, **2015**.

[55] H. Gerischer, "Über den Ablauf von Redoxreaktionen an Metallen und an Halbleitern", *Zeitschrift für Physikalische Chemie* **1960**, *26*, 223–247, DOI 10.1524/zpch.1961.27.1_2.048.

[56] S. Trasatti, "The absolute electrode potential: an explanatory note", *Journal of Electroanalytical Chemistry and Interfacial Electrochemistry* **1986**, *209*, 417–428, DOI 10.1016/0022-0728(86)80570-8.

[57] R. Saito, M. Fujita, G. Dresselhaus, M. S. Dresselhaus, "Electronic structure of chiral graphene tubules", *Applied Physics Letters* **1992**, *60*, 2204–2206, DOI 10.1063/1.107080.

[58] R. Saito, G. Dresselhaus, M. S. Dresselhaus, *Physical Properties of Carbon Nanotubes*, 1. ed., Imperial College Press, London, **1998**.

[59] M. S. Dresselhaus, G. Dresselhaus, R. Saito, "Physics of carbon nanotubes", *Carbon* **1995**, *33*, 883–891, DOI 10.1016/0008-6223(95)00017-8.

[60] M. S. Dresselhaus, G. Dresselhaus, R. Saito, A. Jorio, "Raman spectroscopy of carbon nanotubes", *Physics Reports* **2005**, *409*, 47–99, DOI 10.1016/j.physrep.2004.10.006.

[61] J. Wang et al., "Role of Defects as Exciton Quenching Sites in Carbon Nanotube Photovoltaics", *The Journal of Physical Chemistry C* **2017**, *121*, 8310–8318, DOI 10.1021/acs.jpcc.7b01005.

[62] M. J. Shea, J. Wang, J. T. Flach, M. T. Zanni, M. S. Arnold, "Less severe processing improves carbon nanotube photovoltaic performance", *APL Materials* **2018**, *6*, 056104, DOI 10.1063/1.5026853.

[63] R. B. Weisman, J. Kono, "Introduction to Optical Spectroscopy of Single-Wall Carbon Nanotubes" in *Handbook of Carbon Nanomaterials*, (Eds.: R. B. Weisman, J. Kono), World Scientific Series on Carbon Nanoscience vol. 9-10, pp. 1–43, World Scientific Publishing Co. Pte. Ltd, Singapore, **2019**, DOI 10.1142/9789813235465_0001.

[64] S.-J. Liang, L. K. Ang, "Electron Thermionic Emission from Graphene and a Thermionic Energy Converter", *Physical Review Applied* **2015**, *3*, 014002, DOI 10.1103/PhysRevApplied.3.014002.

[65] T. Hertel, R. Fasel, G. Moos, "Charge-carrier dynamics in single-wall carbon nanotube bundles: a time-domain study", *Applied Physics A* **2002**, *75*, 449–465, DOI 10.1007/s003390201415.

[66] L. van Hove, "The Occurrence of Singularities in the Elastic Frequency Distribution of a Crystal", *Physical Review* **1953**, *89*, 1189–1193, DOI 10.1103/PhysRev.89.1189.

[67] T. Hertel, "Photophysics" in *Carbon Nanotubes and Related Structures*, (Eds.: D. M. Guldi, M. Nazario), pp. 77–101, Wiley-VCH Verlag GmbH & Co. KGaA, Weinheim, **2010**, DOI 10.1002/9783527629930.ch4.

[68] H. Haug, S. Koch, *Quantum Theory of the Optical and Electronic Properties of Semiconductors*, 4th ed., World Scientific Publishing Co. Pte. Ltd, Singapore, **2004**.

[69] A. D. Yoffe, "Low-dimensional systems", *Advances in Physics* **1993**, *42*, 173–262, DOI 10.1080/00018739300101484.

[70] X.-F. He, "Excitons in anisotropic solids", *Physical Review B* **1991**, *43*, 2063–2069, DOI 10.1103/PhysRevB.43.2063.

[71] R. Loudon, "One-Dimensional Hydrogen Atom", *American Journal of Physics* **1959**, *27*, 649–655, DOI 10.1119/1.1934950.

[72] S. B. Nam et al., "Free-exciton energy spectrum in GaAs", *Physical Review B* **1976**, *13*, 761–767, DOI 10.1103/PhysRevB.13.761.

[73] F. Wu, Y. Shi, M. Parenteau, A. Jorio, C. Carlone, "Analysis of Free Exciton Properties in GaAs Epitaxial Layers with the Improved Model of Photoconductivity Spectra", *Physica Status Solidi (b)* **1994**, *186*, 133–141, DOI 10.1002/pssb.2221860111.

[74] T. Ando, "Excitons in Carbon Nanotubes", *Journal of the Physical Society of Japan* **1997**, *66*, 1066–1073, DOI 10.1143/JPSJ.66.1066.

[75] E. B. Barros et al., "Selection rules for one- and two-photon absorption by excitons in carbon nanotubes", *Physical Review B* **2006**, *73*, 241406, DOI 10.1103/PhysRevB.73.241406.

[76] P. M. Vora, X. Tu, E. J. Mele, M. Zheng, J. M. Kikkawa, "Chirality dependence of the K-momentum dark excitons in carbon nanotubes", *Physical Review B* **2010**, *81*, 155123, DOI 10.1103/PhysRevB.81.155123.

[77] Y. Miyauchi, S. Maruyama, "Identification of an excitonic phonon sideband by photoluminescence spectroscopy of single-walled carbon-13 nanotubes", *Physical Review B* **2006**, *74*, 035415, DOI 10.1103/PhysRevB.74.035415.

[78] O. N. Torrens, M. Zheng, J. M. Kikkawa, "Energy of K-Momentum Dark Excitons in Carbon Nanotubes by Optical Spectroscopy", *Physical Review Letters* **2008**, *101*, 157401, DOI 10.1103/PhysRevLett.101.157401.

[79] Y. Murakami et al., "Photoluminescence sidebands of carbon nanotubes below the bright singlet excitonic levels", *Physical Review B* **2009**, *79*, 195407, DOI 10.1103/PhysRevB.79.195407.

[80] C. Voisin et al., "Excitonic signatures in the optical response of single-wall carbon nanotubes", *Physica Status Solidi (b)* **2012**, *249*, 900–906, DOI 10.1002/pssb.201100085.

[81] J. Shaver et al., "Magnetic brightening of carbon nanotube photoluminescence through symmetry breaking", *Nano Letters* **2007**, *7*, 1851–1855, DOI 10.1021/nl070260f.

[82] A. Srivastava, H. Htoon, V. I. Klimov, J. Kono, "Direct Observation of Dark Excitons in Individual Carbon Nanotubes: Inhomogeneity in the Exchange Splitting", *Physical Review Letters* **2008**, *101*, 087402, DOI 10.1103/PhysRevLett.101.087402.

[83] W. Zhou, D. Nakamura, H. Liu, H. Kataura, S. Takeyama, "Relative Ordering between Bright and Dark Excitons in Single-walled Carbon Nanotubes", *Scientific Reports* **2014**, *4*, 6999, DOI 10.1038/srep06999.

[84] S. Berger et al., "Temperature dependence of exciton recombination in semiconducting single-wall carbon nanotubes", *Nano Letters* **2007**, *7*, 398–402, DOI 10.1021/nl062609p.

[85] W. Zhou et al., "Band-edge exciton states in a single-walled carbon nanotube revealed by magneto-optical spectroscopy in ultrahigh magnetic fields", *Physical Review B* **2013**, *87*, 241406, DOI 10.1103/PhysRevB.87.241406.

[86] I. B. Mortimer, R. J. Nicholas, "Role of bright and dark excitons in the temperature-dependent photoluminescence of carbon nanotubes", *Physical Review Letters* **2007**, *98*, 027404, DOI 10.1103/PhysRevLett.98.027404.

[87] S. Tretiak, "Triplet State Absorption in Carbon Nanotubes: A TD-DFT Study", *Nano Letters* **2007**, *7*, 2201–2206, DOI 10.1021/nl070355h.

[88] D. Stich et al., "Triplet-triplet exciton dynamics in single-walled carbon nanotubes", *Nature Photonics* **2014**, *8*, 139–144, DOI 10.1038/nphoton.2013.316.

[89] J. Park, P. Deria, M. J. Therien, "Dynamics and transient absorption spectral signatures of the single-wall carbon nanotube electronically excited triplet state", *Journal of the American Chemical Society* **2011**, *133*, 17156–17159, DOI 10.1021/ja2079477.

[90] C. Mann, T. Hertel, "13 nm Exciton Size in (6,5) Single-Wall Carbon Nanotubes", *Journal of Physical Chemistry Letters* **2016**, *7*, 2276–2280, DOI 10.1021/acs.jpclett.6b00797.

[91] L. Luer et al., "Size and mobility of excitons in (6, 5) carbon nanotubes", *Nature Physics* **2009**, *5*, 54–58, DOI 10.1038/nphys1149.

[92] S. Schmitt-Rink, D. S. Chemla, D. A. B. Miller, "Theory of transient excitonic optical nonlinearities in semiconductor quantum-well structures", *Physical Review B* **1985**, *32*, 6601–6609, DOI 10.1103/PhysRevB.32.6601.

[93] S. Schmitt-Rink, D. S. Chemla, D. Miller, "Linear and nonlinear optical properties of semiconductor quantum wells", *Advances in Physics* **1989**, *38*, 89–188, DOI 10.1080/00018738900101102.

[94] C. Manzoni et al., "Intersubband Exciton Relaxation Dynamics in Single-Walled Carbon Nanotubes", *Physical Review Letters* **2005**, *94*, 207401, DOI 10.1103/PhysRevLett.94.207401.

[95] T. Hertel et al., "Intersubband decay of 1-D exciton resonances in carbon nanotubes", *Nano Letters* **2008**, *8*, 87–91, DOI 10.1021/nl0720915.

[96] D. Schilling, "Zur spektralen Diffusions- und Energietransferdynamik in halbleitenden einwandigen Kohlenstoffnanoröhren", University of Würzburg, **2015**.

[97] L. Lüer, J. Crochet, T. Hertel, G. Cerullo, G. Lanzani, "Ultrafast Excitation Energy Transfer in Small Semiconducting Carbon Nanotube Aggregates", *ACS Nano* **2010**, *4*, 4265–4273, DOI 10.1021/nn100674h.

[98] T. Hertel, S. Himmelein, T. Ackermann, D. Stich, J. Crochet, "Diffusion Limited Photoluminescence Quantum Yields in 1-D Semiconductors", *ACS Nano* **2010**, *4*, 7161–7168, DOI 10.1021/nn101612b.

[99] J. Crochet, M. Clemens, T. Hertel, "Quantum Yield Heterogeneities of Aqueous Single-Wall Carbon Nanotube Suspensions", *Journal of the American Chemical Society* **2007**, *129*, 8058–8059, DOI 10.1021/ja071553d.

[100] L. J. Carlson, S. E. Maccagnano, M. Zheng, J. Silcox, T. D. Krauss, "Fluorescence efficiency of individual carbon nanotubes", *Nano Letters* **2007**, *7*, 3698–3703, DOI 10.1021/nl072014.

[101] Y. Miyauchi, K. Matsuda, Y. Yamamoto, N. Nakashima, Y. Kanemitsu, "Length-Dependent Photoluminescence Lifetimes in Single-Walled Carbon Nanotubes", *The Journal of Physical Chemistry C* **2010**, *114*, 12905–12908, DOI 10.1021/jp1027492.

[102] Y. Miyauchi, H. Hirori, K. Matsuda, Y. Kanemitsu, "Radiative lifetimes and coherence lengths of one-dimensional excitons in single-walled carbon nanotubes", *Physical Review B* **2009**, *80*, 081410, DOI 10.1103/PhysRevB.80.081410.

[103] S. Berciaud, L. Cognet, B. Lounis, "Luminescence decay and the absorption cross section of individual single-walled carbon nanotubes", *Physical Review Letters* **2008**, *101*, 077402, DOI 10.1103/PhysRevLett.101.077402.

[104] J. G. Duque, M. Pasquali, L. Cognet, B. Lounis, "Environmental and synthesis-dependent luminescence properties of individual single-walled carbon nanotubes", *ACS Nano* **2009**, *3*, 2153–2156, DOI 10.1021/nn9003956.

[105] T. Gokus et al., "Mono- and Biexponential Luminescence Decays of Individual Single-Walled Carbon Nanotubes", *The Journal of Physical Chemistry C* **2010**, *114*, 14025–14028, DOI 10.1021/jp1049217.

[106] Y. Miyauchi, "Photoluminescence studies on exciton photophysics in carbon nanotubes", *Journal of Materials Chemistry C* **2013**, *1*, 6499–6521, DOI 10.1039/c3tc00947e.

[107] A. Rajan, M. S. Strano, D. A. Heller, T. Hertel, K. Schulten, "Length-dependent optical effects in single walled carbon nanotubes", *The Journal of Physical Chemistry B* **2008**, *112*, 6211–6213, DOI 10.1021/jp0771441.

[108] V. Perebeinos, P. Avouris, "Phonon and Electronic Nonradiative Decay Mechanisms of Excitons in Carbon Nanotubes", *Physical Review Letters* **2008**, *101*, 057401, DOI 10.1103/PhysRevLett.101.057401.

[109] C. D. Spataru, S. Ismail-Beigi, R. B. Capaz, S. G. Louie, "Theory and ab initio calculation of radiative lifetime of excitons in semiconducting carbon nanotubes", *Physical Review Letters* **2005**, *95*, 247402, DOI 10.1103/PhysRevLett.95.247402.

[110] C. M. Aguirre et al., "The Role of the Oxygen/Water Redox Couple in Suppressing Electron Conduction in Field-Effect Transistors", *Advanced Materials* **2009**, *21*, 3087–3091, DOI 10.1002/adma.200900550.

[111] M. Zheng, B. A. Diner, "Solution redox chemistry of carbon nanotubes", *Journal of the American Chemical Society* **2004**, *126*, 15490–15494, DOI 10.1021/ja0457967.

[112] K. H. Eckstein, H. Hartleb, M. M. Achsnich, F. Schöppler, T. Hertel, "Localized Charges Control Exciton Energetics and Energy Dissipation in Doped Carbon Nanotubes", *ACS Nano* **2017**, *10*, 10401–10408, DOI 10.1021/acsnano.7b05543.

[113] M. W. Graham, Y.-Z. Ma, A. A. Green, M. C. Hersam, G. R. Fleming, "Pure optical dephasing dynamics in semiconducting single-walled carbon nanotubes", *The Journal of Chemical Physics* **2011**, *134*, 034504, DOI 10.1063/1.3530582.

[114] L. Cognet et al., "Stepwise Quenching of Exciton Fluorescence in Carbon Nanotubes by Single-Molecule Reactions", *Science* **2007**, *316*, 1465–1468, DOI 10.1126/science.1141316.

[115] J. J. Crochet et al., "Disorder limited exciton transport in colloidal single-wall carbon nanotubes", *Nano Letters* **2012**, *12*, 5091–5096, DOI 10.1021/nl301739d.

[116] A. J. Siitonen, D. A. Tsyboulski, S. M. Bachilo, R. B. Weisman, "Surfactant-Dependent Exciton Mobility in Single-Walled Carbon Nanotubes Studied by Single-Molecule Reactions", *Nano Letters* **2010**, *10*, 1595–1599, DOI 10.1021/nl9039845.

[117] C. Georgi, M. Böhmler, H. Qian, L. Novotny, A. Hartschuh, "Probing exciton propagation and quenching in carbon nanotubes with near-field optical microscopy", *Physica Status Solidi (b)* **2009**, *246*, 2683–2688, DOI 10.1002/pssb.200982306.

[118] D. M. Harrah, A. K. Swan, "The role of length and defects on optical quantum efficiency and exciton decay dynamics in single-walled carbon nanotubes", *ACS Nano* **2011**, *5*, 647–655, DOI 10.1021/nn1031214.

[119] A. Ishii, M. Yoshida, Y. K. Kato, "Exciton diffusion, end quenching, and exciton-exciton annihilation in individual air-suspended carbon nanotubes", *Physical Review B* **2015**, *91*, 125427, DOI 10.1103/PhysRevB.91.125427.

[120] T. Liu, Z. Xiao, "Exact and Closed Form Solutions for the Quantum Yield, Exciton Diffusion Length, and Lifetime To Reveal the Universal Behaviors of the Photoluminescence of Defective Single-Walled Carbon Nanotubes", *The Journal of Physical Chemistry C* **2011**, *115*, 16920–16927, DOI 10.1021/jp205458t.

[121] J. Xie, T. Inaba, R. Sugiyama, Y. Homma, "Intrinsic diffusion length of excitons in long single-walled carbon nanotubes from photoluminescence spectra", *Physical Review B* **2012**, *85*, 085434, DOI 10.1103/PhysRevB.85.085434.

[122] S. Moritsubo et al., "Exciton diffusion in air-suspended single-walled carbon nanotubes", *Physical Review Letters* **2010**, *104*, 247402, DOI 10.1103/PhysRevLett.104.247402.

[123] C. Thomsen, S. Reich, "Raman Scattering in Carbon Nanotubes" in *Light Scattering in Solid IX*, (Eds.: M. Cardona, R. Merlin), Topics in Applied Physics 108, pp. 115–234, Springer, Berlin, Heidelberg, **2006**, DOI 10.1007/978-3-540-34436-0_3.

[124] S. Lefrant, M. Baibarac, I. Baltog, "Raman and FTIR spectroscopy as valuable tools for the characterization of polymer and carbon nanotube based composites", *Journal of Materials Chemistry* **2009**, *19*, 5690–5704, DOI 10.1039/b821136a.

[125] C. Georgi, A. Hartschuh, "Tip-enhanced Raman spectroscopic imaging of localized defects in carbon nanotubes", *Applied Physics Letters* **2010**, *97*, 143117, DOI 10.1063/1.3499752.

[126] M. S. Dresselhaus, A. Jorio, A. G. Souza Filho, R. Saito, "Defect characterization in graphene and carbon nanotubes using Raman spectroscopy", *Philosophical Transactions of the Royal Society A* **2010**, *368*, 5355–5377, DOI 10.1098/rsta.2010.0213.

[127] D. S. Knight, W. B. White, "Characterization of diamond films by Raman spectroscopy", *Journal of Materials Research* **1989**, *4*, 385–393, DOI 10.1557/JMR.1989.0385.

[128] F. Lapointe et al., "Antiresonances in the Mid-Infrared Vibrational Spectrum of Functionalized Graphene", *The Journal of Physical Chemistry C* **2017**, *121*, 9053–9062, DOI 10.1021/acs.jpcc.7b01386.

[129] F. Lapointe et al., "Fano resonances in the midinfrared spectra of single-walled carbon nanotubes", *Physical Review Letters* **2012**, *109*, 097402, DOI 10.1103/PhysRevLett.109.097402.

[130] V. M. Bermudez, L. M. Ericson, "Infrared spectroscopic study of O_2 interaction with carbon nanotubes", *Langmuir* **2006**, *22*, 2258–2263, DOI 10.1021/la052548v.

[131] T. G. Pedersen, K. Pedersen, H. D. Cornean, P. Duclos, "Stability and Signatures of Biexcitons in Carbon Nanotubes", *Nano Letters* **2005**, *5*, 291–294, DOI 10.1021/nl048108q.

[132] D. Kammerlander, D. Prezzi, G. Goldoni, E. Molinari, U. Hohenester, "Biexciton stability in carbon nanotubes", *Physical Review Letters* **2007**, *99*, 126806, DOI 10.1103/PhysRevLett.99.126806.

[133] T. F. Rønnow, T. G. Pedersen, B. Partoens, "Biexciton binding energy in fractional dimensional semiconductors", *Physical Review B* **2012**, *85*, 045412, DOI 10.1103/PhysRevB.85.045412.

[134] D. J. Styers-Barnett et al., "Exciton Dynamics and Biexciton Formation in Single-Walled Carbon Nanotubes Studied with Femtosecond Transient Absorption Spectroscopy", *The Journal of Physical Chemistry C* **2008**, *112*, 4507–4516, DOI 10.1021/jp7099256.

[135] B. Yuma et al., "Biexciton, single carrier, and trion generation dynamics in single-walled carbon nanotubes", *Physical Review B* **2013**, *87*, 205412, DOI 10.1103/PhysRevB.87.205412.

[136] L. Colombier et al., "Detection of a biexciton in semiconducting carbon nanotubes using nonlinear optical spectroscopy", *Physical Review Letters* **2012**, *109*, 197402, DOI 10.1103/PhysRevLett.109.197402.

[137] M. A. Lampert, "Mobile and Immobile Effective-Mass-Particle Complexes in Nonmetallic Solids", *Physical Review Letters* **1958**, *1*, 450–453, DOI 10.1103/PhysRevLett.1.450.

[138] K. Kheng et al., "Observation of negatively charged excitons X^- in semiconductor quantum wells", *Physical Review Letters* **1993**, *71*, 1752–1755, DOI 10.1103/PhysRevLett.71.1752.

[139] G. Munschy, B. Stébé, "Existence and Binding Energy of the Excitonic Ion", *Physica Status Solidi (b)* **1974**, *64*, 213–222, DOI 10.1002/pssb.2220640125.

[140] I. Filikhin, R. Y. Kezerashvili, S. M. Tsiklauri, B. Vlahovic, "Trions in bulk and monolayer materials: Faddeev equations and hyperspherical harmonics", *Nanotechnology* **2018**, *29*, 124002, DOI 10.1088/1361-6528/aaa94d.

[141] I. Filikhin, R. Y. Kezerashvili, B. Vlahovic, "On binding energy of trions in bulk materials", *Physics Letters A* **2018**, *382*, 787–791, DOI 10.1016/j.physleta.2018.01.017.

[142] B. Stébé, A. Ainane, "Ground state energy and optical absorption of excitonic trions in two dimensional semiconductors", *Superlattices and Microstructures* **1989**, *5*, 545–548, DOI 10.1016/0749-6036(89)90382-0.

[143] Y. Bai, J.-H. Olivier, G. Bullard, C. Liu, M. J. Therien, "Dynamics of charged excitons in electronically and morphologically homogeneous single-walled carbon nanotubes", *Proceedings of the National Academy of Sciences* **2018**, *115*, 674–679, DOI 10.1073/pnas.1712971115.

[144] S. Mouri, Y. Miyauchi, M. Iwamura, K. Matsuda, "Temperature dependence of photoluminescence spectra in hole-doped single-walled carbon nanotubes", *Physical Review B* **2013**, *87*, 045408, DOI 10.1103/PhysRevB.87.045408.

[145] T. Nishihara, Y. Yamada, M. Okano, Y. Kanemitsu, "Trion formation and recombination dynamics in hole-doped single-walled carbon nanotubes", *Applied Physics Letters* **2013**, *103*, 023101, DOI 10.1063/1.4813014.

[146] S. Mouri, K. Matsuda, "Exciton-hole interactions in hole-doped single-walled carbon nanotubes evaluated by absorption spectral changes", *Journal of Applied Physics* **2012**, *111*, 094309, DOI 10.1063/1.4710532.

[147] T. Shiraishi et al., "Determination of Precise Redox Properties of Oxygen-Doped Single-Walled Carbon Nanotubes Based on in Situ Photoluminescence Electrochemistry", *The Journal of Physical Chemistry C* **2015**, 15632–15639, DOI 10.1021/acs.jpcc.5b07841.

[148] T. Uda, S. Tanaka, Y. K. Kato, "Molecular screening effects on exciton-carrier interactions in suspended carbon nanotubes", *Applied Physics Letters* **2018**, *113*, 121105, DOI 10.1063/1.5046433.

[149] K. Watanabe, K. Asano, "Trions in semiconducting single-walled carbon nanotubes", *Physical Review B* **2012**, *85*, 035416, DOI 10.1103/PhysRevB.85.035416.

[150] U. Hohenester, G. Goldoni, "A new quasiparticle in carbon nanotubes", *Physics* **2011**, *4*, 5, DOI 10.1103/Physics.4.5.

[151] R. B. Capaz, C. D. Spataru, S. Ismail-Beigi, S. G. Louie, "Excitons in carbon nanotubes: Diameter and chirality trends", *Physica Status Solidi (b)* **2007**, *244*, 4016–4020, DOI 10.1002/pssb.200776200.

[152] Y. Miyauchi, H. Ajiki, S. Maruyama, "Electron-hole asymmetry in single-walled carbon nanotubes probed by direct observation of transverse quasidark excitons", *Physical Review B* **2010**, *81*, 121415, DOI 10.1103/PhysRevB.81.121415.

[153] M. Combescot et al., "Many-body origin of the "trion line" in doped quantum wells", *Europhysics Letters* **2005**, *71*, 431–437, DOI 10.1209/epl/i2005-10101-8.

[154] D. K. Efimkin, A. H. MacDonald, "Many-body theory of trion absorption features in two-dimensional semiconductors", *Physical Review B* **2017**, *95*, 035417, DOI 10.1103/PhysRevB.95.035417.

[155] M. Sidler, "Many-Body Effects in Optical Excitations of Transition Metal Dichalcogenides", ETH Zürich, **2018**.

[156] M. Sidler et al., "Fermi polaron-polaritons in charge-tunable atomically thin semiconductors", *Nature Physics* **2016**, *13*, 255–261, DOI 10.1038/nphys3949.

[157] Y.-C. Chang, S.-Y. Shiau, M. Combescot, "Crossover from trion-hole complex to exciton-polaron in n -doped two-dimensional semiconductor quantum wells", *Physical Review B* **2018**, *98*, 235203, DOI 10.1103/PhysRevB.98.235203.

[158] D. Pimenov, M. Goldstein, "Spectra of heavy polarons and molecules coupled to a Fermi sea", *Physical Review B* **2018**, *98*, 220302, DOI 10.1103/PhysRevB.98.220302.

[159] M. Fox, *Optical properties of solids*, Oxford University Press, Oxford, **2001**.

[160] P. A. Lee, T. v. Ramakrishnan, "Disordered electronic systems", *Reviews of Modern Physics* **1985**, *57*, 287–337, DOI 10.1103/RevModPhys.57.287.

[161] M. Piraud, P. Lugan, P. Bouyer, A. Aspect, L. Sanchez-Palencia, "Localization of a matter wave packet in a disordered potential", *Physical Review A* **2011**, *83*, 031603, DOI 10.1103/PhysRevA.83.031603.

[162] J. Billy et al., "Direct observation of Anderson localization of matter waves in a controlled disorder", *Nature* **2008**, *453*, 891–894, DOI 10.1038/nature07000.

[163] C. Georgi, A. A. Green, M. C. Hersam, A. Hartschuh, "Probing exciton localization in single-walled carbon nanotubes using high-resolution near-field microscopy", *ACS Nano* **2010**, *4*, 5914–5920, DOI 10.1021/nn101443d.

[164] D. Schilling, C. Mann, P. Kunkel, F. Schöppler, T. Hertel, "Ultrafast Spectral Exciton Diffusion in Single-Wall Carbon Nanotubes Studied by Time-Resolved Hole Burning", *The Journal of Physical Chemistry C* **2015**, *119*, 24116–24123, DOI 10.1021/acs.jpcc.5b06865.

[165] B. O. Tayo, S. V. Rotkin, "Charge impurity as a localization center for singlet excitons in single-wall nanotubes", *Physical Review B* **2012**, *86*, DOI 10.1103/PhysRevB.86.125431.

[166] S. K. Doorn, H. Htoon, S. Tretiak, "Photophysics and Quantum Emission Behaviors of Covalently Introduced Defects in Single-Wall Carbon Nanotubes" in *Handbook of Carbon Nanomaterials*, (Eds.: R. B. Weisman, J. Kono), World Scientific Series on Carbon Nanoscience vol. 9-10, pp. 143–189, World Scientific Publishing Co. Pte. Ltd, Singapore, **2019**, DOI 10.1142/9789813235465_0012.

[167] A. Högele, J. C. Noé, M. S. Hofmann, J. T. Glückert, "Cryogenic Spectroscopy of Carbon Nanotubes: The Role of Exciton Localization" in *Handbook of Carbon Nanomaterials*, (Eds.: R. B. Weisman, J. Kono), World Scientific Series on Carbon Nanoscience vol. 9-10, pp. 223–268, World Scientific Publishing Co. Pte. Ltd, Singapore, **2019**, DOI 10.1142/9789813235465_0006.

[168] N. F. Hartmann et al., "Photoluminescence imaging of solitary dopant sites in covalently doped single-wall carbon nanotubes", *Nanoscale* **2015**, *7*, 20521–20530, DOI 10.1039/C5NR06343D.

[169] Y. Piao et al., "Brightening of carbon nanotube photoluminescence through the incorporation of sp^3 defects", *Nature Chemistry* **2013**, *5*, 840–845, DOI 10.1038/nchem.1711.

[170] X. Ma et al., "Electronic Structure and Chemical Nature of Oxygen Dopant States in Carbon Nanotubes", *ACS Nano* **2014**, *8*, 10782–10789, DOI 10.1021/nn504553y.

[171] M. S. Hofmann, J. Noé, A. Kneer, J. J. Crochet, A. Högele, "Ubiquity of Exciton Localization in Cryogenic Carbon Nanotubes", *Nano Letters* **2016**, *16*, 2958–2962, DOI 10.1021/acs.nanolett.5b04901.

[172] M. Dressel, G. Grüner, *Electrodynamics of solids*, Cambridge University Press, Cambridge, **2002**.

[173] E. Fermi, *Nuclear Physics*, The University of Chicago Press, Chicago, **1950**.

[174] J. Lloyd-Hughes, T.-I. Jeon, "A Review of the Terahertz Conductivity of Bulk and Nano-Materials", *Journal of Infrared Millimeter and Terahertz Waves* **2012**, *33*, 871–925, DOI 10.1007/s10762-012-9905-y.

[175] A. Sommerfeld, "Zur Elektronentheorie der Metalle auf Grund der Fermischen Statistik", *Zeitschrift für Physik* **1928**, *47*, 1–32, DOI 10.1007/BF01391052.

[176] N. W. Ashcroft, N. D. Mermin, *Solid state physics*, Harcourt College Publishers, Fort Worth, **1976**.

[177] S. O. Kasap, *Principles of electronic materials and devices*, 3rd ed., McGraw-Hill, Boston, **2006**.

[178] S. Kasap, C. Koughia, H. E. Ruda, "Electrical Conduction in Metals and Semiconductors" in *Springer Handbook of Electronic and Photonic Materials*, (Eds.: S. Kasap, P. Capper), pp. 19–45, Springer International Publishing, Cham, **2017**, DOI 10.1007/978-3-319-48933-9_2.

[179] T. L. Cocker et al., "Microscopic origin of the Drude-Smith model", *Physical Review B* **2017**, *96*, 205439, DOI 10.1103/PhysRevB.96.205439.

[180] F. A. Hegmann, O. Ostroverkhova, D. G. Cooke, "Probing Organic Semiconductors with Terahertz Pulses" in *Photophysics of Molecular Materials*, (Ed.: G. Lanzani), pp. 367–428, Wiley-VCH Verlag GmbH & Co. KGaA, Weinheim, **2005**, DOI 10.1002/3527607323.ch7.

[181] N. Smith, "Classical generalization of the Drude formula for the optical conductivity", *Physical Review B* **2001**, *64*, 155106, DOI 10.1103/PhysRevB.64.155106.

[182] N. F. Mott, M. Kaveh, "Metal-insulator transitions in non-crystalline systems", *Advances in Physics* **1985**, *34*, 329–401, DOI 10.1080/00018738500101771.

[183] K. Lee, R. Menon, C. O. Yoon, A. J. Heeger, "Reflectance of conducting polypyrrole: Observation of the metal-insulator transition driven by disorder", *Physical Review B* **1995**, *52*, 4779–4787, DOI 10.1103/PhysRevB.52.4779.

[184] K. Lee, A. J. Heeger, Y. Cao, "Reflectance of polyaniline protonated with camphor sulfonic acid: Disordered metal on the metal-insulator boundary", *Physical Review B* **1993**, *48*, 14884–14891, DOI 10.1103/PhysRevB.48.14884.

[185] S. Chen et al., "On the anomalous optical conductivity dispersion of electrically conducting polymers: ultra-wide spectral range ellipsometry combined with a Drude–Lorentz model", *Journal of Materials Chemistry C* **2019**, *7*, 4350–4362, DOI 10.1039/C8TC06302H.

[186] V. Perebeinos, J. Tersoff, P. Avouris, "Electron-phonon interaction and transport in semiconducting carbon nanotubes", *Physical Review Letters* **2005**, *94*, 086802, DOI 10.1103/PhysRevLett.94.086802.

[187] V. Perebeinos, J. Tersoff, P. Avouris, "Mobility in semiconducting carbon nanotubes at finite carrier density", *Nano Letters* **2006**, *6*, 205–208, DOI 10.1021/nl052044h.

[188] F. L. Späth, "Präparation und Charakterisierung einwandiger Kohlenstoffnanorohr-Polyfluoren-Komplexe", University of Würzburg, **2015**.

[189] T. C. Hain, "Entwicklung eines experimentellen Aufbaus zur Charakterisierung nanoskaliger Systeme mittels Fluoreszenzspektroskopie und -mikroskopie", University of Würzburg, **2015**.

[190] D. Stich, "Zur Exziton- und Ladungsträgerdynamik in einwandigen Kohlenstoffnanoröhren, Exciton and charge carrier dynamics in single-wall carbon nanotubes", University of Würzburg, **2012**.

[191] C. Mann, "Exzitonengröße und -dynamik in (6,5)-Kohlenstoffnanoröhren", University of Würzburg, **2015**.

[192] A. Abudulimu, "Chirality Sorted SWNTs and Their Effect on the Performance of Organic Solar Cells", University of Madrid, **2017**.

[193] S. Akturk, X. Gu, M. Kimmel, R. Trebino, "Extremely simple single-prism ultrashort- pulse compressor", *Optics Express* **2006**, *14*, 10101–10108, DOI 10.1364/OE.14.010101.

[194] R. R. Alfano, S. L. Shapiro, "Observation of Self-Phase Modulation and Small-Scale Filaments in Crystals and Glasses", *Physical Review Letters* **1970**, *24*, 592–594, DOI 10.1103/PhysRevLett.24.592.

[195] M. Ziólek, M. Lorenc, R. Naskrecki, "Determination of the temporal response function in femtosecond pump-probe systems", *Applied Physics B* **2001**, *72*, 843–847, DOI 10.1007/s003400100587.

[196] M. Lorenc et al., "Artifacts in femtosecond transient absorption spectroscopy", *Applied Physics B* **2002**, *74*, 19–27, DOI 10.1007/s003400100750.

[197] S. A. Kovalenko, A. L. Dobryakov, J. Ruthmann, N. P. Ernsting, "Femtosecond spectroscopy of condensed phases with chirped supercontinuum probing", *Physical Review A* **1999**, *59*, 2369–2384, DOI 10.1103/PhysRevA.59.2369.

[198] U. Megerle, I. Pugliesi, C. Schriever, C. F. Sailer, E. Riedle, "Sub-50 fs broadband absorption spectroscopy with tunable excitation", *Applied Physics B* **2009**, *96*, 215–231, DOI 10.1007/s00340-009-3610-0.

[199] I. V. Hertel, C. Schulz, *Atome, Moleküle und optische Physik 2*, 1. ed., Springer, Berlin, Heidelberg, **2010**.

[200] H. E. Hartleb, "Spektroelektrochemische Untersuchung von halbleitenden Kohlenstoffnanoröhren", University of Würzburg, **2015**.

[201] C. H. Park, S. B. Zhang, S.-H. Wei, "Origin of p -type doping difficulty in ZnO: The impurity perspective", *Physical Review B* **2002**, *66*, 073202, DOI 10.1103/PhysRevB.66.073202.

[202] W. M. Theis, K. K. Bajaj, C. W. Litton, W. G. Spitzer, "Direct evidence for the site of substitutional carbon impurity in GaAs", *Applied Physics Letters* **1982**, *41*, 70–72, DOI 10.1063/1.93333.

[203] I. Salzmann, G. Heimel, M. Oehzelt, S. Winkler, N. Koch, "Molecular Electrical Doping of Organic Semiconductors", *Accounts of Chemical Research* **2016**, *49*, 370–378, DOI 10.1021/acs.accounts.5b00438.

[204] I. E. Jacobs, A. J. Moulé, "Controlling Molecular Doping in Organic Semiconductors", *Advanced Materials* **2017**, *29*, 1703063, DOI 10.1002/adma.201703063.

[205] S. Mouri, Y. Miyauchi, K. Matsuda, "Tunable Photoluminescence of Monolayer MoS_2 via Chemical Doping", *Nano Letters* **2013**, *13*, 5944–5948, DOI 10.1021/nl403036h.

[206] B. Chandra, A. Afzali, N. Khare, M. M. El-Ashry, G. S. Tulevski, "Stable Charge-Transfer Doping of Transparent Single-Walled Carbon Nanotube Films", *Chemistry of Materials* **2010**, *22*, 5179–5183, DOI 10.1021/cm101085p.

[207] Genoud, Guglielmi, Nechtschein, Genies, Salmon, "ESR study of electrochemical doping in the conducting polymer polypyrrole", *Physical Review Letters* **1985**, *55*, 118–121, DOI 10.1103/PhysRevLett.55.118.

[208] A. Chernikov, C. Ruppert, H. M. Hill, A. F. Rigosi, T. F. Heinz, "Population inversion and giant bandgap renormalization in atomically thin WS_2 layers", *Nature Photonics* **2015**, *9*, 466–470, DOI 10.1038/nphoton.2015.104.

[209] K. F. Mak, L. Ju, F. Wang, T. F. Heinz, "Optical spectroscopy of graphene", *Solid State Communications* **2012**, *152*, 1341–1349, DOI 10.1016/j.ssc.2012.04.064.

[210] S. G. Bratsch, "Standard Electrode Potentials and Temperature Coefficients in Water at 298.15 K", *Journal of Physical and Chemical Reference Data* **1989**, *18*, 1–21, DOI 10.1063/1.555839.

[211] N. F. Mott, "Metal-Insulator Transition", *Reviews of Modern Physics* **1968**, *40*, 677–683, DOI 10.1103/RevModPhys.40.677.

[212] Y. Ohno, S. Kishimoto, T. Mizutani, "Photoluminescence of single-walled carbon nanotubes in field-effect transistors", *Nanotechnology* **2006**, *17*, 549–555, DOI 10.1088/0957-4484/17/2/035.

[213] S. Yasukochi et al., "Gate-induced blueshift and quenching of photoluminescence in suspended single-walled carbon nanotubes", *Physical Review B* **2011**, *84*, 121409, DOI 10.1103/PhysRevB.84.121409.

[214] T. Takenobu et al., "Control of Carrier Density by a Solution Method in Carbon-Nanotube Devices", *Advanced Materials* **2005**, *17*, 2430–2434, DOI 10.1002/adma.200500759.

[215] E. Comfort, J. U. Lee, "Large Bandgap Shrinkage from Doping and Dielectric Interface in Semiconducting Carbon Nanotubes", *Scientific Reports* **2016**, *6*, 28520, DOI 10.1038/srep28520.

[216] X. Liu et al., "A p-i-n junction diode based on locally doped carbon nanotube network", *Scientific Reports* **2016**, *6*, 23319, DOI 10.1038/srep23319.

[217] Y. Miyauchi et al., "Tunable electronic correlation effects in nanotube-light interactions", *Physical Review B* **2015**, *92*, 205407, DOI 10.1103/PhysRevB.92.205407.

[218] M. Steiner et al., "Gate-Variable Light Absorption and Emission in a Semiconducting Carbon Nanotube", *Nano Letters* **2009**, *9*, 3477–3481, DOI 10.1021/nl9016804.

[219] S. Schäfer, N. M. B. Cogan, T. D. Krauss, "Spectroscopic investigation of electrochemically charged individual (6,5) single-walled carbon nanotubes", *Nano Letters* **2014**, *14*, 3138–3144, DOI 10.1021/nl5003729.

[220] T. F. Rønnow, T. G. Pedersen, H. D. Cornean, "Correlation and dimensional effects of trions in carbon nanotubes", *Physical Review B* **2010**, *81*, 205446, DOI 10.1103/PhysRevB.81.205446.

[221] T. F. Rønnow, T. G. Pedersen, B. Partoens, K. K. Berthelsen, "Variational quantum Monte Carlo study of charged excitons in fractional dimensional space", *Physical Review B* **2011**, *84*, 035316, DOI 10.1103/PhysRevB.84.035316.

[222] O. Frank, L. Kavan, A. A. Green, M. C. Hersam, L. Dunsch, "In-situ Vis/NIR spectroelectrochemistry of single-walled carbon nanotubes enriched with (6,5) tubes", *Physica Status Solidi (b)* **2008**, *245*, 2239–2242, DOI 10.1002/pssb.200879609.

[223] Y. Kimoto, M. Okano, Y. Kanemitsu, "Observation of excited-state excitons and band-gap renormalization in hole-doped carbon nanotubes using photoluminescence excitation spectroscopy", *Physical Review B* **2013**, *87*, 195416, DOI 10.1103/PhysRevB.87.195416.

[224] T. Nishihara, Y. Yamada, Y. Kanemitsu, "Dynamics of exciton-hole recombination in hole-doped single-walled carbon nanotubes", *Physical Review B* **2012**, *86*, 075449, DOI 10.1103/PhysRevB.86.075449.

[225] T. Koyama, S. Shimizu, Y. Miyata, H. Shinohara, A. Nakamura, "Ultrafast formation and decay dynamics of trions in p-doped single-walled carbon nanotubes", *Physical Review B* **2013**, *87*, 165430, DOI 10.1103/PhysRevB.87.165430.

[226] H. Shimotani et al., "Continuous Band-Filling Control and One-Dimensional Transport in Metallic and Semiconducting Carbon Nanotube Tangled Films", *Advanced Functional Materials* **2014**, *24*, 3305–3311, DOI 10.1002/adfm.201303566.

[227] I. Heller et al., "Individual single-walled carbon nanotubes as nanoelectrodes for electrochemistry", *Nano Letters* **2005**, *5*, 137–142, DOI 10.1021/nl048200m.

[228] I. Heller, J. Kong, K. A. Williams, C. Dekker, S. G. Lemay, "Electrochemistry at Single-Walled Carbon Nanotubes: The Role of Band Structure and Quantum Capacitance", *Journal of the American Chemical Society* **2006**, *128*, 7353–7359, DOI 10.1021/ja061212k.

[229] V. Sgobba, D. M. Guldi, "Carbon nanotubes–electronic/electrochemical properties and application for nanoelectronics and photonics", *Chemical Society Reviews* **2009**, *38*, 165–184, DOI 10.1039/b802652c.

[230] A. J. Ferguson, O. G. Reid, S. U. Nanayakkara, R. Ihly, J. L. Blackburn, "Efficiency of Charge-Transfer Doping in Organic Semiconductors Probed with Quantitative Microwave and Direct-Current Conductance", *The Journal of Physical Chemistry Letters* **2018**, 6864–6870, DOI 10.1021/acs.jpclett.8b03074.

[231] C. D. Spataru, F. Léonard, "Tunable Band Gaps and Excitons in Doped Semiconducting Carbon Nanotubes Made Possible by Acoustic Plasmons", *Physical Review Letters* **2010**, *104*, 177402, DOI 10.1103/PhysRevLett.104.177402.

[232] C. D. Spataru, F. Léonard, "Quasiparticle and exciton renormalization effects in electrostatically doped semiconducting carbon nanotubes", *Chemical Physics* **2013**, *413*, 81–88, DOI 10.1016/j.chemphys.2012.08.021.

[233] L. Adamska, G. V. Nazin, S. K. Doorn, S. Tretiak, "Self-Trapping of Charge Carriers in Semiconducting Carbon Nanotubes: Structural Analysis", *Journal of Physical Chemistry Letters* **2015**, *6*, 3873–3879, DOI 10.1021/acs.jpclett.5b01729.

[234] R. G. A. Veiga, R. H. Miwa, "Ab initio study of TCNQ-doped carbon nanotubes", *Physical Review B* **2006**, *73*, 245422, DOI 10.1103/PhysRevB.73.245422.

[235] V. Perebeinos, J. Tersoff, P. Avouris, "Radiative lifetime of excitons in carbon nanotubes", *Nano Letters* **2005**, *5*, 2495–2499, DOI 10.1021/nl051828s.

[236] M. Auth et al., "Unpublished manuscript: Quantification of Atmospheric and Chemically Induced p-Doping in Carbon Nanotubes by Electron Paramagnetic Resonance, unpublished manuscript", **2019**.

[237] J. J. Crochet, J. G. Duque, J. H. Werner, S. K. Doorn, "Photoluminescence imaging of electronic-impurity-induced exciton quenching in single-walled carbon nanotubes", *Nature Nanotechnology* **2012**, *7*, 126–132, DOI 10.1038/nnano.2011.227.

[238] K. K. Kim et al., "Fermi Level Engineering of Single-Walled Carbon Nanotubes by $AuCl_3$ Doping", *Journal of the American Chemical Society* **2008**, *130*, 12757–12761, DOI 10.1021/ja8038689.

[239] S. M. Kim et al., "Role of Anions in the $AuCl_3$-Doping of Carbon Nanotubes", *ACS Nano* **2011**, *5*, 1236–1242, DOI 10.1021/nn1028532.

[240] H. C. Choi, M. Shim, S. Bangsaruntip, H. Dai, "Spontaneous Reduction of Metal Ions on the Sidewalls of Carbon Nanotubes", *Journal of the American Chemical Society* **2002**, *124*, 9058–9059, DOI 10.1021/ja026824t.

[241] V. Perebeinos, J. Tersoff, P. Avouris, "Effect of Exciton-Phonon Coupling in the Calculated Optical Absorption of Carbon Nanotubes", *Physical Review Letters* **2005**, *94*, 027402, DOI 10.1103/PhysRevLett.94.027402.

[242] Y. Miyauchi, M. Oba, S. Maruyama, "Cross-polarized optical absorption of single-walled nanotubes by polarized photoluminescence excitation spectroscopy", *Physical Review B* **2006**, *74*, 205440, DOI 10.1103/PhysRevB.74.205440.

[243] J. Lefebvre, P. Finnie, "Polarized photoluminescence excitation spectroscopy of single-walled carbon nanotubes", *Physical Review Letters* **2007**, *98*, 167406, DOI 10.1103/PhysRevLett.98.167406.

[244] B. Langlois et al., "Intraband and intersubband many-body effects in the nonlinear optical response of single-wall carbon nanotubes", *Physical Review B* **2015**, *92*, 155423, DOI 10.1103/PhysRevB.92.155423.

[245] A. Jouyban, S. Soltanpour, H.-K. Chan, "A simple relationship between dielectric constant of mixed solvents with solvent composition and temperature", *International Journal of Pharmaceutics* **2004**, *269*, 353–360, DOI 10.1016/j.ijpharm.2003.09.010.

[246] Z. Gao et al., "Optical detection of individual ultra-short carbon nanotubes enables their length characterization down to 10 nm", *Scientific Reports*, *5*, 17093, DOI 10.1038/srep17093.

[247] D. C. Mattis, J.-P. Gallinar, "What is the Mass of an Exciton?", *Physical Review Letters* **1984**, *53*, 1391–1393, DOI 10.1103/PhysRevLett.53.1391.

[248] B. Y. Balagurov, V. G. Vaks, "Random walks of a particle on lattices with traps", *Soviet Journal of Experimental and Theoretical Physics* **1974**, *38*, 968.

[249] A. T. Giese, C. S. French, "The Analysis of Overlapping Spectral Absorption Bands by Derivative Spectrophotometry", *Applied Spectroscopy* **1955**, *9*, 78–96, DOI 10.1366/000370255774634089.

[250] I. G. McWilliam, "Derivative spectroscopy and its application to the analysis of unresolved bands", *Analytical Chemistry* **1969**, *41*, 674–676, DOI 10.1021/ac60273a032.

[251] R. Esfandiary, J. S. Hunjan, G. H. Lushington, S. B. Joshi, C. R. Middaugh, "Temperature dependent 2nd derivative absorbance spectroscopy of aromatic amino acids as a probe of protein dynamics", *Protein science* **2009**, *18*, 2603–2614, DOI 10.1002/pro.264.

[252] S. Konabe, K. Matsuda, S. Okada, "Suppression of Exciton-Electron Scattering in Doped Single-Walled Carbon Nanotubes", *Physical Review Letters* **2012**, *109*, 187403, DOI 10.1103/PhysRevLett.109.187403.

[253] A. Chernikov et al., "Exciton Binding Energy and Nonhydrogenic Rydberg Series in Monolayer WS_2", *Physical Review Letters* **2014**, *113*, 076802, DOI 10.1103/PhysRevLett.113.076802.

[254] S. Park et al., "Direct determination of monolayer MoS_2 and WSe_2 exciton binding energies on insulating and metallic substrates", *2D Materials* **2018**, *5*, 025003, DOI 10.1088/2053-1583/aaa4ca.

[255] Y. Yu et al., "Exciton-dominated Dielectric Function of Atomically Thin MoS_2 Films", *Scientific Reports* **2015**, *5*, 16996, DOI 10.1038/srep16996.

[256] K. He et al., "Tightly Bound Excitons in Monolayer WSe_2", *Physical Review Letters* **2014**, *113*, 026803, DOI 10.1103/PhysRevLett.113.026803.

[257] E. Courtade et al., "Charged excitons in monolayer WSe_2: Experiment and theory", *Physical Review B* **2017**, *96*, 085302, DOI 10.1103/PhysRevB.96.085302.

[258] H. Buhmann et al., "Electron-concentration-dependent quantum-well luminescence: Evidence for a negatively charged exciton", *Physical Review B* **1995**, *51*, 7969–7972, DOI 10.1103/PhysRevB.51.7969.

[259] S. Ghosh, S. M. Bachilo, R. A. Simonette, K. M. Beckingham, R. B. Weisman, "Oxygen Doping Modifies Near-Infrared Band Gaps in Fluorescent Single-Walled Carbon Nanotubes", *Science* **2010**, *330*, 1656–1659, DOI 10.1126/science.1196382.

[260] A. H. Brozena, J. D. Leeds, Y. Zhang, J. T. Fourkas, Y. Wang, "Controlled Defects in Semiconducting Carbon Nanotubes Promote Efficient Generation and Luminescence of Trions", *ACS Nano* **2014**, *8*, 4239–4247, DOI 10.1021/nn500894p.

[261] Y. Kadria-Vili, S. M. Bachilo, J. L. Blackburn, R. B. Weisman, "Photoluminescence Side Band Spectroscopy of Individual Single-Walled Carbon Nanotubes", *The Journal of Physical Chemistry C* **2016**, *120*, 23898–23904, DOI 10.1021/acs.jpcc.6b08768.

[262] B. Zhu, X. Chen, X. Cui, "Exciton Binding Energy of Monolayer WS_2", *Scientific Reports*, *5*, 09218, DOI 10.1038/srep09218.

[263] J. D. Sau, J. J. Crochet, S. K. Doorn, M. L. Cohen, "Multiparticle Exciton Ionization in Shallow Doped Carbon Nanotubes", *Journal of Physical Chemistry Letters* **2013**, *4*, 982–986, DOI 10.1021/jz400049c.

[264] T. Takagahara, "Dependence on dimensionality of excitonic optical nonlinearity in quantum confined structures", *Solid State Communications* **1991**, *78*, 279–282, DOI 10.1016/0038-1098(91)90197-4.

[265] R. M. Russo et al., "One-dimensional diffusion-limited relaxation of photoexcitations in suspensions of single-walled carbon nanotubes", *Physical Review B* **2006**, *74*, 041405, DOI 10.1103/PhysRevB.74.041405.

[266] M. Hoyuelos, H. O. Mártin, "Rate equation of the A + A → A reaction with probability of reaction and diffusion", *Physical Review E* **1993**, *48*, 3309–3313, DOI 10.1103/PhysRevE.48.3309.

[267] Z. Zhu et al., "Pump-Probe Spectroscopy of Exciton Dynamics in (6,5) Carbon Nanotubes", *The Journal of Physical Chemistry C* **2007**, *111*, 3831–3835, DOI 10.1021/jp0669411.

[268] M. N. Berberan-Santos, E. N. Bodunov, B. Valeur, "Mathematical functions for the analysis of luminescence decays with underlying distributions 1. Kohlrausch decay function (stretched exponential)", *Chemical Physics* **2005**, *315*, 171–182, DOI 10.1016/j.chemphys.2005.04.006.

[269] A. M. Berezhkovskii, Y. Makhnovskii, R. A. Suris, "Mean square displacement of a Brownian particle with traps. The one-dimensional case", *Physics Letters A* **1990**, *150*, 296–298, DOI 10.1016/0375-9601(90)90099-A.

[270] F. van Wijland, "Trapping of a random walk by diffusing traps", *Journal of Physics A: Mathematical and General* **2002**, *35*, 5391–5401, DOI 10.1088/0305-4470/35/26/303.

[271] Szabo, Zwanzig, Agmon, "Diffusion-controlled reactions with mobile traps", *Physical Review Letters* **1988**, *61*, 2496–2499, DOI 10.1103/PhysRevLett.61.2496.

[272] R. Ulbricht, E. Hendry, J. Shan, T. F. Heinz, M. Bonn, "Carrier dynamics in semiconductors studied with time-resolved terahertz spectroscopy", *Reviews of Modern Physics* **2011**, *83*, 543–586, DOI 10.1103/RevModPhys.83.543.

[273] T. Nishihara, M. Okano, Y. Yamada, Y. Kanemitsu, "Review—Photophysics of Trions in Single-Walled Carbon Nanotubes", *ECS Journal of Solid State Science and Technology* **2017**, *6*, M3062–M3064, DOI 10.1149/2.0091706jss.

[274] J. L. Bredas, G. B. Street, "Polarons, bipolarons, and solitons in conducting polymers", *Accounts of Chemical Research* **1985**, *18*, 309–315, DOI 10.1021/ar00118a005.

[275] M. C. Beard, J. L. Blackburn, M. J. Heben, "Photogenerated Free Carrier Dynamics in Metal and Semiconductor Single-Walled Carbon Nanotube Films", *Nano Letters* **2008**, *8*, 4238–4242, DOI 10.1021/nl801913y.

[276] S. J. Tans et al., "Individual single-wall carbon nanotubes as quantum wires", *Nature* **1997**, *386*, 474–477, DOI 10.1038/386474a0.

[277] Á. Pekker, F. Borondics, K. Kamarás, A. G. Rinzler, D. B. Tanner, "Calculation of optical constants from carbon nanotube transmission spectra", *Physica Status Solidi (b)* **2006**, *243*, 3485–3488, DOI 10.1002/pssb.200669141.

[278] Q. Zhang et al., "Plasmonic nature of the terahertz conductivity peak in single-wall carbon nanotubes", *Nano Letters* **2013**, *13*, 5991–5996, DOI 10.1021/nl403175g.

[279] Z. Wu et al., "Transparent, Conductive Carbon Nanotube Films", *Science* **2004**, *305*, 1273–1276, DOI 10.1126/science.1101243.

[280] F. Borondics et al., "Charge dynamics in transparent single-walled carbon nanotube films from optical transmission measurements", *Physical Review B* **2006**, *74*, 045431, DOI 10.1103/PhysRevB.74.045431.

[281] M. J. O'Connell, E. E. Eibergen, S. K. Doorn, "Chiral selectivity in the charge-transfer bleaching of single-walled carbon-nanotube spectra", *Nature Materials* **2005**, *4*, 412–418, DOI 10.1038/nmat1367.

[282] B. Norton-Baker et al., "Polymer-Free Carbon Nanotube Thermoelectrics with Improved Charge Carrier Transport and Power Factor", *ACS Energy Letters* **2016**, *1*, 1212–1220, DOI 10.1021/acsenergylett.6b00417.

[283] F. J. Berger et al., "From Broadband to Electrochromic Notch Filters with Printed Monochiral Carbon Nanotubes", *ACS Applied Materials & Interfaces* **2018**, *10*, 11135–11142, DOI 10.1021/acsami.8b00643.

[284] R. Österbacka, X. M. Jiang, C. P. An, B. Horovitz, Z. V. Vardeny, "Photoinduced quantum interference antiresonances in π-conjugated polymers", *Physical Review Letters* **2002**, *88*, 226401, DOI 10.1103/PhysRevLett.88.226401.

[285] M. Wohlgenannt, X. M. Jiang, Z. V. Vardeny, "Confined and delocalized polarons in π-conjugated oligomers and polymers: A study of the effective conjugation length", *Physical Review B* **2004**, *69*, 241204, DOI 10.1103/PhysRevB.69.241204.

[286] S. Baniya, S. R. Vardeny, E. Lafalce, N. Peygambarian, Z. V. Vardeny, "Amplitude-Mode Spectroscopy of Charge Excitations in PTB7 π-Conjugated Donor-Acceptor Copolymer for Photovoltaic Applications", *Physical Review Applied* **2017**, *7*, 064031, DOI 10.1103/PhysRevApplied.7.064031.

[287] M. D. Peeks et al., "Electronic Delocalization in the Radical Cations of Porphyrin Oligomer Molecular Wires", *Journal of the American Chemical Society* **2017**, *139*, 10461–10471, DOI 10.1021/jacs.7b05386.

[288] J. Rawson, P. J. Angiolillo, M. J. Therien, "Extreme electron polaron spatial delocalization in π-conjugated materials", *Proceedings of the National Academy of Sciences* **2015**, *112*, 13779–13783, DOI 10.1073/pnas.1512318112.

[289] P. A. Lane, X. Wei, Z. V. Vardeny, "Studies of Charged Excitations in π-Conjugated Oligomers and Polymers by Optical Modulation", *Physical Review Letters* **1996**, *77*, 1544–1547, DOI 10.1103/PhysRevLett.77.1544.

[290] E. Ehrenfreund, Z. Vardeny, O. Brafman, B. Horovitz, "Amplitude and phase modes in trans -polyacetylene: Resonant Raman scattering and induced infrared activity", *Physical Review B* **1987**, *36*, 1535–1553, DOI 10.1103/PhysRevB.36.1535.

[291] B. Horovitz, "Infrared activity of Peierls systems and application to polyacetylene", *Solid State Communications* **1982**, *41*, 729–734, DOI 10.1016/0038-1098(82)91126-7.

[292] G. Lanzani, *The Photophysics behind Photovoltaic and Photonics*, Wiley-VCH Verlag GmbH & Co. KGaA, Weinheim, **2012**.

[293] U. Fano, "Effects of Configuration Interaction on Intensities and Phase Shifts", *Physical Review* **1961**, *124*, 1866–1878, DOI 10.1103/PhysRev.124.1866.

[294] J. Göres et al., "Fano resonances in electronic transport through a single-electron transistor", *Physical Review B* **2000**, *62*, 2188–2194, DOI 10.1103/PhysRevB.62.2188.

[295] T.-T. Tang et al., "A tunable phonon-exciton Fano system in bilayer graphene", *Nature Nanotechnology* **2010**, *5*, 32–36, DOI 10.1038/nnano.2009.334.

[296] B. Luk'yanchuk et al., "The Fano resonance in plasmonic nanostructures and metamaterials", *Nature Materials* **2010**, *9*, 707–715, DOI 10.1038/nmat2810.

[297] R. Österbacka, C. P. An, X. M. Jiang, Z. V. Vardeny, "Two-Dimensional Electronic Excitations in Self-Assembled Conjugated Polymer Nanocrystals", *Science* **2000**, *287*, 839–842, DOI 10.1126/science.287.5454.839.

[298] K.-C. Chiu et al., "Strong and Broadly Tunable Plasmon Resonances in Thick Films of Aligned Carbon Nanotubes", *Nano Letters* **2017**, *17*, 5641–5645, DOI 10.1021/acs.nanolett.7b02522.

[299] T. Morimoto et al., "Length-dependent plasmon resonance in single-walled carbon nanotubes", *ACS Nano* **2014**, *8*, 9897–9904, DOI 10.1021/nn505430s.

[300] A. L. Falk et al., "Coherent Plasmon and Phonon-Plasmon Resonances in Carbon Nanotubes", *Physical Review Letters* **2017**, *118*, 257401, DOI 10.1103/PhysRevLett.118.257401.

[301] F. J. García de Abajo, "Graphene Plasmonics: Challenges and Opportunities", *ACS Photonics* **2014**, *1*, 135–152, DOI 10.1021/ph400147y.

[302] T. Nakanishi, T. Ando, "Optical Response of Finite-Length Carbon Nanotubes", *Journal of the Physical Society of Japan* **2009**, *78*, 114708, DOI 10.1143/JPSJ.78.114708.

[303] E. S. Zhukova et al., "Terahertz-infrared electrodynamics of single-wall carbon nanotube films", *Nanotechnology* **2017**, *28*, 445204, DOI 10.1088/1361-6528/aa87d1.

[304] K. F. Mak et al., "Measurement of the optical conductivity of graphene", *Physical Review Letters* **2008**, *101*, 196405, DOI 10.1103/PhysRevLett.101.196405.

[305] J. Horng et al., "Drude conductivity of Dirac fermions in graphene", *Physical Review B* **2011**, *83*, 165113, DOI 10.1103/PhysRevB.83.165113.

[306] K. Yanagi et al., "Intersubband plasmons in the quantum limit in gated and aligned carbon nanotubes", *Nature communications* **2018**, *9*, 1121, DOI 10.1038/s41467-018-03381-y.

[307] F. Schöppler et al., "Molar Extinction Coefficient of Single-Wall Carbon Nanotubes", *The Journal of Physical Chemistry C* **2011**, *115*, 14682–14686, DOI 10.1021/jp205289h.

[308] F. Vialla et al., "Universal nonresonant absorption in carbon nanotubes", *Physical Review B* **2014**, *90*, 155401, DOI 10.1103/PhysRevB.90.155401.

[309] J. C. Del Valle, J. Catalán, "Kasha's rule: a reappraisal", *Physical chemistry chemical physics* **2019**, *21*, 10061–10069, DOI 10.1039/c9cp00739c.

[310] P. Hamm, M. Lim, R. M. Hochstrasser, "Structure of the Amide I Band of Peptides Measured by Femtosecond Nonlinear-Infrared Spectroscopy", *The Journal of Physical Chemistry B* **1998**, *102*, 6123–6138, DOI 10.1021/jp9813286.

[311] R. A. Scheidt, G. F. Samu, C. Janáky, P. V. Kamat, "Modulation of Charge Recombination in $CsPbBr_3$ Perovskite Films with Electrochemical Bias", *Journal of the American Chemical Society* **2018**, *140*, 86–89, DOI 10.1021/jacs.7b10958.

[312] A. Schleife, C. Rödl, F. Fuchs, K. Hannewald, F. Bechstedt, "Optical absorption in degenerately doped semiconductors: Mott transition or Mahan excitons?", *Physical Review Letters* **2011**, *107*, 236405, DOI 10.1103/PhysRevLett.107.236405.

[313] G. La Rocca, "Wannier–Mott Excitons in Semiconductors", *Thin Films and Nanostructures* **2003**, *31*, 97–128, DOI 10.1016/S1079-4050(03)31002-6.

[314] S. Gao, Y. Liang, C. D. Spataru, L. Yang, "Dynamical Excitonic Effects in Doped Two-Dimensional Semiconductors", *Nano Letters* **2016**, *16*, 5568–5573, DOI 10.1021/acs.nanolett.6b02118.

[315] J. L. Blackburn, A. J. Ferguson, O. G. Reid, "Spectroscopy of Ground- and Excited-State Charge Carriers in Single-Wall Carbon Nanotubes" in *Handbook of Carbon Nanomaterials*, (Eds.: R. B. Weisman, J. Kono), World Scientific Series on Carbon Nanoscience vol. 9-10, pp. 237–296, World Scientific Publishing Co. Pte. Ltd, Singapore, **2019**, DOI 10.1142/9789813235465_0014.

[316] M. Brohmann et al., "Temperature-Dependent Charge Transport in Polymer-Sorted Semiconducting Carbon Nanotube Networks with Different Diameter Distributions", *The Journal of Physical Chemistry C* **2018**, *122*, 19886–19896, DOI 10.1021/acs.jpcc.8b04302.

[317] S. P. Schießl, M. Rother, J. Lüttgens, J. Zaumseil, "Extracting the field-effect mobilities of random semiconducting single-walled carbon nanotube networks: A critical comparison of methods", *Applied Physics Letters* **2017**, *111*, 193301, DOI 10.1063/1.5006877.

[318] F. Bottacchi et al., "Polymer-sorted (6,5) single-walled carbon nanotubes for solution-processed low-voltage flexible microelectronics", *Applied Physics Letters* **2015**, *106*, 193302, DOI 10.1063/1.4921078.

[319] M. Rother et al., "Aerosol-Jet Printing of Polymer-Sorted (6,5) Carbon Nanotubes for Field-Effect Transistors with High Reproducibility", *Advanced Electronic Materials* **2017**, *3*, 1700080, DOI 10.1002/aelm.201700080.

[320] I. Namal, "Fabrication and Optical and Electronic Characterization of Conjugated Polymer-Stabilized Semiconducting Single-Wall Carbon Nanotubes in Dispersions and Thin Films", University of Würzburg, **2018**.

[321] F. E. M. Silveira, S. M. Kurcbart, "Hagen-Rubens relation beyond far-infrared region", *Europhysics Letters* **2010**, *90*, 44004, DOI 10.1209/0295-5075/90/44004.

[322] B. I. Greene, J. Orenstein, R. R. Millard, L. R. Williams, "Nonlinear optical response of excitons confined to one dimension", *Physical Review Letters* **1987**, *58*, 2750–2753, DOI 10.1103/PhysRevLett.58.2750.

[323] B. I. Greene, J. Orenstein, S. Schmitt-Rink, "All-Optical Nonlinearities in Organics", *Science* **1990**, *247*, 679–687, DOI 10.1126/science.247.4943.679.

[324] D. Huang, J.-I. Chyi, H. Morkoç, "Carrier effects on the excitonic absorption in GaAs quantum-well structures", *Physical Review B* **1990**, *42*, 5147–5153, DOI 10.1103/PhysRevB.42.5147.

[325] R. J. Elliott, "Intensity of Optical Absorption by Excitons", *Physical Review* **1957**, *108*, 1384–1389, DOI 10.1103/PhysRev.108.1384.

[326] W. Kaim, J. Fiedler, "Spectroelectrochemistry", *Chemical Society Reviews* **2009**, *38*, 3373–3382, DOI 10.1039/B504286K.

[327] Y. Zhai, Z. Zhu, S. Zhou, C. Zhu, S. Dong, "Recent advances in spectroelectrochemistry", *Nanoscale* **2018**, *10*, 3089–3111, DOI 10.1039/c7nr07803j.

[328] T. E. Keyes, R. J. Forster, "Spectroelectrochemistry" in *Handbook of electrochemistry*, (Ed.: C. G. Zoski), pp. 591–635, Elsevier, Amsterdam, **2007**, DOI 10.1016/B978-044451958-0.50027-6.

[329] S. Dhungana, A. L. Crumbliss, "UV-Vis Spectroelectrochemistry of Selected Iron-Containing Proteins" in *Spectroelectrochemistry*, (Eds.: W. Kaim, A. Klein), pp. 31–67, Royal Society of Chemistry, Cambridge, **2008**, DOI 10.1039/9781847558404-00031.

[330] S. P. Best, S. J. Borg, K. A. Vincent, "Infrared Spectroelectrochemistry" in *Spectroelectrochemistry*, (Eds.: W. Kaim, A. Klein), pp. 1–30, Royal Society of Chemistry, Cambridge, **2008**, DOI 10.1039/9781847558404-00001.

[331] H.-C. Chang, L.-C. Wang, A Simple Proof of Thue's Theorem on Circle Packing, **2010**, http://arxiv.org/pdf/1009.4322v1 (visited on 08/10/2019).

[332] A. J. Bard, L. R. Faulkner, *Electrochemical methods*, John Wiley & Sons, Inc, New York, **2001**.

[333] N. Elgrishi et al., "A Practical Beginner's Guide to Cyclic Voltammetry", *Journal of Chemical Education* **2018**, *95*, 197–206, DOI 10.1021/acs.jchemed.7b00361.

[334] C. A. Appleby, R. K. Morton, "Lactic dehydrogenase and cytochrome b_2 of baker's yeast. Purification and crystallization", *Biochemical Journal* **1959**, *71*, 492–499, DOI 10.1042/bj0710492.

[335] O. Impert et al., "Kinetics and mechanism of a fast leuco-Methylene Blue oxidation by copper(II)–halide species in acidic aqueous media", *Dalton Transactions* **2003**, 348–353, DOI 10.1039/b205786g.

[336] J. C. Dean, D. G. Oblinsky, S. Rafiq, G. D. Scholes, "Methylene Blue Exciton States Steer Nonradiative Relaxation: Ultrafast Spectroscopy of Methylene Blue Dimer", *The Journal of Physical Chemistry B* **2016**, *120*, 440–454, DOI 10.1021/acs.jpcb.5b11847.

[337] R. A. Ganeev, A. I. Zvyagin, O. V. Ovchinnikov, M. S. Smirnov, "Peculiarities of the nonlinear optical absorption of Methylene blue and Thionine in different solvents", *Dyes and Pigments* **2018**, *149*, 236–241, DOI 10.1016/j.dyepig.2017.09.063.

List of Figures

2.1 Bohr's model of hydrogen and formation of energy bands 6
2.2 Energy band diagrams of intrinsic, non-degenerately doped and degenerately doped semiconductors 7
2.3 Illustration of the Gerischer model 10
2.4 Concept of a (6,5)-SWNT as a rolled-up graphene sheet 12
2.5 Bandstructure of graphene and carbon nanotubes 12
2.6 Tight-binding bandstructure of (6,5)-SWNTs and experimental absorption spectrum 14
2.7 Effects of dimensionality and dielectric environment on optical properties . . . 15
2.8 Exciton motion and nonradiative exciton decay mechanisms 16
2.9 Coulomb-bound quasiparticles in neutral and doped SWNTs 18
2.10 Illustration of delocalized Bloch waves and localization by disorder 20
2.11 Fluctuations in the exciton energy landscape caused by defects and environmental disorder 21
2.12 Schematic illustration of interband and intraband absorption processes 23
2.13 Illustration of the Drude model 24
2.14 Drude-Smith and localization modified Drude model 26
2.15 Backscattering of a charge carrier in a 1D box 28

3.1 Selective dispersion of (6,5)-SWNTs with the polymer PFO-BPy 31
3.2 Absorption spectra of (6,5)-SWNT dispersions prepared by sonication or shear mixing 32
3.3 Schematic illustration of the PLE setup 35
3.4 Components of the femtosecond laser system 36
3.5 Illustration of the transient absorption setup 37
3.6 White light spectrum in the NIR and VIS spectral region 38
3.7 Measurement principle of transient absorption 39
3.8 Different signal contributions composing a TA spectrum and the sensitivity of the TA setup 40
3.9 Autocorrelation and spectrum of visible pump pulses 41
3.10 Time resolution of the TA experiment 42
3.11 White light chirp correction using the coherent artifact 43
3.12 Electrochemical cell used for time-resolved spectroelectrochemistry at SWNT thin films 44

4.1 Absorption spectra upon electrochemical and redox chemical doping 45

4.2 Illustration of the thermodynamics underlying electrochemical and redox chemical doping . . . 47

5.1 Doping-induced interband absorption changes . . . 52
5.2 Doping-induced changes in S_1 exciton energetics and absorption intensity . . . 54
5.3 Limiting cases of delocalized or localized carriers . . . 55
5.4 Charge carrier localization induced by counterion adsorption . . . 56
5.5 Exciton confinement between localized charges . . . 58
5.6 S_1 absorption band fitting taking into account exciton confinement between localized and inhomogeneously distributed charges . . . 59
5.7 Doping-induced absorption changes in the VIS spectral region . . . 60
5.8 Pump-energy dependent transient absorption spectroscopy . . . 62
5.9 Second derivative absorption spectra in the VIS and S_2 exciton blueshift . . . 63
5.10 Comparison of doping-induced absorption changes for (6,5)-SWNTs, a CdTe quantum well and a WS_2 monolayer . . . 66
5.11 Doping level dependent PL spectroscopy . . . 67
5.12 Comparison of doping-induced changes in S_1 exciton energetics for linear absorption and PL spectroscopy . . . 68
5.13 Trion emission spectra at different $AuCl_3$ concentrations . . . 70
5.14 Modeling of S_1 PL quenching upon doping . . . 71
5.15 Transient absorption spectroscopy of doped SWNTs in dispersion . . . 73
5.16 Analysis of the S_1 photobleach decay . . . 74
5.17 Comparison of the relative PLQY from direct steady-state PL measurement with the analysis of the S_1 photobleach dynamics . . . 76
5.18 Broadband transmission spectroscopy of doped SWNT thin-films using the OA dopant . . . 79
5.19 Correlation between loss of NIR interband oscillator strength and increase in low energy intraband oscillator strength . . . 80
5.20 Doping-induced changes in intraband absorption and antiresonances associated with the D- and G-band . . . 81
5.21 Dependence of D-band antiresonance intensity on S_1 oscillator strength . . . 83
5.22 Optical conductivity spectra for different doping levels . . . 85
5.23 Monte-Carlo simulations of the optical conductivity . . . 87
5.24 Correlation of IR peak positions with Monte-Carlo localization lengths . . . 88
5.25 Model accounting for the transition of localized to delocalized carriers . . . 89

6.1 Absorption spectra of intrinsic, moderately and heavily doped SWNTs in solution 95
6.2 Doping-induced changes in transient absorption spectra . . . 97
6.3 Comparison of steady-state and transient absorption of intrinsic and heavily doped SWNTs . . . 98
6.4 Analysis of the NIR and VIS optical nonlinearities in intrinsic SWNTs . . . 100

6.5 NIR transient absorption spectroscopy of SWNT thin-films with variable doping level . . . 103
6.6 Analysis of the pump-induced photoabsorption band located at the energetic H-band origin . . . 104
6.7 Comparison of doping-induced absorbance changes in 1D and 2D semiconductors 105
6.8 Drude analysis of heavily doped SWNTs and film thickness determination . . . 108
6.9 Analysis of the Beer-Lambert law validity for intrinsic and heavily doped SWNTs 110

7.1 Charge carrier densities based on exciton confinement induced by localized charges . . . 114
7.2 Illustration and results of the phase space filling model applied to doping processes 116
7.3 Dependencies of the relative S_1 exciton bleaching on temperature, exciton size and effective carrier mass . . . 119
7.4 Density of states, Fermi-level dependent carrier density and doping-induced changes in first subband related interband absorption . . . 120
7.5 Comparison of extracted carrier densities using three different models . . . 122

8.1 Schematic illustration of the flow-electrolysis cell HX-301 and the flow cycle . 126
8.2 Modeling of working electrode carbon fibers as closest packing of equal rods . 127
8.3 Cyclic voltammogram of $K_4Fe(CN)_6$ for different scan rates . . . 128
8.4 Conversion efficiency of the flow-electrolysis cell . . . 129
8.5 Determination of the uncompensated resistance using the current interrupt method . . . 131
8.6 Steady-state and time-resolved spectroelectrochemistry of methylene blue . . . 132

Acknowledgement

This work was only possible due to the support of many people during the last years. In the following, I would like to thank all my collaborators and supporters:

- *Prof. Tobias Hertel* for the opportunity to carry out my research in his group and the numerous national and international conferences I could attend. In addition, I would like to thank him for his ongoing support and the fruitful discussions about the experimental results.
- *Pascal Kunkel* for the careful proofreading of this thesis, the pleasant atmosphere in the ultrashort laser lab and the sharing of data regarding his experiments with the flow-electrolysis cell
- *Dr. Friedrich Schöppler* for all the useful comments during the last years, the proofreading of my thesis and his IGOR procedure for nanotube bandstructure calculations
- *Florian Oberndorfer* for his nanotube samples and the proofreading of this thesis
- My collaborators outside the Hertel group: *Larry Lüer*, *Abasi Abidulimu*, and *Florian Hirsch* for their time-resolved and FTIR experiments on doped nanotube films. *Michael Auth* for the determination of nanotube film thicknesses and *Julia Heitmüller* for the collaboration in the project about time-resolved spectroelectrochemistry. I would also like to express my gratitude to *Benedikt Halbig* for the supply of intrinsic silicon substrates.
- *Fabian Glaab*, *Niklas Noll* and *Roman Ickert* for the help during their internships
- The technical assistants *Sabine Stahl*, *Ivonne Vollert*, *Belina Böhm* and *Sabine Fuchs* for the support and providing the chemistry and laser lab infrastructure
- *Sabine Walther* for her help in all the administrative work
- All the so far unmentioned members of the Hertel group for the pleasant atmosphere in the office/lab and during the lunch/coffee breaks. I thank you also for all the lovely activities outside the university
- The members of the electronic and mechanical workshop, namely *Rainer Eck*, *Wolfgang Liebler*, *Ralf Kohrmann*, *Katharina Schreckling* and *Peter Lang* for the fabrication and maintenance of all kind of devices

Finally, I want to express my gratitude to my family. I thank my parents *Edeltraud Eckstein* and *Hermann Eckstein*, who always believed in me and made it possible for me to develop to the person I am now. My deepest gratitude goes to my beloved girlfriend *Sabine Stahl* and my daughter *Mathilda Eckstein*, who tolerated my frequent lousy mood during the writing of this thesis. Thank you, Sabine, for your love and the ongoing support whenever possible. You showed me that the most beautiful aspects of life are located outside the scientific world.